CONFERENCE PROCEEDINGS

ZBORNIK RADOVA

MECHANICAL TECHNOLOGIES AND STRUCTURAL MATERIALS

STROJARSKE TEHNOLOGIJE I KONSTRUKCIJSKI MATERIJALI

Split

Croatia / Hrvatska

21. - 22. September / rujan 2017.

ORGANIZED BY / ORGANIZATOR:

CROATIAN SOCIETY FOR MECHANICAL TECHNOLOGIES, Croatia

HRVATSKO DRUŠTVO ZA STROJARSKE TEHNOLOGIJE, Hrvatska

CO-ORGANIZERS / SURGANIZATORI:

UNIVERSITY OF SPLIT
FACULTY OF ELECTRICAL ENGINEERING, MECHANICAL ENGINEERING AND NAVAL ARCHITECTURE

CROATIAN SOCIETY FOR MATERIALS AND TRIBOLOGY

DUBLIN INSTITUTE OF TECHNOLOGY

SLOVAK ACADEMY OF SCIENCE INSTITUTE OF MATERIALS AND MACHINE MECHANICS

ROGANTE ENGINEERING OFFICE

UNIVERSITY OF SPLIT
UNIVERSITY DEPARTMENT OF PROFESSIONAL STUDIES

SPONSORS / SPONZORI:

UNIVERSITY OF SPLIT

SPLIT – DALMATIA COUNTY

MINISTRY OF SCIENCE, EDUCATION AND SPORTS OF THE REPUBLIC OF CROATIA

EVN CROATIA PLIN d.o.o.

PUBLISHER / IZDAVAČ:

CROATIAN SOCIETY FOR MECHANICAL TECHNOLOGIES, Croatia

HRVATSKO DRUŠTVO ZA STROJARSKE TEHNOLOGIJE, Hrvatska

c/o FESB, Ruđera Boškovića 32, 21000 SPLIT

tel.: +385 21 305 910; fax.: +385 21 463 877

e-mail: info@strojarska-tehnologija.hr

http://www.strojarska-tehnologija.hr

EDITORS / UREDNICI:

PhD Sonja Jozić, Assistant Professor
PhD Branimir Lela, Associate Professor

ISSN 1847-7917

ISSUE / NAKLADA: 55

ORGANIZING COMMITTEE:
ORGANIZACIJSKI ODBOR

- Sonja JOZIĆ (Croatia) - Chairman
- Branimir LELA (Croatia) – Vice Chairman

- Ante ALUJEVIĆ (Croatia)
- Ante BAROVIĆ (Croatia)
- Nikša ČATIPOVIĆ (Croatia)
- Zvonimir DADIĆ (Croatia)
- Igor GABRIĆ (Croatia)
- Nikola GJELDUM (Croatia)
- Dario ILJKIĆ (Croatia)
- Jure KROLO (Croatia)
- Neven KUZMANIĆ (Croatia)
- Petar LJUMOVIĆ (Croatia)
- Zvonimir MRDULJAŠ (Croatia)
- Ivan PEKO (Croatia)
- Stipe PERIŠIĆ (Croatia)
- Slaven ŠITIĆ (Croatia)
- Mario VEIĆ (Croatia)

PROGRAMME AND REVIEW COMMITTEE:
PROGRAMSKI I RECENZIJSKI ODBOR

- Dražen ŽIVKOVIĆ (Croatia) – President
- Dražen BAJIĆ (Croatia) – Vice President

- Boris ANZULOVIĆ (Croatia)
- Frane BARBIR (Croatia)
- Franjo CAJNER (Croatia)
- Goran CUKOR (Croatia)
- Vinko IVUŠIĆ (Croatia)
- Zlatko JANKOSKI (Croatia)
- Jaroslav JERZ (Slovakia)
- David KENNEDY (Ireland)
- Zoran PANDILOV (Macedonia)
- Mladen PERINIĆ (Croatia)
- Massimo ROGANTE (Italy)
- Zdravko SCHAUPERL (Croatia)
- František SIMANČIK (Bratislava)
- Božo SMOLJAN (Croatia)
- Goran ŠIMUNOVIĆ (Croatia)
- Katica ŠIMUNOVIĆ (Croatia)
- Matej VESENJAK (Slovenia)
- Ivica VEŽA (Croatia)

CONTENT

1. ***Tomislav BAZINA, Maja MARKOVIĆ, Duško PAVLETIĆ, Zoran JURKOVIĆ***
APPLICATION OF MACHINE VISION FOR INJECTION MOULDING PRODUCTS DETECTION AND RECOGNITION 1

2. ***Marina CRNJAC, Nikola GJELDUM, Boženko BILIĆ, Marko MLADINEO***
THE APPLICATION OF TAGUCHI METHOD FOR CHOOSING THE OPTIMAL TABLE CONSTRUCTION 11

3. ***Nikša ČATIPOVIĆ, Dražen ŽIVKOVIĆ, Zvonimir DADIĆ, Marin VICEIĆ***
INFLUENCE OF THE SALT BATH AGITATION AND AUSTEMPERING TEMPERATURE ON THE MICROSTRUCTURE OF AUSTEMPERED DUCTILE IRON 17

4. ***Zvonimir DADIĆ, Dražen ŽIVKOVIĆ, Nikša ČATIPOVIĆ,Josip BILIĆ***
HIGH PRESSURE DIE CASTING MOULD REPAIR TECHNOLOGIES 23

5. ***Mario DRAGIČEVIĆ, Sonja JOZIĆ, Dražen BAJIĆ***
FINITE ELEMENT SIMULATION OF STRESSES DISTRIBUTION AND TOOL DISPLACEMENT IN THE CUTTING TOOL DURING HARD END-MILLING IN DIFFERENT MACHINING CONDITIONS 29

6. ***Igor GABRIĆ, Anja MILAVIĆ, Ivan VRLJIČAK***
APPLICATION OF CRAFTS - LAMONT DIAGRAMS FOR ASSESSING THE DISTRIBUTION OF HARDNESS AFTER TEMPERING EN 42CRMO4 STEEL 37

7. ***Fuad HADŽIKADUNIĆ, Nedeljko VUKOJEVIĆ, Amra TALIĆ-ČIKMIŠ***
NUMERICAL ANALYSIS OF THE STRESS-DEFORMATION STATE OF SIGMA PROFILE OF SCRAPER CONVEYOR 43

8. ***Jaroslav JERZ, František SIMANČÍK, Jaroslav KOVÁČIK, Ján ŠPANIELKA***
ALUMINIUM FOAM FOR THERMO-ACTIVE PITCHED ROOFS OF NEARLY ZERO-ENERGY BUILDINGS 49

9. ***Mate JURJEVIĆ, Žarko KOBOEVIĆ, Nikša KOBOEVIĆ, Dragan BEBIĆ***
IMPROVEMENTS ON THE DIESEL ENGINE EXHAUST VALVE TO EXTEND TIME TO MAINTENANCE 59

10. ***Jaroslav KOVÁČIK, Natália MINÁRIKOVÁ, Peter ŠUGÁR, Jana ŠUGÁROVÁ, Martin FRNČÍK, Štefan EMMER, José RODRIGUEZ, Inmaculada CAÑADAS, Joana KULASA, Szymon MALARA, Marcin LIS***
GAS NITRIDING OF TITANIUM IN SOLAR FURNACE 65

11. ***Jure KROLO, Branimir LELA, Petar LJUMOVIĆ***
ELECTRICAL CONDUCTIVITY AND MECHANICAL PROPERTIES OF THE SOLID STATE RECYCLED EN AW 6082 ALLOY 71

12. ***Marko MLADINEO, Ivica VEŽA, Slavica JURČEVIĆ, Ivan ZNAOR***
PERFORMANCE ANALYSIS OF THE RFID-ENABLED MANUFACTURING EXECUTION SYSTEM 77

13. ***Štefan NAGY, Pavol ŠTEFÁNIK, Ivo VÁVRA, Martin NOSKO, Ľubomír OROVČÍK, Andrej OPÁLEK, Karol IŽDINSKÝ, Stanislav KÚDELA Jr., František SIMANČÍK***
METHODICS OF SAMPLE PREPARATION OF MG/CARBON FIBER COMPOSITE FOR TEM AND CHARACTERIZATION OF THE INTERFACE 83

14. ***Iva NAKIĆ, David IŠTOKOVIĆ, Mladen PERINIĆ, Goran CUKOR***
IMPLEMENTATION OF ADDITIVE TECHNOLOGY IN MEDICINE 89

15. ***Ľubomír OROVČÍK, Martin NOSKO, Alica ROSOVÁ***
EBSD OF ALUMINIUM POWDER COMPACTS - PREPARATION METHOD FOR OBSERVATION IN DEPENDENCE ON POWDER SIZE 99

16. ***Ivan PEKO, Jure KROLO, Petra BAGAVAC, Stefan ĐURIĆ, Nikola KOSTIĆ, Andrej BAŠIĆ***
MODELING AND OPTIMIZATION OF TENSILE STRENGTH OF ABS PARTS MANUFACTURED BY THE FUSED DEPOSITION MODELING PROCESS 103

17. ***Massimo ROGANTE, Pavol MIKULA, Pavel STRUNZ, Anatoliy ZAVDOVEEV***
RESIDUAL STRESS DETERMINATION BY NEUTRON DIFFRACTION IN LOW-CARBON STEEL WIRES WITH ACCUMULATED SHEAR DEFORMATION 111

18. ***Massimo ROGANTE, Imre KOVÁCS, Emilio NOTTI, Antonello SALA, Zoltán SZŐKEFALVI-NAGY***
FEASIBILITY STUDY FOR PIXE AND NEUTRON BEAM TECHNIQUES ON FISHING NETS MADE OF POLYMERIC MATERIALS 117

19. ***László ROSTA, Massimo ROGANTE***
NEUTRONS FOR MATERIALS RESEARCH 123

20. ***Božo SMOLJAN, Dario ILJKIĆ, Sunčana SMOKVINA HANZA, Lovro ŠTIC, Andrej BORIĆ, Bojan SENČIĆ, Robert VERTNIK***
NUMERICAL MODELLING AND SIMULATION OF CONTROLLED COOLING OF HOT ROLLED STEEL 133

21. ***Katica ŠIMUNOVIĆ, Sara HAVRLIŠAN, Tomislav ŠARIĆ, Ilija SVALINA, Roberto LUJIĆ, Goran ŠIMUNOVIĆ,***
EFFECT OF SAMPLE DIMENSIONS AND FUSING TEMPERATURE ON COATING/BASE MATERIAL STRUCTURE OBTAINED BY FLAME SPRAYING 141

22. ***Mario VEIĆ, Dražen BAJIĆ, Sonja JOZIĆ***
DEVELOPMENT AND OPTIMIZATION OF SURFACE ROUGHNESS PREDICTIVE MODELS IN TURNING SUPER DUPLEX STAINLESS STEEL BY USING ARTIFICIAL INTELLIGENCE METHODS 149

23. ***Ladislav VRSALOVIĆ, Marko MATULIĆ, Stjepan KOŽUH, Ivana IVANIĆ, Mirko GOJIĆ***
EFFECT OF PH ON CORROSION OF CUALMN ALLOY IN 0.9% NACL SOLUTION 159

24. ***Anatoliy ZAVDOVEEV, Valeriy POZNIAKOV, Massimo ROGANTE, Sergey JDANOV, Andrey MAKSIMENKO***
WELDABILITY OF S460M HIGH STRENGTH LOW-ALLOYED STEEL 163

ORAL CONTRIBUTION

Phase field modeling of the microstructure formation during additive manufacturing of Ni superalloys

Toni Ivas[1]

[1]Empa-Swiss Federal Laboratories for Materials Science and Technologies, Ueberlandstrasse 129, Switzerland

Ni-based superalloys are state-of-art materials used for stationary gas turbine or aero-engine parts. Additive manufacturing (AM) enables unique freedom in shape design and functionality. However, the microstructures of AM processed Ni superalloys are very complex. Modeling and simulation of the microstructure formation may help in optimizing not only the AM process but also the alloy compositions.

In this work, the thermal history in the AM parts during by selective laser melting of the commercial Ni-superalloy CM247LC were modeled and simulated using finite element methods. During the process cooling rates between 10^3 and 10^5 K/s. This rapid solidification of the melt pool may lead to solute trapping and phase transformations far away from equilibrium. The finite interphase dissipation phase field model developed by Steinbach et al. [1,2] addresses the problem of solute trapping by introducing additional kinetic equation that describes the redistribution of the species between the phases. This model has been adapted and phase field simulation results of Ni-Al as a simplified binary model alloy under AM conditions will be presented. The computational analysis is then compared to the experimental results obtained by Electron Microscopy and X-ray diffraction study on additively manufactured CM247LC alloy .

[1] I. Steinbach, L. Zhang, M. Plapp, Phase-field model with finite interface dissipation, Acta Mater. 60 (2012) 2689–2701.

[2] L. Zhang, M. Stratmann, Y. Du, B. Sundman, I. Steinbach, Incorporating the CALPHAD sublattice approach of ordering into the phase-field model with finite interface dissipation, Acta Mater. 88 (2015) 156–169.

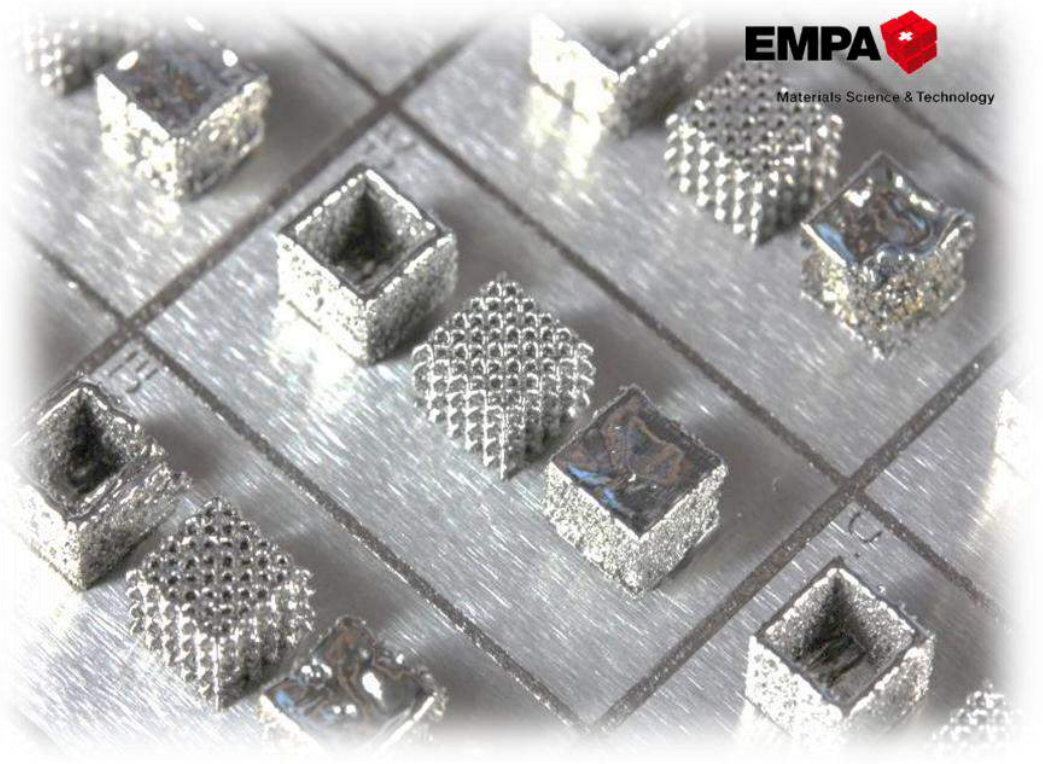

To achieve best results Fesb racing team annually represents Croatia on international formula student competitions. Combining calculations with software simulations our members gain valuable experience for their future careers.

Follow our journey

facebook.com/FesbRacingTeam

instagram.com/fesbracingteam

ups.fesb@gmail.com

+385 91 329 8489

UPS
Udruga Primijenjenog Strojarstva

FESB

ISSN 1847-7917

Primjena strojnog vida za detektiranje i prepoznavanje proizvoda dobivenih ubrizgavanjem u kalup

Tomislav BAZINA, Maja MARKOVIĆ, Duško PAVLETIĆ, Zoran JURKOVIĆ
Sveučilište u Rijeci, Tehnički fakultet/
University of Rijeka, Faculty of Engineering,
Vukovarska 58, 51000 Rijeka,
Hrvatska/Croatia

tbazina@gmail.com
mmarkovic2@riteh.hr
dusko.pavletic@riteh.hr
zoran.jurkovic@riteh.hr

Keywords
Image processing
Injection moulding products
Machine vision
Object detection and recognition
OpenCV

Ključne riječi
Obrada slike
Proizvodi dobiveni ubrizgavanjem u kalup
Strojni vid
Detektiranje i prepoznavanje predmeta
OpenCV

Stručni članak

Sažetak: Strojni vid je pronašao široku primjenu u industriji, posebice u području mjerenja i kontrole kvalitete, te automatskoj manipulaciji robotom. U radu je dan pregled osnovnih pojmova vezanih za obradu slike, kao temelj za primjenu strojnog vida. Kroz teorijsku razradu, uz primjere upotrebe, prikazane su metode analize slike, te metode detektiranja i prepoznavanja objekata. Prikazano je i programsko rješenje, temeljeno na programskom jeziku Python i računalnim paketima OpenCV i NumPy, korišteno kod detektiranja i prepoznavanja proizvoda dobivenih u procesu ubrizgavanja plastike u kalup. Učinkovitost programskog rješenja pri prepoznavanju predmeta, te određivanju njihove konture, pozicije i orijentacije, testirana je na nizu slika prikupljenih industrijskom kamerom.

Application of Machine Vision for Injection Moulding Products Detection and Recognition

Professional paper

Abstract: Machine Vision is found useful in industry, especially at facilities where measuring and quality control are of key importance. Also, where there is requirement for automatic robot manipulation Machine Vision is very valuable. This paper presents an overview of fundamental concepts related to image processing, as a basis for the application of Machine Vision. Different methods of digital image analysis and detection or recognition of objects are presented in this work paper together with their application examples supported by theoretical elaboration. Python programming language and the OpenCV and NumPy program packages, were used for development of software solution for detection and recognition of products manufactured in the plastic injection molding process. The efficiency of the software solution in object recognition, contour detection, position and orientation definition is tested on a series of images obtained with an industrial camera.

1. Uvod (engl. Introduction)

Današnje industrijske kamere su vrlo pristupačne cijenom i kao takve mogu imati značajnu ulogu u proizvodnoj industriji, a sam strojni vid (MV) se sve češće implementira u proizvodne procese. Strojni vid je skup tehnologija za automatsku analizu baziranu na obradi slika, te je svoju primjenu pronašao u industriji, poglavito za automatsko navođenje robota, mjerenje i kontrolu kvalitete, te kontrolu procesa. Temeljen je na računalnom vidu kao računarskoj znanosti, a sam strojni vid spada u inženjerske discipline. Ovaj rad obuhvaća teorijski dio popraćen konkretnim primjerom implementacije strojnog vida u praksi. U prvom dijelu rada objašnjene su korištene metode pri analizi slike prema [1-3]. Detektiranje i prepoznavanje predmeta u prostoru je jedan od velikih izazova MV-a, a pod tim pojmovima se podrazumijeva sposobnost programa da otkrije nalazi li se objekt u zadanom interesnom području, te njegova identifikacija. Za uspješno detektiranje i prepoznavanje predmeta nužno je upotrijebiti čitav niz međusobno komplementarnih tehnika prema [4-17], koje su pojašnjene u drugom dijelu rada. U svrhu prepoznavanja i detektiranja proizvoda dobivenih u procesu ubrizgavanja plastike u kalup, konkretno čepa i koljena cijevi, izrađeno je programsko rješenje u programskom jeziku *Python*. Pri izradi rješenja korišteni su programski paketi za računalni vid *OpenCV* [18] i za znanstveno računalno programiranje *NumPy*, a sam algoritam i testiranje programskog rješenja prikazani su u trećem dijelu rada.

2. Metode analize slike (engl. Image analysis methods)

Slika se, u svrhu analize, prikazuje u matričnom zapisu u *blue-green-red* formatu. Svaki piksel slike ima pripadajući intenzitet boje, kojim se određuje udio svake od tri navedene boje. Matrični zapis slike se može pojednostaviti na način da se tri vrijednosti svakog piksela, koje predstavljaju udjele plave, zelene i crvene boje, zamijene jednom vrijednošću. Na taj način se

Oznake/Symbols

A_K	- površina unutar konture - contour area
b	- parametar funkcije odluke - decision function parameter
C	- regulacijski parametar - regularization parameter
C_x, C_y	- koordinate centroida konture - contour centroid coordinates
$D(\mathbf{X})$	- funkcija odluke - decision function
$f(x, y)$	- funkcija gustoće raspodjele intenziteta - density distribution function of intensity
k	- broj grupa značajki - number of feature clusters
$K(\mathbf{X}_i,\mathbf{X})$	- kernel presjeka histograma - histogram intersection kernel
l	- broj vektora značajki za učenje algoritma - number of training feature vectors
m	- dimenzija vektora značajki - feature vector dimension
M_{pq}	- moment slike reda $(p+q)$ - $(p+q)$-th image moment
p, q	- indeks reda momenta slike - image moment order subscript
x, y	- koordinate slike - image coordinates
$\mathbf{X}$	- vektor značajki za testiranje algoritma - testing feature vector
$\mathbf{X}_i$	- vektor značajki za testiranje algoritma - training feature vector
z_i	- pokazatelj klase - class indicator

Grčka slova/Greek letters

α_i	- parametar funkcije odluke - decision function parameter
θ_K	- kut orijentacije objekta, rad - object orientation angle
μ_{pq}	- centralni moment slike reda $(p+q)$ - $(p+q)$-th central image moment

Indeksi/Subscripts

p, q	- red momenta slike image moment order

Skraćenice/Abbreviations

BOVW	- model zbirki značajki Bag of visual words
C-SVC	- *C*-klasifikacija potpornih vektora *C*-Support Vector Classification
FLANN	- Fast Library for Approximate Nearest Neighbors
MV	- strojni vid - machine vision
NMS	- potiskivanje nemaksimalnih vrijednosti - Non-maximum suppression
ROI	- interesno područje slike - region of interest
SURF	- Speeded-Up Robust Features
SVM	- Metoda potpornih vektora - Support vector machines

dobiva prikaz slike u nijansama sive. U sljedećih nekoliko poglavlja su pojašnjene metode analize slike koje su korištene u programskom rješenju za detektiranje i prepoznavanje predmeta:

- Bilateralno zamagljivanje,
- Morfološke transformacije,
- Detektiranje rubova,
- Detektiranje konture.

2.1. Metoda Bilateralnog zamagljivanja (engl. Bilateral filtering)

Zamagljivanje se koristi za uklanjanje nepoželjnog šuma sa slike. Posljedica uklanjanja šuma je i zamagljivanje rubova promatranih predmeta. Pri tradicionalnom zamagljivanju se za filtriranje pojedinog piksela koriste samo okolni pikseli, odnosno vrijednost izlaznog piksela je samo funkcija prostora.

Kako bi se istovremeno rubovi očuvali oštrima i uklonio šum sa slike, u programskom rješenju se koristi metoda bilateralnog zamagljivanja [1]. Za razliku od tradicionalnog zamagljivanja, pri bilateralnom zamagljivanju se koristi i sličnost pojedinog piksela sa okolnim po vrijednosti, odnosno fotometrijska sličnost. Vrijednost izlaznog piksela je funkcija prostora i razlike u intenzitetu. Pri zamagljivanju se u obzir uzimaju samo pikseli sličnog intenziteta. Kako su na rubovima prisutne velike razlike u intenzitetu piksela, oni se ne zamagljuju. Posljedično, zbog potrebe za dodatnim proračunima, proces bilateralnog zamagljivanja je znatno sporiji od postupaka tradicionalnog zamagljivanja.

2.2. Metoda morfološke transformacije (engl. Morphological transformations)

Morfološke transformacije su jednostavne operacije, koje se izvršavaju na binarnim slikama. Binarne slike su takve slike, čiji pikseli mogu poprimiti samo dvije vrijednosti, odnosno crnu i bijelu. Za morfološku transformaciju je, osim binarne slike, potrebno definirati i veličinu i oblik

okolnog područja koje određuje izlaznu vrijednost svakog piksela, tj. kernel.
U programskom rješenju se koristi morfološka operacija zatvaranja za kompletiranje konture detektiranog objekta. Zatvaranje je složena morfološka transformacija, koja se sastoji od dilatacije, te zatim erozije, kako prikazuje slika 1.

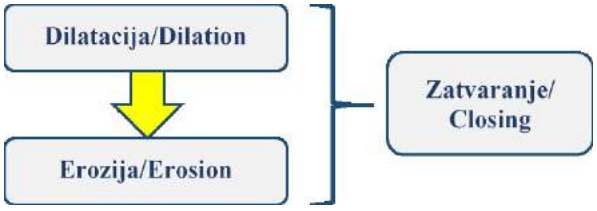

Slika 1. Morfološka transformacija zatvaranja
Figure 1. Morphological transformation closing

Dilatacija se, kao jednostavna morfološka transformacija, koristi za spajanje prekinutih dijelova objekta, odnosno za zatvaranje konture. Posljedica toga je povećana površina objekta, te je zato potrebno primijeniti morfološku operaciju erozije. Erozija smanjuje površinu objekta na početnu, a rezultat je cjeloviti predmet.

2.3. Detektiranje rubova (engl. Edge detection)

Detektiranje rubova na slici je jedan od glavnih zadataka MV-a. Rubovi su definirani kao linije na kojima je prisutna velika razlika u intenzitetu piksela u odnosu na okolna područja. Koriste se pri određivanju konture pojedinih predmeta, te detektiranju i opisivanju značajki objekata. U praksi postoji nekoliko algoritama za detektiranje rubova od kojih će u nastavku biti pojašnjen *Canny* algoritam.
Canny detektor rubova je primijenjen u programskom rješenju zbog svoje visoke učinkovitosti. On se sastoji od pet koraka [2]:

- Gaussovo zamagljivanje slike u svrhu uklanjanja šuma,
- Određivanje gradijenta intenziteta slike, te njegovog smjera,
- Potiskivanje zona u kojima nije maksimum gradijenta intenziteta,
- Filtriranje jakih i slabih rubova pomoću dvije granične vrijednosti,
- Praćenje slabih rubova i njihove povezanosti sa jakim rubovima pomoću histereze.

Standardna implementacija algoritma je izmijenjena na način da je u prvom koraku umjesto Gaussovog zamagljivanja upotrebljeno bilateralno zamagljivanje radi očuvanja rubova. Na slici 2 je prikazan primjer detektiranja rubova cijevnog čepa i cijevnog koljena *Canny* algoritmom.

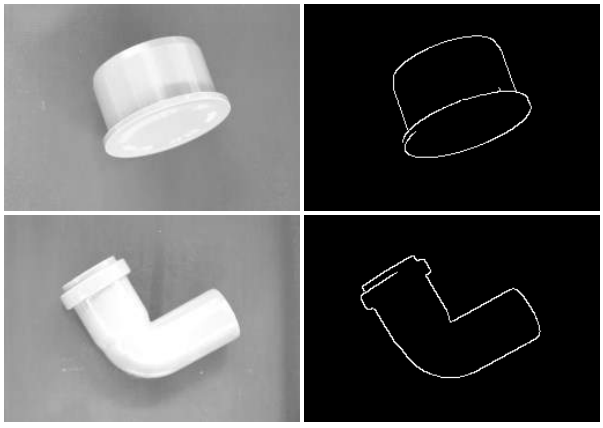

Slika 2. Rubovi čepa i koljena cijevi detektirani *Canny* algoritmom
Figure 2. Pipe cap and elbow edges detected with *Canny* algorithm

2.4. Detektiranje konture (engl. Contour detection)

Konture su kontinuirane linije koje spajaju sve točke istog intenziteta boje. Konture se u sklopu MV-a koriste za određivanje pozicije objekta, njegove orijentacije, aproksimacije oblika, određivanja interesnog područja slike (ROI), te prepoznavanja i praćenja predmeta.
U svrhu određivanja pozicije, orijentacije i površine objekta omeđenog konturom potrebno je odrediti momente slike. Moment slike je težinski prosjek intenziteta piksela slike. Dvodimenzionalni momenti $(p+q)$-tog reda slike, čija je funkcija gustoće raspodjele intenziteta piksela $f(x, y)$, računaju se prema izrazu [3]:

$$M_{pq} = \int_{-\infty}^{\infty}\int_{-\infty}^{\infty} x^p y^q f(x,y)dxdy, \quad p,q = 0,1,2\Lambda\ . \tag{1}$$

Budući da se momenti računaju pomoću konture, potrebno je, pomoću *Greenovog* teorema, prevesti plošni integral iz jednadžbe (1) u krivuljni integral po zatvorenoj konturi.
Pozicija predmeta se može odrediti pomoću geometrijske sredine konture, odnosno centroida, prema [3]:

$$C_x = \frac{M_{10}}{M_{00}}, \quad C_y = \frac{M_{01}}{M_{00}}. \tag{2}$$

Površina unutar konture, koja služi kao kriterij za odbacivanje netočno detektiranih kontura, određena je relacijom [3]:

$$A_K = M_{00}. \tag{3}$$

Za određivanje orijentacije objekta, nužno je odrediti centralne momente slike reda $(p+q)$ prema jednadžbi [3]:

$$\mu_{pq} = \int_{-\infty}^{\infty}\int_{-\infty}^{\infty} (x - C_x)^p (y - C_y)^q f(x,y)dxdy. \tag{4}$$

Jednadžbu (4) je također potrebno prevesti u krivuljni integral po zatvorenoj krivulji pomoću *Greenovog* teorema. Kut orijentacije objekta unutar konture računa se pomoću izraza [3]:

$$\tan(2\theta_K) = \frac{2\mu_{11}}{\mu_{20} - \mu_{02}}, \quad \mu_{20} - \mu_{02} \neq 0. \tag{5}$$

Kako bi se točno odredila pozicija i orijentacija promatranog objekta, od iznimne je važnosti točno opisivanje konture oko istog. Slika 3 prikazuje cijevni čep i koljeno s određenom konturom, centroidom i koordinatnim osima.

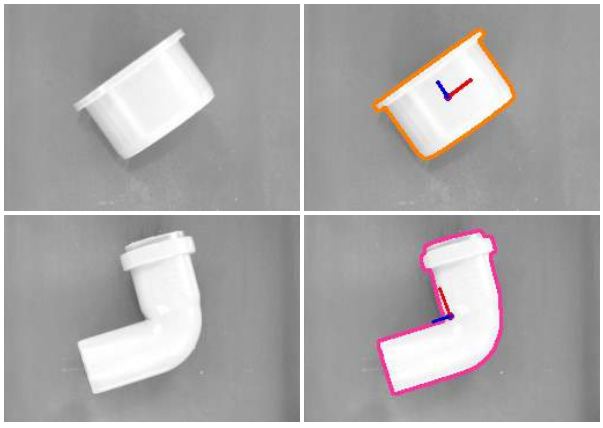

Slika 3. Kontura, centroid i koordinatne osi cijevnog čepa i koljena
Figure 3. Pipe cap and elbow contour, centroid and axes

3. Metode detektiranja i prepoznavanja predmeta (engl. Object detection and recognition methods)

Pod pojmom detektiranje predmeta se podrazumijeva sposobnost programa da otkrije nalazi li se neki objekt u određenom ROI-u, a pod pojmom prepoznavanje predmeta se podrazumijeva identifikacija pronađenog objekta. Za uspješno detektiranje i prepoznavanje predmeta nužno je upotrijebiti čitav niz međusobno komplementarnih tehnika, koje će biti pojašnjene u nastavku [4]:

- Detektiranje i opisivanje značajki slike/Image features detection and description,
- Uspoređivanje značajki slike/Matching image features,
- Piramida slika/Image pyramid,
- Klizajući prozori/Sliding windows,
- *Non-maximum suppression* (NMS),
- Metoda potpornih vektora/Support vector machines (SVM),
- *Bag of visual words model* (BOVW),
- Grupiranje *k*-sredina/*k*-means clustering.

3.1. Detektiranje i opisivanje značajki slike (engl. Image features detection and description)

Značajke slike su jedinstvena i lako prepoznatljiva područja slike, poput kutova i rubova, koja se znatno razlikuju od ostatka slike. One imaju ključnu ulogu u prepoznavanju i razlikovanju promatranih predmeta. Za međusobnu usporedbu značajki, prvo ih je potrebno detektirati, a zatim i opisati. Značajke se opisuju na način da se odabere prikladno područje na slici, koje okružuje detektiranu značajku, a zatim se to područje pronalazi na drugim slikama.

U programskom rješenju je, za pronalaženje i opisivanje značajki slike, primijenjen algoritam pod nazivom *Speeded-Up Robust Features* (SURF) [5]. SURF detektor značajki je baziran na Hesseovoj matrici, odnosno na matrici koja sadrži parcijalne derivacije drugog reda intenziteta piksela slike. Za ubrzano filtriranje slike potreban je brz izračun sume intenziteta piksela slike, pri čemu je iskorišten koncept integralne slike [6]. Značajke slike se pronalaze na područjima slike, gdje je iznos determinante Hesseove matrice maksimalan. Objekti koji se međusobno uspoređuju su često u različitim mjerilima, stoga je potrebno i značajke slike detektirati u različitim mjerilima. Pritom se koristi koncept sličan metodi piramida slika, odnosno prikazu slike u više različitih mjerila, koji je detaljnije pojašnjen u poglavlju 3.3. Jedina razlika je u tome, što se umjesto skaliranja slike mijenja veličina filtera za detektiranje značajki. Za zadržavanje samo najizraženijih značajki primijenjena je NMS metoda prema [7]. Nakon detektiranja, značajke se opisuju na način da im se prvo odredi orijentacija, kako bi se iste značajke mogle pronaći pri različitim orijentacijama promatranog objekta. Orijentacija se određuje pomoću kružnog područja oko značajke, čija veličina ovisi o mjerilu pri kojem je značajka pronađena. Pronađena i opisana značajka se sprema u obliku 64-dimenzionalnog vektora na način da se oko značajke opiše orijentirani kvadrat sa 16 potpodručja. Svako potpodručje je opisano 4-dimenzionalnim vektorom koji predstavlja temeljni intenzitet tog područja. Značajke čepa i koljena cijevi detektirane SURF algoritmom, zajedno s njihovom veličinom i orijentacijom, prikazane su plavom bojom na slici 4.

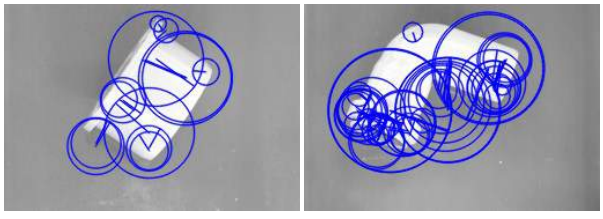

Slika 4. SURF značajke čepa i koljena cijevi
Figure 4. Pipe cap and elbow SURF features

3.2. Uspoređivanje značajki slike (engl. Matching image features)

Uspoređivanje značajki je jedna od nužnih metoda za detektiranje i razlikovanje predmeta. Značajke opisane SURF algoritmom su 64-dimenzionalni vektori, stoga njihovo uspoređivanje spada u problem pretraživanja visoko-dimenzionalnih prostora. Za pretraživanje se

najčešće koriste aproksimativne metode zbog svoje brzine i zadovoljavajuće točnosti.
U ovom radu je upotrebljena metoda *Fast Library for Approximate Nearest Neighbors* (FLANN) [8]. Ova metoda je sastavljena od dva algoritma bazirana na *k*-dimenzionalnim stablima. *k*-dimenzionalna stabla su poseban tip podataka za uređivanje informacija u *k*-dimenzionalnom prostoru, nužan za efikasno pretraživanje značajki. Pretražiuje se pomoću algoritma nasumično generiranih *k*-dimenzionalnih stabala, učinkovitim pri nižem broju dimenzija ili algoritma hijerarhijski strukturiranih stabala *k*-sredina. Odabir algoritma ovisi o preciznosti pretraživanja i tome postoji li korelacija između detektiranih značajki.

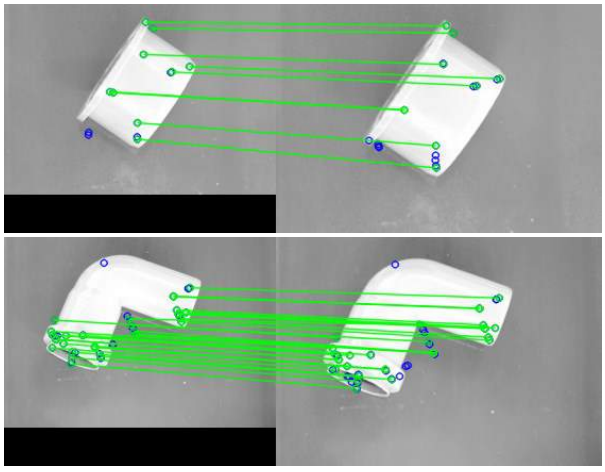

Slika 5. Usporedba SURF značajki čepa i koljena cijevi FLANN metodom
Figure 5. FLANN based matching of pipe cap and elbow SURF features

Algoritmi su samooptimirajući, kombinacija parametara koja pruža najbolje rješenje se automatski odabire prema ustroju ulaznih podataka.
Na slici 5 je prikazana usporedba SURF značajki čepa i koljena cijevi FLANN metodom. Značajke su pronađene na dvije slike, onoj izvorne veličine i onoj uvećanoj za 20%. Podudaranje značajki je prikazano zelenom bojom.

3.3. Piramida slika (engl. Image pyramid)

Piramida slika je prikaz slike u više različitih mjerila [9]. Tehnika je razvijena u sklopu MV-a kako bi se omogućilo detektiranje predmeta u različitim mjerilima. Piramida se konstruira na način da se početna slika smanji određenim proizvoljnim faktorom, te se zamagli kako bi se ublažili prijelazi.
Postupak se nastavlja sve dok se ne dostigne određena minimalna veličina slike, kako je prikazano na slici 6.
U poglavlju 3.6. je objašnjen postupak učenja algoritma za detektiranje i prepoznavanje predmeta pomoću slika. Koncept piramide slike je nužan, obzirom da je vrlo malo vjerojatno pojavljivanje objekata na slici upravo iste veličine kao i na setu slika za učenje algoritma.

Slika 6. Metoda piramide slike
Figure 6. Image pyramid method

3.4. Klizajući prozori (engl. Sliding windows)

Primjenom metode klizajućih prozora omogućuje se pretraživanje manjih područja slike (ROI). Prozor određenih dimenzija se za proizvoljni korak pomiče po slici s lijeva na desno, te po završetku analize reda spušta za proizvoljni korak prema dolje i nastavlja analizu. U području slike koje obuhvaća prozor se detektiraju i uspoređuju značajke, te se na taj način može odrediti gdje se nalazi traženi objekt. Kombinacijom metoda piramide slike i klizajućih prozora se može točno detektirati ROI u kojem se nalazi predmet, i to u odgovarajućem mjerilu. Problem koji nastaje primjenom metode klizajućih prozora je preklapanje prozora unutar kojih postoji određena vjerojatnost pojave traženog objekta. Pri rješavanju tog problema pomaže *Non-maximum suppression* metoda.

3.5. Potiskivanje nemaksimalnih vrijednosti (engl. Non-maximum suppression (NMS))

Non-maximum suppression (NMS) metoda se, u sklopu MV-a, koristi za potiskivanje područja slike u kojima su detektirani predmeti, a preklapaju se u određenoj mjeri. Preklapanje ukazuje na to da je isti objekt detektiran više puta, pa je potrebno zadržati samo ono područje u kojem je vjerojatnost pronalaska objekta najviša. Postoji poveći

broj NMS metoda, od kojih je u programskom rješenju primijenjena vrlo brza verzija prema [10]. Princip metode je prikazan u sljedećih nekoliko koraka:

- Sakupljanje područja slike u kojima je objekt detektiran zajedno s njihovim vjerojatnostima,
- Izračun površine svakog područja,
- Odabir područja s najvišom vjerojatnošću i izračun postotnog preklapanja površine sa svim ostalim područjima,
- Potiskivanje svih područja, čije je postotno preklapanje s odabranim područjem više od proizvoljno određene granice,
- Odabir sljedećeg područja po iznosu vjerojatnosti i ponavljanje postupka, naravno, bez potisnutih područja.

Rezultat obrade područja slike u kojima su detektirani objekti od interesa NMS metodom je slika na kojoj su naznačena samo područja maksimalne vjerojatnosti pojave objekta i to bez znatnih preklapanja.

3.6. Metoda potpornih vektora (engl. Support vector machines (SVM))

Metoda potpornih vektora (SVM) se, kao metoda strojnog učenja, koristi za klasifikaciju podataka u visoko-dimenzionalnom prostoru. Za klasifikaciju je potreban set podataka za učenje kako bi se odredili parametri klasifikacijskog modela. Od niza različitih SVM modela, u programskom rješenju je upotrebljen model pod nazivom *C*-klasifikacija potpornih vektora (C-SVC) [11], [12]. Podaci za učenje algoritma su 64-dimenzionalni vektori SURF značajki $\mathbf{X}_i$ i pokazatelj klase z_i [11]:

$$(\mathbf{X}_1, z_1), (\mathbf{X}_2, z_2), (\mathbf{X}_3, z_3), \mathrm{K}, (\mathbf{X}_l, z_l), \quad i = 1, \mathrm{K}, l, \tag{6}$$

gdje l označava ukupan broj vektora značajki, dobivenih sa slika za učenje algoritma. Pokazatelj klase z_i poprima vrijednost 1, ako vektor značajki $\mathbf{X}_i$ pripada čepu, a -1 ako pripada koljenu [11]:

$$z_i = \begin{cases} 1, & \text{ako je } \mathbf{X}_i \in \text{klase A - čep} \\ -1, & \text{ako je } \mathbf{X}_i \in \text{klase B - koljeno.} \end{cases} \tag{7}$$

Pomoću vektora značajki $\mathbf{X}_i$ i pripadnih pokazatelja klase z_i određuje se funkcija odluke $D(\mathbf{X})$ tijekom faze učenja algoritma [11]:

$$\begin{aligned} &D(\mathbf{X}) = \sum_{i=1}^{l} \alpha_i K(\mathbf{X}_i, \mathbf{X}) + b, \\ &D(\mathbf{X}) > 0, \quad \text{ako je } \mathbf{X} \in \text{klase A - čep}, \\ &D(\mathbf{X}) \le 0, \quad \text{ako je } \mathbf{X} \in \text{klase B - koljeno}, \end{aligned} \tag{8}$$

gdje je $\mathbf{X}$ detektirani vektor značajki na slikama za testiranje algoritma, a α_i i b parametri funkcije odluke, koji se određuju na temelju podataka za učenje prema izrazu (6). Funkcija $K(\mathbf{X}_i, \mathbf{X})$ označava kernel, koji određuje na koji način će biti razdvojene značajke različitih klasa. Na temelju strukture ulaznih podataka je potrebno odabrati pravilan oblik kernela. U programskom rješenju je korišten kernel presjeka histograma oblika [13]:

$$K(\mathbf{X}_i, \mathbf{X}) = \sum_{j=1}^{m} \min(\mathbf{X}_{ij}, \mathbf{X}_j), \tag{9}$$

gdje m označava dimenziju vektora SURF značajki $\mathbf{X}$ i $\mathbf{X}_i$, tj. 64. Kernel presjeka histograma je baziran na histogramu boje slike, odnosno reprezentaciji slike pomoću raspodjele boje. Svaki interval histograma sadrži broj piksela, čiji intenzitet boje se nalazi u zadanom rasponu. Upravo je taj kernel odabran zbog svoje brzine, jednostavnosti i visoke stope prepoznavanja predmeta [13]. Problem određivanja parametara funkcije odluke α_i i b se svodi na problem optimizacije [12].

Vektore značajki $\mathbf{X}_i$ u visoko-dimenzionalnom prostoru je potrebno odvojiti optimalnim hiper-ravninama, odnosno potprostornim područjima, čija dimenzija je za jedan niža od prostora u kojem se nalaze. Optimalne hiper-ravnine se postavljaju tako da je marginalno područje, koje dijeli značajke različitih klasa, što veće [11]. Pri optimizaciji je važno podesiti vrijednost regulacijskog parametra C. Pomoću njega se određuje oštrina algoritma, odnosno osjetljivost na pojavu greške. Pri visokim vrijednostima parametra C je vjerojatnost pogrešne klasifikacije predmeta niža, ali je moguć izostanak detektiranja objekta [4].

Za prihvaćanje, odnosno odbacivanje detektiranih predmeta je upotrebljenja vrijednost funkcije odluke $D(\mathbf{X})$ prema izrazu (8). Dobivena vrijednost predstavlja udaljenost pronađenih značajki od hiper-ravnine razgraničenja klasa. Što je ta udaljenost veća, po apsolutnoj vrijednosti, to je vjerojatnost pronalaska objekta u tom području viša [12].

3.7. Model zbirki značajki (engl. Bag of visual words (BOVW))

Bag of visual words (BOVW) [14] je metoda kategorizacije značajki slike u tzv. rječnike. Rječnik je sačinjen od grupiranih značajki sa slika za učenje. Grupe su oblikovane metodom grupiranja *k*-sredina/*k*-means clustering [15]. To je aproksimativna metoda, kojom se značajke grupiraju prema najvišoj lokalnoj sličnosti. Postupak započinje stvaranjem k grupa i određivanjem njihovog središta. Svaka značajka se dodjeljuje grupi, čije središte joj je najbliže. Nakon toga se ponovno određuju središta grupa. Metoda je iterativna, a postupak se prekida kad se središta prestanu mijenjati.

Nakon grupiranja *k*-sredina, svaka grupa značajki je reprezentirana posebnom vizualnom riječi, odnosno vektorom iste dimenzije kao i značajke. Veličina BOVW rječnika je jednaka broju grupa značajki, odnosno broju vizualnih riječi. Grupiranjem sličnih značajki sa slika za učenje se znatno smanjuje broj vektora za kasniju usporedbu, a da se pritom održava visok stupanj reprezentativnosti. Naravno, kako bi se održala dovoljna raznolikost vizualnih riječi, važno je odabrati prikladan broj k grupa. Pri visokom broju k grupa se znatno usporava proces uspoređivanja značajki, a pri niskom se smanjuje reprezentativnost.

U praksi je određivanje broja *k* grupa kompromis između točnosti i brzine izvođenja, tako da se veličine BOVW rječnika mogu kretati od 200 do 320 000 [16]. Postoji nekoliko pristupa određivanju broja *k* grupa, od kojih je, za procjenu minimuma, korišten jednostavan prema [17]:

$$k \approx \sqrt{\frac{l}{2}}, \tag{10}$$

gdje je *l* već spomenuti broj značajki, dobivenih sa slika za učenje algoritma.

4. Programsko rješenje za detektiranje i prepoznavanje predmeta (engl. Object detection and recognition software)

U svrhu prepoznavanja i detektiranja proizvoda dobiveni ubrizgavanjem u kalup, odnosno cijevnog čepa i cijevnog koljena, izrađeno je programsko rješenje u programskom jeziku *Python*. Korišteni su programski paketi za računalni vid *OpenCV* [18] i za znanstveno računalno programiranje *NumPy*, a dijelovi programskog koda su preuzeti iz [4].

4.1. Algoritam programskog rješenja (engl. Software algorithm)

Postupak rješavanja problema detektiranja i prepoznavanja predmeta je prikazan na slici 7. Algoritam započinje prikupljanjem slika za učenje. Slike su prikupljene pomoću industrijske kamere Basler acA2500-60uc s pripadajućom programskom podrškom za upravljanje pod nazivom *pylon*. Radno okruženje prikazano je na slici 8. Pri prikupljanju slika posebna je pažnja dana kontroliranju količine svjetlosti i nastanka sjene. Baza slika za učenje algoritma je stvorena pomoću skripte, koja slike iz kamere smanjuje na 256 x 179 piksela, pobrojava ih i zapisuje u nijansama sive. Snimljene su 423 slike cijevnog koljena i isti broj slika cijevnog čepa, od kojih je nekoliko prikazano na slikama 2, 3, 4 i 5. Područje snimanja kamere je odabrano tako da obuhvati cijeli objekt, koji je blago rotiran između uzastopnih slika, kako bi se pokrilo što više mogućih orijentacija. Prikupljene slike su iskorištene za detektiranje i opisivanje 29357 značajki SURF algoritmom.

Opisane značajke su grupirane u BOVW rječnik sa 2048 grupa. Broj grupa je određen iz jednadžbe (10), ali je znatno povećan zbog bolje reprezentativnosti. Nakon grupiranja slijedi učenje SVM algoritma. Regulacijski parametar *C* je postavljen na vrijednost 2^8, što je odabrano kao najpogodnija vrijednost nakon testiranja algoritma. Radi kasnije upotrebe, BOVW rječnik i SVM algoritam su pohranjeni u XML datoteke.

Pri testiranju programskog rješenja, učitana je slika za testiranje, veličina klizajućeg prozora je postavljena na 160 x 160 piksela, a korak prozora na 8 piksela. Faktor skaliranja piramide slike postavljen je na vrijednost 1,1.

U području slike, iznad kojeg se nalazi klizajući prozor, vrši se detektiranje i opisivanje značajki, te na temelju njih detektiranje i prepoznavanje predmeta naučenim SVM algoritmom. Područja, čija je vrijednost funkcije odluke $D(\mathbf{X})$, prema izrazu (8), viša od određene vrijednosti se zadržavaju. Visoka apsolutna vrijednost funkcije odluke ukazuje na visoku vjerojatnost pronalaska objekta unutar tog područja.

Područja, čije se površine preklapaju više od 15%, potiskuju se NMS metodom i preostaju samo područja maksimalne vjerojatnosti pojave predmeta. Ta područja se prikazuju na slici za testiranje. Nakon toga slijedi detektiranje rubova predmeta unutar područja *Canny* algoritmom i spajanje prekinutih rubova morfološkom transformacijom zatvaranja. Pomoću detektiranih rubova određena je kontura prepoznatih predmeta, a preko izraza (2) i (5) pozicija i orijentacija predmeta, te su oni prikazani na slici za testiranje.

4.2. Testiranje programskog rješenja (engl. Software testing)

Programsko rješenje je testirano uz pomoć 48 slika, na kojima je mijenjan broj predmeta za detektiranje od jednog do četiri. Ispitana je efikasnost detektiranja i prepoznavanja pri promjeni pozicije, orijentacije i raznolikosti detektiranih objekata. Slike za testiranje su veličine 538 x 660 piksela. Vrijeme izvođenja algoritma je u prosjeku 1,5 minuta, a znatno ovisi o koraku klizajućeg prozora, faktoru skaliranja piramide slike, broju detektiranih značajki i veličini slike. Rezultati testiranja programskog rješenja pri prepoznavanju pojedinačnih predmeta prikazani su na slici 9. Područja slike unutar kojih je detektiran cijevni čep su označena narančastom bojom, a područja unutar kojih je pronađeno cijevno koljeno rozom bojom. Konture predmeta su označene istom pripadajućom bojom. Ishodište koordinatnog sustava određuje poziciju, a koordinatne osi orijentaciju objekta.

Iznad svakog područja slike je upisana apsolutna vrijednost funkcije cilja $D(\mathbf{X})$ kao mjera pouzdanosti rezultata. Prihvatljive vrijednosti funkcije cilja se razlikuju od slučaja do slučaja. Iz rezultata detektiranja i prepoznavanja pojedinačnih proizvoda sa slike 9 se može zaključiti da se cijevni čepovi pouzdanije raspoznaju. Područje slike bolje opisuje pronađeni cijevni čep, nego koljeno. Kontura i orijentacija predmeta je točno određena. Rezultati sa ostalih slika za testiranje pojedinačnih predmeta ukazuju na slične pojave.

Na slici 10 su prikazani rezultati pri prepoznavanju nekoliko čepova, odnosno koljena. Cijevni čepovi, zajedno sa svojom konturom, točno su detektirani u velikoj većini slučajeva, odnosno pri gotovo svim ispitivanim pozicijama i orijentacijama. Prilikom detekcije koljena, veći broj značajki je koncentriran na proširenom dijelu, stoga se može dogoditi da koljeno nije potpuno obuhvaćeno detektiranim područjem slike. To uzrokuje i nemogućnost opisivanja konture detektiranog koljena. Kako bi se povisila točnost detektiranja i prepoznavanja, potrebno je povećati bazu slika za učenje algoritma.

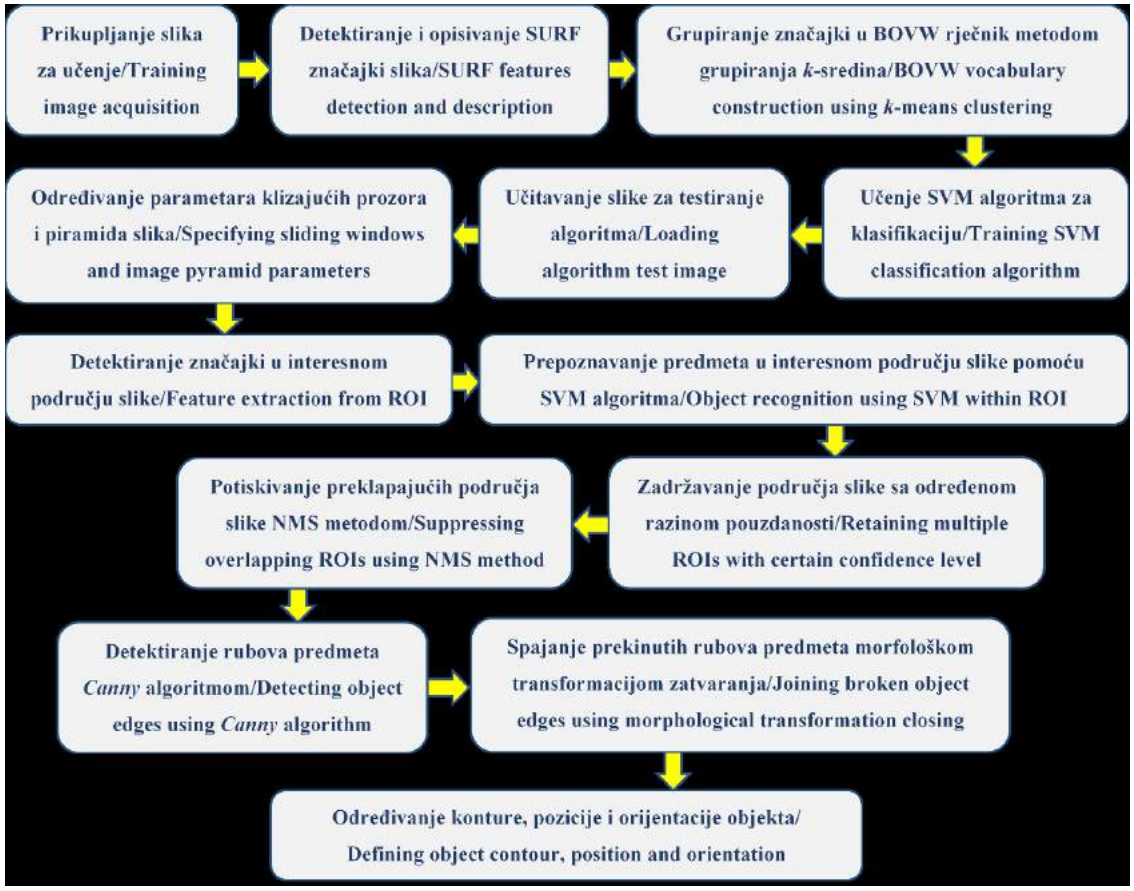

Slika 7. Algoritam programskog rješenja za detektiranje i prepoznavanje predmeta
Figure 7. Object detection and recognition software algorithm

Slika 8. Radno okruženje za prikupljanje slika
Figure 8. Working environment for image acquisition

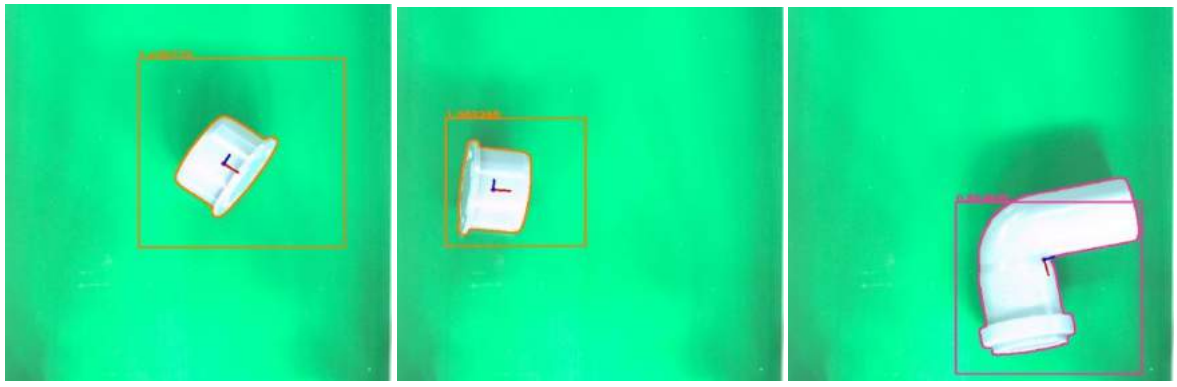

Slika 9. Detektiranje i prepoznavanje pojedinačnih objekata od interesa
Figure 9. Detection and recognition of individual objects of interest

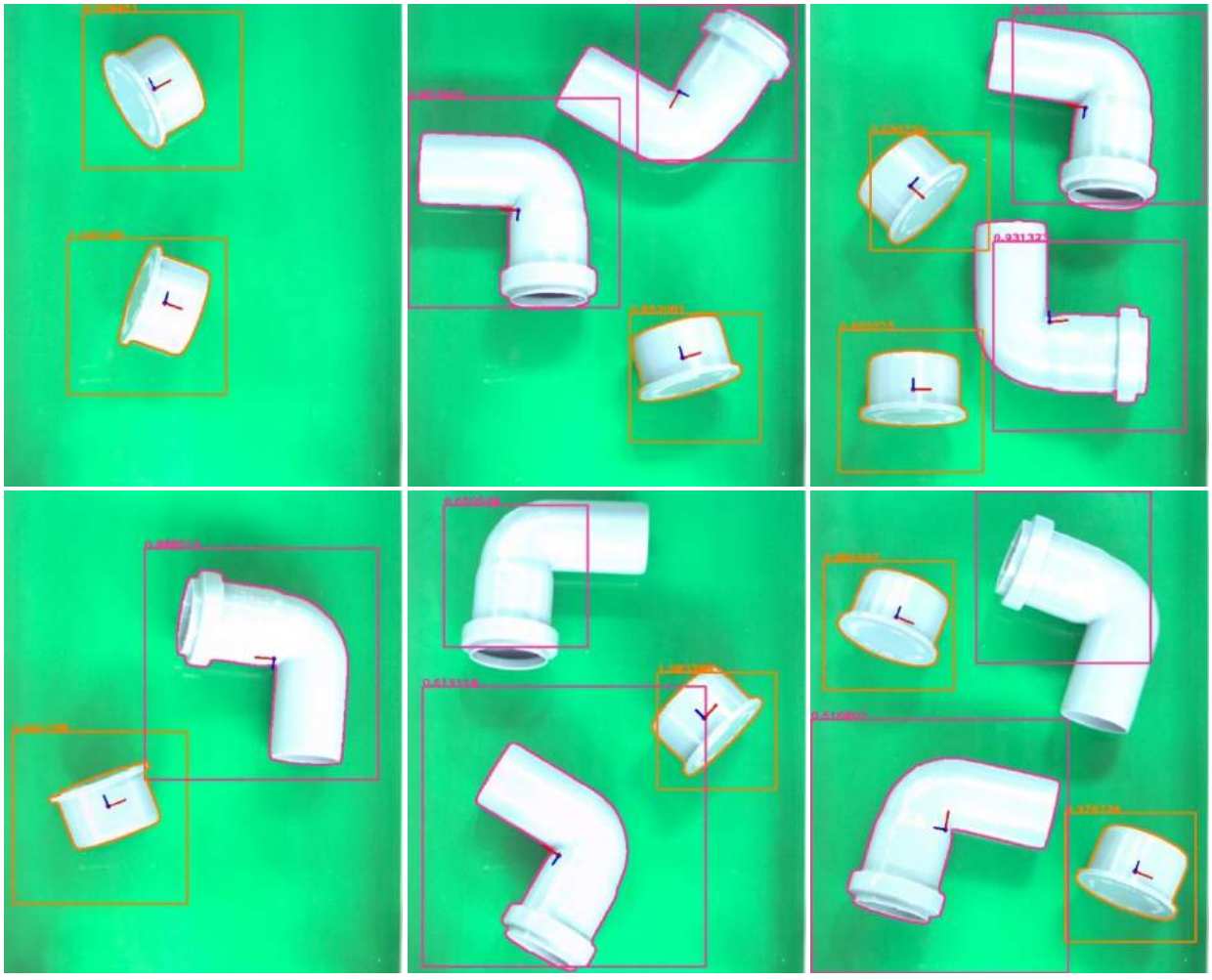

Slika 10. Detektiranje i prepoznavanje nekoliko objekata od interesa
Figure 10. Detection and recognition of several objects of interest

5. Zaključak (engl. Conclusion)

Kroz rad su prikazane korištene metode analize slike koje dovode do detektiranja objekata u interesnom području, te njegove identifikacije, određivanja pozicije i orijentacije. U tu svrhu koristi se mnogo tehnika koje rezultiraju izvođenjem algoritma u trajanju od oko 1,5 minute, što je previše za analizu u trenutku (engl. real-time), stoga bi se u daljnjem istraživanju trebao koristiti noviji i brži detektor značajki poput *Oriented FAST and Rotated BRIEF* (ORB) detektora, koji kombinira tehnike *Features from Accelerated Segment Test* (FAST)

detektora ključnih točaka i *Binary Robust Independent Elementary Features* (BRIEF) deskriptora. Također, ORB deskriptori bolje opisuju značajke od SURF deskriptora [19]. Daljnje povećanje brzine izvođenja algoritma se može postići korištenjem grafičke procesorske jedinice (GPU) za intenzivne izračune. U prethodnim istraživanjima se broj značajki kretao od 100 000 [8], preko 640 000 [14], pa sve do 1 000 000 [16], što je znatno više od oko 30 000 značajki cijevnog čepa i koljena sa slika za učenje korištenih u ovom radu. Kako bi se izradio reprezentativniji BOVW rječnik, potrebno je povećati broj značajki, tj. prikupiti veći broj slika za učenje. Time bi se poboljšalo i samo detektiranje i prepoznavanje objekata prilikom analize slike. Daljnje istraživanje ide u smjeru implementacije programskog rješenja u proizvodni sustav, podrazumijevajući pritom i povezivanje s robotom u svrhu sortiranja i kontrole kvalitete (odnosno odvajanja defektnih proizvoda, upozorenja nakon određenog broja takvih proizvoda i dr.). Također, planirana je i usporedba s postojećim komercijalnim rješenjima i analiza izvedivosti i isplativosti implementacije.

Zahvala/Acknowledgements

Rad je financijski podržan potporom Sveučilišta u Rijeci, ugovor broj 13.09.1.2.10.
This work was supported by the Croatian Science Foundation – project 8722 and the University of Rijeka (contract no. 13.09.1.1.05).

REFERENCE/REFERENCES

[1] Tomasi C., Manduchi R., (1998), *Bilateral filtering for gray and color images*, IEEE International Conference on Computer Vision, Bombay, India

[2] Canny J., (1986), *A Computational Approach to Edge Detection*, IEEE Transactions on Pattern Analysis and Machine Intelligence, Vol. 8, No. 6, p 679-698, Washington, DC, U.S.A

[3] Hu M.-K., (1962), *Visual Pattern Recognition by Moment Invariants*, IRE Transactions on Information Theory, Vol. 8, No. 2, p 179-187

[4] Minichino J., Howse J., (2015), *Learning OpenCV 3 Computer Vision with Python, Second Edition*, Packt Publishing, United Kingdom

[5] Bay H., Ess A., Tuytelaars T., Van Gool L., (2008), *Speeded-Up Robust Features (SURF)*, Computer Vision and Image Understanding, Vol. 110, No. 3, p 346-359

[6] Viola P., Jones M., (2001), *Rapid object detection using a boosted cascade of simple features*, Computer Vision and Pattern Recognition, Kauai

[7] Neubeck A., Van Gool L., (2006), *Efficient Non-Maximum Suppression*, 18th International Conference on Pattern Recognition, Hong Kong

[8] Muja M., Lowe D. G., (2009), *Fast approximate nearest neighbors with automatic algorithm configuration*, Fourth International Conference on Computer Vision Theory and Applications, Lisboa

[9] Adelson E. H., Anderson C. H., Bergen J. R., Burt P. J., Ogden J. M., (1984), *Pyramid Method in Image Processing*, RCA Engineer, Vol. 29, No. 6, p 33-41

[10] Malisiewicz T., (13.08.2011), *Tombone's Computer Vision Blog: blazing fast nms.m (from exemplar-svm library)*, http://www.computervisionblog.com/2011/08/blazing-fast-nmsm-from-exemplar-svm.html, Accessed 05.05.2017.

[11] Boser B. E., Guyon I. M., Vapnik V. N., (1992), *A Training Algorithm for Optimal Margin Classifiers*, 5th Annual ACM Workshop on Computational Learning Theory, Pittsburgh

[12] Chang C.-C., Lin C.-J., (2011), *LIBSVM: A Library for Support Vector Machines*, ACM Transactions on Intelligent Systems and Technology (TIST), Vol. 2, No. 3, p 27:1-27:27

[13] Barla A., Odone F., Verri A., (2003), *Histogram intersection kernel for image classification*, International Conference on Image Processing, 2003. ICIP 2003., Barcelona

[14] Csurka G., Dance C. R., Fan L., Willamowski J., Bray C., (2004), *Visual Categorization with Bags of Keypoints*, Workshop on statistical learning in computer vision, ECCV, Vol. 1, No. 1-22, p 1-16

[15] Duda R. O., Hart P. E., Stork D. G., (2000), *Pattern Classification, Second Edition*, Wiley, New York

[16] Yang J., Jiang Y.-G., Hauptmann A. G., Ngo C.-W., (2007), *Evaluating Bag-of-Visual-Words Representations in Scene Classification*, 9th ACM SIGMM International Workshop on Multimedia Information Retrieval, MIR 2007, Augsburg

[17] Kodinariya T. M., Makwana P. R., (2013), *Review on determining number of Cluster in K-Means Clustering*, International Journal of Advance Research in Computer Science and Management Studies, Vol. 1, No. 6, p 90-95

[18] Bradski G., (2000), *Dr. Dobb's Journal of Software Tools*

[19] Rublee E., Rabaud V., Konolige K., Bradski G., (2011), *ORB: An efficient alternative to SIFT or SURF*, ICCV '11 Proceedings of the 2011 International Conference on Computer Vision, p 2564-2571, Washington, DC, U.S.A

ISSN 1847-7917

The application of Taguchi method for choosing the optimal table construction

Marina CRNJAC, Nikola GJELDUM, Boženko BILIĆ, Marko MLADINEO
University of Split, Faculty of Electrical Engineering, Mechanical Engineering and Naval Architecture, Department for Production Engineering
Sveučilište u Splitu, Fakultet elektrotehnike, strojarstva i brodogradnje, R. Boskovica 32, 21 000 Split, Croatia

mcrnjac@fesb.hr
ngjeldum@fesb.hr
bbilic@fesb.hr

Keywords
Taguchi method
Optimization
Table construction
Design of experiment

Ključne riječi
Taguchi metoda
Optimizacija
Konstrukcija stola
Planiranje pokusa

Original scientific paper
Abstract: New trends in the world show that 3D modeling and simulation of different variants of the product are very often used during the development phase and design of the product. It is very important to shorten the time spent on development and construction of product in today's market conditions. Modelling and simulation can contribute to this. This paper shows the application of the Taguchi method in order to model the table for machining. The table for machining will be used in Lean Learning Factory at Faculty of electrical engineering, mechanical engineering and naval architecture (FESB). The Taguchi method is often used to solve engineer problems, especially in the area of product quality. By using the Design Expert software, a plan for experiments was made for three different versions of the table. According to the plan of experiments, different versions of the table were drawn in the NX Siemens software. The simulations have been made to determine a displacement of each table during the action of vertical and horizontal force. The analysis of displacement and mass was made and the optimal solution was proposed.

Izvorni znanstveni rad
Sažetak: Novi trendovi u svijetu danas pokazuju da se vrlo često prilikom razvoja i konstruiranja proizvoda koristi 3D modeliranje i simuliranje različitih izvedbi proizvoda. S obzirom na vrlo turbulentno tržište, vrlo važno je skratiti ciklus proizvodnje. Modeliranje i simulacija mogu u tome mnogo doprinijeti. U ovom radu je prikazano korištenje Taguchi metode u modeliranju stola za strojnu obradu. Stol za strojnu obradu će biti korišten u Tvornici za učenje na Fakultetu elektrotehnike, strojarstva i brodogradnje (FESB). Metoda je često korištena za rješavanje inženjerskih problema, posebno u području kvalitete proizvoda. Primjenom programskog paketa Design Expert je napravljen plan pokusa za tri različite izvedbe stola. Prema planu pokusa, nacrtane su izvedbe stolova u programskom paketu NX Siemens i napravljene su simulacije kako bi se utvrdio progib pojedine konstrukcije prilikom djelovanja vertikalne i horizontalne sile. Cilj je bio pronaći konstrukciju stola koja ima minimalan progib i minimalnu masu. Provedena je analiza progiba i mase konstrukcije te je predloženo optimalno rješenje.

1. Introduction

Today every organization tries to find different methods to increase their productivity, reduce losses and maximize profits. The project Innovative Smart Enterprise (INSENT) was launched to find different methods for improvement of the production process and product development. Since 2009, Lean Learning Factory has been establishing at Laboratory for Industrial Engineering at Faculty of Electrical Engineering, Mechanical Engineering and Naval Architecture (FESB) in Split. Lean Learning Factory at FESB is based on a didactical concept emphasizing experimental and problem based learning using tools and methods from Lean management [1]. This concept of Lean Learning Factory presents a simulation of real factory environment. It is also important to establish Digital Factory as part of Lean Learning Factory. The main aim is to "see" the product before it is produced, or production system before it is made [2]. There is special equipment that enables students to learn about real processes through simulations. The Taguchi method, 3D modeling, and simulations are used for learning purposes. Whole process is used to show students how different methods and software solutions can help organizations to reduce the time for development and construction and thereby choose an optimal variant of the product. Here in this paper whole process is shown on simple product – table. With optimal construction, it is possible to avoid an oversized product that results with inappropriate weight and higher construction costs. There are three important design stages in the Taguchi method [3]:

1. System Design is characterized by definition of the problem and application of knowledge and achievements to develop a prototype that represents the initial state of the product or process features.
2. Parameter design determines the initial states of all features, which will minimize product or process variations. The orthogonal field is selected depending on the number of controlled parameters, the experiments are performed based on the orthogonal field, the data are analyzed and the optimal state is identified.
3. Tolerance design determines the tolerances of features, which will minimize product or process variations.

Part of Taguchi's method, related to parameter design is a systematic method that applies statistical procedures and tests for shaping function and optimization of shape. P-diagram is used as the base model for Taguchi method, it is shown in figure 1.

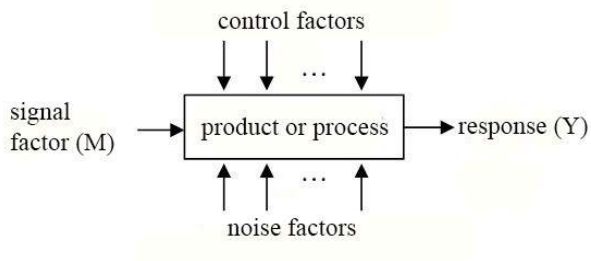

Figure 1. P-diagram [1]
Slika 1. P-dijagram [1]

There are several stages in the planning of experiment:
1) Clear definition and formulation of the problem
2) Review and analysis of all available information about the problem
3) Preparation and selection of the strategy (model use, factor selection, plan of experiments)
4) Performance of first experiment (test)
5) Corrections
6) Performance of other experiments
7) Evaluation of results and comparison with similar research
8) Interpretation of results
9) Conclusion

In this paper, Taguchi method is used to find the optimal construction. The orthogonal arrays are used to organize collected information about effects of controlled factors and about effects of uncontrolled factors and their required levels. With orthogonal arrays and analysis, it is possible to find optimal construction for the table. The optimal construction includes the minimal weight of the table and minimal displacement during the action of vertical and horizontal force. The oversize of construction and big displacement present problems so optimization will be done between three table variants. The basic procedure of this method is by varying the levels of controlled factors, observe their impact on a system response. This approach reduces time and costs of experimenting. The optimization with Taguchi method will be realized through several steps:
1) Defining target values for table construction
2) Determination of control factors
3) Selection of appropriate orthogonal arrays for defined factors that affect table construction (Selection of orthogonal array depends on a number of factors and their levels. In this case, the standard orthogonal array is used but if factors and their levels are not appropriate for standard array there are rules for modification of standard arrays.)
4) Performance of experiments according to conditions in selected orthogonal arrays (Collection of data about influence of selected factors and their levels on defined problems)
5) Analysis of data to select optimal solution

The aim is to achieve a minimal total weight of the table and minimal deflection of the table during the action of horizontal and vertical force.

2. Definition of factors and creation of plan for experiments

According to the defined problem (or target values of the construction), factors of construction are determined. Factors that have the biggest influence on achieving the aim are being considered. They are shown in table 1.

Table 1. Factors and each level

Tablica 1. Parametri i svaka razina

factors	level 1.	level 2.	level 3.
A – frame dimension	80	100	120
B – leg dimension	40	50	60
C – stiffener dimension	40	50	60

The table material is not taken as a factor because it is predefined as well as table height. Table material is constructional steel (St 44-2) and table hight is 900 mm. There are three factors with three levels so orthogonal array L9 is selected. It means that is necessary to do 9 experiments. The software package Design Expert was used for planning experiments and analysis [4]. Three table variants are taken for analysis, the variants are shown in figure 2.

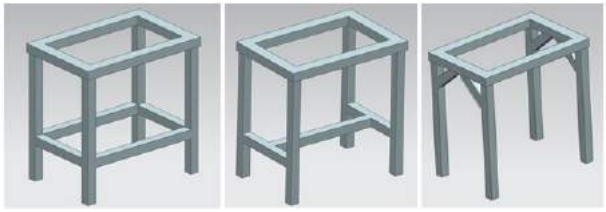

Figure 2. Table variants, experiment 1
Slika 2. Izvedbe stola, pokus broj 1

Three different table variants have been considered, each variant has 9 experiments so there will be 27 experiments. The experiment plan for each table variant is shown in table 2. All data mentioned later in the paper are data relating to the first table variant because of clarity. The procedure is equally done for each other variant in order to find the optimal solution.

Table 2. The plan of experiments

Tablica 2. Plan pokusa

Factor 1 A:A: dim.frame mm	Factor 2 B:B: dim.leg mm	Factor 3 C:C: dim.stiffener mm
80	40	40
80	50	50
80	60	60
100	40	50
100	50	60
100	60	40
120	40	60
120	50	40
120	60	50

Each experiment has three factors: frame dimension, leg dimension and stiffener dimension. The frame of the table is made with tubes that have a rectangular cross section, legs and stiffeners are made with tubes that have a quadratic cross section, where thickness is pre-defined and its amount is 2 mm. The table high is defined in advance and it affects the smaller dimension of rectangular cross section, which is always equal to 60 mm. For each table variant displacement and mass are calculated by using the NX Siemens 10.0 software. The first step is a construction of the 3D model in software module for modeling and the second step is a simulation by using the Finite Element Method – FEM. The Finite Element Method has a wide application in various engineering tasks [5]. The Finite Element Method divides the body into the finite number of simple shape elements that are merged in nodes, figure 3. The displacement in a node is unknown but it is determined by interpolation [6].

Figure 3. The body of the table divided into the finite number of simple shape elements

Slika 3. Tijelo stola podijeljeno na konačne elemente

The forces for the table load are taken as an example, so vertical force is 1000 N and horizontal force is 300 N. The fixed constraint is set on the surface of legs that lay on the floor. The 27 simulations are completed in the program package NX Siemens 10.0, so the results about displacement and mass were obtained. The results of FEM analysis and displacement are shown in Figure 4.

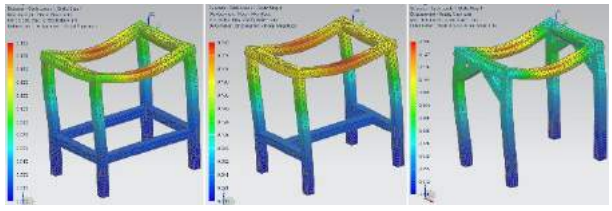

Figure 4. The FEM analysis of different variants, experiment number 1

Slika 4. FEM analiza različitih izvedbi, pokus broj 1

The results collected from analysis were entered in program package Design Expert 10.0.3. The program uses Taguchi method to find the optimal factors and optimal table variant. The collected data about displacement and mass, as well as dimension of the construction profile are shown in Table 3.

Table 3. The data entered in Design Expert 10.0.3. for second table variant

Tablica 3. Podaci uneseni u Design Expert 10.0.3. za drugu izvedbu stola

Factor 1 A:A: dim.frame mm	Factor 2 B:B: dim.leg mm	Factor 3 C:C: dim.stiff... mm	Response 1 R1 displace... mm	Response 2 R2 mass kg
80	40	40	0.26	23.49
80	50	50	0.157	26.42
80	60	60	0.1075	29.24
100	40	50	0.237	31.11
100	50	60	0.144	33.82
100	60	40	0.142	30.36
120	40	60	0.214	35.2
120	50	40	0.185	30.67
120	60	50	0.131	32.97

3. Analysis and results

The results of experiments are analyzed through determination of the influence of certain factor on a response, depending on which level factor is observed. The analysis of variance (ANOVA) verifies the influence on system response when factors are changing [7]. When all data are entered, the program shows design summary of the process. Figure 5. shows the minimum and maximum level of each factor A, B and C. The "Main effects" model is selected although the program offers

more features. The reason for choosing a "Main effects" model is that the system factors are not interdependent. The "Main effects" model is selected although the program offers more features.

The analysis of variance for displacement shows the probability of 1.21% that value "F" could appear because of noise, figure 7. The value "F" is 81.89, what implies that the model is significant. Values of "$Prob > F$" less than 0.05 indicate that model terms are significant, so here are significant terms B and C, while A is not significant.

Study Type	Factorial	**Subtype**	Randomized
Design Type	Taguchi OA	**Runs**	9
Design Mode	Main effects	**Blocks**	No Blocks
Center Point	0		

Factor	Name	Units	Type	Subtype	Minimum	Maximum
A	A: dim.frame	mm	Categoric	Nominal	80	120
B	B: dim.leg	mm	Categoric	Nominal	40	60
C	C: dim.stiffene	mm	Categoric	Nominal	40	60

Response	Name	Units	Obs	Analysis	Minimum	Maximum
R1	R1 displaceme	mm	9	Factorial	0.1075	0.26
R2	R2 mass	kg	9	Factorial	23.49	35.2

Figure 5. Design summary, for the second table variant
Slika 5. Sažetak podataka, za drugu izvedbu stola

Analysis of variance table [Classical sum of squares - Type II]

Source	Sum of Squares	df	Mean Square	F Value	p-value Prob > F
Model	0.021	6	3.578E-003	81.89	0.0121
A-A: dim.fran	*9.056E-006*	*2*	*4.528E-006*	*0.10*	*0.9061*
B-B: dim.leg	*0.019*	*2*	*9.499E-003*	*217.40*	*0.0046*
C-C: dim.stifi	*2.461E-003*	*2*	*1.230E-003*	*28.16*	*0.0343*
Residual	8.739E-005	2	4.369E-005		
Cor Total	0.022	8			

Figure 6. Analysis of the variance for displacement, for the second table variant
Slika 6. Analiza varijance za progib, za drugu izvedbu stola

Each model has "AdeqPrecision" or "S-N" ratio greater than 4, what means that each model can be used to navigate the design space. A main effect plots are shown graphically in figure 7. for each factor. The first graph in figure 7. shows that A is not a significant factor.

The analysis of variance for mass shows that factors with value "$Prob > F$" less than 0.05 indicate that model terms are significant, so here are significant terms A and C, while B is not significant, figure 8. There is "AdeqPrecision" or "S-N" ratio greater than 4, what means that signal is adequate, so the model can be used to navigate the design space. Graphical display of each factor for response mass, depending on the level, is in figure 9. It is visible on the second graph, in figure 9., that factor B is not significant.

4. Optimization between table variants

The main aim of this optimization is to find out how different combination of factors influences on the construction of the table, if there are responses mass and displacement that should be minimum. The used method does not provide a mathematical function that describes a problem, it provides an optimal combination according to a given targets, figure 10. The used method and mentioned analysis resulted with three table variants that are optimal, figure 11. For each table variant, nine experiments were carried out and the best solution was chosen. The third table variant is chosen for Lean Learning Factory, that variant has optimal mass with minimum displacement, figure 12. The table will be integrated into the assembly line that exists already in Lean Learning Factory. It is an assembly line for karet.

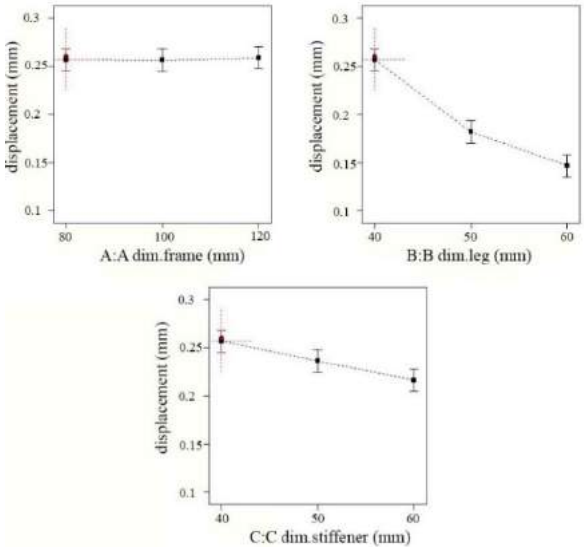

Figure 7. Main effects for response displacement, change of each factor depending on level
Slika 7. Grafički prikaz promjena pojedinog faktora ovisno o razinama, osnovne značajke za odziv progib

Analysis of variance table [Classical sum of squares - Type II]

Source	Sum of Squares	df	Mean Square	F Value	p-value Prob > F
Model	106.36	6	17.73	73.20	0.0135
A-A: dim.fran	*73.42*	*2*	*36.71*	*151.59*	*0.0066*
B-B: dim.leg	*1.30*	*2*	*0.65*	*2.67*	*0.2721*
C-C: dim.stifi	*31.64*	*2*	*15.82*	*65.33*	*0.0151*
Residual	0.48	2	0.24		
Cor Total	106.84	8			

Figure 8. Analysis of the variance for mass, for the second table variant
Slika 8. Analiza varijance za masu, za drugu izvedbu stola

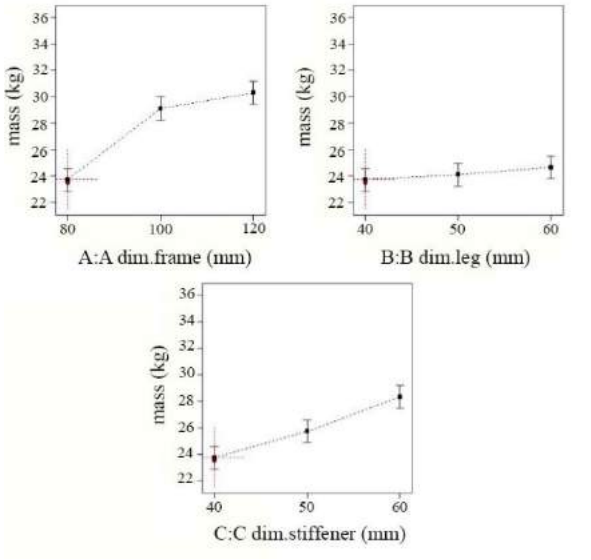

Figure 9. Main effects for response mass**,** change of each factor depending on level
Slika 9. Grafički prikaz promjena pojedinog faktora ovisno o razinama, osnovne značajke za odziv masa

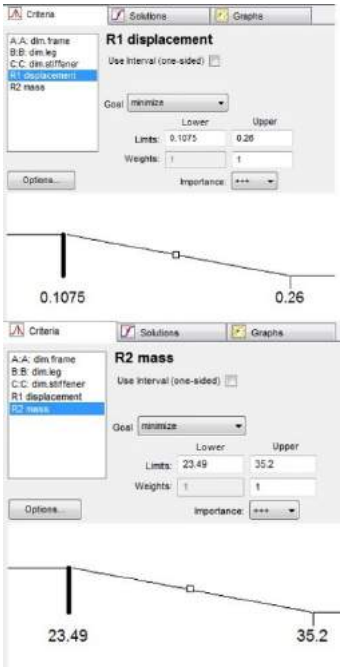

Figure 10. Example of limits for displacement and mass, goal is minimization
Slika 10. Primjer granica za progib i masu, cilj mimimzacija

Constraints

Name	Goal	Lower Limit	Upper Limit	Lower Weight	Upper Weight	Importance
A:A: dim.frame	is in range	80	120	1	1	3
B:B: dim.leg	is in range	40	60	1	1	3
C:C: dim.stiffer	is in range	40	60	1	1	3
R1 displaceme	minimize	0.1158	0.237	1	1	5
R2 mass	minimize	25.36	35.09	1	1	3

Solutions for 27 combinations of categoric factor levels

Number	A: dim.frame	B: dim.leg	C: dim.stiffer	R1 displacem	R2 mass	Desirability
1	80	60	40	0.140	26.974	0.814

Constraints

Name	Goal	Lower Limit	Upper Limit	Lower Weight	Upper Weight	Importance
A:A: dim.frame	is in range	80	120	1	1	3
B:B: dim.leg	is in range	40	60	1	1	3
C:C: dim.stiffer	is in range	40	60	1	1	3
R1 displaceme	minimize	0.1075	0.26	1	1	3
R2 mass	minimize	23.49	35.2	1	1	3

Solutions for 27 combinations of categoric factor levels

Number	A: dim.frame	B: dim.leg	C: dim.stiffer	R1 displacem	R2 mass	Desirability
1	80	60	40	0.147	24.684	0.817

Constraints

Name	Goal	Lower Limit	Upper Limit	Lower Weight	Upper Weight	Importance
A:A: dim.frame	is in range	80	120	1	1	3
B:B: dim.leg	is in range	40	60	1	1	3
C:C: dim.stiffer	is in range	40	60	1	1	3
R1 displaceme	minimize	0.0758	0.195	1	1	3
R2 mass	minimize	21.76	28.19	1	1	3

Solutions for 27 combinations of categoric factor levels

Number	A: dim.frame	B: dim.leg	C: dim.stiffer	R1 displacem	R2 mass	Desirability
1	80	50	40	0.112	23.766	0.692

Figure 11. Solutions for each table variant
Slika 11. Rješenja za svaku varijantu stola

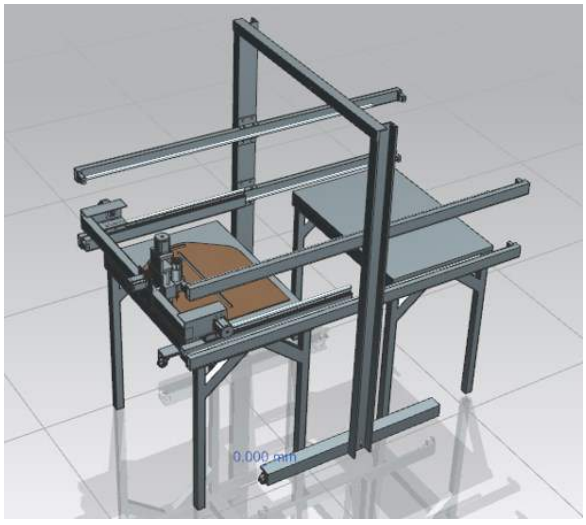

Figure 12. Solution for Lean Learning factory
Slika 12. Rješenje za Lean Learning factory

5. Conclusion

The Lean Learning Factory is a simulation of the real factory environment. This paper presents methods used for the improvement of equipment in Lean Learning Factory. Table variant that is chosen will be integrated into existing karet assembly line.

The first step for the whole process was the definition of factors. The second step was Taguchi method and design of experiments, so after that step FEM analysis for each combination of factors was made according to the plan of experiments.

The mentioned process resulted with optimal table variant that will be used in Lean Learning Factory. The purpose of this paper is to find out best solutions for improvement of equipment using several methods and software support.

Acknowledgement

This work has been fully supported by Croatian Science Foundation under the project Innovative Smart Enterprise – INSENT (1353).

REFERENCES

[1]. Veza, I., Gjeldum, N., & Mladineo, M. (2015). Lean Learning factory at FESB–University of Split. Procedia CIRP, 32, 132-137.

[2]. Gjeldum, N., Mladineo, M., & Veza, I. (2016). Transfer of Model of Innovative Smart Factory to Croatian Economy Using Lean Learning Factory. Procedia CIRP, 54, 158-163.

[3]. Phadke, M. S. (1995). Quality engineering using robust design. Prentice Hall PTR.

[4]. www.statease.com/training.html

[5]. Singiresu S.Rao, The finite element method in engineering, 2010.

[6]. www.plm.automation.siemens.com/en_us/products /nx/index.shtml

[7]. Cardinal, R. N., & Aitken, M. R. (2013). ANOVA for the behavioral sciences researcher. Psychology Press

ISSN 1847-7917

Influence of the salt bath agitation and austempering temperature on the microstructure of austempered ductile iron

Nikša ČATIPOVIĆ, Dražen Živkovi), Zvonimir DADIĆ and Marin VICEIĆ
Fakultet Elektrotehnike, Strojarstva i Brodogradnje, Sveučičišta u Splitu
(Faculty of Electrical Engineering, Mechanical Engineering and Naval Architecture, University of Split)
Ruđera Boškovića 32, 21000 Split,
Republic of Croatia

niksa.catipovic@fesb.hr
drazen.zivkovic@fesb.hr
zvonimir.dadic@fesb.hr
marin.viceic@fesb.hr

Keywords
Austempered ductile iron
Microstructure
Salt bath
Agitation

Ključne riječi
Izotermički poboljšan žilavi lijev
Mikrostruktura
Solna kupka
Miješanje

Original scientific paper
Abstract: In this paper the influence of austempering temperature and salt bath agitation on the final microstructure of the ferritic ductile iron has been studied. 17 samples have been subjected to different process parameters. Different microstructures have been recorded upon the completion of the tests. From the obtained micro images, it is obvious that both the austempering temperature and salt bath agitation affect the final microstructure of the austempered ductile iron. Lower austempering temperatures and salt bath agitation produce more ausferrite in the microstructure hence the harder and tougher phases are present. It is expected to be confirmed through further research of the mechanical properties tests of heat-treated samples.

Izvorni znanstveni rad
Sažetak: U ovom radu ispitivan je utjecaj temperature izotermičkog poboljšavanja i miješanja solne kupke na mikrostrukturu feritnog žilavog lijeva. 17 uzoraka je podvrgnuto različitim parametrima obrade. Snimljene su i različite mikrosturkture po završetku ispitivanja. Iz dobivenih snimaka vidljivo je da i temperatura izotermičkog poboljšavanja i miješanje kupke utječu na konačnu mikrosturkturu izotermički poboljšanog žilavog lijeva. Niže temperature i miješanje kupke daju više ausferita u mikrosturkturi pa samim time i tvrđe i čvršće faze. Očekivati da se to potvrdi kroz nastavak ispitivanja mehaničkih svojstava na toplinski obrađenim uzorcima.

1. Introduction

Over the last years, the market has been facing huge demand for tough, durable and economically viable materials. Ductile cast iron is one such material. When ductile iron is subjected to the isothermal heat treatment a completely new material is produced, known as austempered ductile iron – ADI. ADI has significantly better mechanical properties than plain ductile iron, [1]. Austempered ductile iron possesses a unique microstructure called ausferrite which is a mixture of fine acicular ferrite and stable, high carbon enriched retained austenite, [2, 3]. That new microstructure results with properties that are superior to many iron and aluminium alloys. Compared with perlitic, ferritic or martensitic microstructures, ausferrite exhibits twice the strength for the given ductility level obtained by the conventional heat treatment, [3]. The mechanical properties of the austempered ductile iron depend on its ausferritic microstructure. Austempered matrix provides a better tensile strength and ductility ration than any other type of ductile cast iron. Different combinations of mechanical properties, as a result of ausferritic microstructure of the austempered ductile iron, can be obtained by combination of heat treatment parameters and alloying elements, [4].

Heat treatment of the austempered ductile iron consists of austenitization of the ductile iron, quenching in the austempering medium and holding on the austempering temperature and then cooling to the room temperature, [5], Fig. 1.

Several authors, [2, 3, 6], have correctly stated that during the austempering process, ADI undergoes the two stage transformation process. In the first stage of the transformation, the austenite (γ) decomposes into bainitic ferrite (α) and carbon enriched retained austenite (γ_{hc}), so-called ausferrite. In the second stage of the

transformation, the carbon enriched retained austenite (γ_{hc}) further decomposes on ferrite (α) and carbides. This decomposition will occur if the ductile iron is held for too long at the austempering temperature, [2]. The occurrence of the carbides in the microstructure makes the material brittle and such reaction should be avoided. Therefore, the optimal mechanical properties of ADI are achieved upon the completion of the first stage of the transformation but before the beginning of the second stage of the transformation, i.e. within the so-called "time window", [7, 8].

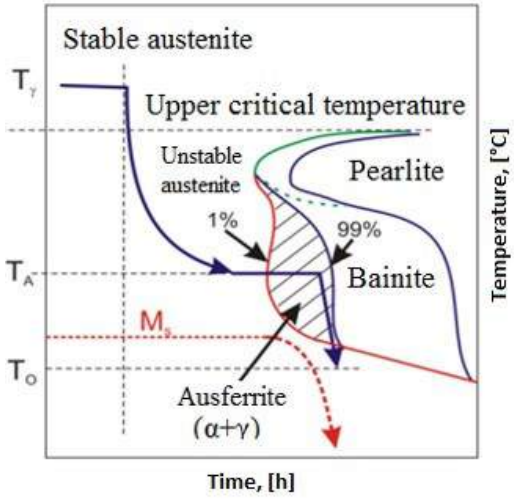

Figure 1. Austempering heat treatment of the ductile iron, [5]
Slika 1. Toplinska obrada izotermičkog poboljšavanja žilavog lijeva, [5]

2. Salt bath

The austempering medium most commonly used is salt bath composed of sodium and potassium nitrate ($NaNO_3$ + KNO_3) in the 50% : 50% ratio. The operating temperature range of this salt composition is between 160°C and 550°C, depending on the chemical composition of the salt. The austempering conversion can be done in lead bath, but since lead has melting point at 327°C that narrows the temperature range of the heat treatment process. An oil bath can be exceptionally used, but with high dose of caution, [9, 10].

Salt baths are most often used for austempering heat treatment. They are also used for: tempering, annealing, austenitization, quenching, etc. Chemical composition of the salt baths plays a key role during the heat treatment. Molten salts are completely dissolved on cations and anions, which are thermally very stable. They have low vapour pressure and excellent thermal and electrical conductivity. Workpieces deformations are very small, if they occur at all, because the heat dissipation is very fast and uniform. Those salts have low viscosity but high solubility. The ability to dissolve the gases is good and increases with rising temperatures. Some molten salts can even dissolve metals, [11].

The salt bath is most commonly used medium for austempering of ductile iron because, [10, 11]:

- the bath working temperature ranges are from 160°C to 550°C,
- it can be used for quenching processes with discontinuous change in cooling rate,
- it conducts heat very fast and it is not flammable,
- it eliminates the problem of the vapour bubble at the initial cooling stage,
- its viscosity is uniform through a wide range of temperatures,
- its viscosity is low at austempering temperatures (almost as the viscosity of water at room temperature), which reduces losses during the removal of the workpiece,
- it remains stable at working temperatures and is completely water-soluble, which eases subsequent cleaning,
- the salt can easily be extracted from the water used for cleaning using evaporation methods,
- by changing the working temperature, agitating and adding water cooling intensity can be significantly affected. It is common that at a working temperatures from 160°C to 290°C the water content is from 0,5% to 2%.

The table 1. shows the compositions and characteristics of the two variations of the most commonly used salt baths. A narrow range salt is only used for austempering heat treatment, while a wide range salt is used for tempering, martempering and other tempering processes.

Table 1. Compositions and characteristics of austempering salt baths, [10]
Tablica 1. Sastav i karakteristike soli za izotermičko poboljšavanje, [10]

	Narrow range	**Wide range**
Sodium nitrate, %	45 – 55	0 – 25
Calcium nitrate, %	45 – 55	45 – 55
Sodium nitrite, %	. . .	25 – 55
Melting point, T [°C]	220	150 – 165
Working temperature, T [°C]	260 – 595	175 - 540

Salts for salt baths are easily available from specialized manufacturers who specializes in heat treatment of metals. One of those manufacturers is *„Hef Durferrit"* [12], which offers a variety of salts, depending on their specific application.

Figure 2.1. Salt AS 140 and salt bath ready for experiments
Slika 2.1. Sol AS 140 i solna kupka soremne za pokuse

3. Experimental work

The task of this paper was to investigate the effect of salt bath agitation and austempering temperature on the final microstructure of the ADI. The characteristic microstructure of ADI is called ausferrite and in previous section is explained how it is obtained.
Based on previous studies, [13, 14], and available literature, [15, 16, 17, 18], these heat treatment parameters have been chosen: austenitization temperature of 900°C, holding time at austenitization temperature of 1 h, holding time at the austempering temperature of 1 h while the austempering temperature ranged from 230°C to 450°C. Experiment plan has been developed using *"Design Expert"* software, which resulted in 17 experiments.
As a starting material, ductile cast iron has been obtained from Split Shipyard. The samples chemical composition is given in Table 2.

Table 2. Chemical composition of the ductile iron
Tablica 2. Kemijski sastav žilavog lijeva

Label	C (%)	Si (%)	Mn (%)	P (%)	S (%)	Cu (%)	Mg (%)
NL40-KF	3,63	2,52	0,20	0,04	0,008	0,04	0,047

From the starting Y-blocks, Fig. 3.1., Charpy test samples have been cut out, Fig. 3.2. After microstructural analysis the hardness and toughness measurement tests were performed. Samples have been made in accordance with ISO 148-1 norm.

Figure 3.1. Y-blocks of ductile iron obtained from Split Shipyard
Slika 3.1. Y-blokovi žilavog lijeva dobiveni iz Brodogradilišta Split

Figure 3.2. Standardized Charpy samples ready for experiments
Slika 3.2. Standardizirane Charpy epruvete spremne za pokuse

Prior to the start of the experimentation, the initial microstructure of the ductile iron has been taken Fig. 3.3. The figure shows ferrite ductile iron with very small amount of perlite in the microstructure.

Figure 3.3. As cast microstructure, magnification 200x
Slika 3.3. Početna mikrostruktura, povećanje 200x

4. Results

After the heat treatment was conducted, all of the samples were prepared for the microstructural analysis. The preparation relates to the sample surfaces adaptation for microstructural analysis after the austempering. Samples have been ground on the abrasive stripes of different grain sizes. The roughness of thus prepared surfaces has been further reduced on the mechanical polishing wheel. As an abrasive agent on the wheel, emulsion with clay as a polishing medium has been applied (aluminium oxide + water). Final step of the surface preparation consisted of etching it with *nital* (mixture of alcohol and 3% nitric acid). The light microscope is connected to a computer that projects a microstructure on the computer screen via the „*DinoCapture,,* program package.
The following figures show different microstructures obtained with respect to the austempering temperature and salt bath agitation. Figures 4.1. - 4.4. show microstructures after austempering at different temperatures with salt bath agitation.

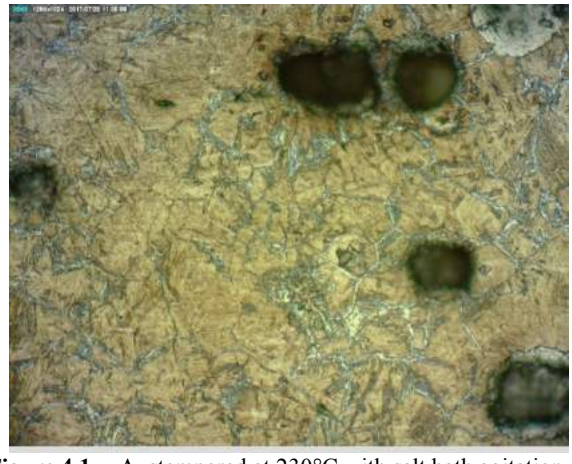

Figure 4.1. Austempered at 230°C with salt bath agitation, magnification 200x
Slika 4.1. Izotermički poboljšano na 230°C sa miješanjem solne kupke, povećanje 200x

Figure 4.2. Austempered at 307°C with salt bath agitation, magnification 200x
Slika 4.2. Izotermički poboljšano na 307°C sa miješanjem solne kupke, povećanje 200x

Figure 4.3. Austempered at 352°C with salt bath agitation, magnification 200x
Slika 4.3. Izotermički poboljšano na 352°C sa miješanjem solne kupke, povećanje 200x

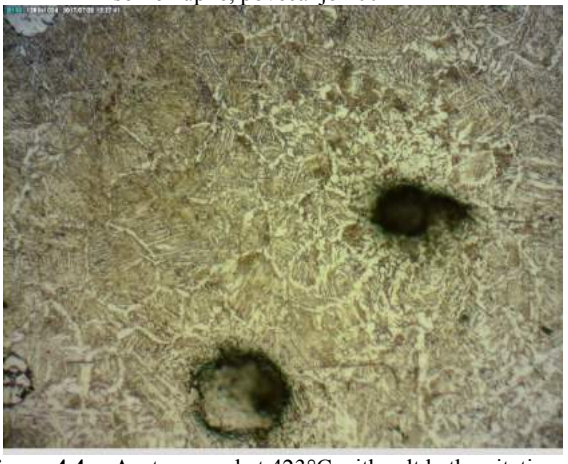

Figure 4.4. Austempered at 423°C with salt bath agitation, magnification 200x
Slika 4.4. Izotermički poboljšano na 423°C sa miješanjem solne kupke, povećanje 200x

Figures 4.5. - 4.8. show microstructures after austempering at different temperatures without salt bath agitation.

Figure 4.5. Austempered at 258°C without salt bath agitation, magnification 200x
Slika 4.5. Izotermički poboljšano na 258°C bez miješanja solne kupke, povećanje 200x

Figure 4.7. Austempered at 395°C without salt bath agitation, magnification 200x
Slika 4.7. Izotermički poboljšano na 395°C bez miješanja solne kupke, povećanje 200x

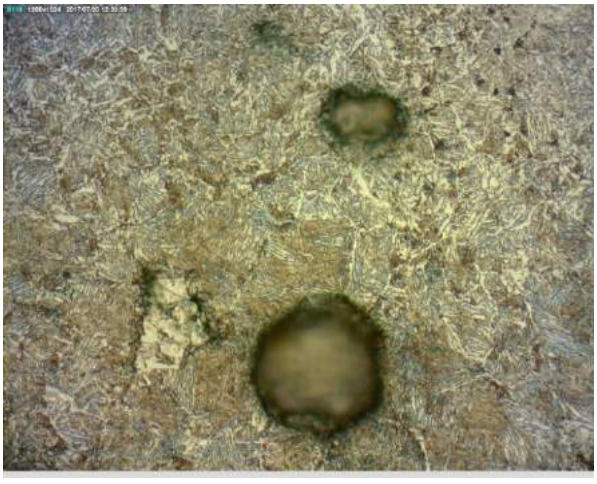

Figure 4.6. Austempered at 368°C without salt bath agitation, magnification 200x
Slika 4.6. Izotermički poboljšano na 368°C bez miješanja solne kupke, povećanje 200x

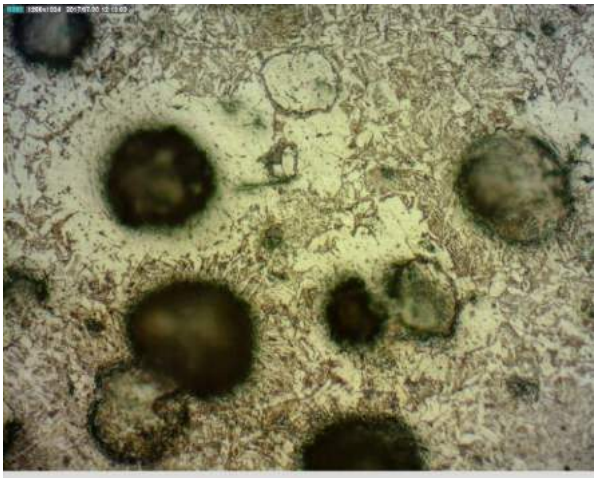

Figure 4.8. Austempered at 450°C without salt bath agitation, magnification 200x
Slika 4.8. Izotermički poboljšano na 450°C bez miješanja solne kupke, povećanje 200x

5. Conclusion

From the obtained microstructure images, it is clear that there has been a significant change in relation to the initial microstructure before the heat treatment.
It is noticed that at the lower austempering temperatures the microstructure is finer than at the higher austempering temperatures, regardless of whether the salt bath was agitating or not.
It is also apparent that there is more ausferrite phase in the samples that have been quenched in the agitating salt bath, unlike the samples that have been quenched in calm salt bath.
However, the fraction of the ausferrite phase in all of the samples is smaller than expected, which means that chemical composition of the ductile iron is questionable. It is possible that carbon content is lower than what is presented in the chemical composition.

Also, the holding time at the austempering temperature should be somewhat greater, up to 2 hours, so that more ausferrite is produced.
The further tests will be based on the confirmation of those conclusions through the hardness and toughness tests for each sample.

Acknowledgements

This work has been fully supported by Croatian Science Foundation under the project 5371.

REFERENCES

[1] Behera G., Sohala S. R., Effect of copper on the properties of austempered ductile iron castings. Bachelor thesis. Department of Metallurgical and Materials Engineering, National Institute of Technology, Rourkela, India, (2012).

[2] Sidjanin L., Smallman R. E., Mater. Sci. Tech. – Lond., 8, pp. 1095, (1992).

[3] Elliot R., Heat Treatments of Metals. 3, pp. 55, (1997).

[4] Chandler H., Heat treaters guide: practices and procedures for irons and steels. ASTM International, 2 Sub edition (December 1995).

[5] Sharma A., Singh K.K., Gupta G.K., "Study on the Effects of Austempering Variables and Copper Addition on Mechanical Properties of Austempered Ductile Iron", AIMTDR, India, 2016.

[6] Harding R. A., Kovove Mater., 45, p. 1, 2007.

[7] Sidjanin L., Smallman R. E., Young J. M., Acta Mater., 42, pp. 3149, (1994). doi:10.1016/0956-7151(94)90412-X.

[8] Rajnovic D., Eric O., Sidjanin L., The standard processing window of alloyed ADI materials. Kovove Mater., 50, pp. 199-208, (2012).

[9] Gagne, M., „The Sorelmetal Book of Ductile Iron", Rio Tinto Iron & Titanium, Montreal, Kanada, 2004.

[10] Hef Durferrit, http://www.hefdurferrit.de/en/.

[11] Živković D., Gabrić I., Dadić Z., Čatipović N., Vrljičak I., "Analysis of austempering treatment parameters on properties of ductile iron EN-GJS-400", Zbornik radova = Proceedings, Hrvatsko društvo za strojarske tehnologije, MTSM 2015, Split, 2015.

[12] Čatipović, N., Živković, D., Dadić, Z., Sučić, A., Ljumović, P., "Utjecaj izotermičke temperature i vremena držanja na mikrostrukturu i tvrdoću izotermičkog žilavog lijeva", MTSM 2015, Split, rujan 2015.

[13] Eric O., Rajnovic D., Zec S., Sidjanin L., Jovanovic M. T., Mater. Charact., 57, pp. 211, (2006). doi: 10.1016/j.matchar.2006.01.014

[14] O. Eric, L. Sidjanin, Z. Miskovic, S. Zec, M. T. Jovanovic, "Microstructure and toughness of Cu, Ni Mo austempered ductile iron", Mater. Lett. 58 (2004) 2707 to 2711.

[15] B.V. Kovacs, „Austempered Ductile Iron: Fact and Fiction", *Mod. Cast.,* March 1990, p 38-41.

[16] L. Sidjanin, D. Rajnovic, O. Eric and R. E. Smallman, "Austempering study of unalloyed and alloyed ductile irons", Materials Science and Technology 26 Vol. 5, (2010), p. 567-571, doi:10.1179/174328409X407524.

ISSN 1847-7917

High pressure die casting mould repair technologies

Zvonimir DADIĆ, Dražen ŽIVKOVIĆ, Nikša ČATIPOVIĆ, Josip BILIĆ

Fakultet elektrotehnike, strojarstva i brodogradnje, Sveučilišta u Splitu
(Faculty of Electrical Engineering, Mechanical Engineering and Naval Architecture, University of Split)
Ruđera Boškovića 32, 21000 Split,
Republic of Croatia

zdadic@fesb.hr;
Drazen.Zivkovic@fesb.hr;
ncatipov@fesb.hr.
jbilic00@fesb.hr

Keywords

Mould wear
Thermal fatigue
Welding
Tool steel

Ključne riječi

Trošenje kalupa
Toplinski umor
Zavarivanje
Alatni čelik

Review paper

Abstract: This paper presents the most commonly used technologies for repairing high pressure die cast moulds. This production technology successfully solves most problems of the conventional casting technologies like: casting porosity, high surface roughness, long casting production times, inability to produce thin cross-sections and low dimensional accuracy. Material used for the high pressure die casting permanent mould is a highly alloyed hot work tool steel H13 (ASTM). During exploitation, the moulds surface is damaged, mostly by thermal cracking. Mould is repaired to extend its life span and reduce costs of production.

Pregledni rad

Sažetak: U ovom radu opisane su najčešće korištene tehnologije popravka kalupa za visokotlačno lijevanje. Ova metoda lijevanja uspješno rješava probleme konvencionalnih postupaka lijevanja kao što su: poroznost odljevka, velika hrapavost površine, mala brzina izrade odljevaka, nemogućnost izrade tanjih presjeka te dimenzijska točnost odljevka. Materijal korišten za trajne kalupe za visokotlačno lijevanje je visokolegirani alatni čelik za rad toplom stanju H13 (ASTM). Tijekom eksploatacije oštećuje se površina kalupa, ponajviše toplinskim umorom. Kalup se popravlja kako bi mu se produžio životni vijek te smanjili troškovi proizvodnje.

1. Introduction

Most complex and most expensive component of the high pressure die casting process is the mould. The mould material must maintain mechanical properties at elevated temperatures, with great mould closing forces reaching up to 40 *kN* [1]. At the same time, the surface of the mould must resist the erosion by the molten casting alloy which enters the mould at high pressure. During the casting process pressure can be increased up to 120 *MPa* and the liquid speed can reach 60 *m/s* [2]. According to previous research, most significant wear mechanism is thermal fatigue. During the casting process, due to great difference in minimum and maximum achieved temperature of the moulds surface, cracks develop on the surface [3, 4]. Because of those aggressive conditions, highly alloyed steel is used as the mould material. Mould material is quenched and tempered and then usually nitrated. In some cases, surface coatings are added on the surface. Those moulds are very expensive, with prices reaching up to 100 000 € [5]. High price and complexity justify the research of reparation technologies with the goal of prolonging the moulds life span.

2. Mould material

Mould material has to be capable to withstand great closing forces while at high temperatures. The mould surface can reach up to 350 °*C* [6]. To reduce thermal shock, mould is preheated from 180 to 350 °*C* by oil or water with additives going through the core of the mould [7]. Changes in dimensions of the mould during heating and cooling should be minimal. Surface of the mould must be resistant to wear to achieve dimensional accuracy and necessary surface roughness. Due to those demands during pressure die casting of aluminium, copper and zinc alloys, high-alloyed tool steel is used. Mostly H10, H11 and H13 (MTSM). Example of this material is "W300" by Böhler [8]. Chemical composition of those hot work tool steel (H11) is given in table 1.

Table 1. Chemical composition of "W300" (H11) , [8]

Tablica 1. Kemijski sastav "W300" (H11) , [8]

C	Si	Mn	Cr	Mo	V
0,38 %	1,1 %	0,4 %	5 %	1,3 %	0,4 %

With thicker cross-sections (>10 *mm*) it is necessary to use alloyed steel to achieve better depth hardenability.

Material of the mould is originally sold in soft state. Heat treatment used to achieve low hardness is "soft annealing". The goal of soft annealing is preparing the material for machining. Usually, heat treatment is done in furnaces with passive atmosphere to prevent oxidation on the surface. Cooling is done slowly, usually in turned off furnace [9]. When treating high-alloyed steel, vacuum furnaces are most often used. Products treated in vacuum furnaces don't require additional treatment. Minimal maintenance costs and ecological aspects make vacuum technology more and more represented [10].

To make machining possible, the material used must have low hardness. Hardness of "Assab 8407 Supreme" moulds by "Assab" in softened state is 180 *HB* [11]. Rough machining causes residual strains in the material. After machining the mould should be tempered. Material is heated to 550 – 700 °*C* and kept at that temperature for 2 – 3 *h*, then slowly cooled, usually in a turned off furnace. Fine machining of the moulds surface follows and finally quenching and tempering of the mould [10].

Austenitization temperature depends on the chemical composition of steel. For steel "Assab 8407 Supreme" austenitization temperature is between 1020 – 1050 °*C*. Usually there are two preheating steps (600 °*C* and 800 °*C*) to reduce risk of deformation and cracks caused by unequal heating. Suggested holding time is 30 *min*. When quenching, cooling is stopped at 50 – 70 °*C* which causes residual austenite (above M_f). Residual austenite also appears due of pressure caused by surrounding martensite. Residual stress can be reduced by step quenching [9, 10, 11].

First tempering reduces pressure on residual austenite and allows it to convert to martensite. Second tempering is used to release carbon from the new martensite, which creates new carbides, and gives material higher strength and hardness. Third tempering is used to release residual stress and achieve dimensional stability. Material is kept at tempering temperature for 2 *h*. Tempering temperatures are from around 580 °*C* and 650 °*C* depending on the required mechanical properties. If nitriding is done afterwards, tempering temperatures must be above nitriding temperature to avoid changes in microstructure during nitriding [8, 10]. Heat treatment diagram is shown in Figure 1.

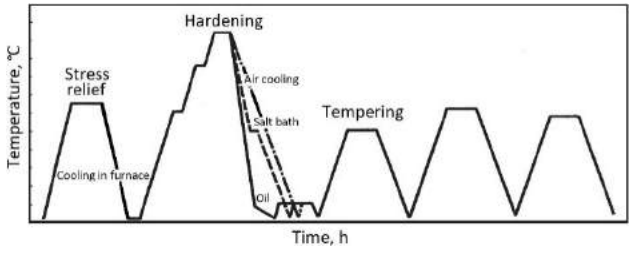

Figure 1. Heat treatment, [8]
Slika 1. Toplinska obrada, [8]

This steel (H11) has high toughness (necessary to avoid crack initiation from thermal fatigue), high strength at elevated temperatures and great hardenability of the surface when quenching by air (but can also endure water quenching) [8]. Special procedures are done to achieve high surface hardness, like [9]:

- Modification of phases on the surface without changing chemical composition;
- Modification of phases on the surface with changing chemical composition;
- Combination of first two procedures (e.g. cementation);
- Surface coatings (application of another material on the surface).

After surface treatment, mould is polished. Typical polishing procedure for this kind of mould would be rough grinding (180 – 320 μm grain size), fine grinding with grinding paper (400 – 800 μm), diamond paste polishing (1 – 15 μm) [11, 12].

3. Wear mechanisms

Thermal fatigue is the most influential wear mechanism [3, 4]. Mould surface temperature can reach over 320 °*C* after filling the mould with liquid alloy. Shortly after ejecting the cast temperature of the mould surface drops to 180 °*C* [6]. High temperature gradient is achieved by massive volume of the mould material and cooling channels. After the cast eject, surface of the mould is sprayed with lubrication media. Lubrication is usually based on graphite, molybdenum disulfida or hexagonal boron nitride dispersed in a water solution [13]. Constant change of temperature causes expansion and contraction of mould material on the surface (mostly martensite) which can lead to crack initiation and propagation [14]. At the beginning, there are microcracks which can't be easily spotted. Repeating of casting process causes the crack propagation. When the crack is large enough, it is filled with molten casting alloy. The cast deflects the surface irregularities and makes it easier to spot the crack. When the cast does not achieve requested dimensional accuracy, the mould must be repaired or replaced to continue the casting process. The example of surface damage, caused by thermal fatigue, of H11 steel is shown in Figure 2.

Figure 2. Thermal fatigue on the surface of H11 steel, [4]
Slika 2. Toplinski umor na površini čelika H11, [4]

Erosion can be initiated when casting alloy enters the mould cavity at high speed. Speed of the molten casting alloy can reach up to *60 m/s* [14]. Mould erosion can be enhanced by mechanical impact of hard particles in molten casting alloy and by cavitation on the mould surface. Molten aluminium casting alloy often contains hard particles of silicon, which has a high melting point (1414°*C*), and aluminium oxide (Al_2O_3, 2072°*C*). Previous research has proven that smaller angles of particle impact have largest effect on erosion wear [15].
Molten aluminium alloy tends to develop intermetallic compounds with mould material. That causes damage on the surface of the mould which results in faulty castings. Lubricant is used to create a physical barrier between casting alloy and mould. In areas where lubricant is washed out, there is a higher tendency to develop intermetallic compounds, especially in slower cooling areas. Intermetallic compounds can often be found around the areas where mould has been repaired by welding. Softened areas in the heat affected zone (HAZ) are favourable for development of intermetallic compounds [14].

4. Repair technologies

Life span of mould is correlated with the number of thermomechanical stress cycles (number of casting cycles) [3, 4]. As mentioned before, main reasons of mould wear are thermal fatigue, erosion, adhesion of aluminum on the mould and tribo-corrosion. The mould surface wear cannot be observed during casting operation. Therefore, wear is usually noticed by checking surface of castings. When there is too much wear, mould can be replaced or repaired. It is usually economically feasible to repair the mould, rather than buying a new one. The repair price is from few percent to 10 % of the mould initial value [16]. Moulds are usually repaired by welding. Advantage of mould repair is quick production resumption. Average mould price is lowered by prolonging its life span. Mould can be repaired by welding more than once [16, 17].
Mould needs to be repaired or replaced when castings do not achieve dimensional accuracy. The castings surfaces need to be monitored continuously so mould can be repaired before it produces low quality castings. On that way number of rejects is minimal and costs of production are lower. Although the weldability of this type of mould steel is complex and difficult, with the right procedure and an experienced welder it is possible to achieve very good results.
Manual metal arc welding is used when it is necessary to deposit large amounts of material [18]. **Tungsten inert gas welding (TIG)** is mostly used repairing method. The reason is optimal control of the operator over the welding process. Other methods that are used for mould repair are laser welding, electro-spark deposition (ESD) and metallization.
Mould steel has between 0,3-0,5% (by mass) of carbon content and other alloying elements like: manganese, molybdenum, vanadium, chromium, tungsten and nickel. During welding process preheating has to be done to avoid hardened and brittle areas in the HAZ. Cracks that could initiate in the weld may spread through the rest of the mould [19]. Moulds are usually preheated by furnaces. Flame heating is not recommended as it is not precise and can lead to importation of hydrogen. Hydrogen contamination causes porosity into the mould material [19, 20].
Preparation of the welding groove greatly effects the weld quality. Before removing material, it is necessary to drill holes at end of cracks to eliminate crack propagation [21]. Areas with cracks or other faults are prepared for the welding process removing the material with the minimal angle of 30°. Width in the bottom of the groove should be greater than the welding electrode diameter. Considering this, the groove is made with minimal dimensions to reduce costs and welding time. Grooves are prepared by: manual grinders, electrical discharge machining (EDM) or by laser [19, 20, 22].
Before welding, it is necessary to inspect the prepared grooves with liquid penetrants, to be sure all the cracks have been removed. Welding can begin when the groove and the surrounding surface are cleaned from particles that can cause hydrogen contamination of the weld. Groove is oval shaped with groove radius of 4-6 *mm* [19]. Welding filler rods are usually recommended by the manufacturer of the mould. They consist of a chemical composition like base material but with larger addition of alloying elements (possible combustion of some elements as: Ti, Cr, Al, Zr) [16]. Rods with high tungsten content have been researched for that purpose. High content of tungsten grains distributed in the nickel–iron weld matrix resulted in low impact toughness of 5.1 *J*. [23].
Welding starts with covering the entire groove with weld material. Weld should spread about 0,3 *mm* on the base material [19, 22]. Welding is done in several layers to minimize heat input and temper the previous layer. Weld should be cleaned with a steel brush and inspected after applying next layer. Groove is filled with the weld above the surface of the base material. Excess of weld is grinded and brought to plane with the base material. If the groove is relatively large, it can be filled by welding rods of higher diameter, but the last layer should be applied with thinner rods and lower current. Example of mould repair by TIG welding is show in Figure 3.

Figure 3. Mould surface repaired by TIG welding
Slika 3. Površina kalupa popravljena TIG zavarivanjem

Immediately after welding, all possible irregularities need to be eliminated and weld face has to be grinded to the plane of base material [19, 22]. During welding, several irregularities can develop, like: distortion of thin parts, welding undercuts, weld oxidation, porosity, cracks etc. Research has proven that laser welding deliver best results when repairing weld undercuts [24]. Weld should be protected from oxidation by gas flow of 8-10 *l/min* [22]. During welding the sensitive areas can be protected with copper plates (2-3 *mm*) [20]. Repair of welding undercuts can be seen in Figure 4.

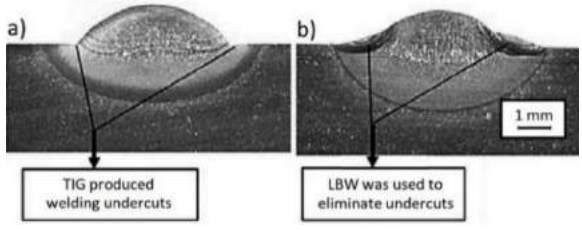

Figure 4. Repair of undercuts, [24]
Slika 4. Popravak zajeda, [24]

Cooling must be done slowly, by still air. In some cases, it is even slower (30-50°*C*), depending on the chemical composition of mould material. The weld is fine grinded. It is polished after the heat treatment [20, 22]. Tempering temperature is set so that base material and weld have similar hardness. Maximum tempering temperature is 20°C less then temperature of previous tempering.

Recently, there are more and more cases of mould reparation by **laser beam welding (LBW)**. Advantages to TIG welding are: higher energy density (103 times larger), very narrow HAZ, and minimal subsequent machining. Disadvantages are: low productivity, expensive equipment and materials and necessary trained welder [24].

Previous research has indicated that laser welding is very effective when doing mould repair. Cracks were measured on castings every 1000 cycles with the total of 40000 cycles. It was shown that intensity of crack propagation for repaired moulds was the same as for a new mould. Welded cracks did not spread but new cracks appeared. It was shown that, in the case of proper welding equipment and an experienced welder, the life span of mould can be doubled. Most influential factor on the weld quality is the weld groove preparation [19].

Another research on laser welding was done by the "DIEVAR" mould steel from "Uddeholm". Some samples were nitrated and others coated with: CrN, TiAlN and TiN coatings (PVD). The weld control has shown a high amount of porosity developed by inclusion of nitrogen from the nitrated layer into the weld. High carbon and chromium content of the welding rod causes cracks in the weld. Laser welding uses a concentrated heat input. The weld quickly cools down and the gas cannot exit the weld. This can be avoided by using the right welding parameters (e.g. choosing most adequate impulse shape). Dropping impulse shape is better for this purpose than constant or rising impulse. Higher impulse power leads to lower porosity, but increases cracking on the surface. Before welding, several experiments are needed to determine the optimal parameters [12].

Usually, a polished surface or a low surface roughness of the mould is required. After welding, differences in hardness of HAZ result with the emergence of surface waviness. Research that a Nd:YAG laser was used for welding process on H13 steel showed a strong connection between hardness and surface roughness in HAZ [25]. Suitable focus for the laser beam is 1,2 times larger than the thickness of the welding rod. That time there is melting of the base and filler material [25].

Metallization can also be used to repair the surface of moulds. Spray coating can be used to apply various metals, oxide layers or ceramics. Plasma spraying method is usually used for mould repair. Base material is not melted and the connection is achieved mostly by mechanical anchoring. That implies lower mechanical properties than achieved by welding. That kind of coating usually does not last long and starts to separate from the base material after a relatively small number of castings.

The **electro-spark deposition (ESD)** is a process for surfacing of hard metal alloys, e.g. carbides and steallites, on the surfaces of new or old machine elements [26]. ESD process is essentially a pulsed-arc microwelding process that uses: short-duration, high-current electrical pulses to weld an electrode material to a metallic substrate. A principal advantage of the ESD process is that the coatings are fused to a metal surface with such a low total heat input that the base material remains at or near ambient temperature. That eliminates thermal distortions or changes in material metallurgical structure. Since the coating is alloyed with the surface, or metallurgically bonded, it is inherently more resistant to damage and spalling than the mechanically bonded coatings produced by most other low-heat-input processes, such as: detonation gun, plasma-spray, electrochemical plating, etc. Unlike arc welding, during

ESD, the electrode contacts the substrate surface with a light pressure. It is, therefore, necessary to maintain a continual electrode motion with respect to the substrate material to prevent welding of two surfaces together [27]. During coating process electrical pulses pass through the contacting surface asperities and move across the very short ionized column of gas. The electrical current pulse may be as high as 2000 A and thus provides an intense heat source sufficient to melt and partially vaporize a portion of the contacting electrode asperities and substrate in a very short time. The spark duration, though intense, is only a few microseconds. The resulting material transfer is equally rapid and self-quenching is extremely quick. Total heat input to the substrate is very small, and distortion effects or changes in metallurgical structure of the substrate are typically negligible. On the macro level, the temperature of workpiece surface ranges below 100 $°C$ [27].

Research on mould (H13) repair with ESD showed excellent results. Layer added by that technology has proven to be very resistant to tribological wear mechanisms [25, 28]. In electro-spark deposition, the use of inert shielding gases has to be used. The inert shielding gas will protect the electrode tip and the molten surface on the workpiece. On the average, around 100 droplets per second are transferred from the electrode to the workpiece. Surface roughness of the deposit ranges between 0,8 and 5,5 μm. The thickness of deposits ranges up to 50 μm and is strongly dependent on the welding current. The dilution zone width of the deposit with the base material is around 4 μm. Schematic of ESD process and equipment is shown in Figure 5.

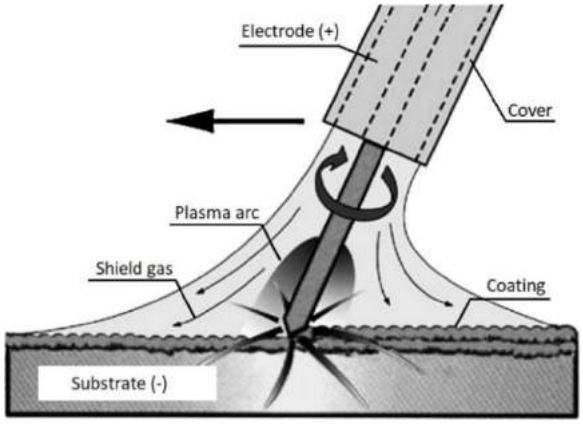

Figure 5. Electro-spark deposition (ESD), [29]

Slika 5. Electro-spark deposition (ESD), [29]

5. Conclusion

Mould material must maintain necessary mechanical properties at high temperatures and great closing forces during the casting process. Complex manufacturing procedure and expensive material result in a very high price of die casting mould. During mould exploitation wear develops on the surface, mostly because of thermal fatigue due to periodic changes in temperature. That causes cracks on the surface [4]. When the dimension of cracks exceeds the allowed value, mould has to be repaired or replaced. The mould repair is usually more cost effective than buying a new mould. Repair costs can reach up to 10% price of a new mould [16]. Repair is usually done by welding. Laser welding was proven to achieve high quality results, where life span of the mould could be doubled. High equipment price and required additional training of the welder is the reason that method is not widely used. TIG welding is dominant technology of mould repair due to its availability and relative easy handling.

For a successful welding repair, it is imperative to correctly prepare the moulds surface. Cracks should be thoroughly removed from the nonaffected part of the material and surface has to be cleaned from all impurities and grease. If using welding, parameters of welding should be carefully selected and previously tested. Preheating temperature should be precisely controlled and maintained. Most adequate filler material, preheating temperature and heat treatment parameters are usually provided by the mould manufacturer.

After welding repair, the mould it is heat treated. Intensity of heating and cooling must be strictly controlled. Best way for heat treating is in a vacuum furnace for easy supervision and protection of the moulds surface.

Other methods, like ESD, should be taken in consideration. Some of the benefits for ESD are a very narrow HAZ, good wear resistance and availability of ESD machines dedicated to mould repair.

Acknowledgements

This work has been fully supported by Croatian Science Foundation under the project 5371.

The authors are thankful to Professor N. Mišina for professional help in developing this paper.

REFERENCES

[1] Albert Handtmann Metallgusswerk GmbH & Co. KG: High-pressure die casting, www.handtmann.de/en/light-metal-casting/technologies/high-pressure-die-casting/, april 2017.

[2] C. Mitterer, F. Holler, F. Ustel, D. Heim: Application of hard coatings in aluminium die casting — soldering, erosion and thermal fatigue behaviour, Surface and Coatings Technology 125, 233–239, 2000.

[3] A. Persson: On Tool Failure in Die Casting, ACTA Universitatis Upsalinensis, Uppsala 2003.

[4] Z. Dadić, D. Živković, N. Čatipović: Surface wear of steel X38CrMoV5-1 in conditions of die casting, MTSM 2016, Split, 41-45, 2016.

[5] International Zinc Association: Tooling, http://zinc-diecasting.ionainteractive.com/db-en/HTML/9-3.php, july 2016.

[6] D. Matiskova, Š. Gašpar, L. Mura: Thermal Factors of Die Casting and Their Impact on the Service Life of Molds and the Quality of Castings, Acta Polytechnica Hungarica Vol. 10, No. 3, 65-78, 2013.

[7] R. Molina, P. Amalberto: Mechanical characterization of aluminium alloys for high temperature applications Part1: Al-SiCu alloys, Metallurgical Science and Technology, 29(2011)1.

[8] Böhler: „W300", http://www.bohleredelstahl.com/english/files/W300DE.pdf , april 2014.

[9] R. Deželić: "Metali 2", Fakultet elektrotehnike strojarstva i brodogradnje, Split, 1987.

[10] Uddeholm: "Heat treatment of tool steel", http://www.uddeholm.com/files/heattreatment-english.pdf, 2012.

[11] Assab Singapore: „Assab 8407 supreme", http://www.assab-singapore.com/media/ASSAB_8407_Supreme.pdf, july 2016.

[12] T. Muhić, J. Tušek, M. Pleterski, D. Bombač: "Problems in repair-welding of duplex-treated tool steels", Metalurgija 48, 2009.

[13] P.C. Sharma: "A textbook of production technology", S. Chand & Co. Ltd, 2012.

[14] E. J. Vinarcik: "High integrity die casting processes". John Wiley & Sons, Hoboken, New Jersey, 2003.

[15] A.H. Mohammed: "Experimental Simulation of Reduction of Erosion Damage in Dies Used in Aluminium Casting", Doktorski rad, 2013.

[16] J. Tušek, B. Taljat, D. Klobčar: "How to extend the life of die-casting tools", Metalurgija 46, 2007.

[17] D. Klobčar, A. Muhić, M. Pletenski, J. Tušek: "Thermo-mechanical cracking of a new and laser repair welded die casting die", Metalurgija 51, 2012.

[18] Unitor®: "Maritime Welding Handbook", https://www.wilhelmsen.com/globalassets/marine-products/welding/documents/wilhelmsen-ships-service---unitor-welding-handbook.pdf, april 2017.

[19] Uddeholm: "Welding of tool steel", www.uddeholm.com, april 2017.

[20] S. Thompson: "Handbook of mold, tool and die repair welding", William Andrew Publishing, USA, 1999.

[21] FSH Welding Group: "Tool and Die Welding", http://www.fsh-welding.com/en/welding-en.htm, preuzeto s interneta 15.4.2017.

[22]] Ellwood Specialty Steel Co, New Castle: "Standard Welding Procedure for ExELL H-13 SMDQ – N, ExEll Tuf Die and ExEll Hot Die", http://ess.elwd.com/wp-content/uploads/2015/04/ESS-H-Steel-Welding-Spec.pdf, preuzeto s interneta 18.4.2017.

[23] A. Skumavc, J. Tušek, A. Nagode, Ladislav Kosec: Tungsten heavy alloy as a filler metal for repair, Int. J. Mater. Res. (formerly Z. Metallkd.) 104 (2013) 11.

[24] J. Tušek, A. Skumavc, K. Pompe, D. Klobčar: "Refurbishment of damaged tools using the combination of GTAW and laser beam welding", Metalurgija 53, 2014.

[25] A. Skumavc, J. Tušek, M.Mulc, D. Klobčar: "Problems in laser repair welding of polished surfaces", Metalurgija 53, 2014.

[26] J. Tušek, L. Kosec, A. Lešnjak, T. Muhič: Electrospark deposition for die repair, Metalurgija 51(1), 17-20,2 012.

[27] R. N. Johnson, G. L. Sheldon: Advances in the electrospark deposition coating process, Journal of Vacuum Science & Technology A 4, 2740 (1986).

[28] H. Feng, L. Tian, Y. Ma, B. Tang: Tribological Behavior of Molybdenum Alloying layer on H13 Steel by Electrospark Deposition Technique, Advanced Materials Research Vols 97-101 (2010) 1356-1359.

[29] D.W. Heard, M. Brochu: Development of a nanostructure microstructure in the Al–Ni system using the electrospark deposition process, Journal of Materials Processing Technology, 892–898, 210 (2010).

ISSN 1847-7917

Finite element simulation of stresses distribution and tool displacement in the cutting tool during hard nd-milling in different machining conditions

Mario DRAGIČEVIĆ [1)], ***Sonja JOZIĆ*** [2)], ***Dražen BAJIĆ*** [2)]
1) University of Mostar
Faculty of Mechanical Engineering and Computing,
Matice hrvatske b.b.
88 000 Mostar
Bosnia and Hercegovina
2) University of Split
Faculty of Electrical Engineering Mechanical Engineering and Naval Architecture,
R. Boškovića 32, Split,
Croatia

mario.dragicevic@sve-mo.ba
sonja.jozic@fesb.hr
drazen.bajic@fesb.hr;

Keywords
Numerical modeling
Finite element method
Ansys software
Stress Distribution
Hard milling

Ključne riječi
Numeričko modeliranje
Metoda konačnih elemenata
Ansys softver
Raspodjela naprezanja
Tvrdo glodanje

Original scientific article

Abstract: This paper presents an analysis of stresses value and tool displacement in the cutting tool during hard end-milling of 42CrMo4 steel. During machining cutting parameters: cutting speed (v_c), depth of cut (a_e), feed per tooth (f_t) as well as different machining conditions like dry machining, conventional emulsion cooling and cooling by cold compressed air were varied. Numerical simulations by the Ansys Workbench 17.1 software were used to study the influence of machining parameters in different machining conditions on stresses distribution and tool displacement. Analysis was based on finite element method (FEM) and all procedure is demonstrated by using experimental observations of cutting forces F_x, F_y and F_z. The results of this study indicated that machining conditions have a significant impact to the cutting forces. The cutting force results are great indicators of stress value and tool displacement where through the finite element analysis (FEA) can to observe their impact on critical areas in the cutting tool. Having knowledge of FEA results is of great importance for selection of optimal cutting parameters and for define optimal conditions during machining. It is concluded that FEA results in the zone of total tool displacement and maximal stress value is relatively matched with the zone of tool wear observed by experimentally.

Izvorni znanstveni rad

Sažetak: Ovaj rad predstavlja analizu naprezanja i pomaka alata tijekom tvrdog obodnog glodanja čelika 42CrMo4. Tijekom obrade promjenjivi parametri obrade bili su brzina rezanja (v_c), radijalna dubina rezanja (a_e), posmak po zubu (f_z) te različiti uvjeti obrade poput suhe obrade, konvencionalnog hlađenja emulzijom i hlađenja hladnim komprimiranim zrakom. Za analizu utjecaja parametara i uvjeta obrade na raspodjelu naprezanja i pomaka alata primjenjivane su numeričke simulacije pomoću Ansys Workbench 17.1. softvera. Analiza je temeljena na metodi konačnih elemenata (MKE) te su iste temeljene na eksperimentalnim vrijednostima sila rezanja F_x, F_y i F_z. Rezultati istraživanja ukazuju da uvjeti obrade imaju značajan utjecaj na sile rezanja. Sile rezanja su veliki pokazatelji vrijednosti naprezanja i pomaka alata gdje se kroz MKE analizu može zapaziti njihov utjecaj na kritična područja na reznom alatu. Imajući saznanja o rezultatima analize MKE od velikog je značaja za izbor optimalnih parametara i uvjeta obrade. Može se zaključiti da se rezultati MKE u zoni ukupnog pomaka alata relativno poklapaju sa zonom trošenja alata koja je zabilježena eksperimentalno.

1. Introduction

Everyday development of computer capabilities and different software solutions enable numerical modeling and simulation of machining processes. Finite element method (FEM) is becoming an indispensable tool for numerical prediction of output values of machining process. In that view, scientists are made the space for improving machining processes and reducing total production costs associated with long and expensive experimental tests. In recent years more attention has been devoted in respect to FEM capabilities of numerical prediction of cutting temperatures, cutting forces, shapes and thickness of separated chips and tool wear during machining [1], [2], [3], [4].

Many researchers have used different FEM software packages to simulate machining processes such as: Abaqus/Explicit [5], Ansys/Explicit [6], Deform 2D/3D [7], AdvantEdge [8], Ls Dyna [9] and others. Arrazola et al. presented the-state-of-the art in 3-D FEM modeling and simulations of machining processes [10]. Constantin et al. [11] in their study presented FEM modelling and simulation through steps: pre-processing, simulating and postprocessing of data for the established machining

process and experiments during milling process. Tamizharasan and Kumar [12] have investigated the influence of tool geometry on tool wear during turning of AISI 1045 steel. The optimal tool geometry were successfully confirmed by FEM model using Deform 3D software. Thakare and Nordgren [13] have predicted temperature distribution in coated cemented carbide cutting tools during turning of AISI 4340 steel. Authors used an AdvantEdge 2D software package. Kurt and Seher [14] have investigated the effects of the cutting forces on the cutting tool stresses during machining of Inconel 718 alloy. The stress distributions on the cutting tool were successfully confirmed by FEM model using Ansys software. Pu et al. [15] confirmed that residual stresses simulated by DEFORM 2D software were consistent with experiments data. Experiments were carried out during turning of AZ31B Mg alloy with different edge radius and machining conditions. Caruso et al. [16] implemented FEM model with the aim to predict microstructural changes and dynamic recrystallization during dry turning of Waspaloy (397 ± 10 HV0.05). The results have shown very good agreement between experimental and simulated results of grain size, micro hardness, depth of the affected layer, cutting forces, temperature, and chip morphology. Ucun et al. [17] predicted the forces, temperatures and thickness of the separated chips during micro-milling of Inconel 718 alloys using Deform 2D software. The results have shown that the greatest difference between numerical and experimental results are occurred when predicting the thickness of separated chips at higher feed rates. It has been confirmed that predictions of temperatures are accurate in the range from 92 % to 95 %, and the cutting force between 77 % and 94 % compared to the experimental results. Zebala and Słodki [18] predicted the stress and temperatures during machining of the Inconel 718 alloy during turning processes. The results of the simulation in AdvantEdge have shown that the impact of the cutting edge radius significantly influences on stress distribution and temperature in the cutting tool. Also, authors stated that the difference between the simulated and measured values of cutting forces was below 21%. Malikzada et al. [19] have developed numerical model for predicting of tool wear during turning of hardened 20MnCr5 steel with uncoated cutting tool. Mamedov and Lazoglu [20] successfully applied a 3D numerical model for predicting the temperature during micro-milling of Ti-6Al-4V alloys. Based on the results of the simulation, the authors concluded that besides the temperature in the cutting zone, on the tool wear significantly impact have the stresses and dimensional accuracy of the cutting tool and workpiece. The results have shown that the predicted temperature in the cutting zone is only 12 % different with the temperature obtained experimentally. Parid and Maity [21] varied the three different cutting tool edge: 0.4 mm, 0.8 mm and 1.2 mm and analyse their influence on the forces, stresses, temperature, shape and thickness of the separate chips during turning of Inconel 718 alloys. The simulation results in Deform 2D software shown good correlation with the experimental data. The authors argue that finite element analysis is the best tool for prediction stress and temperatures in machining process. Having knowledge of cutting forces which affect on the cutting tool during machining can be one of essential indicators for selecting the optimal machining parameters and conditions. The influence of different machining conditions on stress value and tool displacement has not sufficiently been simulated by researchers. The main aim of this paper is to analyse different cutting parameters and machining conditions on the cutting tool stress value and tool displacement during hard end milling of 42CrMo4 steel. The cutting forces were measured experimentally and stress value and tool displacement on the cutting tool were analysed by FEM using Ansys Workbench 17.1 software.

2. Experimental Research

2.1. Materials and methods

During machining 30 cutting experiments were carried out in three different machining conditions. The cutting conditions are characterized by dry machining, conventional emulsion cooling and cooling by cold compressed air. Cooling process with the use of cold compressed air is enabled from the compressed air network with the device Cold Air Gun of the manufacturer Vortec. Dry machining conditions imply the absence of any medium for cooling, flushing and lubrication. The application of wet emulsion in hard milling is enabled with chemical emulsion TU 30 T through 4 nozzles with a flow rate of 36 L/min. The experiments are performed on the vertical machining centre CNC SPINNER VC560. The input cutting parameters and machining conditions used in experiments are presented in Table 1.

Table 1. Input values with associated levels
Tablica 1. Ulazne veličine s pripadajućim razinama

Levels of factors	Cutting speed v_c [m/min] A	Depth of cut a_e [mm] B	Feed rate per tooth f_t [mm/tooth] C	Machining conditions *Mc* D
1.	100	1	0.05	Dry machining
2.	125	1.5	0.08	Cutting fluids
3.	150	2	0.11	Cold compressed air

The workpiece used in hard milling is heat-treated low alloy steel 42CrMo4. Measurement results confirmed workpiece hardness of 47 HRC. Chemical composition of workpiece is presented in Table 2.

Table 2. Chemical Composition of the workpiece
Tablica 2. Kemijski sastav obratka

CHEMICAL COMPOSITION %								
C	Si	Mn	P	S	Cr	Ni	Mo	Cu
0.430	0.278	0.77	0.018	0.028	1.09	0.08	0.185	0.08

Thermal improvement was carried out in order to obtain increased hardness of workpiece. Face and circumferential cutter COROMILL 390 cutting diameter 20 mm, product code R390-020A20-11M with three cutting inserts code R390-11 T3 08M-PM were used during machining. The substrate of cutting inserts is a hard metal chemical composition: WC 80%, TiC 8%, TaC 5%, and Co 7%. The cutting inserts were coated with a PVD high-strength TiAlN coating. The quality label of inserts is GC 1030. The cutting inserts are intended for machining of hard materials with a hardness more than 36 HRC. The recommended values of the machining parameters for these cutting inserts in the milling process are: v_c = 260 m/min to 275 m/min, ft = 0.08 mm/t to 0.12 mm/t. The cutting forces are measured by Kistler piezoelectric dynamometer type 9257A with Multi-channel charge amplifier type 5070 A with three-component force sensor.

3. Finite Element Method Analysis

The cutting forces measured during end-milling were used to analyze the stresses value and tool displacement in ANSYS software based on the FEM. The cutting tool insert was modelled in Solidworks software and then sent to ANSYS in .step format, Figure 1.

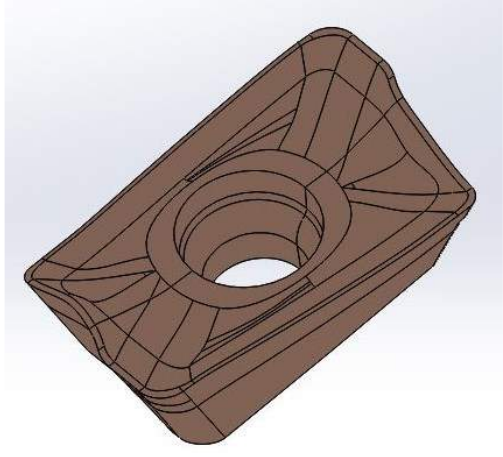

Figure 1. CAD model of cutting insert
Slika 1. CAD model rezne pločice

The material properties are modulus of elasticity E=600 GPa, Poisson's ratio ν=0.25 and density ρ=5220 kg/cm^3. Determination of cutting tool properties, define type and sizes of finite elements, the meshing of the cutting tool model, determination of boundary conditions and external loads are necessary steps before FEM analysis. Meshing of the tool insert was carried out with Solid 185 element type. The mesh density was selected 0.05 mm in the chip–tool contact zone and 0.5 mm in the other parts of the tool insert, Figure 2.

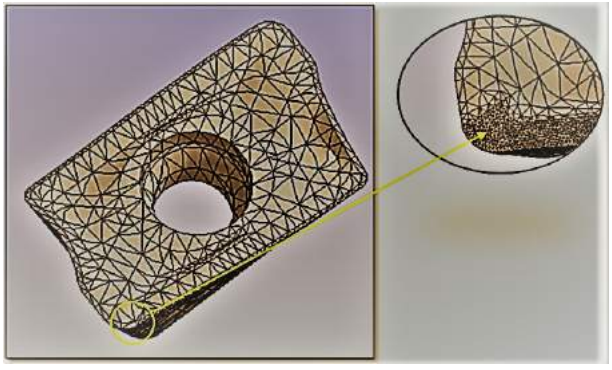

Figure 2. Meshing of the cutting insert and tool-chip zone
Slika 2. Mreža konačnih elemenata na reznoj pločici

The total 9 669 nodes and 5 277 elements for the cutting insert were used in the numerical analysis. The interaction between the cutting insert and the tool holder is defined as fixtures zone. Defined fixed support simulates a strong connection between the cutting inserts and the tool holder, Figure 3.
During analysis the static analysis solution method was used. External loads in terms of cutting forces F_x, F_y, F_z are applied on the cutting tool. The action of the cutting blade on the workpiece and impact of stress in the Cartesian coordinate system is shown in the Figure 4.
External loads are defined along the chip–tool contact length and the depth of cuts. In the section 4 is detailed described the influence of external loads on stress value and tool displacement for defined machining parameters and conditions.

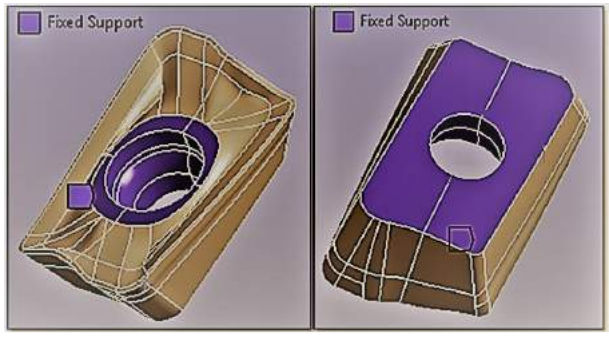

Figure 3. Fixtures between the cutting insert and the tool holder
Slika 3. Čvrsta veza između rezne pločice i držača alata

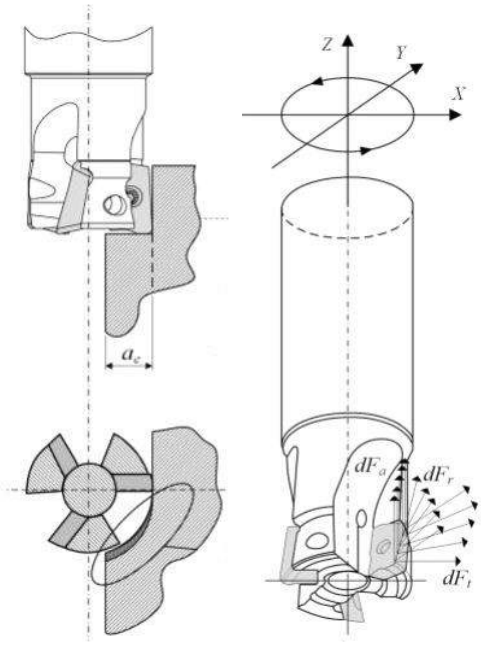

Figure 4. Stress distribution along the cutting blade
Slika 4. Raspodjela naprezanja duž rezne oštrice

4. Results and discussions

Analyses were carried out for all 30 cutting experiments. The cutting forces measured by the cutting experiments during different machining conditions are shown in Figures 5, 6, 7. Diagrams are shown that by increasing in cutting speed, the value of F_x and F_y components of the milling forces decreases. Due to accelerated tool wear during hard end-milling with emulsion cooling, higher values of F_x and F_y forces are visible. In the same conditions at higher cutting speed with constant feed rate the lower value of F_x and F_y are achieved. Increasing of F_x and F_y despite the increase in cutting speed occurs after a certain time of machining as a result of tool wear. Increasing feed rates directly affects to increase of F_x and F_y forces. The reason of that is increase in cross-section of the separated layer of material as form of separated chips. It is evident that measured cutting force values for the depth of cut 2 mm are higher than in the lower values of depth of cut. Due to the continuous tool wear with increase of the machining time components of cutting forces during hard milling are increased. Lower values and slower growth of the cutting force components when the machining time is increased in dry machining and cold compressed air machining can be explained by the stabilization of multilayer TiAlN coatings.

In all of the cutting experiments, the F_y cutting force is measured too higher than other cutting forces. Mostly lower values of F_x and F_y forces at higher machining time under cold compressed air machining are due to less tool wear compared to dry and wet emulsion machining. By observing results for hard milling under cold compressed air, the average increase in tool life is 26 % compared to dry machining and 198 % compared to conventional wet machining.

From the analysis of stress value and total deformation of cutting tool inserts it is evident that the highest stresses and deformation are obtained with the lowest depth of cut, Figure 8 and Figure 9.

The cutting stresses distribution increase with decreasing the depth of cut because the contact zone between tool-chip decreasing. Besides, the tool-chip contact zone with an increase in depth of cut increase. When increasing the cutting speed and the depth of cut, the cutting forces and cutting stresses decrease.

The cutting stresses and tool displacement in this study slightly increase by decreasing of cutting speed, and it is different for different machining conditions. The relation between forces and displacements and forces and stress value in each iterative solution step in this analysis was observed. The results of stress value and tool displacement were investigated according to changing the input cutting parameters and machining conditions. The minimum stress value of 4343.9 MPa was obtained from machining with emulsion cooling.

The Equivalent von Mises stress value in all machining conditions (9064.6 MPa dry, 11025 MPa, emulsion machining, and 13655 MPa cold compressed air machining) was presented in Figure 8. The total tool displacement in all machining conditions are shown in Figure 9. It can be concluded that the biggest displacement value was during dry machining. During FEM analysis of tool displacement in Ansys, large deflection of results was not shown because the cutting insert did not expose to the large displacement.

During FEA analysis zone of maximum stress concentration and zone of large tool displacement give information about critical tool zone and that is possible tool wear area. Figure 10. shows the zone of total displacement in FEM analysis for different cutting parameters and conditions. Compared to the results of tool wear obtained experimentally for the same conditions the greatest tool displacement were obtained

in the same places by FEM simulation. FEM results show that the cutting tool wear may be occur in the zone with maximum stress distribution and tool displacement.

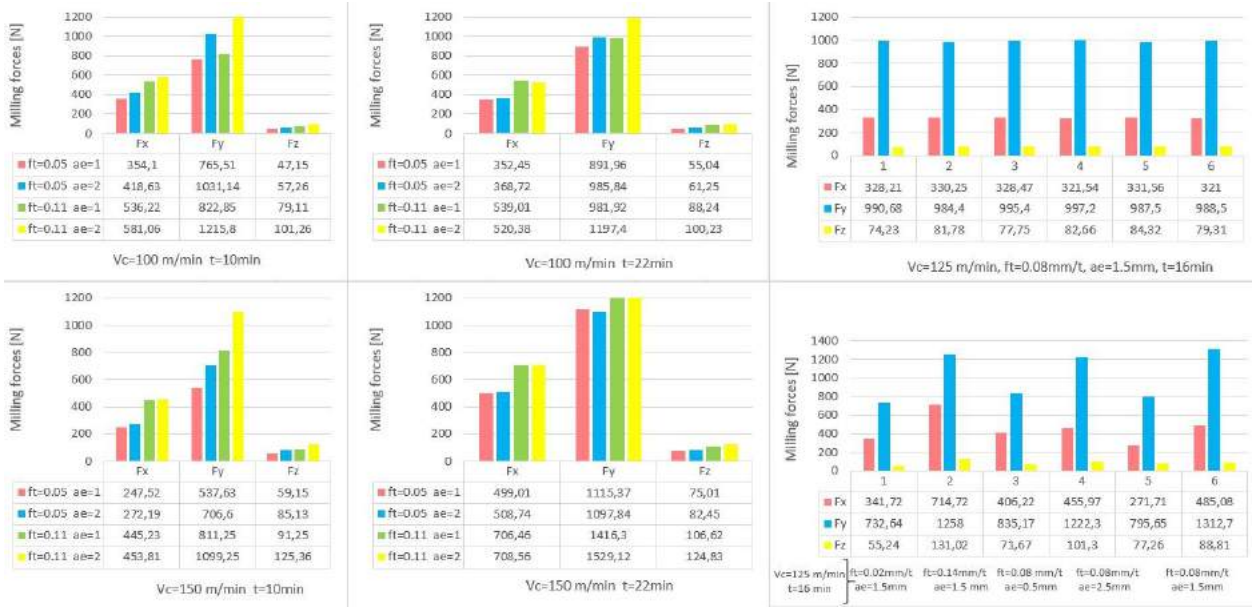

Figure 5. Cutting forces F_x, F_y, F_z during dry hard end-milling
Slika 5. Sile rezanja F_x, F_y, F_z tijekom tvrdog glodanja u uvjetima suhe obrade

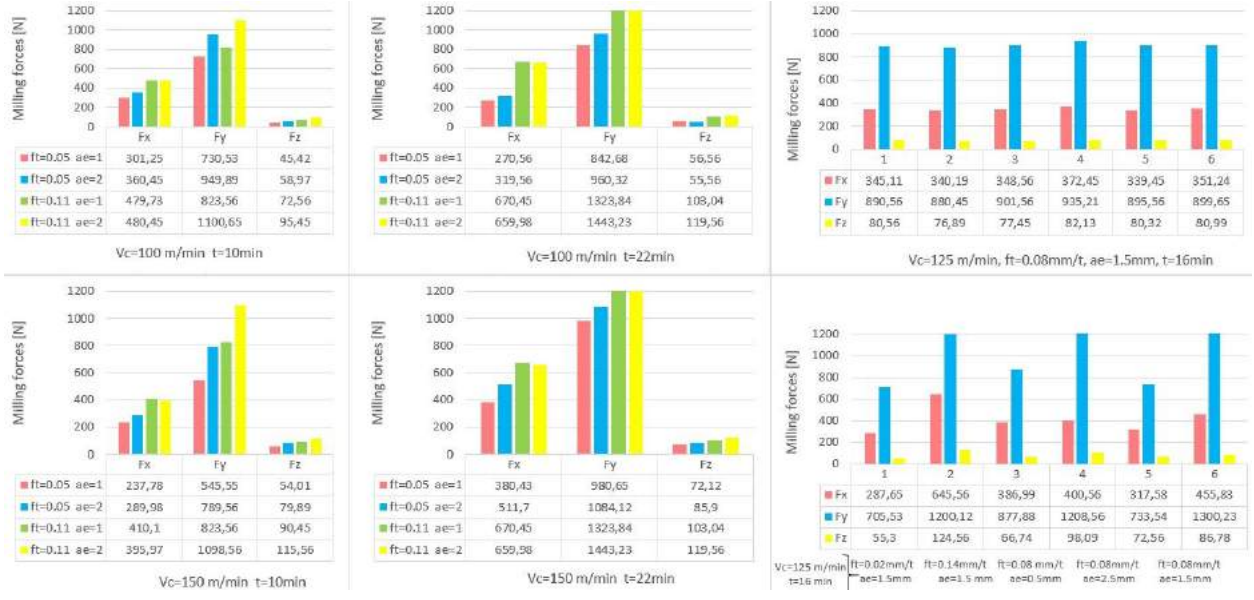

Figure 6. Cutting forces F_x, F_y, F_z during hard end-milling with cold compressed air
Slika 6. Sile rezanja F_x, F_y, F_z tijekom tvrdog glodanja u uvjetima hladnog komprimiranog zraka

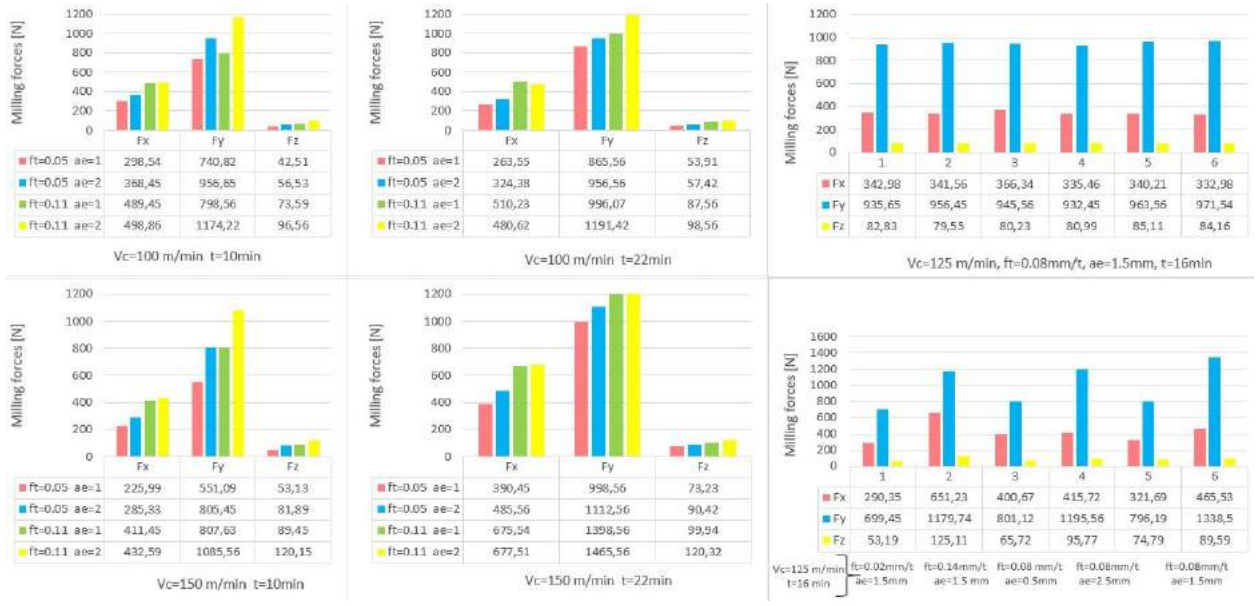

Figure 7. Cutting forces F_x, F_y, F_z during hard end-milling with emulsion
Slika 7. Sile rezanja F_x, F_y, F_z tijekom tvrdog glodanja uz korištenje emulzije

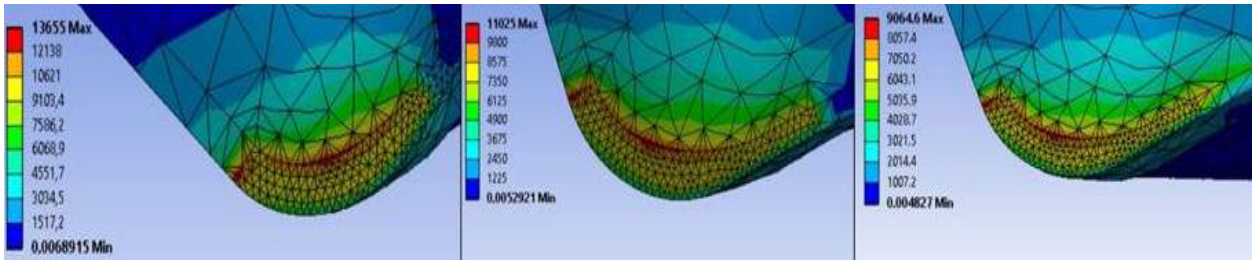

Figure 8. Equivalent von Mises stress distributions during dry, emulsion and cold compressed air machining
Slika 8. Ekvivalentno von Mises naprezanje u uvjetima suhe obrade, primjenom emulzije i hladnog komprimiranog zraka

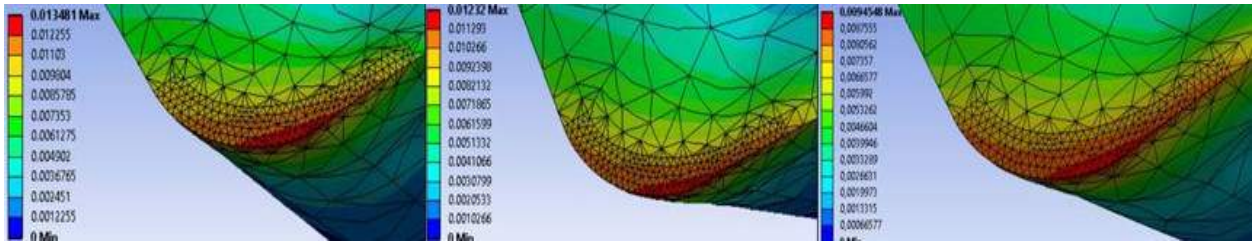

Figure 9. Maximal tool displacement during dry, emulsion and cold compressed air machining
Slika 9. Maksimalni pomak alata tijekom obrade u uvjetima suhe obrade, primjenom emulzije i hladnog komprimiranog zraka

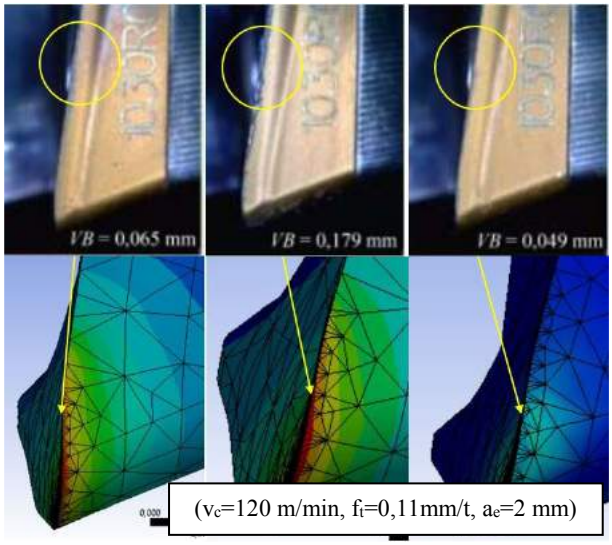

Figure 10. Total tool displacements obtained by FEA for dry, emulsion and cold compressed air machining
Slika 10. Ukupno pomjeranje alata dobiveno analizom konačnih elemenata za uvjete suhe obrade, emulzije i hladnog komprimiranog zraka

According to microscope image, tool wear zone obtained experimentally is compatible with those zones for all machining conditions.

5. Conclusion

In this study, FEM analyses were performed in order to determine the stresses value and cutting tool displacement during hard end-milling of 42CrMo4 steel with three TiAlN tool inserts. Different machining conditions: dry machining, conventional emulsion cooling and cooling by cold compressed air and different cutting parameters was varied. Increasing machining time causes increase of F_x and F_y forces. Different machining conditions in combination with different machining parameters gave a different effect on the cutting force distribution. Based on the experimental results of the cutting forces, and microscopic analysis a conclusion about tool wear in different machining conditions can be obtained. Results of analyses indicated that cold compressed air machining results in lower stress value and tool displacement compared to the dry and emulsion machining. Cutting speeds, depth of cut and machining time are most influential on stress value and tool displacement during machining in all machining conditions. FEM analysis showed that stress value increase with decreasing the depth of cut because contact zone between tool and chip is decreased. This study confirms that the cutting tool stress value and tool displacement can be successfully predicted by FEM analysis. Results of analysis by help with Ansys software provide opportunity to provide the critical area of the tool wear for combination of different machining parameters and conditions.

References

[1] Niesłony, P., Grzesik, W., Habrat, W., (2015), *Experimental and simulation investigations of face milling process of Ti6Al4V titanium alloy*, Advances in Manufacturing Science and Technology, Vol. 39, No. 1, pp. 40-50, DOI: 10.2478/amst-2015-0003.

[2] Fu, Z. T., Yang, W. Y., Zeng, S. Q., Guo, B. P., Hu, S. B., (2016), *Identification of constitutive model parameters for nickel aluminum bronze in machining*, Transactions of Nonferrous Metals Society of China, vol. 26, No. 4, pp. 1105–1111.

[3] Thepsonthi, T., Özel, T., (2015), *3-D finite element process simulation of micro-end milling Ti-6Al-4V titanium alloy: Experimental validations on chip flow and tool wear*, Journal of Materials Processing Technology, vol. 221, pp. 128–145.

[4] Sun, Y., Huang, B., Puleo, D. A., Jawahir, I. S., (2015), *Enhanced Machinability of Ti-5553 Alloy from Cryogenic Machining: Comparison with MQL and Flood-cooled Machining and Modeling*, Procedia CIRP31, Vol. 31, pp.. 477 – 482.

[5] Mabrouki T., Rigal, J. F., (2006), *A contribution to a qualitative understanding of thermo-mechanical effects during chip formation in hard turning*, Journal of Materials Processing Technology, Vol. 176, No. 1–3, pp. 214–221.

[6] Ku, K. K., Srinivas, N., (2016), *Optimization and Process Control in Small Diameter End Mill*, International Journal of Engineering Science and Computing, vol. 6, no. 8, pp. 2581–2585.

[7] Özel, T. (2006), *The influence of friction models on finite element simulations of machining*, International Journal of Machine Tools and Manufacture, vol. 46, no. 5, pp. 518–530.

[8] Maranhão, C., Davim, J. P., (2010), *Finite element modelling of machining of AISI 316 steel: Numerical simulation and experimental validation*, Simulation Modelling Practice and Theory, Vol. 18, No. 2, pp.139–156

[9] Ambati, R. R. S. (2013), *Simulation of Cutting Stresses and Temperatures on tool geometry at the onset of Turning operation by Finite Element Method*, Indian Journal of Medical Research, Vol. 2, No. 3, pp. 123–125.

[10] Arrazola P. J., Özel T., Umbrello D., Davies M., Jawahir I. S., (2013), *Recent Advances in Modelling of Metal Machining Processes*. CIRP Annals-Manufacturing Technology Vol.62, No. 2: pp.695–718.

[11] Constantin, C., Bisu, C., Croitoru, S. M, Constantin, G., (2010), *Milling analysis by 3D FEM and*

experimental tests, Annals of DAAAM & Proceedings, pp. 337-338.

[12] Tamizharasan, T., Senthil Kumar N., (2012), *Optimization of cutting insert geometry using Deform 3-D: Numerical simulation and experimental validation*, International Journal of Simulation Modelling - Simulation Journals, pp. 65-76, ISSN 1726-4529.

[13] Thakare, A., Nordgren, A., (2015), *Experimental Study and Modeling of Steady State Temperature Distributions in Coated Cemented Carbide Tools in Turning*, Procedia CIRP, Vol. 31, pp.234 – 239.

[14] Seker, U., Kurt, A., (2006), *The mathematical modelling of the compressive stresses in machining of Inconel 718*, Advances in Materials Processing Technologies, Vol. 526, pp.229–234,

[15] Pu, Z., Umbrello, D., Dillon O. W., Jawahira, I. S., (2014), *Finite Element Simulation of Residual Stresses in Cryogenic Machining of AZ31B Mg Alloy*, Procedia CIRP, Vol. 13 pp. 282 – 287.

[16] Caruso, S., Imbrogno, S., Rinaldi, S., Umbrello, D., (2016), *Finite element modeling of microstructural changes in Waspaloy dry machining*, The International Journal of Advanced Manufacturing Technology, Vol. 89, pp.227-240. DOI 10.1007/s00170-016-9037-y.

[17] Ucun, I., Aslantas, K., Bedir, F., (2016), *Finite element modeling of micro-milling: Numerical simulation and experimental validation*, Machining Science and Technology, Vol. 20, 1, pp. 148–172.

[18] Zębala, W., Słodki, B., (2013), *Cutting data correction in Inconel 718 turning, International Journal of Advanced Manufacturing Technology*, Vol. 65, No. 5–8, pp. 881–893.

[19] Malakizadi, A., Gruber, H., Sadik, I., Nyborg, L., (2016), *An FEM-based approach for tool wear estimation in machining*, Wear, Vol. 368–369, pp. 10–24.

[20] Mamedov, A., Lazoglu, I., (2016), *Thermal analysis of micro milling titanium alloy Ti-6Al-4V*, Journal of Materials Processing Technology, Vol. 229, pp. 659–667.

[21] Parida, A. K., Maity, K., (2016), *Effect of nose radius on forces, and process parameters in hot machining of Inconel 718 using finite element analysis*, Engineering Science and Technology, an International Journal, Vol. 20, No. 2, pp. 687–693.

ISSN 1847-7917

Primjena Crafts – Lamont dijagrama za procjenu raspodjele tvrdoće nakon poboljšavanja čelika EN 42CrMo4

Igor Gabrić Anja Milavić Ivan Vrljičak
Sveučilište u Splitu - Sveučilišni odjel za stručne studije
(University of Split - The university department of professional studies)
Kopilica 5, 21000 Split,
Sveučilište u Splitu
igor.gabric@oss.unist.hr
Anja Milavic cigla5@live.com
ivan.vrljicak@oss.unist.hr

Keywords
Crafts – Lamont method
Tempering
Heat treatment

Ključne riječi

Crafts-Lamont metoda
Popuštanje
Toplinska obrada

Application of Crafts - Lamont Diagrams for Assessing the Distribution of Hardness after Tempering EN 42CrMo4 Steel

Professional article

Abstract: This paper analyses possibility of applying Crafts – Lamont method to estimate the distribution of hardness across the small diameter steel specimen cross - section area after quenching and tempering. Several Jominy specimens were prepared from 42CrMo4 steel, which are tempered at various temperatures according to the design of experiment after standard heat treatment. The recorded Jominy curves were used to estimate the hardness distribution by cross - section area according to the Crafts - Lamont method. For the purpose of verifying the obtained results, several specimens of different diameters from the same steel were prepared. Each specimen is quenched and tempered according to the design of experiments. Finally, a comparison of the results obtained by measuring of the treated samples and the results obtained by the Crafts - Lamont method was performed and conclusions were adopted on the possibility of applying the method.

Stručni rad

Sažetak: U radu je analizirana mogućnost primijene Crafts – Lamont metode za procjenu raspodjele tvrdoće po okruglom poprečnom presjeku nakon klasičnog poboljšavanja čelika za izratke manjih promjera. U svrhu primjene metode pripremljeno je više Jominy epruveta iz čelika za poboljšavanje 42CrMo4 koje su nakon standardnog tretmana popuštene na različitim temperaturama prema planu pokusa. Snimljene Jominy krivulje su korištene za procjenu raspodjele tvrdoće po presjeku prema Crafts – Lamont metodi. U svrhu verifikacije dobivenih rezultata pripremljeno je više uzoraka različitih promjera iz istog čelika. Svaki uzorak je nakon kaljenja popušten na odgovarajućoj temperaturi prema planu pokusa. Na koncu je izvršena usporedba rezultata dobivenih mjerenjem tretiranih uzoraka i Crafts – Lamont metodom te su izvedeni zaključci o mogućnosti primjene metode.

1. Uvod

Do sada je razvijeno više metoda za procjenu raspodjele tvrdoće okruglih i neokruglih poprečnih presjeka zakaljenih izradaka. Jedna od navedenih je i Crafts – Lamont metoda. Crafts – Lamont metoda se zasniva na primjeni dijagrama izrađenih na temelju korelacija prijelaza topline, a za procjenu položaja presjeka Jominy epruvete koji ima odgovarajuću krivulju hlađenja tj. istu tvrdoću kao i specifična lokacija u okruglom poprečnom presjeku [1].

Korištena Crafts – Lamont metoda je ograničena na izratke punog okruglog poprečnog presjeka. Temelji se na nizu dijagrama od kojih svaki odgovara za točno određenu udaljenost od površine izratka. Jedan od takvih dijagrama prikazan je na slici 1 [1]. U svakom dijagramu je ucrtano više krivulja za različite intenzitete rashladnog sredstva. Dijagrami povezuju različite promjere uzoraka i odgovarajuće udaljenosti od kaljenog čela Jominy epruvete. Metoda je dobra za procjenu debljine zakaljenog sloja kod vratila i osovina okruglog poprečnog presjeka, a nakon hlađenja u rashladnom sredstvu poznatog intenziteta.

Analogno primjeni metode za zakaljene izratke za očekivati je da se primjenom iste metode, a korištenjem Jominy krivulja za popuštene Jominy epruvete (vidi sliku 2.), može procijeniti raspodjela tvrdoće zakaljenog i na istoj temperaturi popuštenog uzorka okruglog poprečnog presjeka.

Symbols/Oznake

P	- Hollomon-Jaffe parameter - Hollomon-Jaffe parametar	- **Greek letters/Grčka slova**	
t	- Temperature in °C - Temperatura u °C	τ	- time in hours - vrijeme u satima
HV	- Hardness according Vickers - Tvrdoća po Vickersu	γ	- austenite - austenit
h	- Distance from surface in mm - Udaljenost od površine u mm		

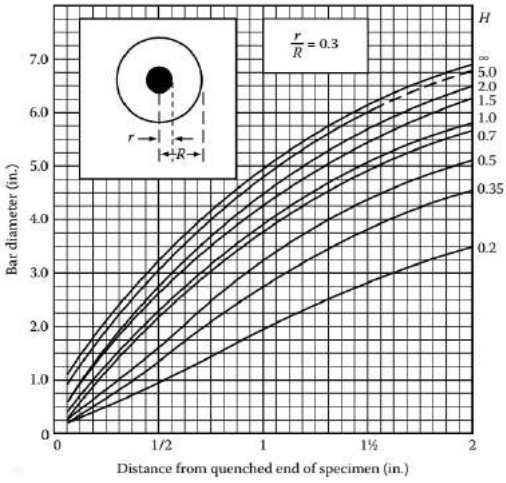

Figure 1. Crafts – Lamont curve for 30% radius of quenched specimen [1]

Slika 1. Crafts – Lamont krivulje za 30% promjera kaljenog uzorka [1]

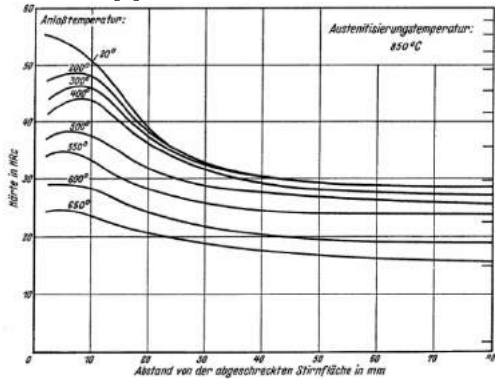

Figure 2. Hardness distribution along Jominy specimens, tempered at various temperatures, prepared from 42CrMo4 steel [2]

Slika 2. Raspodjela tvrdoće duž Jominy epruvete za različite temperature popuštanja čelika 42CrMo4 [2]

2. Eksperimentalni dio

2.1. Planiranje pokusa

Kako bi se potvrdila pretpostavka iz istog komada čelika pripremljene su tri šipke promjera 25, 32 i 40 mm duljine 100 mm iz čelika 42CrMo4, vidi sliku 3. Šipke su austenitizirane i zakaljene u vodi. Nakon kaljenja provedeno je visokotemperaturno popuštanje na tri različite temperature za sva tri promjera. Dimenzije i plan popuštanja uzoraka prikazani su u tablici 1. Pripremljene su i tri Jominy epruvete, za svaku korištenu temperaturu popuštanja po jedna, kako bi se odredile Jominy krivulje za odabrane temperature popuštanja (vidi sliku 4). Nakon toplinskog tretmana uzoraka izvršeno je mjerenje tvrdoće po promjeru poprečnog presjeka cilindričnih uzoraka, te mjerenje tvrdoće duž izvodnice Jominy epruveta.

Figure 3. Bars of different diameter from which specimens were taken

Slika 3. Šipke različitog promjera iz kojih su izrezane epruvete

Table 1. Tempering temperature of cylindrical specimens 12 mm thick prepared for testing

Tablica 1. Temperature popuštanja cilindričnih uzoraka debljine 12 mm pripremljenih za ispitivanje

Uzorak br.	Promjer uzorka, mm	Temperatura popuštanja, °C
1	25	450
2	25	525
3	25	630
4	32	450
5	32	525
6	32	630
7	40	450
8	40	525
9	40	630

Figure 4. Jominy probes tempered at temperatures 450, 525 i 630°C
Slika 4. Jominy epruvete popuštene na temperaturama 450, 525 i 630°C

2.2. Provedba pokusa

2.2.1. Obrada cilindričnih uzoraka

Iz šipke promjera 40mm izrezana su tri cilindrična uzorka i obrađena na promjere 25, 32 i 40 mm, duljine 100 mm. Uzorci su austenitizirani i zakaljeni u vodi sobne temperature.

Nakon kaljenja izvršeno je visokotemperaturno popuštanje u trajanju 1 sat na temperaturi 450 °C. Ohlađeni uzorci su prerezani na udaljenosti od 20 mm od čela odakle su izrezane epruvete debljine 10 mm. Preostali dulji dio uzoraka je ponovno popušten u trajanju 1 sat na temperaturi 525 °C, nakon čega je ponovno na 20 mm od čela uzoraka izrezana po jedna epruveta debljine 10mm. Preostali dijelovi uzoraka su popušteni na temperaturi 630 °C u trajanju 1 sat, te su iz njihovog središnjeg dijela izrezane preostale epruvete (slika 5).

Figure 5. Specimens after heat treatment and cutting from the bar
Slika 5. Uzorci nakon toplinske obrade i izrezivanja iz šipki

Kako bi se umanjio utrošak materijala i vremena potrebnih za izvođenje pokusa, isti zakaljeni uzorci su popuštani na sve tri odabrane temperature u trajanju jedan sat, a nakon svakog popuštanja je izrezana po jedna epruveta iz svakog uzorka. Kumulativni utjecaj prethodnih popuštanja je provjeren prema Hollomon-Jaffe zakonu popuštanja:

$$P = \frac{273{,}15+t}{1000} \cdot [C + log(\tau)] \quad (1)$$

$$\frac{T_1}{1000} \cdot [C + log(\tau_1)] = \frac{T_2}{1000} \cdot [C + log(\tau_2)] \quad (2)$$

$$C = 21{,}3 - (5{,}8 \cdot \%C) \quad (3)$$

gdje je:

T_1, K - niža temperatura popuštanja
τ_1, h - trajanje popuštanja na nižoj temperaturi
T_2, K - viša temperatura popuštanja
τ_2, h - trajanje popuštanja na višoj temperaturi
C - konstanta za konkretni čelik
%C - sadržaj ugljika za konkretni čelik

Naime, izračunato je ekvivalentno trajanje popuštanja za niže temperature primjenom izraza (2). Popuštanje na temperaturi 450 °C u trajanju jedan sat je ekvivalentno popuštanju na 525 °C u trajanju svega 52 sekunde. Isto tako popuštanje na temperaturi 525 °C u trajanju jedan sat je ekvivalentno popuštanju na 630 °C u trajanju svega 19 sekundi. Iz navedenog se da zaključiti da je razlika u temperaturama popuštanja dovoljno velika da trajanje popuštanja na nižoj temperaturi nema gotovo nikakvog utjecaja na popuštanje na višim temperaturama pa se stoga može zanemariti.

2.2.2. Obrada Jominy epruveta

Iz istog komada šipke pripremljene su tri Jominy epruvete i tretirane prema standardu (slika 6).

Figure 6. Jominy probe cooling
Slika 6. Hlađenje Jominy epruvete

Nakon tretmana prema standardu Jominy epruvete su popuštene na odabranim temperaturama u trajanju od 1 sat.

2.2.3. Mjerenje tvrdoće po promjeru cilindričnih uzoraka

Mjerenje je izvršeno prema Vickers postupku uz silu utiskivanja 294 N. Na slici 7 su prikazani uzorci nakon mjerenja po promjeru. Tvrdoće su izmjerene po izvodnici na deset različitih, ravnomjerno raspoređenih, udaljenosti od površine epruvete. Rezultati mjerenja prikazani su u tablici 2.

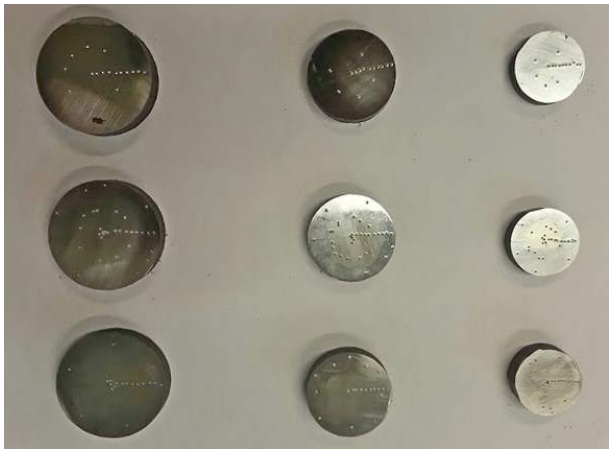

Figure 7. Specimens after hardness measuring
Slika 7. Uzorci nakon mjerenja tvrdoće

Table 2. Results of hardness measuring across specimen's cross-sections
Tablica 2. Rezultati mjerenja tvrdoće po promjeru uzoraka

R	25	32	40	25	32	40	25	32	40
t_{pop}	450	450	450	525	525	525	630	630	630
r/R									
0.0	409	428	390	381	361	345	291	275	275
0.1	424	427	396	377	363	348	294	273	268
0.2	439	423	389	385	365	345	290	275	273
0.3	430	434	386	377	352	356	293	288	264
0.4	427	431	394	368	368	370	295	288	270
0.5	431	435	409	373	374	366	295	293	266
0.6	436	440	409	370	379	359	292	298	289
0.7	434	433	410	378	382	371	298	296	291
0.8	436	429	414	378	374	360	303	290	288
0.9	427	410	400	367	370	322	288	286	267

2.2.4. Mjerenje tvrdoće duž izvodnice Jominy epruvete

Mjerenje tvrdoće je izvršno prema standardu Vickers postupkom uz silu utiskivanja 294 N.
Rezultati ispitivanja prikazani su u tablici 3, te u dijagramu na slici 8.

Table 3. Results of hardness measuring of Jominy probes
Tablica 3. Rezultati mjerenja tvrdoće Jominy epruveta

	Tvrdoća, HV30		
J- udaljenost, mm	t_{pop}=450°C	t_{pop}=525°C	t_{pop}=630°C
2	406	378	288
4	424	379	292
6	429	377	291
8	426	374	288
10	416	368	283
12	404	362	278
14	390	354	273
16	377	346	268
20	353	330	261
24	336	314	257
28	325	301	255
32	318	291	253
36	314	285	249
40	310	283	245
44	306	283	239
48	303	286	234
52	301	288	230
56	302	289	229
60	303	284	231
64	299	271	230

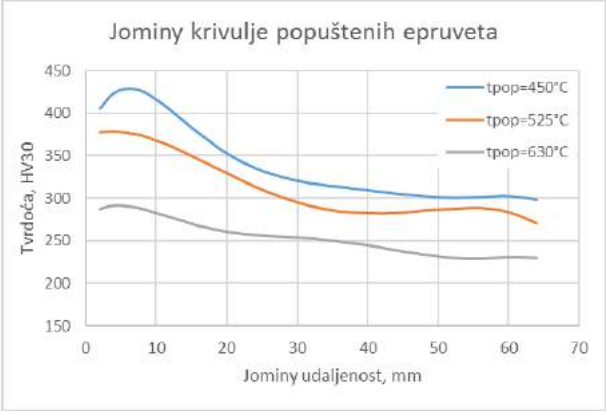

Figure 8. Jominy curves of tempered probes
Slika 8. Jominy krivulje popuštenih epruveta

2.3. Određivanje tvrdoće Crafts-Lamont metodom

Raspodjela tvrdoće popuštenih cilindričnih uzoraka određena je primjenom Crafts-Lamont modela uz korištenje Jominy krivulja popuštenih Jominy epruveta na odgovarajućim temperaturama.
Kako bi se proces automatizirao sve Crafts-Lamont i Jominy krivulje su aproksimirane polinomom šestog stupnja primjenom analize varijance uz pomoć programskog paketa Design-Expert [3], te implementirane u MS Excel tablicu. Za određivanje ekvivalentne Jominy udaljenosti za okrugle presjeke

korišten je intenzitet rashladnog sredstva H=1 jer je kaljenje šipki iz kojih su izrezani cilindrični uzorci izvršeno u mirnoj vodi sobne temperature. Rezultati dobiveni primjenom Crafts-Lamont metode za epruvete promjera 25, 32 i 40 mm prikazani su u tablicama 4, 5 i 6.

Table 4. Results given by Crafts-Lamont method for specimens of 25mm diameter

Tablica 4. Rezultati dobiveni Crafts-Lamont metodom za uzorke promjera 25mm

d = 25 mm		Tvrdoća HV30		
r/R	h, mm	t_{pop}=450°C	t_{pop}=525°C	t_{pop}=630°C
0	12,5	426	379	292
0,1	11,25	427	379	292
0,2	10	427	379	292
0,3	8,75	427	379	292
0,4	7,5	425	379	292
0,5	6,25	422	379	292
0,6	5	422	379	292
0,7	3,75	422	379	292
0,8	2,5	419	379	291
0,9	1,25	414	379	290

Table 5. Results given by Crafts-Lamont method for specimens of 32 mm diameter

Tablica 5. Rezultati dobiveni Crafts-Lamont metodom za uzorke promjera 32 mm

d = 32 mm		Tvrdoća HV30		
r/R	h, mm	t_{pop}=450°C	t_{pop}=525°C	t_{pop}=630°C
0	16	429	377	291
0,1	14.4	429	377	291
0,2	12.8	429	377	291
0,3	11,2	429	377	291
0,4	9,6	429	378	291
0,5	8	428	379	292
0,6	6,4	428	379	292
0,7	4,8	427	379	292
0,8	3,2	424	379	292
0,9	1,6	418	379	291

Table 6. Results given by Crafts-Lamont method for specimens of 40 mm diameter

Tablica 6. Rezultati dobiveni Crafts-Lamont metodom za uzorke promjera 40 mm

d = 40 mm		Tvrdoća HV30		
r/R	h, mm	t_{pop}=450°C	t_{pop}=525°C	t_{pop}=630°C
0	20	425	374	287
0,1	18	425	374	287
0,2	16	425	374	287
0,3	14	425	374	287
0,4	12	427	375	289
0,5	10	429	377	290
0,6	8	429	377	291
0,7	6	429	378	291
0,8	4	428	379	292
0,9	2	423	379	292

3. Usporedba rezultata dobivenih pokusom i primjenom Crafts-Lamont modela

U istim dijagramima, na slikama 9, 10 i 11, su prikazane „U-krivulje" dobivene primjenom Crafts-Lamont metode i „U-krivulje" dobivene pokusom za svaki promjer i temperaturu popuštanja.

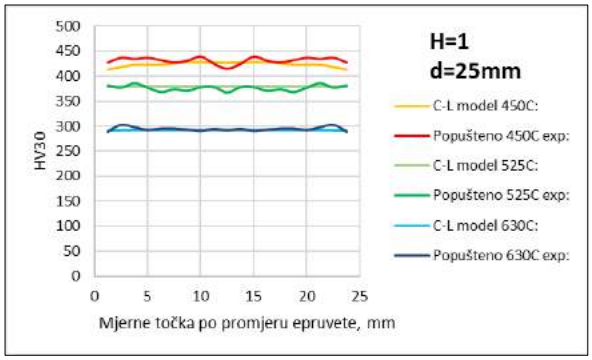

Figure 9. "U curves" for diameter 25 mm and tempering temperatures 450°C, 525°C and 630°C

Slika 9. "U krivulje" za promjer 25 mm i temperature popuštanja 450°C, 525°C i 630°C

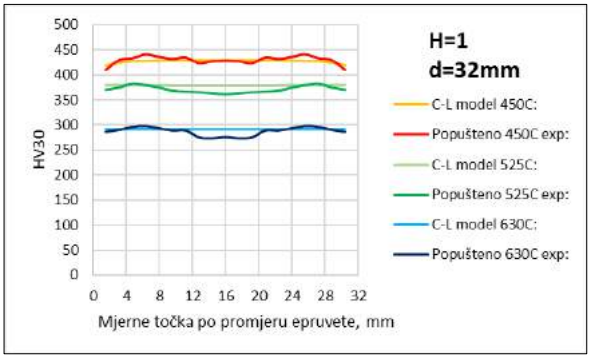

Figure 10. "U curves" for diameter 32 mm and tempering temperatures 450°C, 525°C and 630°C

Slika 10. "U krivulje" za promjer 32 mm i temperature popuštanja 450°C, 525°C i 630°C

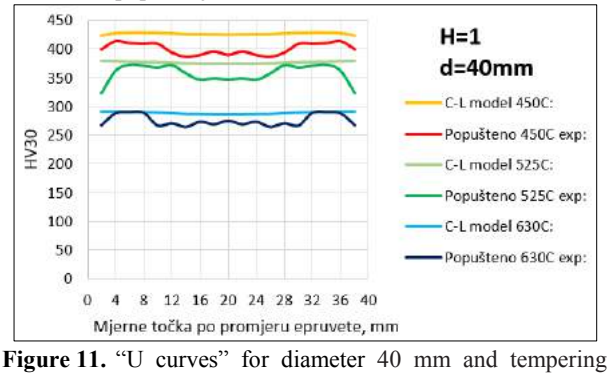

Figure 11. "U curves" for diameter 40 mm and tempering temperatures 450°C, 525°C and 630°C

Slika 11. "U krivulje" za promjer 40 mm i temperature popuštanja 450°C, 525°C i 630°C

Na slikama 9 i 10 prikazani su rezultati ispitivanja za uzorke promjera 25 i 32 mm. Uočava se dobro podudaranje proračunskih i eksperimentalnih rezultata ispitivanja.
Na slici 11 prikazani su rezultati ispitivanja za uzorke promjera 40 mm. Uočavaju se nešto niže vrijednosti rezultata dobivenih pokusom u odnosu na proračunske rezultate dobivene primjenom Crafts-Lamont metode.
Nešto niže vrijednosti tvrdoće na površini tretiranih izradaka mogu se pripisati pojavi razugljičenja površine za vrijeme austenitizacije i popuštanja u komornim pećima bez posebne zaštitne atmosfere. Ova pojava se najviše uočava na uzorcima promjera 40 mm.
Obzirom da su uzorci promjera 40 mm istog promjera kao i dobavljena šipka (iz koje su svi uzorci izrezani), za pretpostaviti je da je dobavljena šipka prethodno bila tretirana na visokim temperaturama bez zaštitne atmosfere, te je u dobavljanom stanju već imala niži sadržaj ugljika u površinskom sloju. Naknadnom toplinskom obradom dodatno je smanjen sadržaj ugljika što se odrazilo na niže postignute tvrdoće u površinskom sloju uzoraka.

4. Zaključak

Na temelju dobivenih rezultata uočeno je prilično dobro podudaranje Crafts-Lamont modela i rezultata dobivenih pokusima za promjere 25 i 32 mm. Nešto veće odstupanje uočljivo je za uzorke promjera 40mm.
Opseg ispitivanja koji je proveden očito nije dovoljan kako bi se sa sigurnošću mogla donijeti konačna ocjena primjenjivosti Craf-Lamont metode za procjenu raspodjele tvrdoće zakaljenih i popuštenih izradaka punog okruglog poprečnog presjeka. Craft-Lamont dijagrami pokrivaju područje promjera okruglih poprečnih presjeka od 20 do 200 mm, pa su odabrani promjeri tretiranih uzoraka iz donjeg dijela navedenog raspona.
Ispitivanje bi trebalo proširiti u smislu tretmana uzoraka većih promjera i uzoraka iz drugih čelika za poboljšavanje.

Literatura

[1] Liščić Božidar, Hans M. Tensi, Lauralice C. F. Canale, George E. Totten *"Quenching Theory and Technology"*, CRC Press, Taylor and Francis Group, 2010

[2] Franz Wever, Adolf Rose: *"Atlas zur Wärmebehandlung der Stähle"* Max-Planck Institut fur Eisenforschung, Dusseldorf

[3] STAT EASE,Inc.: DESIGN – EXPERT v.10.0.3.1, Minneapolis, MN 55413

ISSN 1847-7917

Numerička analiza naprezanja i deformacija sigma profila skrepernog transportera

***Fuad HADŽIKADUNIĆ*, Nedeljko VUKOJEVIĆ, Amra TALIĆ-ČIKMIŠ**
Faculty of Mechanical Engineering of University of Zenica
Department of constructions and CAD technologies
Fakultetska br 1, Zenica, **Bosna i Hercegovina**
hfuad@mf.unze.ba
vukojevicn@mf.unze.ba
acikmis@mf.unze.ba

Keywords
Scraper conveyor
Trough sigma profile
Numerical analysis
Stress
Deformation

Ključne riječi
Skreperni transporter
Sigma profil korita
Numerička analiza
Naprezanje
Deformacija

Numerical Analysis of the Stress-deformation State of Sigma Profile of Scraper Conveyor

Original scientific paper

Abstract: The paperwork presents a part of the research on the complex construction of the scraper conveyor trough, as a part of the total coal digging system. In addition, the overall research, in addition to the present study, includes research on material, wear resistance, residual stress measurement, etc. This paper presents a brief analytical approach to determining the forces relevant for numerical analysis of trough whose basic geometric feature is the sigma profile. FEM analysis was carried out for various cases of predetermined loads and boundary conditions of relieving, where conditions were determined when the occurrence of maximum stress and maximum deformation of the trough structure occurred.

Izvorni znanstveni rad

Sažetak: Predmetni rad predstavlja dio istraživanja na kompleksnoj konstrukciji korita skrepernog transportera, kao dijela ukupnog sustava za otkopavanje uglja. Inače, ukupno istraživanje, pored ovdje prikazanog, obuhvaća i istraživanje materijala, otpornosti na trošenje, mjerenja zaostalih naprezanja itd. U ovom radu je prikazan kratak analitički pristup za određivanje sila mjerodavnih za numeričku analizu korita čija je osnovna geometrijska značajka sigma profil. MKE analiza je izvršena za razne slučajeve pretpostavljenih opterećenja i graničnih uvjeta oslanjanja, gdje su određeni uvjeti kada se dešava pojava maksimalnog naprezanja i maksimalne deformacije konstrukcije korita.

1. Uvod

Mehanizirani tehnološki proces na širokim čelima zasniva se na samohodnoj hidrauličnoj podgradi i mehaniziranom otkopavanju ugljena, koji se otkopava otkopnim strojevima. Svaka sekcija samohodne hidraulične podgrade povezana je s otkopnim skrepernim transporterom, koji ujedno služi kao radna staza za kretanje otkopnog stroja i svi ti elementi predstavljaju mehanizirani kompleks širokog čela.

Osnovni elementi mehaniziranog kompleksa širokog čela su: samohodna hidraulična podgrada koja štiti radni prostor u zoni širokog čela, otkopni stroj za otkopavanje i utovar ugljena u otkopni skreperni transporter, otkopni skreperni transporter za transport otkopanog uglja i istovremeno služi kao radna staza za kretanje otkopnog stroja duž širokog čela. Sekcije hidraulične podgrade u kopleksu širokog čela su poredane jedna pored druge. Svaka sekcija vezana je za skreperni transporter, pomoću dvosmjernog hidrauličnog cilindra, koji jednom pomiče skreper za jedan korak, jednak dubini reza otkopnog stroja, a drugi put povlači sekciju do skrepernog transportera za isti korak.

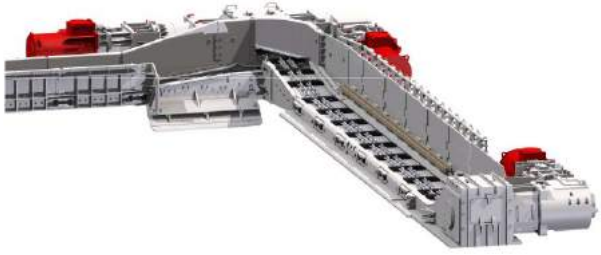

Figure 1. General layout of scraper conveyor

Slika 1. Opći prikaz skrepernog transportera

Skreperni transporteri se uglavnom koriste za transport stjenastih masa u jamama, separacijama i sličnim pogonima, slika 1. Osnovni dijelovi skrepernog transportera su: pogonska stanica, povratna stanica, prijelazna korita, korita, lanci sa skreperima i dodatne stanice. Stjenska masa se transprotira tako što grabulje, koje su međusobno povezane sa jednim ili više lanaca, klize duž metalnih korita, pri čemu zgrću i transportiraju stjensku masu prema pogonskoj stanici, odnosno u pravcu kretanja lanca sa skreperima.

Symbols/Oznake

K	- conveyor capacity, th^{-1} - kapacitet skrepernog transportera
A	- surface of the material cross section, m^2 - površina popr. presjeka nasipa materijala
v	- material velocity, ms^{-1} - brzina materijala
B	- scraper part width, m - širina elementa skrepera
h	- scraper part height, m - visina elementa skrepera
N	- power, kW - snaga
F_o	- circumference force, N - obimna sila
M	- torque/moment, Nm - moment
F_1	- piston force of the pusher section, kN - sila na klipu gurača sekcije
F_2	- piston rod force of the pusher sect., kN - sila na klipnjači gurača sekcije
d	- sprocket kinematic diameter, mm - podioni prečnik lančanika
n	- number of revolutions, min^{-1} - broj obrtaja
F_{max}	- max. force, kN - maksimalna sila
F_{min}	- min. force, kN - minimalna sila
F_{K1}	- trough force, kN - sila opterećenja korita
F_{K2}	- trough side force, kN - bočna sila na koritu

Greek letters/Grčka slova

$\sum$	- profile type signification, - - oznaka vrste profila
ρ	- material density, kgm^{-3} - gustoća materijala
β	- elevation coefficient, - - uglovna značajka
ψ	- coefficient of volume fulfillment, - - značajka ispune volumena
η	- loss coefficient, Pa s - značajka gubitaka
ω	- angular velocity, rad s^{-1} - kutna brzina
ζ	- increasing force coefficient, - - značajka povećanja sile

Subscripts/Indeksi

o	- circumference - obimni
1	- piston of the section pusher - klip gurača sekcije
2	- piston rod of the section pusher - klipnjača gurača sekcije
max	- maximal - maksimalna
min	- minimal - minimalna
K1	- at the trough - na koritu
K2	- side to the trough - bočno na koritu

Na pogonskoj stanici lanci prelaze preko pogonskog lančanika, a na povratnoj stanici preko gonjenog lančanika. Lanac sa skreperima se vraća donjom stranom korita. Utovar materijala je moguć duž cijele trase transportera. Korita skrepernih transportera zavise od njegove namjene. Otkopni skreperni transporteri imaju niska korita i nešto veću širinu i moraju biti prilagođeni pogonskom mehanizmu otkopnog stroja pošto služi kao staza za kretanje te mašine. Korita se sastoje od dva sigma profila međusobno spojena pločom odnosno podom korita. Pod korita trpi velika trošenja te se nakon trošenja može zamijeniti. Sigma profili se izrađuju najčešće valjanjem za manje dimenzije skrepernih transportera, dok se kod teških skrepernih transportera izrađuju lijevanjem. Način izrade sigma profila uzrokuje pojavu zaostalih naprezanja u samom profilu, a čije prisustvo može uzrokovati negativne posljedice na životni vijek konstrukcije.

2. Proračun korita sa sigma profilom

2.1. Osnovne tehničke karakteristike

Predmet proučavanja rada je korito skrepernog transportera tip TOT 732 koje se sastoji od dva ∑ - profila izrađena valjanjem i poda korita, koji su međusobno spojeni zavarivanjem, a materijal od kojega su napravljeni sigma profili je čelik za poboljšanje oznake ČL3130 odnosno 40Mn4 oznaka materijala W.N.1.1157. Tehničke karakteristike otkopnog skrepernog transportera su:

- Tip: TOT - 732,
- Transportna duljina: 120 m,
- Brzina transportnog lanca: 0,92 m/s,
- Širina transportnog korita: 732 mm,
- Visina transportnog korita: 215 mm,
- Dimenzije transportnog lanca: ∅30 x 108 mm,
- Snaga elektromotora: 2 x 90 kW,
- Lokacija: Širokočelno otkopno radilište Kakanj, BiH

- Teoretski kapacitet transportera: 500 t/h,
- Tip reduktora: MK II – 7,2,
- Prijenosni odnos: 39,86,
- Izlazni moment: 23,2 kNm.

Osnovni nosivi element konstrukcije teškog skrepernog transportera je tzv. ''sigma profil''. Zbog izuzetno teških uvjeta rada članci (korita), kojih ima u nizu cca do 100 komada izloženi su vrlo složenim vanjskim i unutrašnjim opterećenjima. Cjelokupni transport otkopnog materijala (uglja i kamena) cca 500 t/h ide preko skrepernog transportera. Otkopni stroj je naslonjen na transporter, dok neravna konfiguracija terena čini dopunsko opterećenje pri pomicanju transportera i hidraulične podgrade.

Osnovnu stabilnost članka daju dva ''sigma'' profila spojeni međusobno limenim nosačem preko kojeg klizi lanac sa skreperima, izložen intenzivnom trošenju, savijanju i uvijanju u već opisanim uvjetima, slika 2. Ovaj konstrukcijski element prvi strada pri eksploataciji i prema njemu se uglavnom određuje vijek trajanja skrepernog transportera.

Iznalaženje prikladnog modela ''sigma'' profila za efikasno ponašanje članaka teškog skrepernog transportera u zadanim radnim uvjetima je osnovna pretpostavka za pouzdanost ovako složenog sustava.

Na osnovi snage motora od cca 2 x 90 kW, dužine transporta L = 120 m, zatim opterećenja izazvanim hidrauličnom podgradom i otkopnim strojem provest će se dimenzioniranje, odnosno provjera postojećih mehaničkih karakteristika. Numeričkom analizom će se, između ostalog, potvrditi dobijeni rezultati analitičkog proračuna.

Žljebovi sa kosim stranama imaju prednost nad ravnim žljebovima jer stvaraju manje otpore pri kretanju materijala kroz žlijeb (i do 20%), ali su složeniji za izradu i održavanje.

Kod otkopavanja uglja u rudarskim kopovima u radu skrepernog transportera dolazi do situacije da skreperi i korita bivaju prekrivena materijalom, tako da skreperi u svom radu teže da smaknu sloj materijala koji je iznad njih i između skrepernih segmenata, po sloju iznad njih. Međutim, kako je otpor trenja materijala o žlijeb manji od otpora koji bi se javio pri smicanju slojeva, to se cijeli materijal i između i iznad skrepera kreće kontinuirano.

2.2. Osnovni analitički proračun

Kapacitet skrepernih transportera je, [1]:

$$K = 3600 \cdot A \cdot v \cdot \rho \ (t/h), \quad (1)$$

$$K = 3600 \cdot B \cdot h \cdot \beta \cdot \psi \cdot v \cdot \rho \ (t/h). \quad (2)$$

Na osnovi dimenzija gornjeg dijela profila sa skreperima orijentacijska površina poprečnog presjeka zahvata materijala je A = 0,06 m^2.

Karakteristike transportiranih materijala u rudnicima su:
- Kameni ugalj: 0,8 do 0,85 t/m^3,
- Lignit i mrki ugalj: 0,65 do 0,8 t/m^3,
- Lignit, sušen: 0,45 do 0,55 t/m^3.

Koeficijent ispune volumena za komadne materijale je: ψ = 0,7 do 0,8.

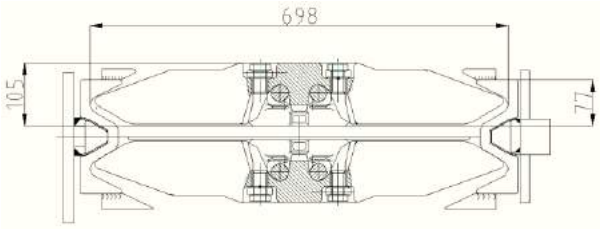

Figure 2. Section view of sigma profile with scrapers
Slika 2. Poprečni presjek sigma profila sa skreperima

Na osnovi izraza (2), slijedi da je:

$$K = 3600 \cdot 0{,}06 \cdot 1 \cdot 1 \cdot 0{,}92 \cdot 0{,}85 = 169 \ (t/h). \quad (3)$$

To znači da, prema teoretskom kapacitetu od 500 t/h, proizilazi da je površina popunjenosti korita veća od procijenjene 3 puta, tj. da transportovani materijal umnogome prekriva zapreminski kapacitet između skrepernih elemenata.

Proračun snage elektromotora za pogon skrepernog transportera se može odrediti pomoću formule:

$$N = \frac{F_o \cdot v}{\eta} = \frac{M \cdot \omega}{\eta} \ (kW). \quad (4)$$

U analitičkom dijelu proračuna dat će se osnovne postavke i parametri bitni za provođenje numeričke analize, odnosno potrebno je dati osnovne parametre za pretpostavljena opterećenja na koritu skrepernog transportera.

Najčešća korištena metoda za analizu sila opterećenja segmenata transportera je "metoda obilaska po konturi". Međutim, na osnovi definirane snage elektromotora pogona moguće je ne ići u detaljan proračun nego izvršiti analizu prema definiranim silama na osnovi ulaznih parametara.

Stoga, osnova za ulazne parametre proračuna bit će snaga elektromotornog pogona i opterećenja izazvana hidrauličkom podgradom i otkopnim strojem.

Sekcije skrepernog transportera se prema zahtjevima tehnologije otkopavanja pomiču (guraju) hidrauličnim sustavom preko klipa i klipnjače gurača, odnosno plate gurača.

Sile koje su dobivene proračunom tog sustava su:
- F_1 = 189,97 kN – sila na klipu gurača sekcije,
- F_2 = 89,47 kN – sila na klipnjači gurača sekcije.

Radni tlak u sustavu je 200 bara.

Prema tehničkoj dokumentaciji skrepernog transportera težina transportnog korita je 348 kg/kom, a težina grabulja sa lancem 912 kg/kom.

Na osnovi tehničke dokumentacije konstruktivne mjere pogonskog lančanika su:
- promjer tjemene kružnice: 520 mm,
- promjer podnožne kružnice: 434 mm,

- podioni promjer: 477 mm.

Na osnovi kinematskog proračuna ulaznih parametara, na osnovi brzine transporta v = 0,92 m/s i podionog promjera lančanika d = 477 mm, može se odrediti broj okretaja lančanika:

$$n = \frac{v \cdot 60}{d \cdot \pi} = \frac{0{,}92 \cdot 60}{0{,}477 \cdot \pi} = 36{,}85 \ \ (o/min). \qquad (5)$$

Ugaona brzina je:

$$\omega = \frac{\pi \cdot n}{30} = \frac{\pi \cdot 636{,}85}{30} = 3{,}86 \ (s^{-1}). \qquad (6)$$

Na osnovi izraza (4) obimna sila je:

$$F_o = \frac{N \cdot \eta}{v} = \frac{90000 \cdot 0{,}9}{0{,}92} = 88043 \ \ (N). \qquad (7)$$

Navedeni proračun se približno podudara sa navedenom vrijednošću momenta 23,2 kNm.

Mjerodavnu sila opterećenja se može odrediti na osnovi odnosa obimne, maksimalne i minimalne sile:

$$F_o = F_{max} \cdot \zeta - F_{min} \ \ (N). \qquad (8)$$

Na osnovi momenta i polumjera lančanika, maksimalna vrijednost sile je F_{max} = 97270 N.

Stoga će se za numeričku analizu za mjerodavnu vrijednost sile opterećenja korita uzeti sila F_{K1} = 100 kN, a za vrijednost sile pri bočnom guranju F_{K2} = 189,97 kN.

2.3. FEM/MKE analiza

Za numeričku analizu je korišten softver I-DEAS sa modulima za analizu naprezanje-deformacija. Numerička analiza podrazumijeva, između ostalog: formiranje 3D modela na osnovi tehničke dokumentacije, formiranje FEM modela, formiranje graničnih uvjeta, vanjskih opterećenja, mreže konačnih elemenata i rezultata analize, [2], [3], [4], [5].

Na slici 3 prikazan je 3D model realnog stanja korita skrepernog transportera.

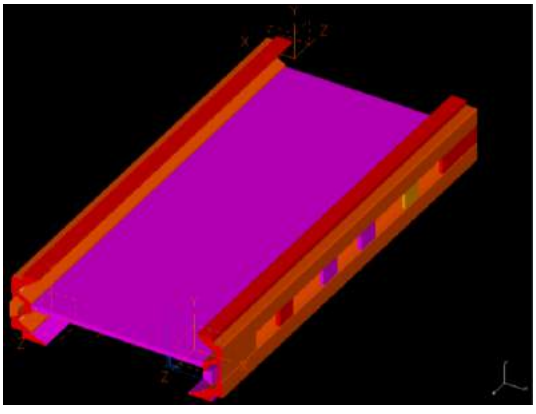

Figure 3. 3D discretization of scraper trough

Slika 3. 3D dikretizacija korita grabuljara

Na slici 4 je prikaz s naglaskom na sigma profil. Na osnovu izrađenog 3D modela korita sa sigma profilom, moguće je napraviti niz analiza sa kreiranjem različitih graničnih uvjeta i opterećenja.

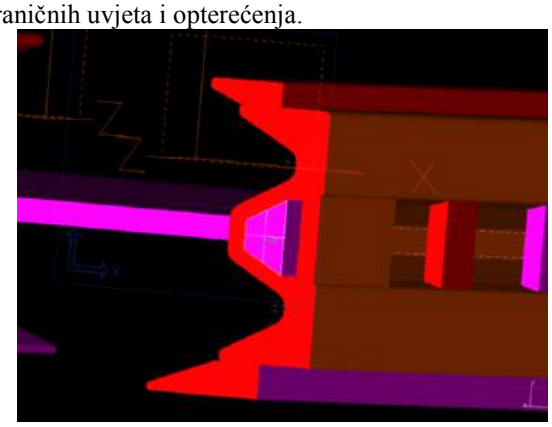

Figure 4. Sigma profile part of scraper trough

Slika 4. Izgled sigma profila korita

U proračunu su korištene simulacije očekivanih stanja opterećenja na koritu, a koje mogu biti izazvane težinama elemenata, zaklinjavanjem skrepernih elemenata u sigma profil, zaglavljivanjem komada materijala, itd., a koja mogu izazivati opterećenja savijanjem, pritiskom, ekscentričnim pritiskom, uvijanjem, itd. U daljem dijelu rada su prikazani ukratko sedam slučajeva graničnih uvjeta i opterećenja, kojima može biti izloženo korito transportera u radu. Kao bitni parametri numeričke analize su određeni maksimalno naprezanje i maksimalna deformacija. Rezultati analize za sve slučajeve će biti prikazani u tablici 1.

<u>Slučaj 1</u>: Opterećenje silom 50 kN

Prvi slučaj opterećenja korita je opterećenje od stroja za otkop uglja.

Na slici 5 dan je prikaz početnih graničnih uvjeta za ovu analizu, a koji su se mijenjali za druge slučajeve, zavisno od slučaja opterećenja i ostalih uvjeta proračuna. Mreža konačnih elemenata je korištena i za ostale slučajeve analize.

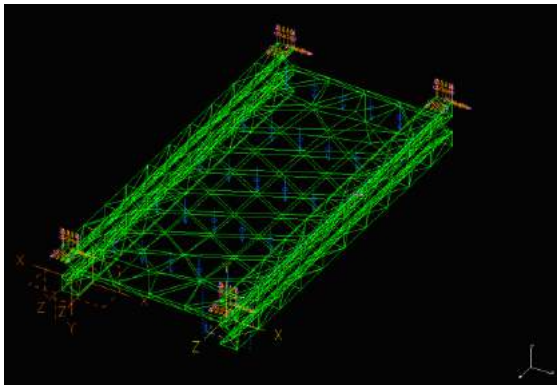

Figure 5. Boundary conditions and FEM

Slika 5. Granični uvjeti i MKE mreža

Na slikama 6 do 12 su dani prikazi prostornog stanja naprezanja i deformacija korita transportera za slučajeve analize 1 do 7, respektivno.

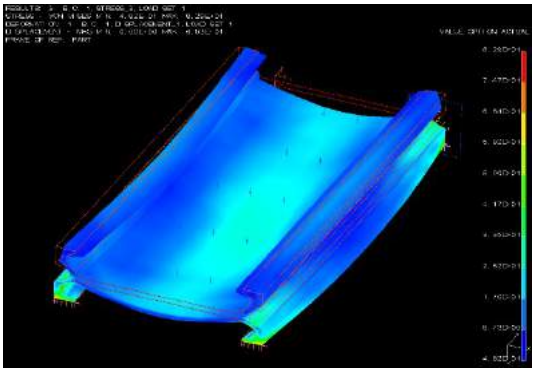

Figure 6. Stress-deformation state of Case 1

Slika 6. Stanje naprezanje-deformacija Slučaja 1

Slučaj 2: Pritisak silama 2 x 50 kN

Drugi slučaj je pritisno opterećenje sa silama na oba kraja.

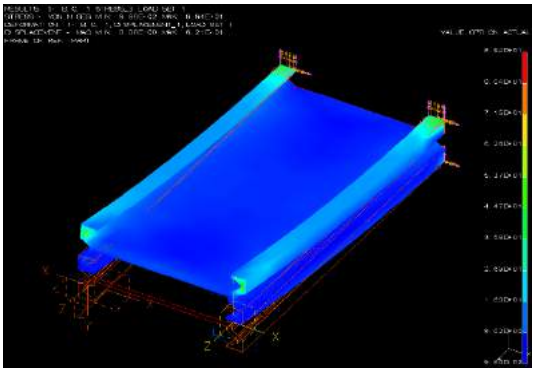

Figure 7. Stress-deformation state of Case 2

Slika 7. Stanje naprezanje-deformacija Slučaja 2

Slučaj 3: Savijanje silama 2 x 25 kN

Treći slučaj opterećenja je savijanje silama od tereta i neravnog tla.

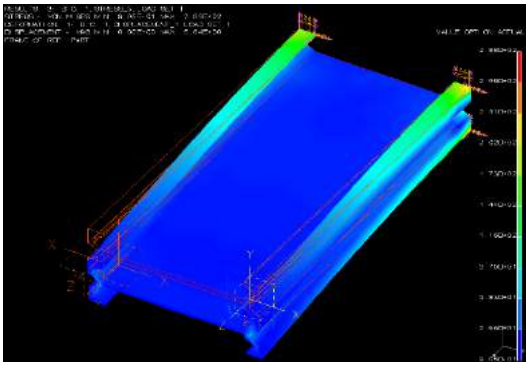

Figure 8. Stress-deformation state of Case 3

Slika 8. Stanje naprezanje-deformacija Slučaja 3

Slučaj 4: Ekscentrični pritisak sa 2 x 50 kN silama

Četvrti slučaj je izazivanje ekscentričnog pritiska sa dvije sile na suprotnim krajevima korita.

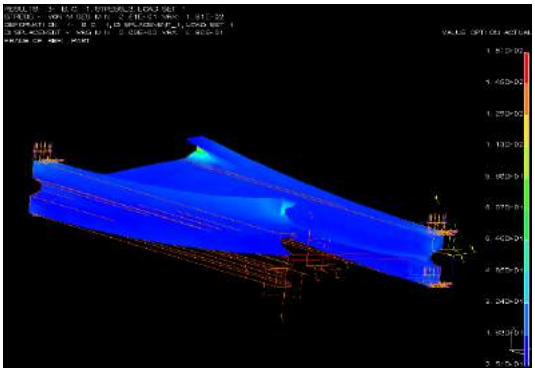

Figure 9. Stress-deformation state of Case 4

Slika 9. Stanje naprezanje-deformacija Slučaja 4

Slučaj 5: Uvijanje po horizontalnoj osi

Peti slučaj opterećenja je uvijanje po horizontalnoj osi.

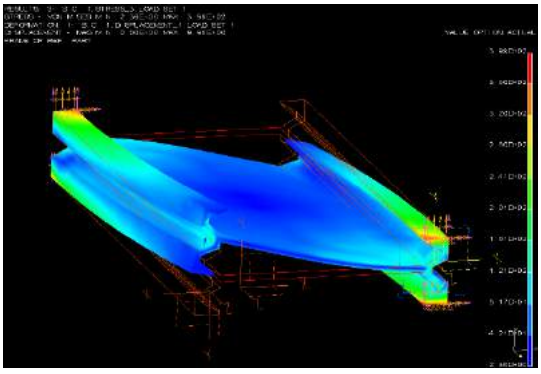

Figure 10. Stress-deformation state of Case 5

Slika 10. Stanje naprezanje-deformacija Slučaja 5

Slučaj 6: Zatezanje silama 2 x 50 kN

Šesti slučaj opterećenja je zatezanje silama na oba kraja korita.

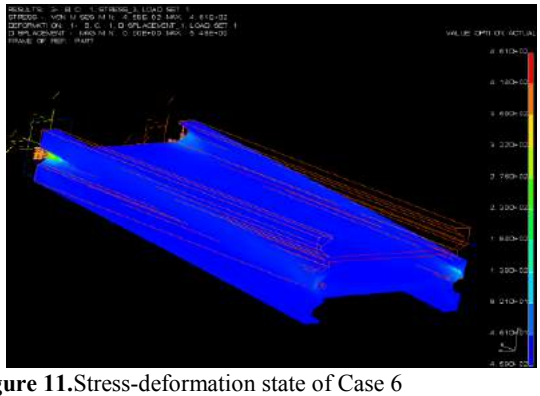

Figure 11. Stress-deformation state of Case 6

Slika 11. Stanje naprezanje-deformacija Slučaja 6

Slučaj 7: Potiskivanje sigma profila silom 200 kN

Sedmi slučaj opterećenja je slučaj potiskivanja korita silom kreiranom hidrauličkim sistemom.

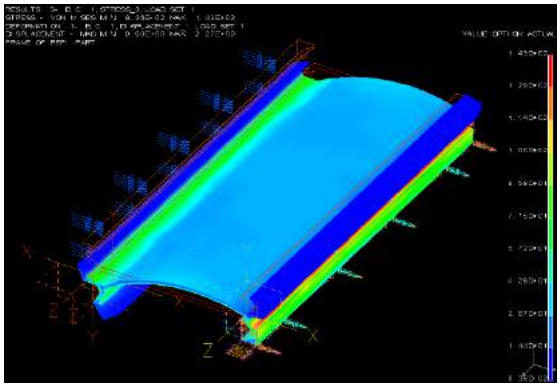

Figure 12. Stress-deformation state of Case 7

Slika 12. Stanje naprezanje-deformacija Slučaja 7

2.4. Prikaz rezultata analize

Potrebno je uzeti u obzir da numerička analiza predstavlja određenu vrstu aproksimacijskog proračuna, kojom se može analizirati složena konstrukcija kod pretpostavljenih slučajeva opterećenja.

U realnim situacijama eksploatacije složenih konstrukcija uvijek se radi o kompleksnim kombinacijama više vrsta opterećenja, a koje je nekada teško sveobuhvatno pretpostaviti.

Stoga, npr. mjerenje određivanje naprezanje i deformacija eksperimentalnim metodama u karakterističnim segmentima složenih konstrukcija predstavlja jedinu pravu informaciju odziva konstrukcije na realne uvjete opterećenja. No, numerička analiza predstavlja veoma bitan alat za preliminarnu ili optimizacijsku fazu sagledavanja dijela ili kompletne konstrukcije.

Na osnovi dobivenih rezultata numeričke analize moguće je dati zbirni prikaz karakterističnih vrijednosti analize, koji su prikazani u tablici 1.

Table 1. Values of stress and deformation parameters for different case studies

Tablica 1. Vrijednosti parametara naprezanja i deformacije za različite slučajeve analize

	Case st. 1/ Slučaj 1	Case st. 2/ Slučaj 2	Case st. 3/ Slučaj 3	Case st. 4/ Slučaj 4	Case st. 5/ Slučaj 5	Case st. 6/ Slučaj 6	Case st. 7/ Slučaj 7
Max. stress/ Max. naprezanje, σ_{max}, N/mm^2	82,9	30	288	161	399	**461**	143
Max. deformat./ Max def., f_{max} , mm	0,683	0,621	5,64	0,49	**9,98**	5,48	2,27

3. Zaključna razmatranja

Na osnovi gore navedenih maksimalnih vrijednosti naprezanja korita uočljivo je da najnezgodnije opterećenje za korito predstavlja dvostrani slučaj zaglavljivanja skrepernog elementa u sigma profilu koja pod djelovanjem sile u lancu izaziva značajno zatezno naprezanje.

S aspekta deformacija najveća vrijednost nastupa u slučaju uvijanja korita po horizontalnoj osi, što je i logično zbog manjeg otpornog momenta korita u odnosu na taj položaj poprečnog presjeka i opterećenja.

REFERENCES

[1] Tošić S., (1994), *Proračun mašina neprekidnog transporta i dizaličnih uređaja*, Mašinski fakultet, Beograd

[2] Maneski T., (1998), *Kompjutersko modeliranje i proračun struktura*, Mašinski fakultet, Beograd

[3] Hutton D.V., (2004), *Fundamentals of Finite Element Analysis,* McGraw Hill, USA

[4] Harishchndra A., Ganiger S. G., *Design and Experimental Analysis of Flight of Drag Chain Conveyor Belt with respect to its Breaking Strengthby Varying Materials*, International Engineering Research Journal, p. 856-863

[5] Wankhade1 V., Sharma S., (2015), *Design Improvement for Enhancing the Performance of drag Conveyor Chain and its Cost Reduction*, Int. Journal of Engineering Research and General Science Vol. 3, p. 524-531.

ISSN 1847-7917

Aluminium foam for thermo-active pitched roofs of nearly zero-energy buildings

Jaroslav JERZ, František SIMANČÍK, Jaroslav KOVÁČIK Ján ŠPANIELKA
Institute of Materials & Machine Mechanics, Slovak Academy of Sciences, Dúbravská cesta 9, 845 13 Bratislava, **Slovakia**
ummsjerz@savba.sk

Keywords
aluminium foam
heat absorptivity
solar radiation
heat storage
zero-energy buildings

Ključne riječi
aluminijske pjene
apsorpcija topline
solarno zračenje
skladištenje topline
zgrada s nultom energijom

Professional article

Abstract: Nearly zero-energy demands for a building need to be secured to a large extent by renewable sources available in the building or its proximity. The architectural and technical design of the building has to be drafted with a targeted orientation of the glazed windows, exclusion of thermal bridges, controlled ventilation and heat recovery in order to use heat gains efficiently and so to reduce pointless heat losses. The energy efficiency of residential buildings is today mostly improved by upgrading the energy performance of the building envelope and facilities. However, huge energy reductions can also be achieved by a focus on the development of new systems enabling to cover natural energy fall-outs resulting from generation much excess heat during the peak time (summer, day) which is almost not possible to use during periods of excessive energy consumption (winter, night). This main drawback of the solar energy can be very efficiently solved by storing and later evolving of accumulated heat according to the day-night as well as the seasonal, i.e. summer-winter cycle (Fig. 1).
This contribution deals with the system of thermo-active aluminium foam cladding for pitched roofs of the buildings covered by innovative coating sufficiently resistant to weathering, frost, intense solar radiation, summer heat, chemicals presented in the air, chemically polluted water vapor and to mechanical damage caused by adverse weather conditions (e.g. heavy rainfall, groats, etc.). The objective of the ongoing R&D activities is to achieve excellent mechanical and physical properties related to highly energy efficient solar radiation and heat harvesting as well as the ability to dissipate an undesirable heat accumulated in the building interior to the surroundings of building via the roof surface during colder summer nights. This smart roofing system allows expanding the use of aluminium foam in the building industry by the achievement of its surface quality suitable for mechanical load, corrosion, chemical environment, strong solar radiation, large temperature fluctuations between winter and summer season, etc.

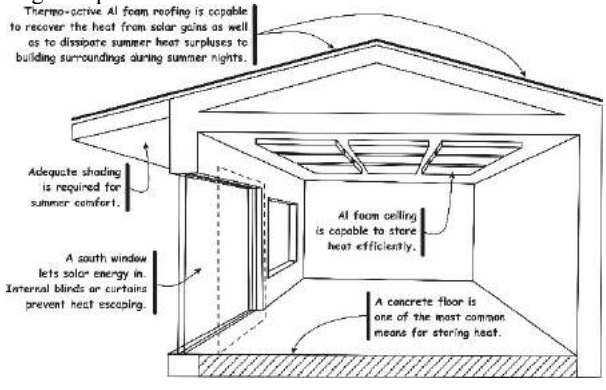

Figure 1. House with passive solar direct gain heating system supplemented by novel aluminium foam heat exchangers.

1. Introduction

As the world population continues to grow and the limited amount of fossil fuels begin to diminish, it is impossible to provide the amount of energy demanded by the world by only using fossil fuels to convert energy. Even though that there are plenty of ways to convert renewable energy, and many techniques are already being used, the energy free available in nature is unfortunately exploited not nearly to its full potential. We are permanently and aimlessly running out of fossil fuels, and that is why in the very short period of time

we have consumed an incredible amount of them. Their decreasing availability in the nearest future combined with requirements to reduce carbon emissions reveals the necessity for more rational and efficient energy use. The European Union, therefore, states the urgency of developing new solutions to improve energy efficiency and energy savings in the building sector by the 2010/31/EU Directive [1]. The implementation of new technical solutions suitable for construction of new buildings as well as for the restoration of existing ones should be easy, and their production should be industrially viable. According to the estimated energy consumption in 2020, the energy used in European households and services will be bigger compared to the energy consumed by transport and industry.

Moreover, European Commission considered that the largest savings potential was estimated at 27% and 30% in residential and commercial buildings respectively (from 1990 levels) while the potential to reduce energy consumption in the industry and transport is only about 19 – 20% [6]. According to the target of Europe 2020 strategy for smart, sustainable and inclusive growth to achieve "20-20-20" goal, which was set by EU leaders in 2007, the EU aims to reduce its greenhouse gas emissions by at least 20%, increase the share of renewable energy to at least 20% of consumption, and achieve energy savings of at least 20% in comparison with the levels in 1990. Reducing heat losses, optimizing energy system and implementing the legislation of EU to the necessity to build exclusively nearly-Zero Energy Buildings (nZEBs), are the activities which can help to gain this goal in the whole Europe. The thorough optimization of the energy system is therefore mandatory in order to achieve nZEBs targets based on the requirement that total energy consumption of every new building built after 2020 will have to be roughly equal to the amount of renewable energy obtained on the site [3].

The heating and cooling of interiors play an important part within energy systems of current buildings. As the heating and cooling loads are in nZEBs very small, it is a chance to develop totally new system solutions capable of minimizing operational cost and reduce energy consumption by combining the heating and cooling systems. During autumn and spring periods is usually the operative temperature in south oriented building zone higher than cooling set point (ca 26°C) due to sufficient solar gains while the operative temperature in the other building zone is under heating set point (ca 20°C). The water loop system might be installed in order to cool the south zone down and simultaneously to heat the north zone up as energy efficiently as possible. Moreover, the energy efficient concept of nZEBs presented in [2] based on the storage of energy obtained through the aluminium foam roof or facade cladding is capable of absorbing the desired as well as take away the excess heat to the surroundings if necessary. This allows effectively to distribute the heat by means of heating liquid medium/coolant to interior or dissipate the heat from interior to building surroundings using ceiling heat exchangers made of aluminium foam enabling additionally due to filling by Phase-Change Materials (PCMs) to store the energy required for heating/cooling for a period of at least several hours. An optimal thermal comfort of building interiors is in such a way achieved with minimal costs for energy consumption [7].

The present contribution describes the novel thermo-active aluminium foam cladding for pitched roofs based on the findings from the results of technological experiments related to the production of aluminium foam heat exchangers. This innovative technical solution of roofing performs the function of highly efficient heat exchanger between surroundings of the building and the heat transfer medium for heating and air conditioning of interiors as well as for domestic hot water (DHW) preparation required for the operation of residential and non-residential buildings.

2. Energy efficiency of nZEBs with respect to the heating/cooling loads

The energy consumption for heating and cooling of the buildings is currently minimized mostly by sufficiently isolated building envelope keeping the heat inside of the building during winter and outside of the building during summer without significant heat transfer through the envelope. The suitable window size and orientation allow maximizing solar energy gains of currently built passive houses during the winter season. However, this approach causes considerable difficulties during hot summer days, when solar energy gains need to be, on the contrary, minimized. The costs for maintaining sufficient thermal comfort during days with tropical summer weather is therefore increased by demands for adequate shading blinds, air conditioning units, air ventilation and recuperation units gaining air from relatively cooler underground spaces in the building vicinity, etc.

Applying of following new technical solutions, therefore, appears to be a great opportunity to reduce significantly the energy demands for heating/cooling, heating of DHW and consequently reduction of costs for construction and operation of future buildings (Fig. 2):

- ✓ the heat comfort of the interior is maintained during whole year round by stabilization of the temperature using the system of aluminium foam heating/cooling ceiling heat exchangers that allow short term storage of the heat for at least several hours in the form of latent heat of phase transformation of PCMs impregnated in the porous structure of aluminium foam for later use or, for removal of undesirable heat to the building surroundings (at the time when it is possible, e.g. during comparatively colder summer nights),

- ✓ the base plate of the building is designed to have the capability for seasonal storage of summer heat surpluses that can be used for heating of interiors and DHW especially during winter season,
- ✓ the thermo-active roofing which can not only get heat from the solar gains and heat around the building for heating of both the interior and the DHW but also take away an undesirable heat to the surroundings during cooler summer nights.

3. Latent heat storage of solar gains

The use of a latent heat storage (LHS) system using PCMs is an effective way of storing thermal energy and has the advantages of both the extremely high energy storage density and the isothermal nature of the storage process. LHS is based on the heat absorption or releases when the storage material undergoes a phase change from solid to liquid or vice versa. The storage capacity of the system with LHS ability during phase change between solid and liquid stage is given by:

$$Q = \int_{T_i}^{T_m} m \cdot C_p \cdot dT + m \cdot a_m \cdot \Delta h_m + \int_{T_m}^{T_f} m \cdot C_p \cdot dT =$$
$$= m \cdot \left[C_{sp}\left(T_m - T_i\right) + a_m \cdot \Delta h_m + C_{lp}\left(T_f - T_m\right) \right]$$

where:

Q – quantity of heat stored (J)
T – temperature (K)
T_i – initial temperature (K)
T_m – melting temperature (K)
T_f – final temperature (K)
m – mass of heat storage medium (kg)
C_p – specific heat (J/kg·K)
C_{sp} – average specific heat between T_i and T_m (J/kg·K)
C_{lp} – average specific heat between T_m and T_f (J/kg·K)
a_m – fraction melted
Δh_m – heat of fusion per unit mass (J/kg) [7].

Solid–liquid transitions have proven to be economically the most attractive for the use in thermal energy storage systems. However, the PCMs themselves cannot be used as heat transfer medium. A separate heat transfer medium must be employed with a heat exchanger in between to transfer energy from the source to the PCM and from PCM to the load. The appropriate heat exchanger has to be designed specially, given the extremely low thermal conductivity of almost all PCMs in general.

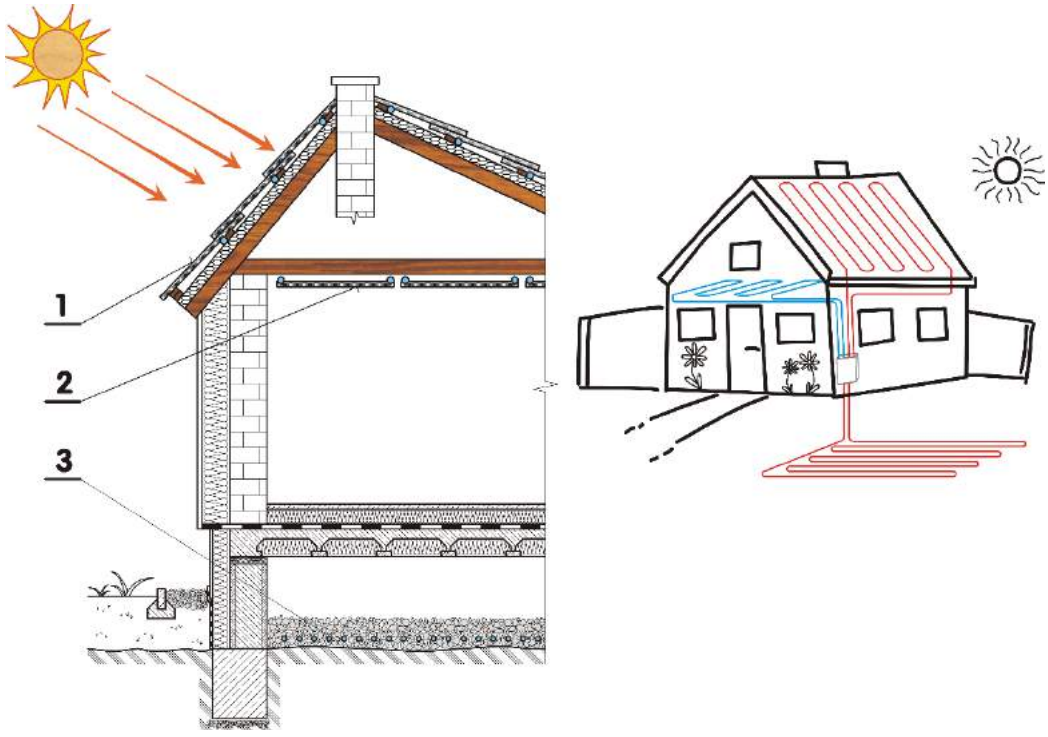

Figure 2. A graphic illustration of nearly-Zero Energy Building (nZEB) which includes:
1 – thermo-active aluminium foam roofing performing efficient heat exchange between building surroundings and heat transfer medium for heating/cooling of interiors, domestic hot water (DHW) preparation and seasonal heat storage,
2 – aluminium foam interior heating/cooling ceiling panels impregnated by PCM,
3 – an underground collector situated under the base plate of the building allowing the seasonal storage of summer heat surpluses for using them predominantly for heating of the interior and DHW during the winter season.

Table 1. Melting point and latent heat of fusion of selected PCMs (paraffins and fatty acids).

PCM	Ref.	Melting temperature [°C]	Heat of fusion [J/g]
paraffin 18-carbons, Octadecane $CH_3(CH_2)_{16}CH_3$	[7]	28	244
PARAFOL 18-97, Octadecane – purity min. 97 wt.%	[8]	27.5	220
RUBITHERM® RT28HC	[9, 13]	28	250
capric (decanoic) acid (CA), $CH_3(CH_2)_8COOH$	[11]	32.1	168.77
lauric acid (LaA), $CH_3(CH_2)_{10})COOH$	[15]	42.6	176.4
myristic acid (MA), $CH_3(CH_2)_{12}COOH$	[11]	54.7	178.79
stearic acid (SA), $CH_3(CH_2)_{16}COOH$	[11]	58.22	180.56
caprylic (octanoic) acid (COA), $CH_3(CH_2)_5COOH$	[14]	15.42 (melting) 8.82 (solidifying)	150.99 152.56
palmitic acid (PA), $CH_3(CH_2)_{14}COOH$	[15]	58.9	189.6
oleic acid (OA), $CH_3(CH_2)_7CH=CH(CH_2)_7COOH$ – melting of α-form – melting of β-form	[17-20]	13.2 16.2	140.19 183.73
linoleic acid (LA), $CH_3(CH_2)_4CH=CHCH_2CH=CH(CH_2)_7COOH$	[20]	– 5.8	119.81
67/33 capric-lauric acid eutectic (67 wt.% CA + 33wt. % LA)	[11]	22.81	154.16
72/28 capric-myristic acid eutectic	[11]	25.36	139.2
77/23 capric-stearic acid eutectic	[11]	27.78	122.58
58/42 lauric-myristic acid eutectic	[11]	35.18	162.27
69/31 lauric-palmitic acid eutectic	[14]	35.2	166.3
coconut oil (~ 50.8 wt.% LaA + 19.6% MA + 8.2% PA + 6.7% COA + 5.8% CA + 5% OA + 2.7% SA + 1.2% LA)	[12, 16]	25	249

The highly porous metallic structures with high thermal conductivity and interconnected pores (with micro-cracks in the pore walls) such as aluminium foams are the best solution for the construction of highly efficient heat exchangers suitable for storage of a large amount of latent heat.

The aluminium foam cell walls with an excellent heat conductivity allow transferring heat uniformly to the large volume of PCM that fills the space of the pores. PCMs on the base of paraffin waxes or fatty acids (Tab. 1) provide by this way the possibility to store and to release large volumes of latent heat during its phase change from solid to the liquid stage and vice versa (~ 200 – 250 J/g) at a nearly constant temperature. This allows keeping the temperature of the heat exchanger at required temperature for a longer time without the need to dissipate heat into the surroundings of the exchanger immediately. The charging of the heat exchanger with the function of latent heat storage is possible also by the fluid with the temperature only slightly higher than the melting point of used PCM. In the case that the heat exchanger is used for the purpose of undesirable excessive heat removal from the building interior, the heat is consumed for melting of PCM thus keeping the temperature at a required level until all paraffin wax is melted.

However, values of heat of fusion for various PCMs given in Table 1 are only approximate estimates. This is because no PCM melts and solidifies in the entire volume at exactly constant temperature. According to [9] the heat storage capacity of PCM with trade mark RUBITHERM® RT28HC produced by German company Rubitherm Technologies GmbH is approximately 250 kJ/kg (e.g. ~ 70 Wh/kg) ± 7.5%. This heat is the sum of latent and sensible heat in a temperature range from 21°C to 36°C. The distribution of heat capacity of this PCM during heating and cooling within said temperature range is shown in Fig. 3.

Following experiment has been done to examine the possibility to store reversibly latent heat of phase transition by paraffin wax impregnated in the porous structure of aluminium foam heat exchangers.

An experimental climatic chamber has been used in order to test the ability of PCM to store the latent heat of phase transition during multiple thermo-cycling of flat-shaped panels with the area 600 × 600 mm made of aluminium foam filled by PCM (Fig. 4). The chamber allows to measure and record temperature in these places: T1 – air temperature at a distance of 200 mm from the sample, T2 – temperature of the air at a distance of 500 mm from the sample, T3 – temperature of the air at a distance 800 mm from the sample, T4 – temperature of aluminium plate located on the bottom of climatic chamber, T5 – ambient temperature, T6 – temperature of the water in thermostat ensuring the maintenance of the temperature of the climatic chamber at a constant level, T7 – temperature of the water circulating from the reservoir through tested panel and T8 – temperature of the tested panel.

The aluminium plate located at the bottom of the chamber was heated and maintained by flowing water stabilized by thermostat at a constant temperature of 40°C during experiments demonstrating the ability of aluminium foam panel to remove the heat from the interior of the climatic chamber. The tested panel of aluminium foam impregnated by 770 g (1000 cm^3) of PCM RUBITHERM® RT28HC with the melting range 27 – 29°C has been attached to a ceiling of the climatic chamber interior. 12.6 liters of water were circulating during experiments from the container through tested aluminium foam panel, which was thermally insulated so as to minimize thermal losses, causing inaccuracies in the measured quantity of the heat taken up to the tested panel by the water circulating in the tubes placed inside the structure of the aluminium foam panel.

The thermal behavior of tested panels is shown in Fig. 5 at the conditions described above without heat supply or removal by heat transfer fluid.

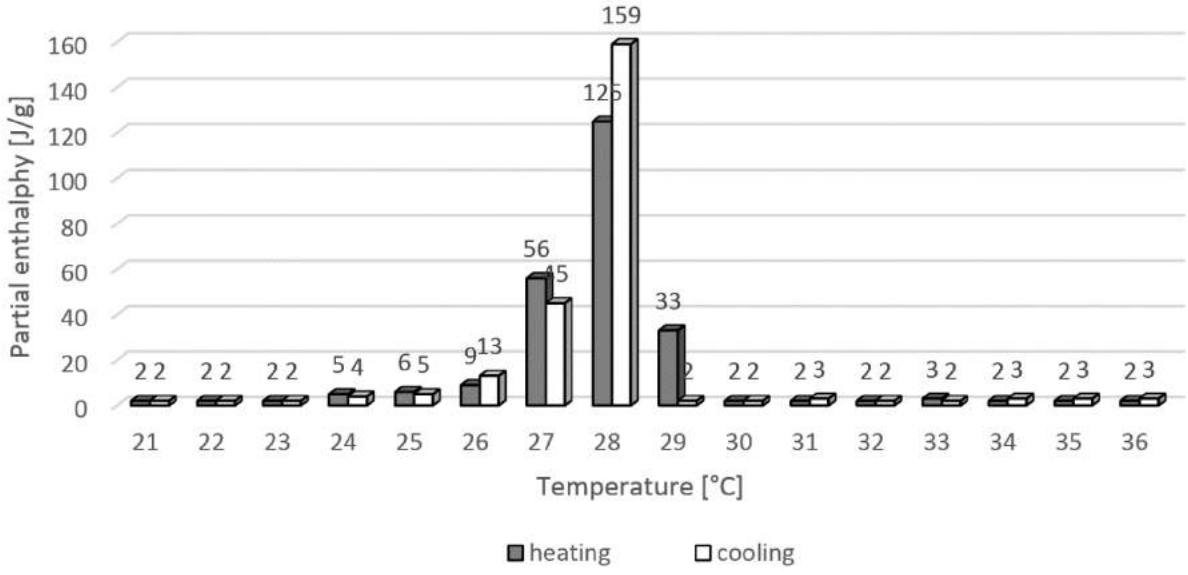

Figure 3. The distribution of heat storage capacity of PCM RUBITHERM® RT28HC during heating and cooling within temperature range from 21°C to 36°C [9].

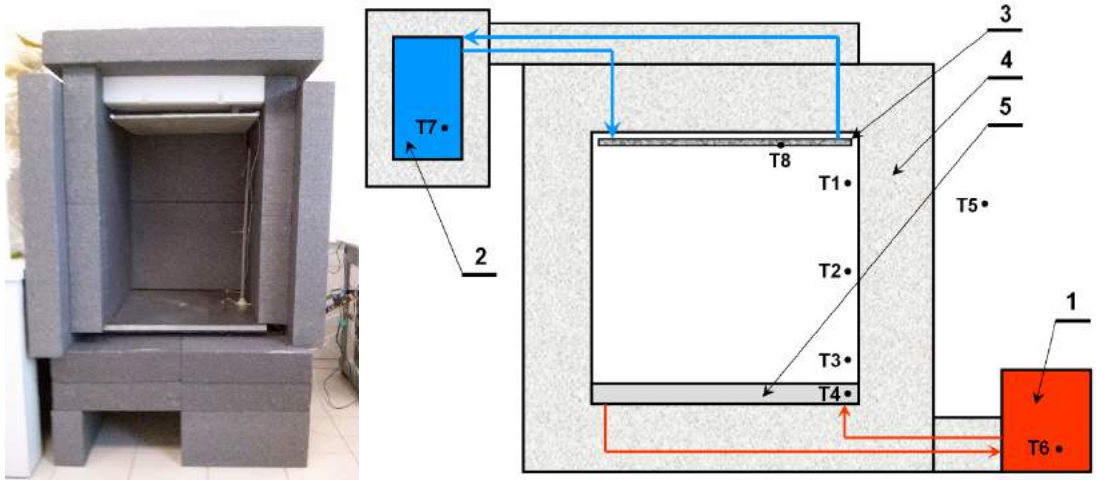

Figure 4. Experimental climatic chamber designed for measurement of the ability to store latent heat of phase transition by heating/cooling panels of aluminium foam impregnated by PCM and testing their performance under various conditions of cooling and heating (1 – thermostat, 2 – reservoir with 12.6 liters of water, 3 – tested panel of aluminium foam impregnated by PCM, 4 – thermal insulation, 5 – aluminium plate with dimensions 700 × 700 × 25 mm stabilizing the temperature in the chamber).

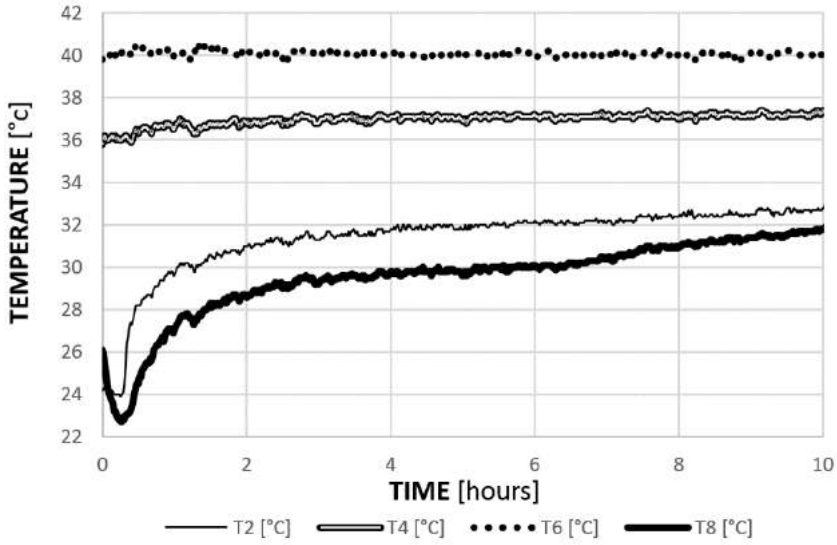

Figure 5. The thermal behavior of the tested panel during the experiment by which the interior of the climatic chamber was cooled by solidified and slowly melted PCM impregnated in aluminium foam panel. The temperature difference between tested panel and aluminium plate with stabilized temperature creating the bottom of the climatic chamber was during storing of latent heat ~ 7°C (T2 – air temperature at the middle space of the climatic chamber, i.e. at a distance of 500 mm from tested panel, T4 – temperature of aluminium plate creating the bottom of climatic chamber, T6 – temperature of the water in thermostat and T8 – temperature of the tested panel).

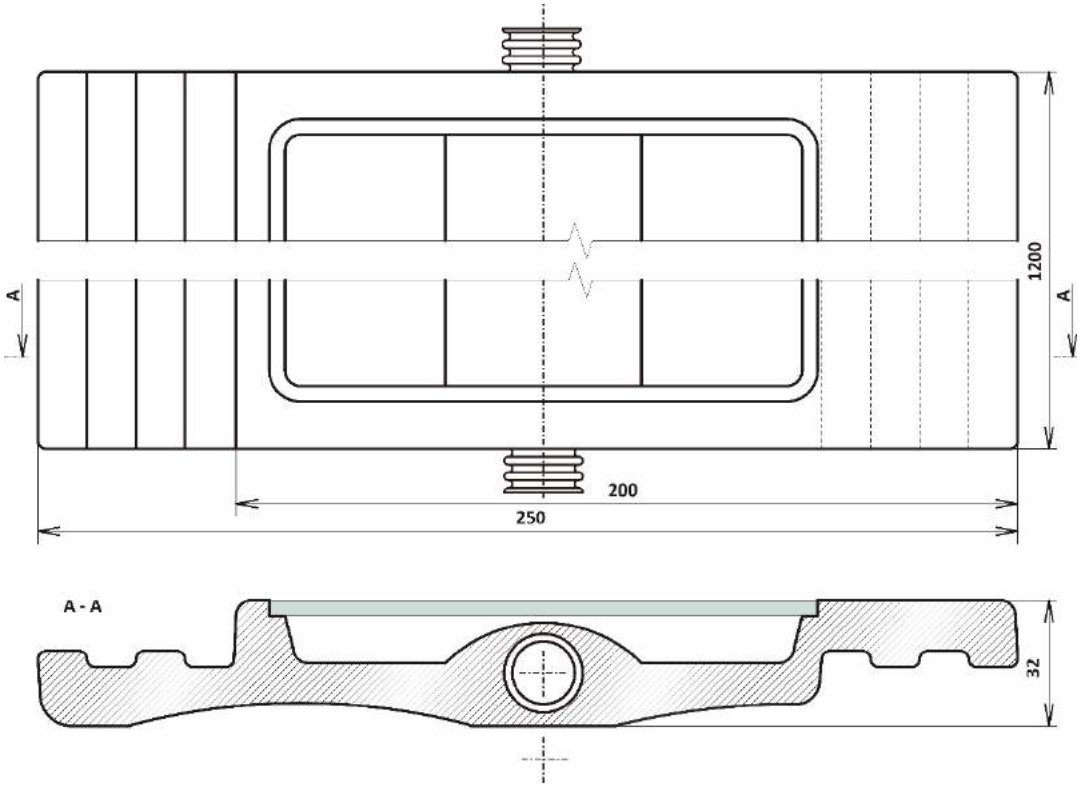

Figure 6. Schematic drawing of thermo-active aluminium foam roofing appropriate for moderate climatic zone, which is able to efficiently recover the heat from solar gains even during colder sunny days, when the sun shines through the translucent glass panel, heats both the absorption surface layer of aluminium foam roofing and the air enclosed in the space under the glass cover.

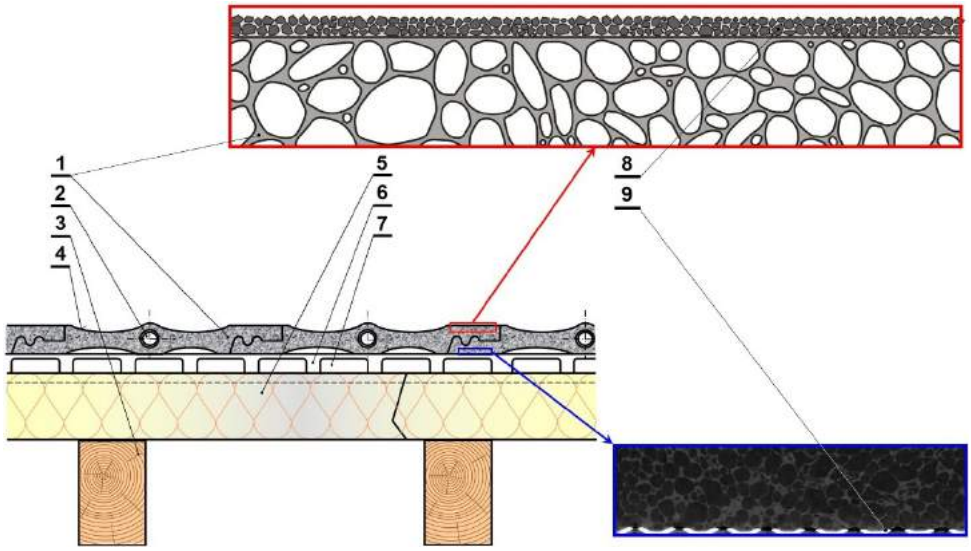

Figure 7. The design of thermo-active ultra-light aluminium foam solar roofing appropriate for subtropical climatic conditions shown in the cross-section perpendicular to the direction of the sloping roof rafters.
1 – roofing components made of aluminium alloy foam,
2 – corrugated tubes made of corrosion-resistant chromium-nickel austenitic steel used for distribution of liquid heat-transfer fluid,
3 – construction of sloping roof made from wooden rafters,
4 – surface layer of aluminium foam roofing ensuring a high solar heat absorptivity,
5 – the thermal insulation layer above the rafters of sloping roof ensuring its waterproofing and creating a barrier to water vapor,
6 – rails of galvanized steel integrated into the insulation layer above rafters,
7 – venting air gap between the top layer of aluminium foam roofing and waterproof insulation with vapour barrier above the rafters of sloping roof,
8 – coating of polymer matrix composite reinforced with metallic or ceramic particles (alternatively basalt granules, crushed natural stones, etc.) protecting surface layer of aluminium foam casting against mechanical damage caused by adverse weather conditions and providing highly efficient heat transfer,
9 – expanded stainless steel sheet reinforcing tensile loaded surface of thermos-active ultralight solar aluminium foam roofing.

The heat-insulated tested panel was before the start of the experiment described in this contribution cooled by flowing cold water to a temperature below 23°C and subsequently the experiment started by stopping the water circulation through the tested panel. The latent heat was during this experiment stored and slowly dissipated from paraffin wax in order to determine dependence between the temperature and time in the experimental climatic chamber during free cooling of chamber interior by tested panel near the phase transition temperature. Tested flat aluminium foam panel with the area 600 mm × 600 mm and weight of 3240 g (2100 g is the weight of aluminium foam, 470 g is the weight of steel tubes, and 670 g is the weight of the outer layer of aluminium sheet) has been covered by the aluminium sheet of thickness 0.5 mm bent on all four sides beyond the lateral edges of the panel.

This experiment demonstrated that PCM impregnated in the structure of tested aluminium foam panel during cooling of air space was able after reaching panel temperature of about 28°C to maintain its temperature below 30°C for up to 5 hours although the temperature of aluminium plate stabilizing the bottom of the climatic chamber remained held at about 37°C.

The following calculations can be used to quantify the amount of latent heat, which is capable of being stored and later dispersed to the air or heat transfer fluid at a constant temperature by aluminium foam panels filled by PCM. Let us consider the aluminium foam panel with dimensions 600 × 600 × 10 mm, volume of 3600 cm^3, a density of 0.5 g/cm^3 and a weight of 1800 g.

The weight of 1 m^2 of panels is 5.4 kg. They can be fully filled with about 7.24 kg of PCM RUBITHERM® RT28HC with the melting range 27 – 29°C (PCM density in the solid state is 0.88 g/cm^3, in the liquid stage 0.77 g/cm^3, the average density is ~ 0.825 g/cm^3). Since 1 kg of PCM is able to accumulate about 250 kJ latent heat, and thus even 1810 kJ (e.g. ~ 503 Wh) of latent heat can be accumulated during phase transition of PCM into 1 m^2 of aluminium foam panels with pores fully filled by PCM in this way.

4. Roofing of pitched roofs reducing energy consumption

The possibility to accumulate large amounts of latent heat in the ceiling panels in order to reduce energy demands for maintaining sufficient thermal comfort in the interiors of buildings brings a huge opportunity to adapt the requirements prescribed on the properties of the roofing so as to efficiently use heat surpluses from solar gains that the current building industry does not use almost at all. The construction of roofing utilized benefits of an efficient heat storage system for nZEBs presented in this contribution, allows not only the heat accumulated at a time when heat from solar gains is sufficient (during hot summer days) to use preferably for heating of DHW, seasonal heat accumulation under the base plate of the building, but also very energy efficient heat dissipation of large amount of excess heat accumulated during whole day in the interior through the roofing to the building surroundings during cooler summer nights.

The main requirements for thermo-active roofing of pitched roofs reducing the energy consumption of a building constructed according to this concept can be summarized as follows:

- ✓ roofing must be sufficiently resistant to weathering, frost, intense solar radiation, summer heat, chemicals presented in the air, chemically polluted water vapor and to mechanical damage caused by adverse weather conditions (e.g. heavy rainfall, groats, etc.),
- ✓ roofing must provide considerable heat gains even when the temperature around the building is low, but the sunshine on the roof is sufficiently intense,
- ✓ the amount of the heat accumulated by roofing during hot summer days is low enough to dissipate it to the building surroundings during summer nights as efficiently as possible together with the heat of the liquid heat transfer medium flowing through the pipelines integrated into the structure of aluminium foam from which the roofing is made,
- ✓ the manufacturing cost of a thermo-active roof covering for pitched roofs of buildings must be only slightly higher compared with the manufacturing cost of classic roofing used in the current building which fulfills together with an additional heat insulation layer in particular only the functions of thermal insulation of the roof and the protection against the penetration of rainwater and water vapor into the interior,
- ✓ thermo-active roofing must be architecturally designed so that it is the part of the roof without being possible to recognize at first sight the places from which the heat of solar gains is gained from the rest of the roof.

The structural design of innovative thermo-active aluminium foam roofing capable of efficient recovering the heat from solar gains also during spring, autumn, and sometimes even winter sunny days is shown in Fig. 6. When the sun shines intensively during the sunny day through the translucent glass sheet creating the surface layer of the south-facing pitched roof, it heats very intensively not only the radiation-absorbent surface layer of aluminium foam roofing but also the whole volume of the air enclosed in the space under the glass cover of the roofing.

Moreover, the huge advantage of this roofing design is that the surface between the individual glass sheets can be covered by polycrystalline photovoltaic (PV) cells. This modification changes the roof to hybrid PV/solar thermo-active roofing suitable especially for covering the southern sloping roofs of nZEBs in cold and mild climatic regions.

In regions where the sun is intensively shining on the surface of the southern sloping roofs for almost the whole year long, it is much more advantageous to use roofing design as shown in Fig. 7. The main advantage of this roofing is that the excess heat accumulated in the interior can be intensively removed during each cooler night by the liquid heat transfer medium and dispersed in the surroundings of the building. The roofing surface has to be adapted for these reasons so that the heat exchange between the ambient air and the heat transfer fluid flowing in the tubes embedded in the structure of the heat-conducting aluminium foam roofing is as intense as possible. The covering of the roofing by various composite systems based on thermosetting polymer matrix (e.g. epoxy resins, graphite filled polyimide, polyurethane, etc.) composites reinforced by particles (metallic or ceramic particles, basalt granules, aluminium scrap granules, crushed natural stones, glass foam splinters, etc.) seems to be very beneficial as the roofing surface must be sufficiently resistant also to any mechanical damage caused by heavy rainfall, groats, and any other adverse weather conditions. The variability of different surfaces opens up the possibility to accomplish appropriate aesthetic appearance of the coating layer, its color fastness, and simultaneously to maintain high mechanical and chemical resistance to atmospheric agents for the different climatic zones for which this roofing is intended. To achieve both the high stiffness and the ultra-lightness of the roofing, it is very advantageous to reinforce the bottom roofing surface with perforated expanded stainless steel sheet which significantly improves the bending stiffness of the roof loaded by its weight or by snow cover during cold winter season.

5. Conclusions

This contribution highlights the possibility of using aluminium foam for novel large-scale roofing with an integrated heat exchanger capable of effectively gaining low potential heat from the surroundings and to transfer it via liquid heat transfer fluid to the building

interior. The same roofing is simultaneously able to dissipate excess heat accumulated in the building to its surroundings during the summer nights when the outside temperature drops below 20°C.

Moreover, approximately 500 Wh can be stored in each m^2 of building interior equipped with aluminium foam ceiling panels impregnated by PCM in the form of latent heat of its solid-liquid phase transition. This heat is during winter enough for keeping sufficient thermal comfort about 9 hours without delivering additional energy from source as an average winter monthly heat demand is ~ 40 kWh/m^2. The temperature of the ceiling panels does not drop below the phase transition temperature during this time even when they accumulate no more heat from the source. This means that during those days of the heating season that can be obtained from solar gains through a roof at least 500 Wh of heat (by heating the liquid heating medium to a temperature of at least 30°C) for every 1 m^2 of living space, sufficient thermal comfort can be assured by the daily charging and discharging of said ceiling heating/cooling panels. The sufficient amount of solar gains is available in the region of Central Europe for this purpose almost throughout whole spring as well as autumn. The energy required to drive the circulating pump that distributes liquid head transfer fluid heated by thermo-active roofing into the interior is almost negligible in comparison with the energy required for classical heating. During period of an excessive energy need at the beginning of the heating season, i.e. especially during very cold winter days, part of the energy needs can be covered by using of energy surpluses stored during hot summer days in (or below) the baseplate of the building. Each 1 m^2 of 30 cm thick base plate made of concrete with the density 2400 kg/m^3 and a specific heat 0.88 kJ/kg can store during the summer season by heating from 20°C to 50°C about 19000 kJ, i.e. ~ 5.28 kWh of heat.

Fig. 8 shows an approximate estimate of the monthly energy demand for the operation of a self-standing single-storey family house built in the Central European region and the expected reduction of its energy demand in the case of use foamed aluminum heat exchangers described in this contribution supplemented by the seasonal storage of summer heat surpluses in 30 cm thick isolated concrete base plate. However, the greater savings of energy needed during winter for heating of the house can be achieved by the construction of the base plate, which is shown in fig. 2 by using a larger amount of stones to which the heat is stored during the summer. It is convenient and economical to have this earth collector insulated from the foundation plate by an air layer. It is also desirable to provide thoroughly watertight insulation from the side of ground, especially in the case that the earth under the house is bather by underground water. However, if the underground water is sufficiently deep under the house, a good heat transfer capability between the ground collector and the earth below the base of the house even helps to increase the amount of heat that can be stored in the seasonal earth collector during whole summer season.

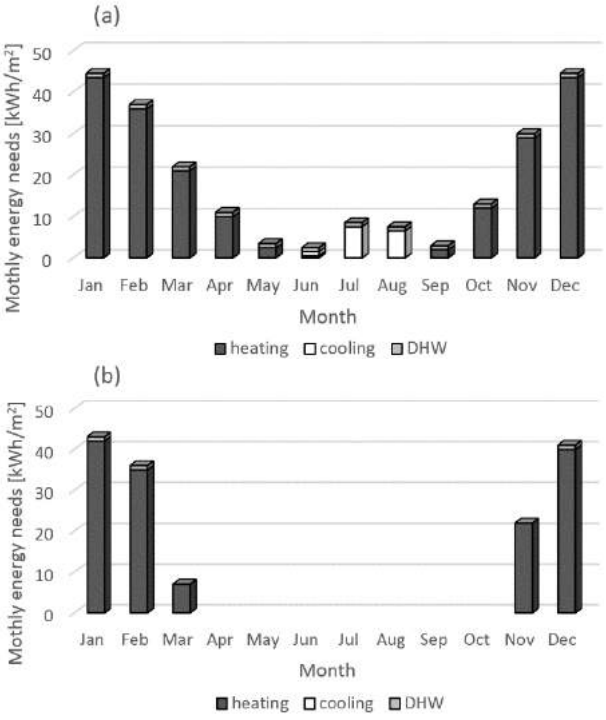

Figure 8. Comparison of energy needs for heating, cooling and domestic hot water (DHW) preparation of (a) classic family house and (b) the house that uses novel aluminum foam heat exchangers, both built in the region of Central Europe.

The innovative ultra-light and sufficiently stiff roofing system described in this contribution is based on reinforced aluminium foam with integrated corrugated stainless steel pipes for the distribution of the heat transfer fluid. The roofing is designed to cover entire pitched roofs of future nZEBs. However, the principles analyzed in this paper can generally be used in the building sector for designing of any structural part forming an outer building envelope with an integrated function of energy efficient heat exchanger.

Acknowledgement

The financial support by the Slovak Grant Agency for Science under the contract VEGA 2/0152/17 (project: Investigation of advanced materials suitable for highly effective heat storage) and by European Regional Development Fund under the contract ITMS 26240220028 (project: Efficient controlling of the production and consumption of energy from renewable sources, acronym: ENERGOZ) is gratefully acknowledged.

REFERENCES

[1] Directive 2010/31/EU of the European Parliament and of the Council of 19 May 2010 on the energy performance of buildings.

[2] Jerz, J. – Simančík, F. – Šebek, J. – Kováčik, J. and Španielka, J. Application of aluminium foam for heat exchangers on building facades and interior ceilings. In: *Mechanical Technologies and Structural Materials 2016*. – Split: Croatian Society for Mechanical Technologies, 2016, pp. 61-66. ISSN 1847-7917.

[3] Jerz, J. – Simančík, F. and Orovčík, Ľ. Advanced solution for energy storage in net zero-energy buildings. In: *Mechanical Technologies and Structural Materials 2014*. – Split: Croatian Society for Mechanical Technologies, 2014, pp. 47-54. ISSN 1847-7917.

[4] Jerz, J. – Tobolka, P. – Michenka, V. and Dvorák, T. Heat storage in future zero-energy buildings. In: *International Journal of Innovative Research in Science, Engineering and Technology, 2015*, vol. 4, iss. 8, pp. 6722-6728. ISSN 2319-8753.

(http://www.ijirset.com/upload/2015/august/3_Heat.pdf)

[5] Diarce, G. – Urresti, A. – García-Romero, A. Delgado, A. – Erkoreka, A. – Escudero, C. and Campos-Celador, Á. Ventilated active façades with PCM. In: *Applied Energy 109 (2013)*, pp. 530-537.

[6] Gomez Leon, J. Water-based radiative heating and cooling ceiling for nearly-zero energy buildings, Master thesis, Technical University of Denmark, Kgs. Lyngby, 2015.

[7] Sharma, A. – Tyagi, V. V. – Chen, C. R. and Buddhi, D. Review on thermal energy storage with phase change materials and applications. In: *Renewable and Sustainable Energy Reviews 13 (2009)*, pp. 318-345.

[8] PARAFOL C_{12} – C_{22} – High purity normal paraffins, Corporate brochure of Sasol Performance Chemical, Organics Division, Hamburg, Germany, 2016.

[9] RUBITHERM® RT28HC Data sheet, Rubitherm Technologies GmbH, Berlin 2016.

[10] Socaciu, L. G. Thermal Energy Storage with Phase Change Materials. In: *Leonardo Electronic Journal of Practices and Technologies, Issue 20 (2012)*, pp. 75-98, ISSN 1583-1078.

[11] Wang, L. and Meng, D. Fatty acid eutectic/ polymethyl methacrylate composite as form-stable phase change material for thermal energy storage. In: *Applied Energy 87 (2010)*, pp. 2660-2665.

[12] Chernousov, A. A. and Chan, B. Y. B. Novel form-stable phase change material composite for high-efficiency room temperature control. In: *Solar Energy Materials and Solar Cells 170 (2017)* pp. 13-20.

[13] http://en.wikipedia.org/wiki/Phase-change_material

[14] Zuo, J. – Li, W. and Weng L. Thermal performance of caprylic acid/1-dodecanol eutectic mixture as phase change material (PCM). In: *Energy and Buildings 43 (2011)*, pp. 207-210.

[15] Tunçbilek, K. – Sari, A. – Tarhan, S. – Ergüneş, G. Kaygusuz, K. Lauric and palmitic acids eutectic mixtures as latent heat storage material for low temperature heating applications. In: *Energy 30 (2005)*, pp. 677-692.

[16] Putri, W. A. – Fahmi, Z. – Sutjahja, I. M. – Kurnia, D. and Wonorahardjo, S. Thermophysical parameters of coconut oil and its potential application as the thermal energy storage system in Indonesia. In: Journal of Physics: Conference Series 739 (2016)

doi: 10.1088/1742-6596/739/1/012065

[17] http://pubchem.ncbi.nlm.nih.gov/compound/oleic_ acid

[18] http://webbook.nist.gov/cgi/cbook.cgi?ID=C112801&Mask=6F

[19] Sato, K. – Yoshimoto, N. – Suzuki, M. – Kobayashi, M. and Kaneko, F. Structure and transformation in polymorphism of petroselinic acid (cis-ω-12-octadecenoic acid). In: *J. Phys. Chem. 94 (1990)*, pp. 3180-3185.

[20] Pi, F. – Kaneko, F. – Iwahashi, M. – Suzuki, M. and Oyaki, Y. Solid-State Low Temperature – Middle Temperature Phase Transition of Linoleic Acid Studied by FTIR Spectroscopy. In: *J. Phys. Chem. B, 115 (2011)*, pp. 6289-6295.

ISSN 1847-7917

Poboljšanja na ispušnom ventilu brodskog dizelskog motora u svrhu produljenja vremena do zahvata održavanja

Mate Jurjević[1)]***, Žarko Koboević***[1)]***, Nikša Koboević***[1)] ***Dragan Bebić***[2)]

1) University of Dubrovnik, Maritime Department, Ćira Carića 4, 20000Dubrovnik, Croatia
Sveučilište u Dubrovniku, Pomorski odjel, Ćira Carića 4, 20000 Dubrovnik, Hrvatska
2) GearbulkNorway AS
Damsgard Svein 165
N-5160 Lakfevag
Bergen, Norway

mjurjevic@unidu.hr
zarko.koboevic@unidu.hr
niksa@unidu.hr
dragan.bebic@gearbulk.com

Keywords

exhaust valve,
exhaust valve seat,
time between faults,
maintenance,
AMOS

Ključne riječi

ispušni ventil,
sjedište ispušnog ventila,
vrijeme između kvarova,
održavanje,
AMOS

Improvements on the diesel engine exhaust valve to extend time to maintenance

Professional paper

Abstract: In this paper structural inovations on the MAN B&W marine diesel engine series MC, MC-C and ME-C, which contribute to a significant increase in the correct operation of the engine between two maintenance operations on the exhaust valve and cylinder head, have been presented. NIMONIC 80A valve with "W" seat is described in the paper. Component and engine performance monitoring are also described informatively as dispensable elements when prolonging the engine running time between two maintenance operation.

Stručni rad

Sažetak: U ovom radu dan je prikaz konstrukcijskih noviteta na brodskom dizel motorima MAN B&W serije MC, MC-C i ME-C koji doprinose znatnom povećanju ispravnog rada motora između dva zahvata održavanja na ispušnom ventilu i glavi motora. U radu su opisane značajke „NIMONIC 80A" ventil sa „W" sjedištem. Nadzor stanja komponenti i performansi motora je također informativno obrađen kao neophodan element pri produljavanju rada motora između dva zahvata održavanja .

1. Uvod

U posljednjih desetak godina vrijeme između zahvata na cilindrima brodskog dizel motora je postepeno povećavano zahvaljujući konstrukcijskim rješenjima i tehnološkim poboljšanjima. Ohrabren povratnim informacijama iz eksploatacije MAN B&W u posljednjih par godina ispituje mogućnosti produljenja vremena između zahvata na 32000 sati. Podatci su uzeti iz baze podataka programskog paketa AMOS za održavanje broda [1].

U svrhu ispitivanja MAN B&W je odabrao motore najnovije generacije MC-C i ME-C (ME-C je elektronički upravljan motor). Ta skupina motora je dizajnirana i isporučena sa posljednjim dostupnim novitetima. Jedan od njih je „NIMONIC 80A" ispušni ventil sa sjedištem ventila „W" tipa.

2. Poboljšanja kod ispušnih ventila na dvotaktnim MAN B&W dizelskim motorima

Tendencija svih proizvođača brodskih dizelskih motora je oduvijek bila što pouzdaniji motor i što dulji vijek komponenata između planiranih zahvata održavanja.

MAN B&W je u posljednje vrijeme konstrukcijski preinačeno sjedište ventila i ventil tako da je uobičajeno vrijeme rada do zahvata održavanja produljeno sa 8000 na 16000 sati. Baza sjedišta ventila, umjesto punog profila, je prvotno poprimila izgled komore (slika 2) u svrhu smanjivanja temperature dodirnih površina baze sjedišta i ventila.

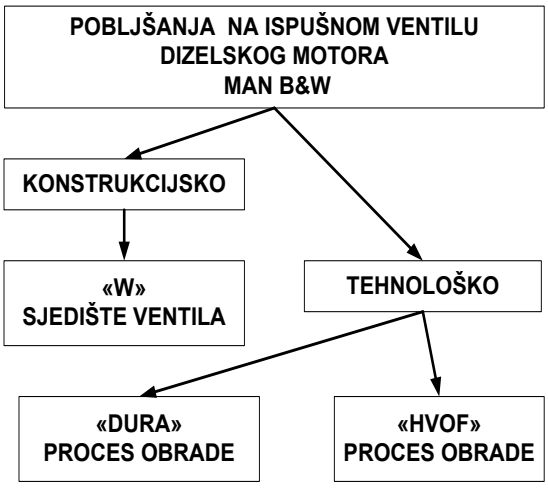

Slika 1. Zahvat poboljšanja na ispušnom ventilu MAN B&W dizelskog motora
Figure 1. Improvement of MAN B&W diesel engine exhaust valve

3. Konstrukcijsko "W" poboljšanje sjedišta ispušnih ventila na dvotaktnim MAN B&W dizelskim motorima

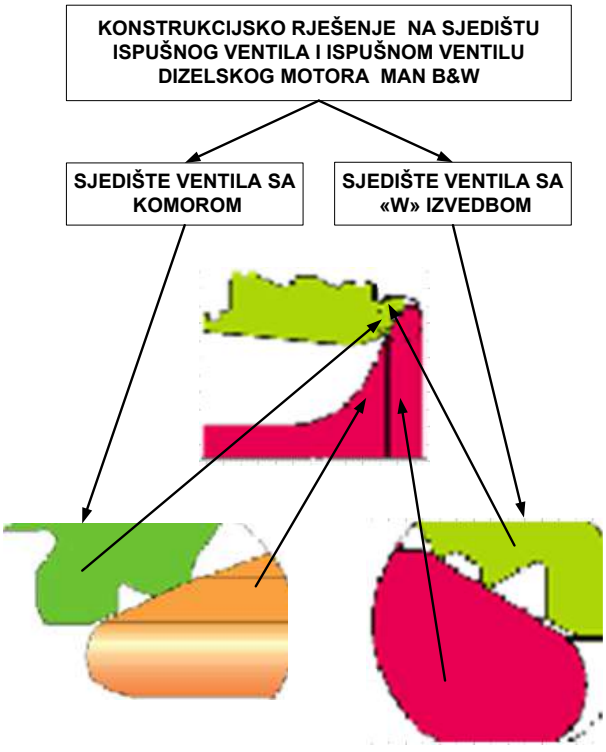

Slika 2. Sjedište ventila sa „komorom" i „W" sjedište, [2][3][4][5][6][7][8][9][10][11][12]
Figure 2. Valve seat with "chamber" and "W" seat, [2][3][4][5][6][7][8][9][10][11][12]

Dulji radni vijek sjedišta ventila je postignut sa novom geometrijom „W-sjedišta". Nova konstrukcija zadržava prednosti predhodnog riješenja sjedišta s komorom (smanjivanje temperature na dodirnim površinama) i kombinira prednosti uskih koncentričnih dodirnih površina.
Svi čvrsti produkti izgaranja, koji ostaju između dodirnih površina, bivaju usitnjeni i eliminirani. Na taj način se smanjuje rizik pojavljivanja udubina nastalih prešanjem čvrstih produkata u široke dodirne površine ventila i sjedišta ventila.
Ventil i sjedišta se mogu upotrebljavati sve dok:

- postoji dodir duž cijeloga obima unutrašnjeg sjedišta,
- nema poprečnih tragova propuhivanja na sjedištu.

4. Proces obrade ispušnog ventila na dvotaktnim MAN B&W motorima

Današnja tehnologija obrade materijala omogućava, neslućene vremenske granice rada prije redovnog zahvata održavanja.

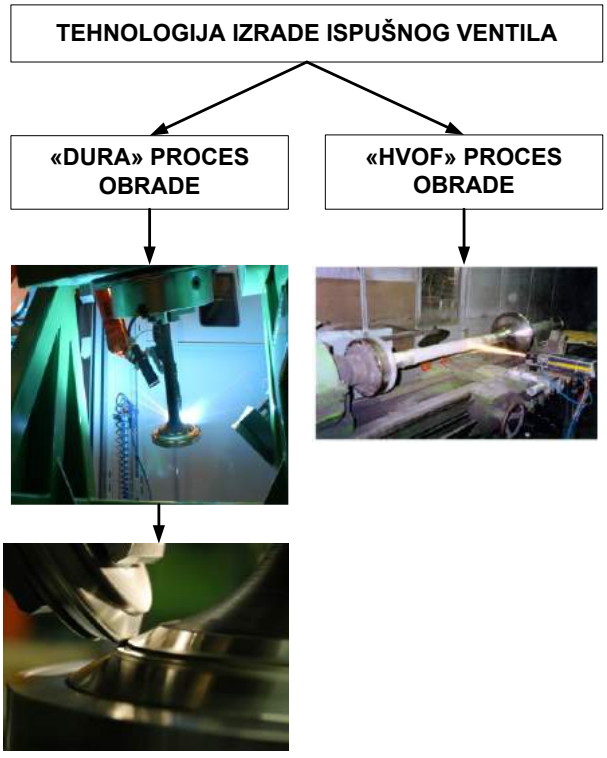

Slika 3. Suvremene tehnologije izrade ispušnih ventila, [2][5][7][8][9][10][11][12]
Figure 3. Contemporary exhaust valve manufacturing technologies, [2][5][7][8][9][10][11][12]

Jedan od klasičnih primjera je ispušni ventil (do nedavno uobičajeno vrijeme rada do zahvata održavanja je bilo 8000 radnih sati).

4.1. Proces obrade ispušnog ventila "HVOF" tehnologijom

HVOF (High Velocity Oxy-Fuel process) tehnologijom se produljava radni vijek samoga ventila. Vreteno ventila je podvrgnuto „HVOF" procesu. Tim procesom se samo na vreteno nanosi sloj materijala NIMONIC 80A, debljine 0.25 mm, koji je veoma otporan na habanje. Proces nanošenja karbida i posebne legure je termički.

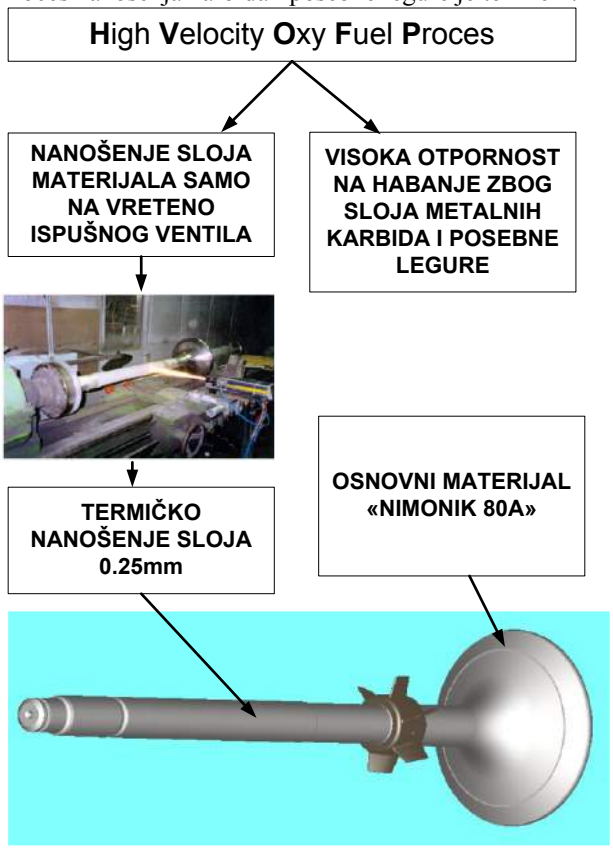

Slika 4. Obrada vretena ventila „HVOF" procesom (High Velocity Oxy-Fuel process), [2][5][7][8][9][10][11][12]

Figure 4. Process of "HVOF" machining valve spindle (High Velocity Oxy-Fuel process), [2][5][7][8][9][10][11][12]

4.2. Proces obrade ispušnog ventila "DURA" tehnologijom obrade valjanjem materijala

Proces je kombinacija nanošenja legure nikla na pladanj, utiskivanjem materijala u području pladnja (uz pomoć valjka pri sili od 10 tona) te naknadne termičke obrade u peći. Završni rezultat obrade je „DURA" ventil sa izuzetnom tvrdoćom u području pladnja ventila.

Na slici 6 je prikazan mikroskopski snimak valjanog materijala te distribucija tvrdoće iste sekcije nakon termičke obrade.

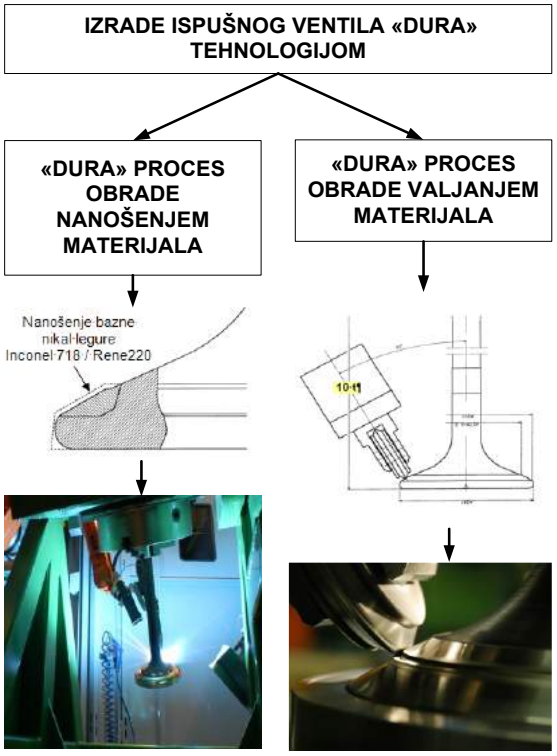

Slika 5. Proces izrade „DURA" ventila, [2][5][7][8][9][10][11][12]

Figure 5. The "DURA" valve manufacturing process, [2][5][7][8][9][10][11][12]

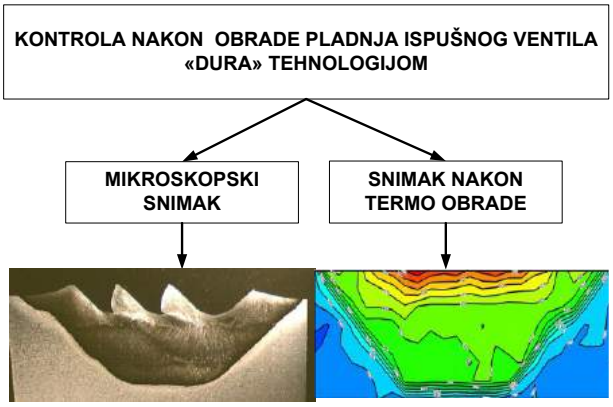

Slika 6. Mikroskopski snimak sekcije „DURA" ventila, [2][5][7][8][9][10][11][12]

Figure 6. Microscopic survey of the "DURA" valve section, [2] [5] [7] [8] [9] [10] [11] [12]

5. Rezultati ispitivanja ispušnih ventila na dvotaktnim MAN B&W motorima tipa MC, MC-C i ME-C dobiveni iz baze podataka programskog paketa "AMOS"

U radu je praćeno nekoliko brodara domaćih i stranih koji imaju brodske motore MAN B&W proizvedene u domaćim brodogradilištim Brodosplit i Uljanik. Svaki brod ima svoj program AMOS za održavanje i u sklopu njega povijest radova na komponentama motora, gdje se vide kad i što je rađeno na motoru od ugradnje do trenutka uzimanja podataka.

Baza podataka (history) u svom programu ima registar komponenti i povijest svih zahvata na sustavima i komponentama. U radu je korišten program „AMOS" kako bi se mogla provesti analiza uzoraka ispušnih ventila na MAN B&W dizelskim motorima za različite tipove. Ispušni ventil je kao i svaka druga komponenta koja se mijenja zbog dotrajalosti ili loma na ventili.

Na slikam 7,8,9 i 10 se vidi prikaz komponenti za tip motora 6S50MC-C u programskom paketu „AMOS" koji služi za daljnju analizu aktivnosti nad komponentama. Nakon analize sirovih podataka dobivena je tablica 1 i slike 11 i 12.

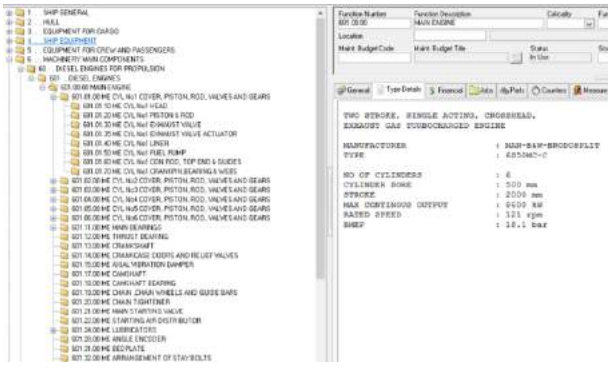

Slika 7. Prikaz komponenti i karakteristika MAN B&W 6S50MC-C, [12] [13]

b. Display of components and parameters MAN B&W 6S50MC-C, [12] [13]

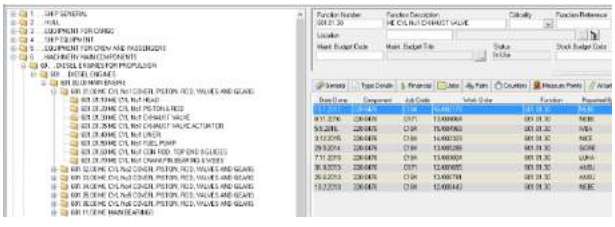

Slika 8. Radnje na komponentama, [1][6][7]

Figure 8. Components actions, [1][6][7]

Nakon odabira ispušnog ventila kao jedne od komponenti prikazuje se na ekranu sve vezano za ispušni ventil od tehničkog opisa pa sve do povjesti rada na ispušnom ventilu što se vidi na slici 8.

Opcija „History" u programu AMOS, koja prikazuje ispis svih zahvata na ispušnim ventilima kod dizelskog motora. Zahvata može biti i više tokom radnog perioda brodskog dizelskog motora za pojedine komponente što je vidljivo iz slika 9 i 10.

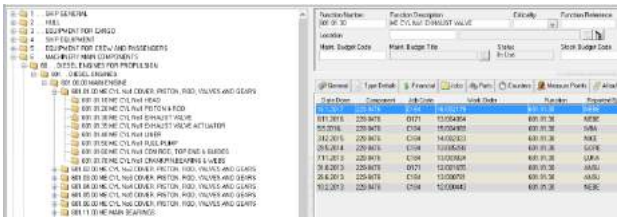

Slika 9. Ispis povijesti zahvata održavanja za ispušni ventila, [1][6][7]

Figure 9. Print out of the maintenance history of the exhaust valve, [1][6][7]

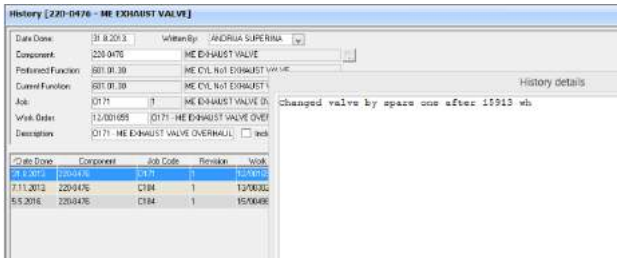

Slika 10. Detaljan opis izvršenog zahvata održavanja nad ispušnim ventilom (MAN B&W brodski dizelski motor), [1][6][7]

Figure 10. A detailed description of the maintenance performed on the exhaust valve (MAN B&W marine diesel engine), [1][6][7]

Program nam omogućuje i provjeru podataka o izvještenom zahvatu, tj. detaljan opis nekog zahvata koji nas zanima nad određenom komponentom.

5.1. Rezultati ispitivanja ispušnog ventila na motorima tipa MC, MC-C i ME-C

Rezultati ispitivanja provedeni na većem uzorku brodova (preko trideset), koji imaju MAN B&W dizel motore tipa MC, MC-C i ME-C, prikazani su u tablici 1, slika 11 i slika 12, gdje je prikazano vrijeme između zahvata održavanja na ispušnim ventilima za gore navedene tipove MAN B&W dizel motora.

Tablica 1. Produljeno vrijeme između dva zahvata održavanja
Table 1. Extended time between two maintenance action

TRENUTAK PROMATRANJA	STARI TIP MOTORA MC	NOVI TIP MOTORA MC-C "KOMORA"	ELEKTRONSKI KONTROLIRAN MOTOR MC-E "W"
8000	1	0	0
32000	4	2	1
64000	8	4	2
80000	10	5	0
UKUPAN BROJ ZASTOJA	**23**	**11**	**3**

Tablica 1 prikazuje postupno povećanje vremena između dva zahvata održavanja na ispušnom ventilu. Rezultati su uzeti u periodu od 80 000 radnih sati, za MAN B&W dizel motorima tipa MC, MC-C i ME-C.

Slika 11. Prikaz funkcija vremena izmedju zahvata održavanja za MAN B&W dizelskim motorima tipa MC, MC-C i ME-C.
Figure 11. Diagram of the time function between maintenance procedures for MAN B&W diesel engine series MC, MC-C i ME-C

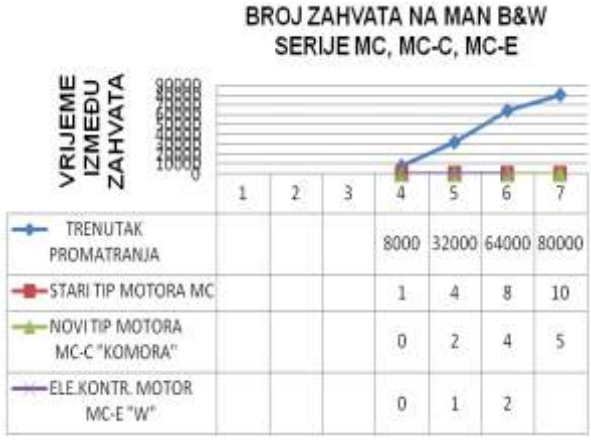

Slika 12. Prikaz funkcije trenda vremena između zahvata MAN B&W dizel motorima tipa MC, MC-C i ME-C
Figure 12. Diagram of the time function between maintenance procedures for MAN B&W diesel engines series MC, MC-C i ME-C

Iz slike 12 vidljivo je da vrijeme između zahvata raste. Iskustveni rezultati dobiveni s brodova su analizirani i biti će iskorišteni za određivanje vremena između zahvata na ispušnom ventilu. Rezultat jednog od takvih pregleda je vidljiv na slici 13.

Slika 13. Izgled „NIMONIC 80A" ispušnog ventila i „W" sjedišta nakon 36400 radnih sati, [7][9][10][11]

Figure 13. Appearance of „NIMONIC 80A" exhaust valve and „W" seat after 36400 operating, hours [7][9][10][11]

Izgled pladnja „NIMONIK 80A" ventila i „W" sjedišta nakon 36400 radnih sati, bez zahvata održavanja, potvrđuje dobro konstrukcijsko i tehnološko rješenje.

6. Zaključak

MAN B&W dizelski motor tipa ME-C je, u usporedbi sa prijašnjim tipovima MC i MC-C, pokazao veću pouzdanost. Zbog navedenog daljnja primjena elektronike na pogonskim uređajima je neosporna, posebno kod sustava dijagnostike, jer je granica jedino inovativnost proizvođača i interes brodara.
Nova tehnološka i konstrukcijska rješenja „DURA i HVOF" pomiču granice prosječnog radnog vijeka komponenti.
Dosadašnja analiza koristi se za predviđanje održavanja, starenja i pouzdanosti komponenti sustava.
Ovakvi rezultati ispitivanja idu u korist planskog održavanja koje će doživjeti velike promjene, u korist održavanja na osnovi stanja komponenti i karakteristika uređaja.
U radu se nastojalo iznijeti što više informacija iz prakse kako bi se mogao dobiti uvid u prednosti koje pruža programski paket AMOS.
Suvremene tehnologije obrade ispušnog ventila („DURA" i „HVOF" proces) produljuju vrijeme rada ventila bez pojave oštećenja, a time smanjuju učestalost potrebnih redovitih pregleda.

LITERATURA

[1] M. Jurjević; B. Bilić; I. Milić-Beran; H. Zekić: *Application of the software package „AMOS" in maintenance of the marine propulsion system*; 2nd International maritime scientific conference – IMSC, June 17-21, 2008, Lumbarda, Croatia.

[2] D. Bebić, Elektronički kontroliran motor MAN B&W 6S60ME-C, „Završni rad" Sveučilište u Dubrovniku, Dubrovnik 2010..

[3] J. Lovrić, Osnove brodske terotehnologije, Pomorski fakultet u Dubrovniku, Dubrovnik (1989.)

[4] Časopis "The Motor Ship", February 1997.

[5] www.manbw.com (Containership propulsion-beyond Post-Panamax)

[6] SpecTec-Split. AMOS, Priručnik za rukovanje programskim paketom.

[7] Tehnička dokumentacija; AP plovidba-Dubrovnik, Tankerska plovidba-Zadar, ULJANIK plovidba-Pula, Jadroplov-Split, Uljanik-Strojogradnja-Pula, BRODOSPLIT- Strojogradnja-Split

[8] MAN B&W – „diesel Academy 2006"

[9] MAN B&Wdiesel – „service experience 2016"

[10] MAN B&W turbo – „PrimeServ Academy 2015"

[11] MAN B&W diesel – „CoCoS-EDS" user guide Internet:

[12] http://www.ship-technology.com

[13] http://www.powergeneration.com

[14] http://www.marineengineering.org.uk

[15] http://www.hightechfinland.com

[16] http://www.marinelog.com

ISSN 1847-7917

Gas Nitriding of Titanium in Solar Furnace

Jaroslav KOVÁČIK and Natália MINÁRIKOVÁ
Institute of Materials & Machine Mechanics, Slovak Academy of Sciences, Dúbravská cesta 9, 84513 Bratislava, **Slovakia**
Peter ŠUGÁR, Jana ŠUGÁROVÁ and Martin FRNČÍK
Department of Machining and Forming, Faculty of Materials Science and Technology in Trnava, Slovak University of Technology, Jána Bottu č. 2781/25, 917 24 Trnava, **Slovakia**
Štefan EMMER
Institute of Technologies and Materials, Faculty of Mechanical Engineering, IVMA STU, Slovak University of Technology, Pionierska 15, 831 02 Bratislava, **Slovakia**
José RODRIGUEZ and Inmaculada CAÑADAS
Plataforma Solar de Almeria, Ctra de Senes Km 4, 04200 Tabernas (Almeria), **Spain**
Joana KULASA, Szymon MALARA and Marcin LIS
Institute of Non-Ferrous Metals, ul. Sowińskiego 5, 44-100 Gliwice, **Poland**
ummsjk@savba.sk

Professional article

Abstract:
In the present work we study the use of concentrated solar energy for gas nitriding of powder metallurgy (PM) prepared titanium compacts and CP Grade 2 Titanium (CP Ti Gr2) sheets as an economical alternative to conventional techniques of gas nitriding in electric furnaces, plasma nitriding, CVD, PVD, or laser treatments. Gas nitriding of titanium was performed at various temperatures using 5kW vertical solar furnace at Plataforma Solar de Almeria, Tabernas, Spain. It was observed that the solar process presents great advantages over the conventional surface treatments: significant decrease of the heating time to few minutes (up to 5 minutes at temperatures between 500 - 1000 °C), clean and non-polluting high temperature process. The formation of continuous and homogeneous surface layers of TiN, Ti_2N and their mixture according to nitriding temperature were investigated using electron microscopy and RTG diffraction. Finally, the higher hardness was achieved for all nitriding attempts with respect to hardness of the base materials.

Keywords
solar energy
powder metallurgy
nitriding
titanium,
titanium powder

Ključne riječi
solarna energija
metalurgija praha
nitriranje
titan
titanijev prah

1. Introduction

Titanium and its alloys are increasingly being used in industrial applications because of their good mechanical and chemical properties, as well as low density and high melting point. However, their use is partially limited by their low wear resistance. To improve their tribological properties it is necessary to perform surface modification processes via surface treatments or application of coatings [1-6]. One of the most common processes is to perform a thermo chemical treatment via gaseous or gas nitriding [1]. Gas nitriding is a surface treatment in which nitrogen is supplied into the furnace at a relatively high temperature. This treatment requires titanium and titanium alloys to be heated for long periods of time (between 6 and 10 hours) to high temperatures (> 900 °C) in nitrogen atmosphere.

It was originally proposed by G. Herranz et al. [7] to use solar energy for gas nitriding of Ti6Al4V titanium alloy. On the contrary, in this study, samples of pure titanium (PM compacts/ CP Ti Grade 2 sheets) were treated by gas nitriding using solar radiation in nominally pure nitrogen atmosphere. The treatment time, and the treatment temperature were varied at constant flow rate of nitrogen

gas. The effect of these process parameters on the formation of the modified layers was investigated. Here, we present shortly the first results of Ti nitriding using solar furnace.

2. Experimental

Two different Ti materials were used for gas nitriding in solar furnace. The first material was bulk commercial CP Ti Grade 2 (CP Ti Gr2). The bulk material was 1 mm thick sheet (supplied by Bibus Metals AG, Gemany) that was cut into the pieces of 15 x 10 mm, which were used for gas nitriding in solar furnace in as received (no cleaning or polishing of sample surface takes place). Together 11 samples were prepared for the investigations. The second one was powder metallurgy (PM) prepared bulk compact made from HDH Ti powder (150 μm powder size, purity 99.4 %, Kimet Special Metal Precision Casting Co., Ltd., China) using low temperature extrusion technology [8]. For the experiments 3 pieces from broken tensile test sample with threads and also inner holes were used. The used PM Ti samples had theoretical density of 99.13 %, modulus of elasticity 94.5 GPa, yield stress $R_{p0.2}$ 541 MPa, tensile strength of 687 MPa and ductility of 4.08 %. Oxygen, nitrogen and hydrogen content were 0.207 %, 0.010 % and 0.026 %, respectively.

The nitriding experiments were performed in the vertical axis solar furnace SF5 [9] in Plataforma Solar de Almeria, Spain. SF5 is able to deliver up to 5 kW power at peak concentration ratios exceeding 6000 kW/m^2. This solar furnace operates in a vertical axis, i.e. parabolic concentrator and heliostat are vertically aligned on the optical axis of the paraboloid. The main advantage of vertical axis solar furnaces is that the focus is arranged on a horizontal plane; hence the samples are placed without any fixation (see Figs. 1-2) [10].

The prepared PM Ti sample was placed on molybdenum plate (200 x 200 x 0.7 mm) which was located on zirconia plate (400 x 400 x 3 mm). On the contrary, CP Ti Gr2 sheets were directly placed on zirconia plate. Then the samples were positioned into a spherical vacuum chamber in the solar furnace SF5: Vacuum chamber consists of a 5l borosilicate Duran sphere, which is closed at its bottom by a cooled flange fixed by a clamp and O-ring. The chamber is evacuated through a Pfeiffer turbomolecular pump and gas system is connected to it. The sample was placed to be in optimal focusing distance with regard to solar spot size. The size of solar spot was approximately 50 mm (see Fig. 3). Then the chamber was closed and evacuated (approximate value of the vacuum was around 0.8 Pa) and nitrogen gas flow (400 l/hour under the pressure of 3 bars, technical purity) was used during all experiments.

The temperature of the sample was measured by thermocouple at bottom of molybdenum plate for complex PM Ti samples and directly at bottom of titanium sheets for CP Ti Gr2 material. Constant heating and cooling rate of 100 K/minute was used during experiments. Three experimental complex PM samples were nitrided at 600 °C for 30 seconds, at 750 °C for 30 seconds and 5 minutes. The set of CP Ti Gr2 sheets were nitrided at 700, 800, 900 and 1000 °C for 1 and 5 minutes. After the experiments the samples were cut and samples for microstructure observations were prepared. The microstructure and microhardness of the samples were investigated and measured: Microstructure of samples was observed at PSA`s Materials Lab using Leica DMI 5000 Minverted digital microscope and at IMMS SAS using scanning electron microscope JEOL 7600F, equipped with a Schottky thermal-emission cathode (thermal FEG - W-coated ZrO_2) as well as energy and wavelength spectrometers from Oxford Instruments. Measurement of microhardness of sintered samples was performed at PSA`s Materials Lab using Struers Duramin HMV-2 micro hardness tester at the corresponding loads for 10 seconds.

3. Results and discussions

It was proved that it is possible to use solar furnace for successful gas nitriding of titanium. The created nitride layer is continuous and covers all surfaces of samples. Moreover also threads and deep holes in PM samples were nitrided successfully.

Besides creation of thin nitride layer on the surface of the samples, the diffusing nitrogen also affects the structure just beneath the sample surface by creating solid solution of α-Ti(N). This area depends on the temperature and time of gas nitriding. For example in the case of PM Ti sample gas nitrided at 750 °C for 5 minutes the affected area is approximately 200 – 300 μm thick (see Fig. 4). It confirms the basic assumption that the thickness of α-Ti(N) zone increases with increasing temperature and/or longer time of gas nitriding.

Electron microscopy confirmed the creation of thin titanium nitride layers on the surface of Ti samples. Again nitride layer thickness increases with increasing temperature and/or longer time of gas nitriding. This can be illustrated on microstructures of CP Ti Gr2 samples gas nitrided in solar furnace for 1 and 5 minutes at 900 and 1000°C (Fig. 5). With increasing temperature of gas nitriding at constant exposure time of 1 minute the thickness of created nitride layers increased from approximately 15 μm up to almost 50 μm. Anyway the porosity at thicker layer is observed at 1000°C.

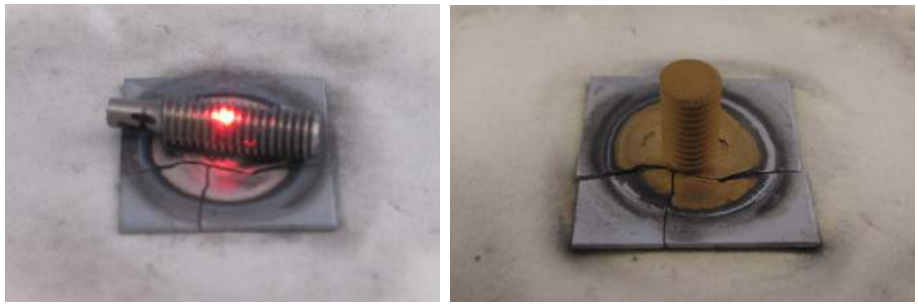

Figure 1. Examples of complex PM samples before and after gas nitriding at solar furnace.

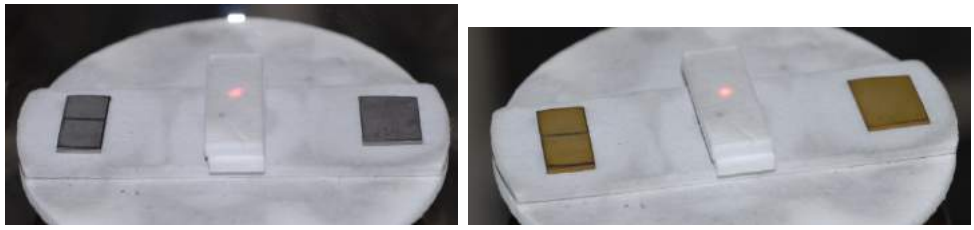

Figure 2. CP Ti Gr2 sheet samples before and after gas nitriding at solar furnace.

Figure 3. Vacuum/gas chamber used for gas nitriding (left) and sample with solar spot during experiment (right).

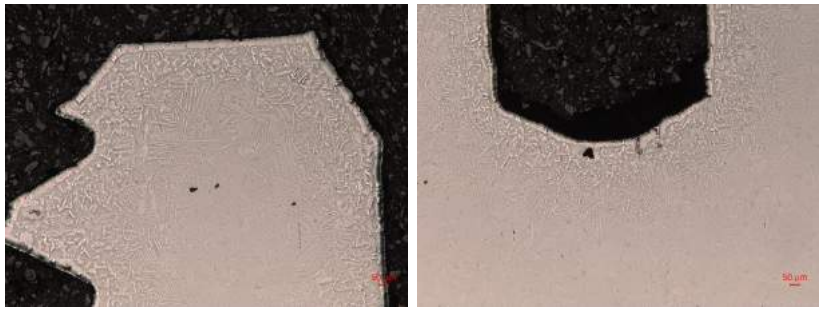

Figure 4. Microstructure of PM Ti sample gas nitrided at 750 °C for 5 minutes: left – thread with beginning of deep hole, right – bottom of the same deep hole (light microscopy).

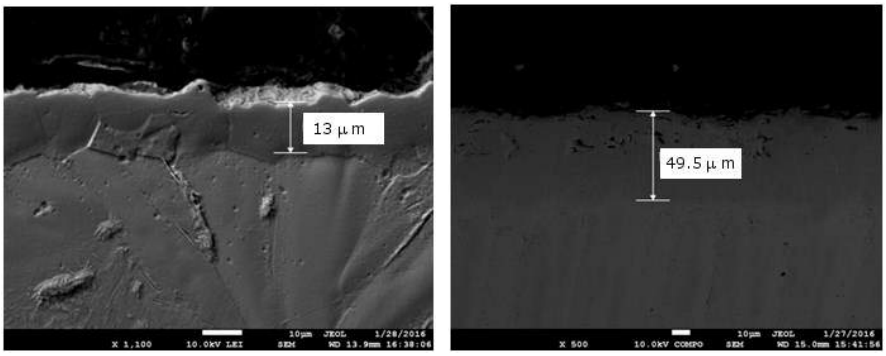

Figure 5. Microstructures of CP Ti Gr2 samples gas nitrided in solar furnace for 1 minute at 900 (left) and 1000°C (right) and corresponding thickness of created TiN layers (SEM).

The observed porosity can be probably explained by structural changes of nitrides inside of layer. The change in the microstructure is due to the volume transformations that occur during nitriding at increasing temperature and phase transformations between δ - TiN and ε - Ti_2N.

The first step for nitride formation involves nitrogen adsorption on metallic sites. However, nitrogen concentration profiles in the metal will be governed by diffusion laws depending on the crystallization state of the metal and on the temperature. When diffusion occurs in a polycrystalline Ti substrate, diffusion mostly proceeds along the grain boundaries. This lowers the activation barrier and enhances the diffusion coefficient. Due to the nitrogen concentration profiles into the matrix, the nitride formation will first take place on the substrate surface since the 33 % minimum nitrogen content will be reached first at this position. Once this concentration is reached the hexagonal crystal lattice of titanium changes towards the face centred cubic lattice of titanium nitride (NaCl type crystal) [11].

The compound layer is mainly composed of titanium nitrides Ti_2N and TiN, followed by a diffusion zone that consists of an interstitial solution of nitrogen in α or β titanium phases.

RTG analysis confirmed that both phase's δ - TiN and ε - Ti_2N are present on the surface of the investigated Ti samples. As the penetration depth is relatively small in the case of bulk solids the α-Ti peaks were not observed in this penetration depth, thus indicating the thickness of nitrides to be over 20 μm (see Fig. 6).

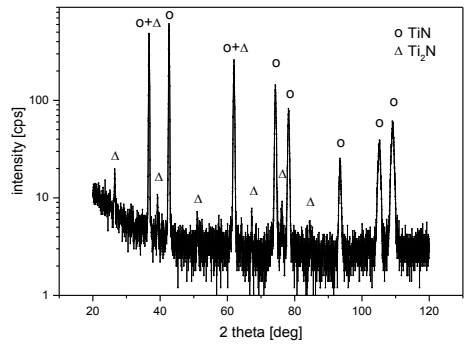

Figure 6. RTG analysis of CP Ti Gr2 sample gas nitrided in solar furnace for 1 minute at 900 °C.

Then nitrogen diffuses inward toward the metal substrate, forming a compound layer on the surface of the material (see Fig. 7). Herranz at el. [7] showed that this process with time leads in solar furnace to creation of double nitride layers with surface layer of TiN and subsequent layer of Ti_2N on TiAl4V substrate. In their observation upper TiN layer is also significantly porous.

Basically δ - TiN possesses cubic structure with volume of cell 76.3 x 10^6 particle per m^3, and density of 5.36 $g.cm^{-3}$. On the other hand ε - Ti_2N has tetragonal structure with volume of cell 74.19 x 10^6 particle per m^3, and density of 4.91 $g.cm^{-3}$. Thus rearranging of TiN phase into Ti_2N under the surface requires volumetric changes of layer. The new created phase occupies less volume, thus creating pores inside of layers. The pores tend to the surface to minimise surface energy, however the diffusion of nitrogen inside of materials changes local concentrations. This is evident especially at high temperatures (1000°C). For this reason it is recommended that nitriding must not exceed 980°C, since at higher temperatures the fragility of superficial layer increases rarely.

CP Ti Gr2 samples gas nitrided in solar furnace at 900 °C for 1 minute and 5 minutes showed significant changes of line profiles of nitrogen diffusion into the sample interior. As illustrates Fig. 7 for 1 minute of gas nitriding the significant diffusion is around 10 μm, however then the amount of diffused nitrogen remains almost constant with increasing distance from surface. On the contrary for 5 minutes the diffusion depth decreased down to 7 μm, however evident linear decrease of nitrogen concentration is observed with the increasing distance from the surface. As this temperature is just above α to β transition temperature of titanium, the most probably the diffusion of nitrogen is affected by α to β Ti phase transition and time of exposition.

For PM Ti samples gas nitrided in solar furnace at 750 °C for 5 minute the depth MHV0.2 profile of hardness indicates that nitrogen is already diffused over 500 μm inside of titanium sample. While the hardness of nitride layer on the sample surface is almost 883.9 MHV0.2 it finally decreases in the depth of sample down to 316.1 MHV0.2. Fig. 8 indicates also how the size of indentation is increasing with decreasing amount of nitrogen in titanium matrix.

For CP Ti Gr2 samples gas nitrided at 900 °C the following MHV values were observed: The as received sample has surface hardness of 230 ± 57 MHV1, the sample nitrided for 1 minute has surface hardness of 1190 ± 360 MHV1 and finally sample nitrided for 5 minutes has surface hardness of 2180 ± 810 MHV1. These results coincide with observed phases and microstructures in Fig. 5.

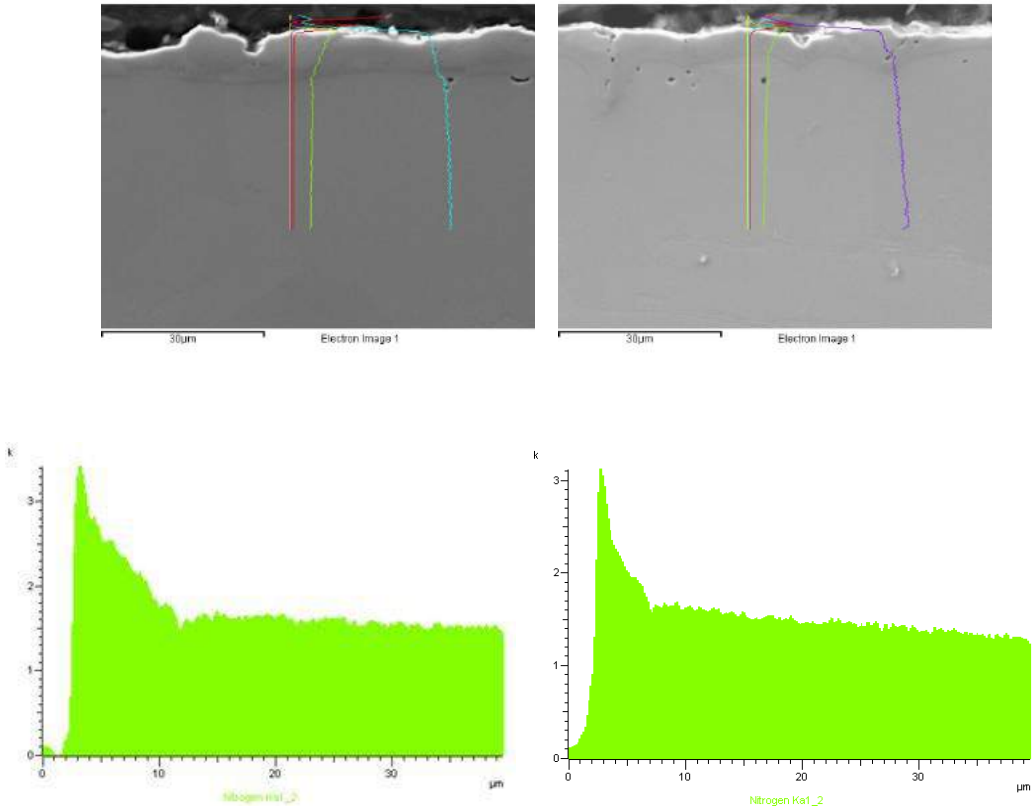

Figure 7. CP Ti Gr2 samples gas nitrided in solar furnace at 900 °C for 1 minute (left) and 5 minutes (right) and line profiles of nitrogen diffusion into the sample interior.

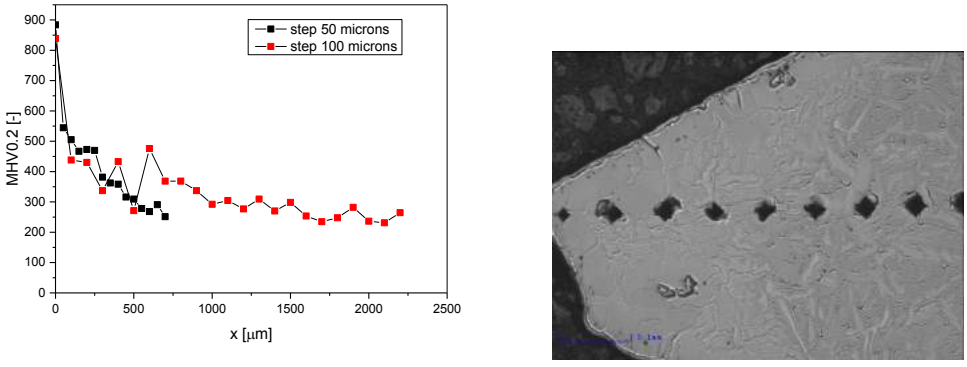

Figure 8. PM Ti sample gas nitrided in solar furnace at 750 °C for 5 minute: Depth profile of hardness due to titanium nitrides formation for various steps of measurement at the different places of samples. Right – an example of sample microstructure with indentation cones.

4. Conclusions

Gas nitriding of PM prepared Ti or CP Ti Gr2 samples at high temperature with concentrated solar energy were performed in nitrogen atmosphere. Gas nitriding of titanium was performed at various temperatures using 5kW vertical solar furnace at Plataforma Solar de Almeria, Tabernas, Spain. The solar process presents great advantages over the conventional treatments:

- It is clean and non-polluting high temperature process
- Significant decrease the heating time by the using of concentrated solar energy (100 K/minute)

- Creation of continuous nitride layer consisting of δ - TiN and ε - Ti_2N over all surfaces of samples
- Creation of a continuous and homogeneous surface nitride layer of high hardness of sample surface up to 2180 MHV1 with solar treatments for 5 minutes at 900 °C

The high number of hours of sunshine in a lot of world countries together with the shortness of the tests allows us to think of their industrial application.

Acknowledgements

Financial support by the Access to Research Infrastructures activity in the 7th Framework Programme of the EU (SFERA Grant Agreement n. 228296) is gratefully acknowledged. Financial support of the SFERA II project – Transnational Access activities (EU 7th Framework Programme Grant Agreement n° 312643) is also gratefully acknowledged. Slovak Grant Agency VEGA grant 2/0044/17 and SRDA agency grants APVV-14-0936 and APVV SK-PL-2015-0003 financial supports are gratefully acknowledged.

REFERENCES

[1] Strafford K.N., Towell, J.M., (1976), *The interaction of titanium and titanium alloys with nitrogen at elevated temperatures. I. The kinetics and mechanism of the titanium-nitrogen reaction.* Oxidation of Metals, Volume 10, Issue 1, p. 41–67

[2] Bell T., Bergmann H. W., Lanagan J., Morton P. H., Staines A. M., (1986), *Surface Engineering of Titanium with Nitrogen*, Surface Engineering, Vol. 2 No.2, p. 133-143

[3] de Souza G. B., de Silva B.A., Steudel G., et al., (2013), *Structural and tribo-mechanical characterization of nitrogen plasma treated titanium for bone implants*. Surface & Coatings Technology, Volume: 256, p. 30-36

[4] Shamsipur A., Kashani-Bozorg S.F., Zarei-Hanzaki A., (2013) *Production of in-situ hard Ti/TiN composite surface layers on CP-Ti using reactive friction stir processing under nitrogen environment.* Surface & Coatings Technology, Volume: 218, p. 62-70

[5] Sha W., Malinov S., (2009) *Nitriding: modelling of hardness profiles and the kinetics. Titanium Alloy: Modelling Of Microstructure, Properties And Applications*, Woodhead Publishing in Materials, Elsevier, p. 497-531

[6] Kováčik J., Baksa P., Emmer Š., (2016) *Electro spark deposition of TiB_2 layers on Ti6Al4V alloy*. Acta Metallurgica Slovaca, Vol. 22, No. 1, p. 52-59. ISSN 1338-1156

[7] Herranz G., Rodríguez G.P., Alonso R., (2011), *Comportamiento frente al desgaste de la aleación Ti6Al4V nitrurada con energía solar concentrada.* In *XVIII Congreso Nacional De Ingeniería Mecánica*, Intl. Federation for the Promotion of Mechanism and Machine Science, Curran Associates, Inc., Red Hook, USA, pp. 729 - 732 (in Spanish), ISBN 9781617827761

[8] Balog M., Viskic J., Krizik P., Schauperl Z., Snajdar M., Stanec Z., Catic A.,(2016), *CP Ti fabricated by low temperature extrusion of HDH powder: application in dentistry*, Key Eng. Mater. 704, p. 351 -359

[9] Rodríguez J., Cañadas I., Zarza E., (2013), *PSA vertical axis solar furnace SF5*, Energy Procedia, 49, p. 1511-1522

[10] Kováčik J., Emmer Š., Rodríguez J., Cañadas I., (2017), *Sintering of HDH Ti powder in a solar furnace at Plataforma Solar de Almeria.* Journal of Alloys and Compounds, Vol. 695, p. 52-59

[11] Scardi P., Tesi B., Bacci T., Gianoglio C., (1990), *Characterization Of Ion-Nitrided Titanium Layers By Means Of X-Ray Microdiffractometry,* Surface and Coatings Technology, Vol. 41, p. 83 - 91

ISSN 1847-7917

Electrical conductivity and mechanical properties of the solid state recycled EN AW 6082 alloy

Jure KROLO*, *Branimir LELA
Petar LJUMOVIĆ
University of Split, Faculty of Electrical Engineering, Mechanical Engineering and Naval Architecture, Department for Production Engineering
Sveučilište u Splitu, Fakultet elektrotehnike, strojarstva i brodogradnje, R. Boskovica 32, 21 000 Split, Croatia
jkrolo@fesb.hr
blela@fesb.hr
petarlj@fesb.hr

Keywords
Solid state recycling
Aluminum
Severe plastic deformation
Electrical conductivity

Ključne riječi
Recikliranje u čvrstom stanju
Aluminij
Velika plastična deformacija
Električna provodljivost

Original scientific paper
Abstract: In the last few years there is a demand for the new technologies development in order to increase scrap reuse potential and CO_2 emission savings. This paper deals with novel aluminum recycling process using severe plastic deformation (SPD). Aluminum was recycled from machined chips without any remelting (solid state recycling-SSR) in order to reduce environmental pollution and to increase material yield during the process. Machined chips were cleaned, compacted and hot extruded. After hot extrusion semi-finished product (aluminum bar) was processed with equal channel angular pressing (ECAP) in order to improve mechanical properties and electrical conductivity. ECAP process temperature and the number of recycled samples pass through tool where varied. After SSR process electrical conductivity and mechanical properties of recycled samples were evaluated. The efficiency of the SSR process was confirmed and quality recycled samples were produced.

Izvorni znanstveni rad
Sažetak: Posljednjih godina postoji potreba za razvijanje novih tehnologija s ciljem povećanja potencijala ponovne upotrebe otpada i smanjenja emisije CO_2. Ovaj rad se bavi inovativnom tehnologijom recikliranja aluminija koristeći veliku plastičnu deformaciju (engl. "severe plastic deformation"-SPD). Aluminij je recikliran iz odvojene čestice bez pretaljivanja (recikliranje u čvrstom stanju, engl. solid state recycling- SSR) s ciljem smanjenja zagađenja okoliša i povećanjem iskorištenja materijala tokom procesa. Odvojene čestice su očišćene, sabijene i istisnute u toplom stanju. Nakon istiskivanja u toplom stanju, polu-proizvod (aluminijska šipka) je obrađen s kutnim kanalnim istiskivanjem (engl. "equal channel angular pressing"-ECAP) s ciljem poboljšanja mehaničkih svojstva i električne provodljivosti. Temperatura ECAP procesa i broj prolaza recikliranih uzoraka kroz alat su varirani. Nakon SSR procesa električna provodljivost i mehanička svojstva recikliranih uzoraka su određena. Učinkovitost SSR procesa je potvrđena i dobiveni su kvalitetni reciklirani uzorci.

1. Introduction

In the last few years there is a demand for development new technologies in order to increase scrap reuse potential and emission savings [1]. Aluminum is second most recycled metal and it is of the main importance for further development in aluminum recycling technology. In this paper aluminum recycling without remelting was used, so called solid state recycling (SSR). The main difference compared with conventional recycling is in energy and material savings. High metal reactivity and material losses are responsible for lower material yield in conventional recycling process [1-2]. Usually, machining chips are recycled by SSR process.
Nevertheless, sheet, foils or wire could also be recycled. The most used method for SSR is hot extrusion, but lately severe plastic deformation processes are utilized in order to improve recycled samples mechanical properties. Some of the used processe are: incremental equal channel angular pressing (iECAP) integrated into hot extrusion [3], high pressure torsion (HPT) [4], friction stir extrusion (FSE)[5].
It has been shown by various authors that if all necessary conditions are fulfilled quality recycled samples can be obtained via solid state recycling route. These conditions are the combination of high temperature, plastic deformation and pressure [6]. Other authors have developed the mathematical model to describe influence on metal material solid bonding and according to the model high temperature, increase in normal contact stress, shear stress and strain lead to better material bonding [7].
In this paper, solid state recycling was performed by the combination of direct hot extrusion (DE) and following ECAP process. Mechanical and physical properties (electrical conductivity) are compared after DE and also after combination DE+ECAP. However, ECAP was

performed at various process parameters in order to evaluate process influence on SSR samples quality. Usually, researchers have investigated mechanical properties of SSR samples, microstructure and density. [8]. According to literature review, electrical conductivity of SSR samples was not investigated. The Al-Mg-Si alloys (6xxx) have been widely used as conductors due to the good combination of strength and electrical properties compared with other Al alloys [9]. Selected metal for this research is relatively new alloy EN AW 6082 due to excellent behavior during machining process.

Production of Al-Mg-Si wires usually include thermo-mechanical processing which consist of solution treatment, water quenching and cold drawing into wires. Following this procedure second-phase precipitates Mg_2Si are formed in the grain interior. Such microstructure show enhanced precipitation hardening and electrical conductivity slightly increment. The reason for such material behavior is explained as a result of partial purification of the Al matrix from Mg and Si solute atoms since the solute atoms dissolved in the matrix and Guinier-Preston (GP) zones are responsible for the determinal effect on electrical conductivity [9-10]. Usually, well-known Matthiessen's rule [10] is used to describe electrical resistivity (ρ) dependence on several microstructural features:

$$\rho=\rho_0 +\Delta\rho_S+\Delta\rho_P+\Delta\rho_V+\Delta\rho_D+\Delta\rho_B \quad (1)$$

ρ_0 describe resistivity of pure solvent metal and $\Delta\rho$ stand for the increase in electrical resistivity due to atoms in solid solution (S), precipitates (P), vacancies (V), dislocation (D) and grain boundaries (B). Electrical resistivity is the inverse value of the electrical conductivity. Good combination of mechanical and physical properties has always been a great challenge for electric conductors production. Lately, , the number of attempts increases in order to produce electrically conductive materials with high strength by severe plastic deformation approach without any electrical conductivity decrement [9-13].

With this approach, SPD is used to refine microstructure to ultra-fine grain structure (UFG), while SPD at elevated temperature cause decomposition of solid solution and formation of nano-sized second phase precipitates via dynamic aging. UFG materials with second phase precipitates can have high mechanical properties, but also enhanced electrical conductivity due to the very low content of solute atoms and absence of GP zones in Al matrix. These nano-sized precipitate have been identified as β'- Mg_2Si, and they are formed during SPD processing of Al-Mg-Si aluminum alloy at elevated temperatures [11-13].

The main aim of this paper is to show the possibility to produce material with good mechanical properties from small metal waste and with good electrical conductivity by solid state recycling process utilizing severe plastic deformation.

2. Experimental procedure

In order to investigate the possibility of EN AW 6082 alloy recycling via SSR recycling route, direct hot extrusion (DE) in combination with ECAP process was utilized. Chemical composition of selected aluminum alloy EN AW 6082 : 0,7-1,3 % Si, 0-0,5% Fe, 0-0,1% Cu, 0,4-0,1 % Mn, 0,6-1,2 % Mg, 0-0,25% Cr, 0-0,2% Zn, 0-0,1% Ti, Other 0-0,1%.

Metal waste in form of machined chips from milling and turning are taken from the real industrial manufacturing process. There were few steps to perform SSR route:

- Cleaning of contaminated machined chips by the ultrasonic bath at temperature of 60°C in a time of 20 min utilizing universal detergent, Fig. 1b.
- Briquetting of machined chips into 38 mm diameter and 70 mm high briquettes with 300 kN force, Fig. 1a.
- Briquettes preheating in a time of 30 min on extrusion temperature and direct hot extrusion at 400 °C and 450°C with 7.11 extrusion ratio.
- ECAP processing of the extruded bars with 15 mm diameter at three temperatures: 20°C, 160°C and 300°C. At 20°C and 160°C 1 and 3 passes were applied, while at 300 °C only one pass was applied.

a b

Figure 1. a) Chips cleaning utilizing ultrasonic bath b) Machined chips briquetting phase

Figure 1. a) Čišćenje odvojene čestice ultrazvučnom kupkom b) Faza briketiranja odvojenih čestica

Force measurement during briquetting phase was achieved utilizing HBM load cell C6A 1MN. After SSR route (DE+ECAP) mechanical properties and electrical conductivity of all obtained samples were evaluated. Properties of recycled samples obtained only with DE are also evaluated and compared with referent values of extruded bar from manufacturer in O (annealed), T4 (solution heat treated and naturally aged) and T6 (solution heat treated and artificially aged) temper conditions. Systematized overview for all 7 solid state recycling processing routes is given in Tab. 1, as well as mechanical and physical properties of recycled samples.

Table 1. Mechanical and physical properties of solid state recycled samples

Tablica 1. Mehanička i fizička svojstva reckliranih uzorka u čvrstom stanju

Properties of solid state recycled samples obtained utilizing DE+ECAP route							
Sample	ECAP temperature [°C]	ECAP pass	DE temperature [°C]	σ_{UTS} [MPa]	$\sigma_{0,2\%}$ [MPa]	δ [%]	IACS [%]
1	300	1	450	139,7	73	31,3	47,48
2	160	1	400	174,7	127	23,8	46,05
3	160	3	450	174,6	144	18,3	46,54
4	20	1	450	249,4	236	8,2	43,80
5	20	3	400	265,9	227	10	44,01
Properties of solid state recycled samples obtained utilizing DE route							
Sample	DE temperature [°C]	σ_{UTS} [MPa]	$\sigma_{0,2\%}$ [MPa]	δ [%]		IACS [%]	
6	400	150	91	24,3		43,05	
7	450	160	101	24,6		44,5	
Conventionally produced EN AW 6082 extruded bar properties							
	State	σ_{UTS} [MPa]	$\sigma_{0,2\%}$ [MPa]	δ [%]		IACS [%]	
	O	≤160	≤110	≥14		/	
	T4	≥205	≥110	≥14		42	
	T6	≥295	≥250	≥8		44	

In Tab. 1 σ_{UTS} stands for ultimate tensile strength (UTS), $\sigma_{0,2\%}$ stands for yield strength, δ stands for elongation and % IACS is the unit for electrical conductivity. Fig. 2a shows utilized ECAP tool and Fig. 2b shows obtained recycled samples after the process. The main goal of the ECAP process is to introduce notable plastic strain into the material and to refine microstructure. Tool geometry in ECAP process is mainly defined by two angles, inner die angle ϕ and outer die angle ψ. Iwahashi et al. [14] established simple analytical approach according to which plastic shear strain γ in the shear zone determined by the outer corner angle is function of the die angles ϕ and ψ:

$$\gamma = 2\cot\left(\frac{\phi}{2}+\frac{\psi}{2}\right)+\psi\,\mathrm{cosec}\left(\frac{\phi}{2}+\frac{\psi}{2}\right) \qquad (2)$$

ECAP tool in this work have inner die corner angle value 90°, and outer die angle 12° defined with 3 mm radius. The diameter of the ECAP tool channel is 15.1 mm. The lubrication used on room temperature and 160 °C was graphite grease, while on 300°C lubrication based on Mo_2S was utilized. Temperature measurement was taken with K-type thermocouple probe and regulation was achieved using HOTSET cartridge heaters and PID controller. Every sample was preheated 10 min inside ECAP tool and 10 min after channel pass. ECAP was performed by pressing one sample on the other in order to achieve semi-continuous process.

Mechanical testing was performed according to the ASTM E8 standard for metal material tensile testing. The used device was "Instron 8801" 5 kN universal machine, Fig. 4a. Tensile specimens were prepared with gauge original length 11 mm and diameter 2.5 mm.

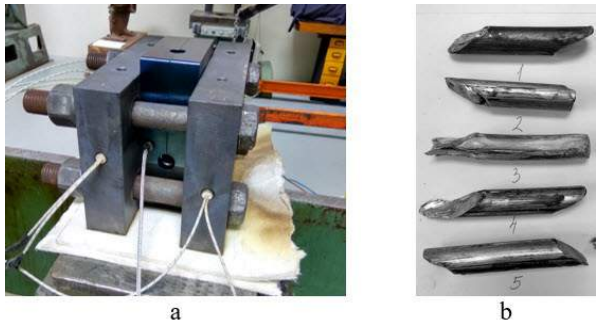

a b

Figure 2. a) ECAP tool b) Recycled samples (DE+ECAP),

Slika 2. a) ECAP alat, b) Reciklirani uzorci (DE+ECAP)

Samples were machined from the central part of the recycled samples in order to obtain homogeneous microstructure. Tensile testing was performed at room temperature and initial strain rate was $1.8 \cdot 10^{-3}$ s^{-1}. Fig. 3a shows engineering stress vs. engineering strain diagrams for all 7 solid state recycled samples. Tensile samples after testing are presented in Fig. 3b. The electrical conductivity of the alloy was measured at room temperature using the eddy current method on Olympus NORTEC 600C device according to the ASTM E 1004 standards, Fig. 4b. The electrical conductivity was expressed as IACS (%) unit, which stands for International Annealed Cooper Standard. At least 20 electrical conductivity measurements were taken for each sample and the arithmetic value was taken as the final value.

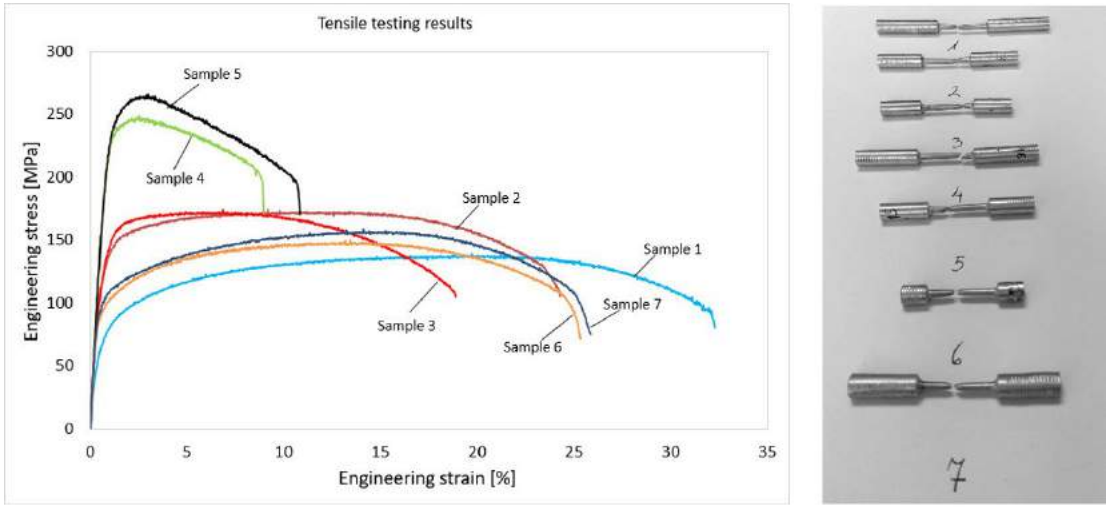

Figure 3. a) Engineering stress vs. engineering strain b) Samples after tensile testing
Slika 3. a) Dijagram naprezanje u odnosu na relativno produljenje b) Uzorci nakon vlačnog testiranja

Figure 4. a) Universal tensile testing machine ''Instron 8801'' b) Eddy current measuring device
Slika 4. a) Univerzalna vlačna kidalica ''Instron 8801'' b) Uređaj za mjerenje vrtložnim strujama

3. Results and analysis

After experiments, obtained results for the ultimate tensile strength are in the range from 139,7 MPa to 265,9 MPa, elongation is in the range from 8,2 % to 31,3% and yield strength is in the range 73 MPa to 227 MPa. These properties are achieved without any additional heat treatment, such as artificial aging.

Specimens that were recycled only by hot extrusion have similar UTS (sample 6 UTS=150 MPa and sample 7 UTS= 160 MPa) as EN AW 6082 aluminum alloy in annealed condition (O), Tab. 1. However for both mentioned recycled samples elongation seems to be twice of the minimum elongation for annealed EN AW 6082, Tab. 1. However electrical conductivity (EC) of the recycled samples is 43,05% IACS (sample 6) and 44,5% IACS (sample 7) which is closer to EN AW 6082 in T6 temper (44% IACS).

According to the results, electrical conductivity can be increased by ECAP procedure at elevated temperature (300 °C) and for sample 1 EC is 47.48% IACS. However, UTS and YS are low, 139.7 MPa and 73 MPa, respectively, while elongation is, 31.3%.

In order to increase recycled samples quality and mechanical properties, some of the samples are processed with ECAP tool at room temperature. For samples 4 and 5 UTS is 249.4 MPa and 265.9 MPa, respectively. These values are much higher than EN AW 6082 in T4 temper and little lower than mentioned alloy in T6 temper, Tab 1. Sample 4 and 5 have EC 43.80% IACS and 44.01% IACS, respectively. YS for sample 4 and 5 is 236 MPa and 227 MPa, respectively. This means an increase for 114% in YS for sample 4 and 106% for sample 5 compared with EN AW 6082 in T4 temper. Sample 5 also have 25% higher elongation than EN AW 6082 in T6 temper. Sample 2 and 3 after hot extrusion are processed with ECAP tool at 160 °C and UTS is 174.7

MPa and 174.6 MPa, respectively. The electrical conductivity of sample 2 and 3 is 46.05% IACS and 46.54% IACA, respectively. This means enhanced EC compared with EN AW 6082 in T6 and T4 temper, Fig. 5c. Despite lower UTS than EN AW 6082 in T4 and T6 temper, elongations are much higher while for samples 2 and 3 they are 23.8% and 18.3%, respectively. YS compared with minimum listed value EN AW 6082 in T4 temper is increased for 15% and 30% for samples 2 and 3, respectively.

Fig. 5a show values of electrical conductivity compared with UTS, Fig. 5b shows values of EC compared with YS and Fig. 5c shows values of EC compared with elongation for 7 SSR samples. .

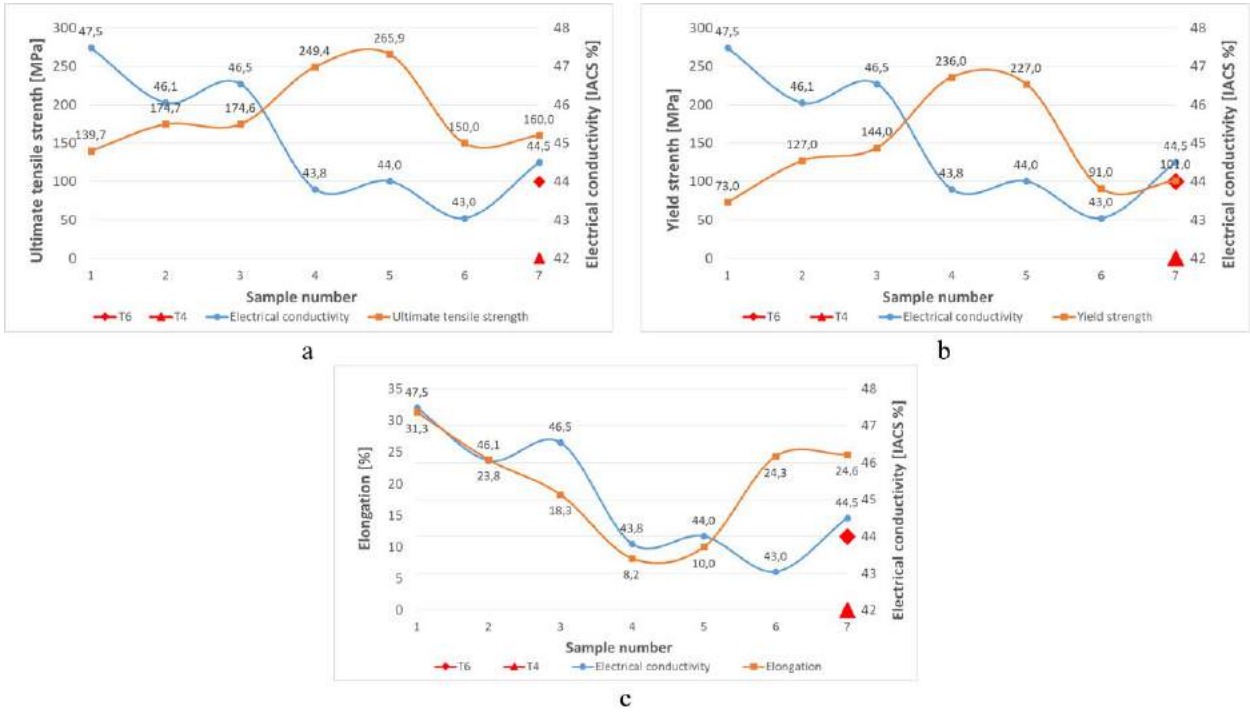

Figure 5. a) Ultimate tensile strength and electrical conductivity for 7 SSR samples b) Yield strength and electrical conductivity for 7 SSR samples c) Elongation and. electrical conductivity for 7 SSR samples

Slika 5. a) Vlačna čvrstoća i električna provodljivost 7 uzoraka recikliranih u čvrstom stanju b) Granica razvlačenja i električna provodljivost 7 uzoraka recikliranih u čvrstom stanju c) Elongacija i električna provodljivost 7 uzoraka recikliranih u čvrstom stanju

According to Fig. 5a and Fig. 5b it can be clearly indicated that with increase in ultimate tensile and yield strength electrical conductivity decrease. On the other hand with elongation decrement, electrical conductivity decrease, except for samples recycled only with DE, Fig. 5c. However, samples processes only with DE have lower YS and UTS, without any EC increment, Fig. 5a and 5b.

The attention should be at sample 2 and 3, which have considerably higher UTS and YS and enhanced electrical conductivity compared with EN AW 6082 in T4 and T6 temper. Electrical conductivity and mechanical properties are increased compared with samples 6 and 7. This indicates that with severe plastic approach quality SSR samples can be obtained and with enhanced electrical conductivity. Furthermore, additional improvement in UTS and YS are showed for samples 4 and 5, without any EC properties degradation.

Finally, due to a large number of influential parameters and their interaction further optimization of the SSR process should be performed in order to achieve even better combination of mechanical and physical properties.

4. Conclusion

According to this investigation, solid state recycling of EN AW 6082 alloy can be successfully and effectively performed by the combination of DE and ECAP process. Obtained recycled samples have an excellent combination of mechanical and physical properties without any remelting phase, which means low energy consumption. Manipulation of recycled samples properties can be easily achieved by changing process parameters. Following conclusion can be drawn:

- Improvement of mechanical properties and physical properties of SSR samples produced only with DE can be achieved by additional SPD utilizing ECAP process.

- Samples processed with DE+ECAP at room temperature have enhanced UTS and YS, without any heat treatment, while EC remains high. Sample 5 has 10% lower UTS and 9% lower YS compared with EN AW 6082 in T6 conditions, while elongation is 25% higher and electrical conductivity is equal. However, only 3 pass through ECAP were performed. Increase in pass number should result with higher mechanical properties.
- Samples processed with DE+ECAP at 160°C have an excellent combination of mechanical properties and EC. Sample 3 has higher YS, elongation and EC than minimum listed values of EN AW 6082 aluminum alloy at T4 temper for 30%, 30.7% and 10.8%, respectively. However, UTS is 15% lower.
- Samples processed with DE and ECAP at 300 °C have 47.48% IACS. However, UTS and YS are 139.7 MPa and 73 MPa, respectively, while elongation is very high, 31.3%.

Finally, further investigation directions for solid state recycling should be based on severe plastic deformation approach with DE and ECAP at the temperature range between 100° and 200°C in order to optimize dynamic recrystallization influence on physical and mechanical properties. Except electrical conductivity, it is very important to determine recycled samples density, metallography and microstructure. Investigation of additional heat treatment on mechanical properties and especially physical properties should also be included.

REFERENCES

[1] Duflou, J.R., Tekkaya, A.E., Haase, M., Welo, T., Vam,eemsel, K., Kellens, K., Dewulf, W., Paraskevas, D., (2015), *Environmental assessment of solid state recycling routes for aluminium alloys: Can solid state processes significantly reduce the environmental impact of aluminium recycling?*, CIRP Annals- Manufacturing Technology, Vol. 64, pp. 37-40.

[2] Gronostajski, J., Marciniak, H., Matuszak, A., (2000), *New methods of aluminium and aluminium-alloy chips recycling,* Journal of Materials Processing Technology, 106, pp. 34-39.

[3] Haase, M., Ben Khalifa, N., Tekkaya, A.E., W.Z., Misiolek, (2012), *Improving mechanical properties of chip-based aluminum extrudates by integrated extrusion and equal channel angular pressing (iECAP)*, Materials Science and Engineering A, 539, pp. 194–204.

[4] Mohamed Ibrahim, A.E.A., Eun Yoo, Y., Hyoung S.K., (2013), *Recycling of AlSi8Cu3 alloy chips via high pressure torsion,* Materials Science & Engineering A, 560, pp. 121–128.

[5] Tang, W. , Reynolds, A.P., (2010), *Production of wire via friction extrusion of aluminum alloy machining chips,* Journal of Materials Processing Technology, Vol. 210, pp. 2231–2237.

[6] Tekkaya, A.E, Schikorra, M., Becker, D., Biermann, D., Hammer, N., Pantke,K., (2009), *Hot profile extrusion of AA-6060 aluminum chips*, journal of materials processing technology, Vol. 209, pp. 3343–3350.

[7] Cooper, D.R., Allwood, J.M., (2014), *The influence of deformation conditions in solid-state aluminium welding processes on the resulting weld strength*, Journal of Materials Processing Technology, Vol. 214, pp. 2576–2592.

[8] Shamsudin, S., Lajis, M.A., Zhong Z.W., (2016), *Solid-state recycling of light metals: A review*, Advances in Mechanical Engineering, Vol. 8(8), pp. 1–23.

[9] Valiev, R.Z., Murashkin, Y.M., Sabirov, I., (2014), *A nanostructural design to produce high-strength Al alloys with enhanced electrical conductivity*, Scripta Materialia, Vol. 76, pp. 13-16.

[10] Lipińska,. M., Bazarnik, P., Lewandowska, M., (2016), *The influence of severe plastic deformation processes on electrical conductivity of commercially pure aluminium and 5483 aluminium alloy,* archives of civil and mechanical engineering, Vol. 16, pp. 717-723.

[11] Murashkin, M., Medvedev, A., Kazykhanov, V., Krokhin, A., Raab, G., Enikeev, N., Valiev, R.Z., (2015), *Enhanced Mechanical Properties and Electrical Conductivity in Ultrafine-Grained Al 6101 Alloy Processed via ECAP-Conform,* Metals 2015, Vol. 5(4), pp. 2148-2164.

[12] Murashkin. M.Y., Sabirov I., Kazykhanov, V.U., Bobruk, E.V., Dubravina A.A., Valiev, R.Z., (2013), *Enhanced mechanical properties and electrical conductivity in ultrafine-grained Al alloy processed via ECAP-PC*, Journal of Material Science, Vol. 48, pp. 4501–4509.

[13] Sauvage, X., E.V., Bobruk, Murashkin, M.Yu, Nasedkina, Y., Enikeev, N.A., Valiev, R.Z., (2015), *Optimization of electrical conductivity and strength combination by structure design at the nanoscale in Al–Mg–Si alloys*, Acta Materialia, Vol. 98, pp. 355–366.

[14] Iwahashi Y., Wang J., Horita Z., Nemoto M., Langdon T.G. (1996), *Principle of equal-channel angular pressing for the processing of ultra-fine grained materials*, Scripta Materialia, Vol. 35, pp. 143-146.

ISSN 1847-7917

Performance analysis of the RFID-enabled Manufacturing Execution System

Marko MLADINEO, Ivica VEZA Slavica JURCEVIC, Ivan ZNAOR
University of Split, Faculty of Electrical Engineering, Mechanical Engineering and Naval Architecture
Sveučilište u Splitu, Fakultet elektrotehnike, strojarstva i brodogradnje
R. Boskovica 32, 21000 Split, **Croatia**
mmladine@fesb.hr
iveza@fesb.hr
sjurce00@fesb.hr
iznaor@fesb.hr

Keywords
Industry 4.0
RFID
Manufacturing Execution System

Ključne riječi
Industrija 4.0
RFID
Sustav za praćenje izvršavanja proizvodnje

Original scientific paper
Abstract: New industrial revolution, called Industry 4.0, is based on the evolution of information-communication technology. One of significant possibilities is to track manufacturing execution by using the RFID (radio-frequency identification) system, creating a system called RFID-enabled Manufacturing Execution System. RFID technology enables, not just identification of some product like bar-code technology, but it enables writing the data on the RFID tag attached to the product. Data about process times, ERP product data, or similar. This kind of live tracking of manufacturing execution can significantly improve production planning, especially for the small-lot and single-item production. However, RFID technology has its limitations, also. In this research, a performance of the industrial RFD system has been experimentally tested regarding the speed of passing near antenna and the distance from the antenna. Presented results give guidelines for the design of the workplace, based on Industry 4.0 principles, regarding the limitation of the RFID system.

Izvorni znanstveni članak
Sažetak: Nova industrijska revolucija, nazvana Industrija 4.0, utemeljena je na napretku informacijsko-komunikacijske tehnologije. Jedna od značajnih mogućnosti je praćenje proizvodnje pomoću RFID („radio-frequency identification") sustava, stvarajući sustav koji se naziva „RFID-enabled Manufacturing Execution System". RFID tehnologija omogućuje, ne samo očitavanje proizvoda kao kod „bar-kod" tehnologije, već i zapisivanje podataka na „RFID tag" koji se nalazi na proizvodu. Podataka kao što su vremena procesa, podaci o proizvodu iz ERP-a, i slično. Takvo praćenje proizvodnje „uživo" može uvelike unaprijediti planiranje proizvodnje, pogotovo kod malo-serijske i jedno-komadne proizvodnje. Međutim, RFID tehnologija ima i svoja ograničenja. U ovom istraživanju eksperimentalno je testirana učinkovitost industrijskog RFID sustava s obzirom na brzinu prolaska kroz polje antene, kao i s obzirom na udaljenost od antene. Predstavljeni rezultati daju smjernice za dizajn radnog mjesta, utemeljenog na principima Industrije 4.0, s obzirom na ograničenja RFID sustava.

1. Introduction

1.1. Smart Factory

The introduction of the Information-Communication Technology together with Internet of Things and Services into the manufacturing environment has started fourth industrial revolution (Figure 1), called Industry 4.0 [1]. This new type of industry is based on Smart Factory model. The Smart Factory has a completely new approach to production: smart products are uniquely identifiable, may be located at all times and know their own history, current status and alternative routes to achieving their target state [1]. Smart Factories allow individual customer requirements to be met and makes single-item production profitable. To achieve this an enterprise must become 'smart', i.e. it must incorporate its machinery, warehousing systems and production facilities in the shape of Cyber-Physical System.

The Cyber-Physical System of Smart Factory is crucial to support new business models for manufacturers called: Manufacturing-as-a-Service [2], Industrial Product-Service Systems [3] [4], or similar. Idea of Industrial Product-Service Systems is extended product [3], i.e. product and service integrated into single product for delivering value in use to the customer during the whole life cycle of a product [5]. However, the idea of Manufacturing-as-a-Service is to transform manufacturer of product or part to manufacturing service provider. Both business models incorporate services into manufacturing enterprises [4], and both require usage of state-of-the-art ICT. Because of that these models can only function around a Cloud computing service or Internet portal.

These new paradigms result with single-item production in most of the cases. Hence, the importance of ICT

integration into enterprise's processes and organization is crucial [7].
Products are unique (single-item), therefore they need to be identifiable, may be located at all times and know their own history, current status and alternative routes to achieving customer [1].

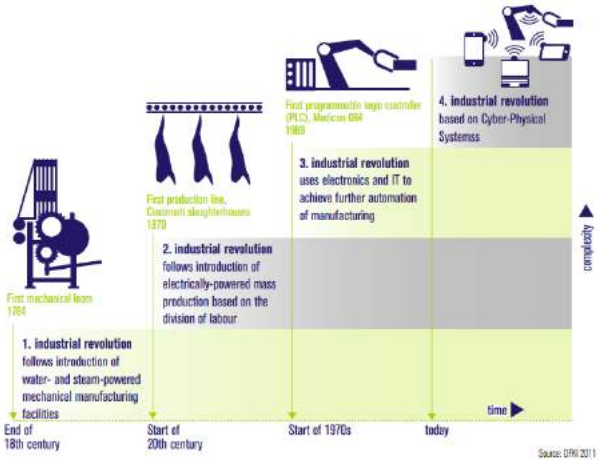

Figure 1. The four stages of the Industrial Revolution [5]
Slika 1. Četiri razdoblja industrijske revolucije [5]

The technology that can enable these requirements is radio-frequency identification (RFID) technology. This technology is based on RFID tags for storing data in their memory, and RFID antennas to read data from the tag or write data to the tag. RFID technology is already well-known technology, therefore it could be implemented into Manufacturing Execution System (MES) with ease [8], thus creating RFID-enabled Manufacturing Execution System [9]. This kind of live tracking of manufacturing execution connected with Enterprise Resource Planning (ERP) system can significantly improve production planning, especially for the small-lot and single-item production, making them more profitable [1].

1.2. RFID-enabled Manufacturing Execution System

Manufacturing data collection, or real-time tracking, was emerging in the era of Computer Integrated Manufacturing (CIM), mostly based on the bar-code technology. In order to facilitate the real-time data collection, RFID technology has been proposed. Since RFID technology has lot of advantages over bar-code technology, like [10] longer reading distance, larger data storage, and possibility to write date instead of read-only data, the RFID-enabled Manufacturing Execution System were born.
The main aim of RFID-enabled Manufacturing Execution System is to have real-time manufacturing execution data, i.e. to have Real-time MES. However, the MES must be seen as an extended framework, that goes beyond MES itself, consisting of a different layers (Figure 2) that are used to ensure information flow from the shop-floor to the production planning. Therefore, the main layers of the Real-time MES that create MES framework are [10]:

- shop-floor layer,
- MES layer,
- interface layer,
- decision-making layer.

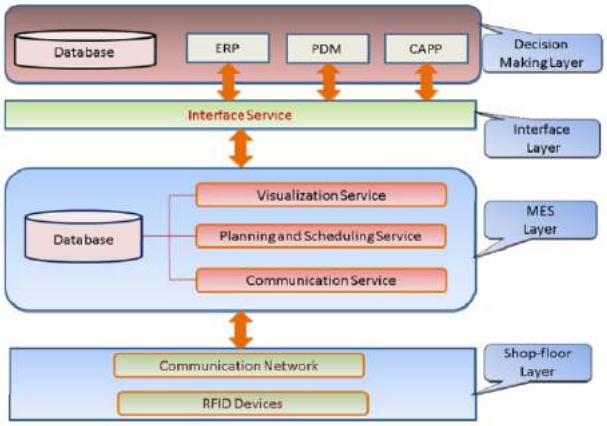

Figure 2. Real-time MES framework [10]
Slika 2. Okvir „Real-time MES" koncepta [10]

The shop-floor layer includes various hardware devices: RFID readers, RFID tags, and other communication devices like WiFi network, or similar. MES layer contains three core services: communication service, planning and scheduling service, and visualization service. Interface layer is an interface service that is aiming at real-time intercommunicating with other enterprise systems, with ERP in general. At last, decision-making layer consist of the information systems: ERP, Resources Planning), PDM (Product Data Management), and CAPP (Computer-aided Process Planning). These information systems are used for decision-making in planning and scheduling.
The Real-time MES framework forms a closed-loop by enabling information flow from down level, where f RFID devices are used to collect real-time manufacturing data, to the top level, i.e. to the ERP system. Furthermor, sometimes PDM, CAPP and other information systems are seen as a part of ERP. However, MES cannot be seen as a part of EPR, nor it is completely subordinated to EPR. MES is overlapping with ERP, because it gives an insight into real-time manufacturing execution. If the manufacturing plans are not executed as planned, it triggers replaning and decision-making affecting the changes in ERP and other information system.
To conclude, RFID-enabled MES can serve as an very good ICT platform to support new manufacturing challenges drived by Industry 4.0. However, RFID tehcnology has its limitations, so in this research a performance analysis of the RFID-enabled Manufacturing Execution System has been made and some conclusions and suggestions are proposed.

2. Performance analysis of the RFID-enabled MES

2.1. Methodology

The aim of this research was to test the performance of the industrial RFID system (from TURCK Company) in a case of manual assembly workstation. Manual assembly is specific, because worker and the part are out of the range of the RFID antenna. Therefore, worker needs to bring the RFID tag, attached to the part, near RFID antenna to read or write some data on it. However, it takes some time to read or write data to the RFID tag, so the worker must not do it too fast.

So, the following methodology was proposed to analyze the performance of the RFID system:

- collecting the data about the read/write speed and distance of the RFID antenna and RFID tags using the simulator (from TURCK Company);
- measuring of how fast worker moves the RFID tag over the RFID antenna;
- comparison of the worker's data with the RFID antenna's data.

The official TURCK Company's RFID system simulator was used to collect the data about the read/write speed and distance of the RFID antenna and RFID tags. One type (13,56 MHz) of the RFID antenna was used (TN-M30-H1147) and two types of RFID tags were used: EEPROM memory type (TW-R16-B128) with capacity of 128 bytes and FRAM memory type (TW-R20-K2) with capacity of 2048 bytes. The RFID equipment is presented on Figure 3, and three different sets of experiments, made in this research, are presented on Figure 4.

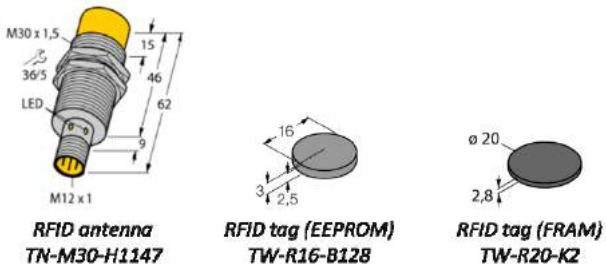

Figure 3. RFID equipment used in the experiments

Slika 3. RFID oprema korištena u eksperimentima

Figure 4. Simulation of the RFID antenna performance for three different sets of experiments:
a) EEPROM type RFID tag experiments with constant data quantity and variable distance from the antenna
b) FRAM type RFID tag experiments with constant data quantity and variable distance from the antenna
c) FRAM type RFID tag experiments with variable data quantity and variable distance from the antenna

Slika 4. Simulacija učinkovitosti RFID antene za tri različita skupa eksperimenata:
a) Eksperimenti EEPROM vrste RFID tag-a s konstantnom količinom podataka i varijabilnom udaljenošću od antene
b) Eksperimenti FRAM vrste RFID tag-a s konstantnom količinom podataka i varijabilnom udaljenošću od antene
c) Eksperimenti FRAM vrste RFID tag-a s varijabilnom količinom podataka i varijabilnom udaljenošću od antene

First set of experiments was with EEPROM type RFID tag: the data quantity was constant (20 bytes) and six variations of the distance from antenna were used. EEPROM type has different read and write speed, therefore different maximal speeds were determined (Figure 5). The maximum speed of 1,09 m/s for reading the 20 bytes of data was achieved on the 20 mm distance from the antenna. However, the maximum speed for writing the 20 bytes of data on the same 20 mm distance is 0,73 m/s.

Second set of experiments was with FRAM type RFID tag: the data quantity was constant (20 bytes) and six variations of the distance from antenna were used. FRAM type has the same read and write speed, therefore the same maximal speeds were determined (Figure 6). The maximum speed of 3,19 m/s for reading the 20 bytes of data was achieved on the 15 mm distance from the antenna.

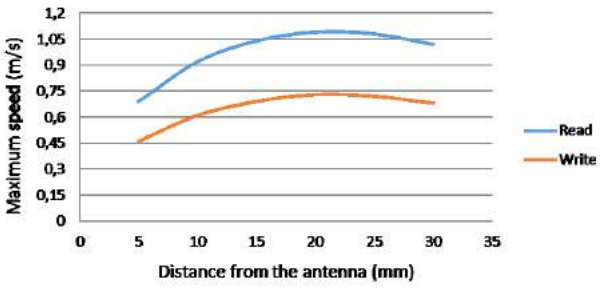

Figure 5. Maximum speed of read/write vs. distance for EEPROM type RFID tag

Slika 5. Najveća brzina čitanja/zapisivanja u usporedbi s udaljenošću za EEPROM vrstu RFID tag-a

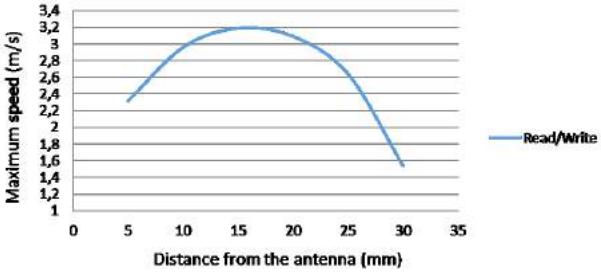

Figure 6. Maximum speed of read/write vs. distance for FRAM type RFID tag

Slika 6. Najveća brzina čitanja/zapisivanja u usporedbi s udaljenošću za FRAM vrstu RFID tag-a

Third set of experiments was with FRAM type RFID tag: six variations of the data quantity and five variations of the distance from antenna were used (Figure 7).

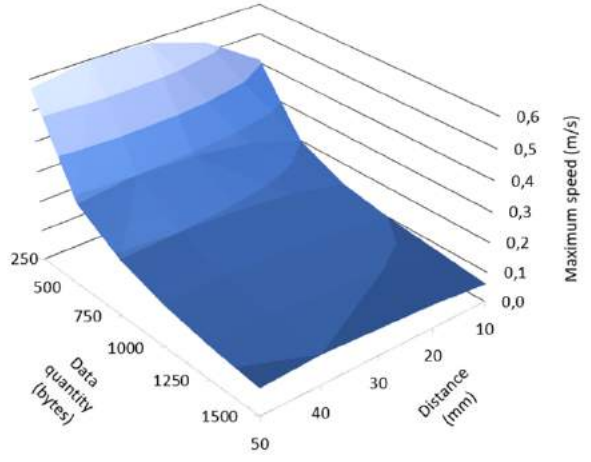

Figure 7. Maximum speed of read/write vs. different combination of the data quantity and the distance for FRAM type RFID tag

Slika 7. Najveća brzina čitanja/zapisivanja u usporedbi s različitim kombinacijama količine podataka i udaljenosti za FRAM vrstu RFID tag-a

The analysis resulted with the 3D chart which represents different maximal read/write speeds for different combinations of the distance from the antenna and data quantity. The maximum speed of 0,60 m/s for reading the 250 bytes of data was achieved on the 40 mm distance from the antenna.

In the first two sets of experiments, 20 bytes of data was used and it can to store only 20 characters, aproximately. It means that it can store only the lot number and part ID number, or similar. However, to store more data about the part or product, more memory must be used, like in this third set of experiments.

The following step was to determine how fast worker could move the part (with RFID tag attached on it) over the RFID antenna. In Figure 8, measuring of the worker's times is presented.

The aim of the measuring was to capture the normal speed of the worker that he/she will use to pass the part over the antenna. In order to calculate his/her speed, one meter marker was placed on the table and high frame rate video was captured. After that, it was easy to calculate the worker's speed using the one meter marker and captured times. Two different workers made 30 movements each.

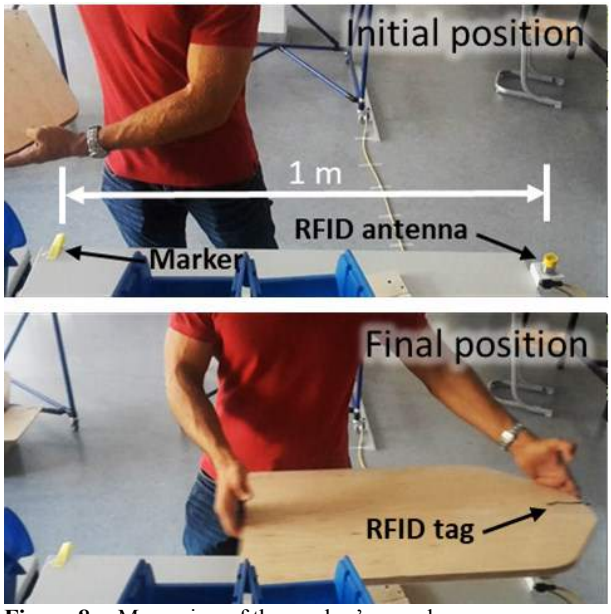

Figure 8. Measuring of the worker's speed

Slika 8. Mjerenje brzine operatera

The data of the workers' speed is presented in the following table and figure (Table 1 and Figure 9).

The average speed of a worker was 0,95 m/s, the minimum was 0,67 m/s and the maximum was 1,23 m/s, the normal distribution perfectly fits the data (Figure 9).

The final step to determine the performance of the RFID system was to compare distribution of the worker's speed with the range of reading speed of a RFID antenna.

For each of three sets of experiments, the experiment with highest percentage of successful readings is presented (Figure 10):

Table 1. **G**rouped workers' speed data

Tablica 1. Grupirani podaci o brzini radnika

Group	*Lower limit (speed in m/s)*	*Upper limit (speed in m/s)*	*Frequency*
1	0,67	0,75	5
2	0,75	0,83	7
3	0,83	0,91	9
4	0,91	0,99	16
5	0,99	1,07	11
6	1,07	1,15	8
7	1,15	1,23	3
8	1,23	1,31	1
			Σ = 60

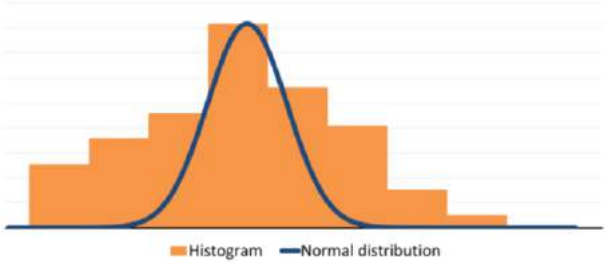

Figure 9. Histogram and normal distribution of the workers' speed

Slika 9. Histogram i normalna razdioba brzine radnika

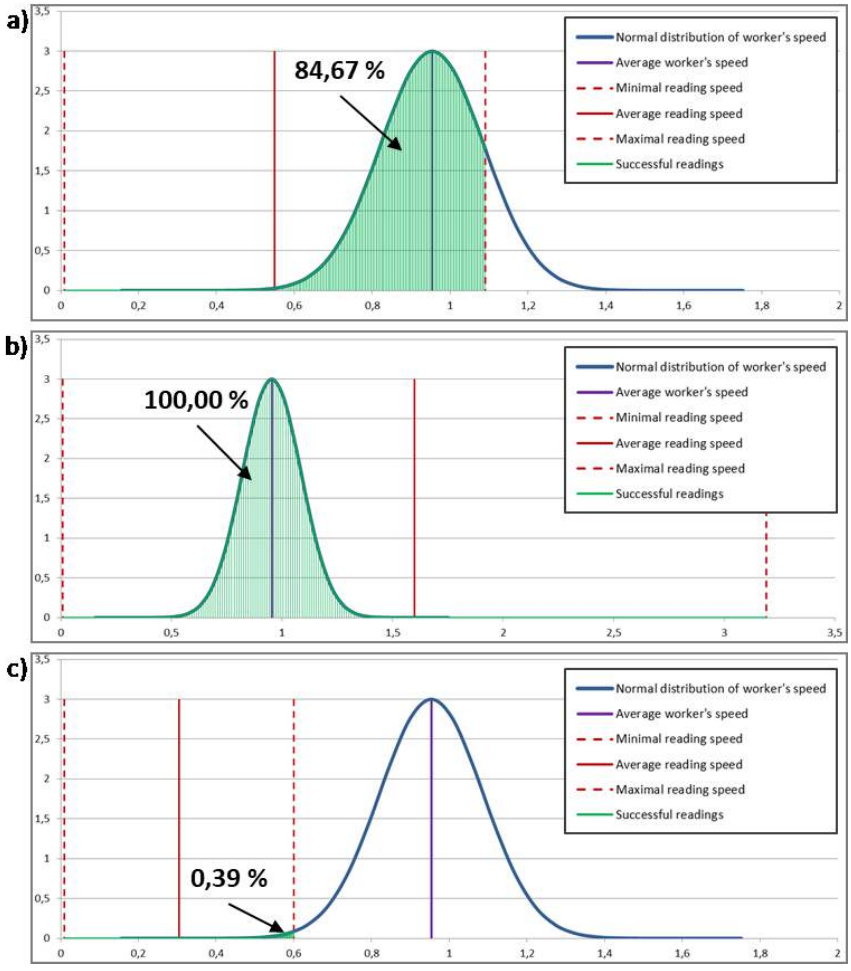

Figure 10. Presentation of the most successful readings of the RFID tags for each of three sets of experiments:
a) Percentage of the successful readings of the 20 bytes from EEPROM type RFID tag on 20 mm of distance
b) Percentage of the successful readings of the 20 bytes from FRAM type RFID tag on 15 mm of distance
c) Percentage of the successful readings of the 250 bytes from FRAM type RFID tag on 40 mm of distance

Slika 10. Prikaz najuspješnijih očitavanja RFID tag-ova za svaki od tri skupa eksperimenata:
a) Postotak uspješnih očitavanja 20 byte-ova s EEPROM vrste RFID tag-a na udaljenosti od 20 mm
b) Postotak uspješnih očitavanja 20 byte-ova s FRAM vrste RFID tag-a na udaljenosti od 15 mm
c) Postotak uspješnih očitavanja 250 byte-ova s FRAM vrste RFID tag-a na udaljenosti od 40 mm

2.2. Results

- from the first set of experiment (EEPROM type RFID tag), maximal speed was 1,09 m/s for reading the 20 bytes on the 20 mm distance;
- from the second set of experiment (FRAM type RFID tag), maximal speed was 3,19 m/s for reading the 20 bytes on the 15 mm distance;
- from the third set of experiment (FRAM type RFID tag), maximal speed was 0,60 m/s for reading the 250 bytes on the 40 mm distance.

3. Discussion

The results of this research have showed that for higher quantity of data an RFID could result with very bad performance, with very small percentage of successful readings (Figure 10c). However, for the small quantity of data, like lot number or product ID, a performance of the FRAM type RFID readers (Figure 10b) is better than the EEPROM type RFID readers (Figure 10a).
However, it must be mentioned that unsatisfying performance of the RFID reader for higher quantity of the data is caused by the low range of the RFID antenna, thus decreasing the time that RFID tag will spend in the range of an antenna. Antennas used in this research (13,56 MHz) could have range up to 1000 mm, but they are limited to below 100 mm, because of the fear that a long-range antenna could put a worker under the influence of its radiation. It is a non-ionizing type of radiation, but some researches show that it could have a negative impact on the human body in a long-term period [11, 12]. So, for the safety reasons, manufacturers of the RFID systems have limited the range of the RFID antennas used in their systems.

4. Conclusion

Although the RFID technology was seen as a platform that enables real-time tracking of the manufacturing execution, the industrial RFID system analyzed in this research showed limited performances. The read/write range of the 13,56 MHz RFID antennas is below 100 mm and it takes more than few seconds to read or write some data in some cases. However, these antennas could have range up to 1000 mm, but that would put workers under the influence of the radiation of the RFID antenna, especially in the manual assembly processes. Since some researches show that RFID radiation could have a negative impact on the human body in a long-term period, manufacturers of the RFID systems are designing the systems with small range antennas, thus avoiding negative influence on the workers. So, it is very important to take into account limited performance of the RFID antennas when designing a workstation for manual assembly. An extra training of the workers is probably needed to ensure that they are aware that it takes up to few seconds until the data is read on the RFID.

Acknowledgements

This work has been fully supported by the Croatian Science Foundation under the project 1353 Innovative Smart Enterprise (INSENT).

REFERENCES

[1] Kagermann H., Wahlster W., Helbig J., (2013), *Recommendations for implementing the strategic initiative INDUSTRIE 4.0*. Heilmeyer und Sernau, Germany
[2] Meier M., Seidelmann J., Mezgár I., (2010), *ManuCloud: The Next-Generation Manufacturing as a Service Environment*. ERCIM News 83, p33-35
[3] Meier H., Roy R., Seliger G., (2010), *Industrial Product-Service Systems - IPS2*. CIRP Annals – Manufacturing Technology 59, p. 607-627
[4] Váncza J., Monostori L., Lutters D., Kumara S.R., Tseng M., Valckenaers P., Van Brussel H., (2011), *Cooperative and responsive manufacturing enterprises*. CIRP Annals - Manufacturing Technology 60, p. 797-820
[5] Saaksvuori A., Immonen A., (2005), *Product Lifecycle Management*. Springer, Berlin, Germany
[6] Ten Dam D.C., Anema H.F.A., Van Houten F.J.A.M., Lutters D., (2009), *CNC Worknet: A Network of Flexible Production Plants*. Proceedings of the CIRP Conference on Manufacturing Systems, Grenoble, France
[7] Boucher T., Yalcin A., (2006), *Design of Industrial Information Systems*. USA
[8] Huang G.Q. , Zhang Y.F., PY Jiang, (2008), *RFID-based wireless manufacturing for real-time management of job shop WIP inventories*, Int. J. Adv. Manuf. Technol. 36, p. 752–764
[9] Zhong R.Y., Dai Q.Y., Qu T., Hu G.J., Huang G.Q. (2013), *RFID-enabled real-time manufacturing execution system for mass-customization production*, Robotics and Computer-Integrated Manufacturing 29, p. 283–292
[10] Zhong R.Y., Huang G.Q., Dai Q.Y., Zhou K., Qu T., Hu G.J. (2011), *RFID-enabled Real-time Manufacturing Execution System for Discrete Manufacturing: Software Design and Implementation*. 2011 International Conference on Networking, Sensing and Control, Delft, the Netherlands
[11] Arumugam D.D., Engels D.W. (2008), *Impacts of RF Radiation on the Human Body in a Passive RFID Environment*. IEEE Xplore Conference 2008: Antennas and Propagation Society International Symposium, Manchester, USA.
[12] IEEE (1999), *Std C95.1 IEEE Standard for Safety Levels With Respect to Human Exposure to Radio Frequency Electromagnetic Fields, 3 kHz to 300 GHz*. IEEE Standards Department, International Committee on Electromagnetic Safety, USA.

ISSN 1847-7917

Methodics of sample preparation of Mg/Carbon fiber composite for TEM and characterization of the interface

Štefan NAGY, Pavol ŠTEFÁNIK, Ivo VÁVRA, Martin NOSKO, Ľubomír OROVČÍK, Andrej OPÁLEK, Karol IŽDINSKÝ, Stanislav KÚDELA Jr., and František SIMANČÍK
Institute of Materials and Machine Mechanics, Slovak Academy of Science, Dúbravská cesta 9,84513, **Slovakia**
nagy.stefan@savba.sk

Keywords
Metal matrix composite
Carbon fibre
Magnesium
Interface
TEM specimens preparation

Original scientific paper

Abstract: Appropriate interface formation between matrix and reinforcement within metal matrix composites (MMC) is essential to assure required properties of the MMC. In this paper, preparation method and characterization of the interface between carbon fiber composite and Mg based matrix were discussed. MMC was prepared through gas pressure infiltration of unidirectionally aligned carbon fibers by liquid magnesium alloyed with Si. Thin foil for TEM observation was prepared via support titanium slotted grid technique. Results were supported by SEM and EDS analysis. Interface between carbon fiber and Mg consist of the interaction layer based on the MgO and Mg_2Si.

1. Introduction

Metal matrix composites based on magnesium matrix reinforced with carbon fibers are promising candidates for lightweight structures. In conjunction with high modulus carbon fibers, magnesium matrix composites with specific thermal properties related to high thermal conductivity and low thermal expansion can be produced [1].

Efficiency of the composite properties depends on the properties of the interface between fiber and matrix. However non-reactive C/Mg system leads to weak bonding between C-fiber and Mg matrix. Therefore, there is requirement for the enhancement of the interfacial bonding between C and Mg [2] which could be performed by addition of carbide forming elements into Mg matrix. Silicon is one of these elements which is more easily dissolved in Mg melt, but the reaction between Si and C at the temperatures below 1200°C is very slow although thermodynamic values (delta G) indicates that reaction can run even in solid state. During solidification of Mg-Si alloy with high Si content the Mg_2Si intermetallic phase is created. According to thermodynamic assumption this phase can react with carbon to form SiC only above 1000°C. Gas pressure infiltration (GPI) technology is suitable for producing composites offering controllable production parameters such as: pressure, temperature and infiltration atmosphere. Increasing the infiltration pressure at the manufacturing process can lead to increased rate of reactions on the interface.

In case of fibers, the type and manufacturing process of carbon fiber itself also influence the quality of the fiber/matrix interface. According to their mechanical properties carbon fibers can be classified into two main categories: high-strength and high-modulus carbon fibers [3], [4].

Interfacial study of the composite with different matrix and reinforcement via TEM is difficult. It needs devising methods as well as realizing/demonstrating them in a defined process with reproducibility [5], [6].

The aim of this work is therefore focused on the study of interface between C fibers and MgSi alloy and on preparation technique for appropriate TEM specimens of Mg/C fibre composites via support slotted grid.

2. Experimental methods

2.1. Materials and composite preparation

Preparation of the MMC was performed in autoclaves using GPI technique. Defined amount of pure Si was immersed and dissoluted in Mg melt to obtain the Mg alloy. Subsequently the alloy was melted in steel crucible under argon gas pressure. Prior to infiltration, the autoclave was evacuated (10 Pa) to remove reactive elements from the chamber. After melting of the alloy; the preform - unidirectional fibre array of continuous C fibres was immersed into melt at 800 °C. Then, the Ar pressure in the vessel was increased up to 4 MPa and the melt was forced to infiltrate the fibrous preform. After several seconds the preform was withdrawn from the crucible and the molten matrix solidified under gas pressure. Two samples (ST, SG) were prepared in order to study interfacial reaction, using two types of carbon fibers: PAN based Torayca T300 (ST), and pitch based Granoc (SG). Their basic properties are shown in Table

1. Chemical composition of the Mg alloy was: Mg, 96.8 wt. %; Si, 3.2 wt. %.
Structural observations and chemical compositions analysis were performed using field emission scanning electron microscopy (Jeol 7600F) equipped by EDS detector (X-max 50mm^2). For interface observations, transmission electron microscopy (Jeol 2100EX) and HRSTEM FEI - Titan Themis were used.

Table 1. Properties of carbon fibers used in the experiments

Fibre/	Producer/	Fibre type/	Tensile modulus/ (GPa)	Tensile strength/ (GPa)	Density/ (g/cm3)
Torayca T-300	Toray	PAN	230	3.53	1.76
Granoc XN90-60S (CN90-60S)	Nippon Graphite	PITCH	860	3.5	2.2

2.2. Sample preparation for TEM

In general, in case of MMC, the interface between reinforcement and matrix are of interest [5]. Mechanical grinding and polishing with ion beam thinning is advantageous method to prepare electron transparent specimen. However, in case of prepared fiber reinforced MMC, grinding of the specimen slices of unsupported material lead to cracking and disintegration of the specimen itself. To prevent disintegration, thick (0.5 mm) slotted grids made by titanium sheet were used to support the composite during grinding and polishing process. Wire electrical discharge machine was used to cut the 3 mm diameter support slotted grids (SSG) with different slots as seen in Fig. 1b. Thicker SSG allows better and safer manipulation with the sample without disintegration. Piece of the composite was then mounted in the slot (Fig. 1c) and fixed with Araldite AT1 powder adhesive. Gatan grinding system was used to thin the sample to 50 μm with grinding papers and polishing cloths. The final thinning of the sample was performed via ion polishing machine PIPS II using 4 KeV for 2-3h at angle 4° and 20 minutes at 2°. Both samples ST and SG were prepared according to above mentioned procedure.

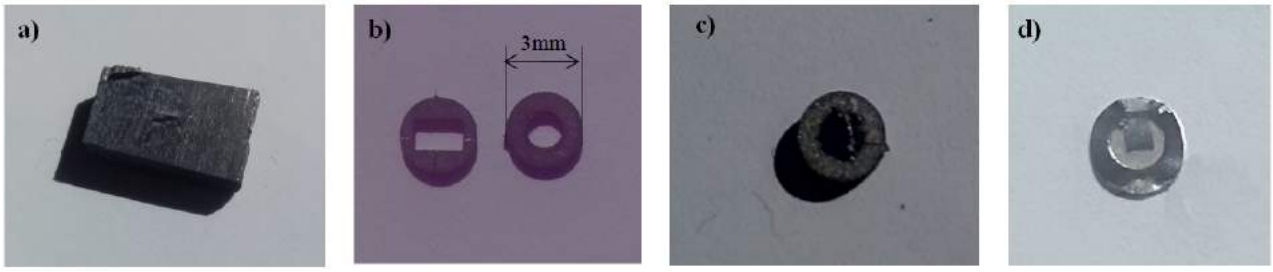

Figure 1. TEM sample preparation stages: a) composite material; b) support slotted grids with different slots; c) composite sample mounted in SSG; d) mechanically thinned sample with thickness 50 μm.

3. Results and discussion

3.1. Microstructure

Cross-section of sample ST is shown in Fig. 2. As can be seen from macrostructure, unidirectional fiber array made from continuous C fibers was successfully infiltrated by MgSi alloy. There is no residual porosity observed and fibers are relatively homogeneously distributed within matrix, with presence of clustered carbon fibers. The average fiber volume content determined via image analysis is 44 ± 2 %. Moreover, in some areas, larger amount of the grey phase surrounding couple of carbon fibers could be seen. The macrostructure of sample SG is identical, no significant differences are observed.
Fig. 3 represents character of carbon fibers, microstructures of the composite and EDS elemental map analysis of Si for both samples ST and SG. As can be seen in Fig. 3 a-b, morphology of the fibers is different, T300 fibers are rough while Granoc fibers surface is rather smooth. Si distribution within cross-section of the MMC (Fig. 3 e-f) revealed that Si is distributed mostly at the matrix/fibers interface. However, Si areas are also observed within matrix of the MMC.
In case of ST, Si is predominantly distributed in the matrix and vice-versa, in SG with pitch based Granoc fibers, Si is preferentially distributed at fiber/matrix interface. Moreover, distribution of Si is more consistent and continuous in case of SG. From EDS analysis in Fig.4b and phase diagram of Mg-Si, it could be concluded that Si forms intermetallic Mg_2Si phase at the interface. This assumption is also confirmed by SAED pattern obtained from the interface region showing Fig. 6c. The grey phase which surrounds the carbon

fibers shown in Fig. 2 was also identified as Mg_2Si intermetallic phases.
Carbon fiber surface properties also influence the formation of the interface; in case of smoother surfaces Si layer around C fibres is more continuous and rigid.

3.2. Interface observation

Contrary to SEM and EDS observations, STEM bright field image of sample SG (Fig.4a) show two Mg_2Si phase layers formed at the interface between carbon fiber and Mg. Directly at the fiber boundary, there is observed other phase and microporosity. The EDS line scan reveals oxide layer between the carbon fiber and Mg_2Si phase. Oxygen is increased directly in vicinity of the carbon fiber; Si is increased with Mg confirming presence of the Mg_2Si phase.

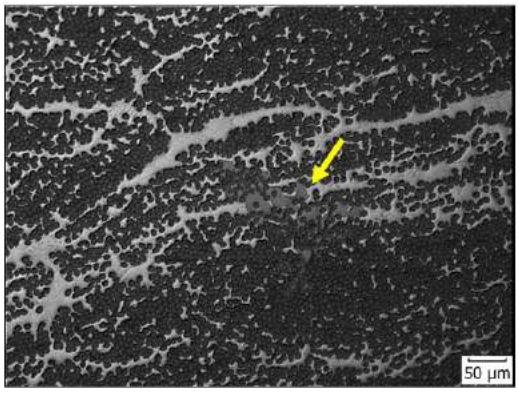

Figure 2. Macrostructure of sample ST: MgSi –T300; arrow indicate larger Mg_2Si area

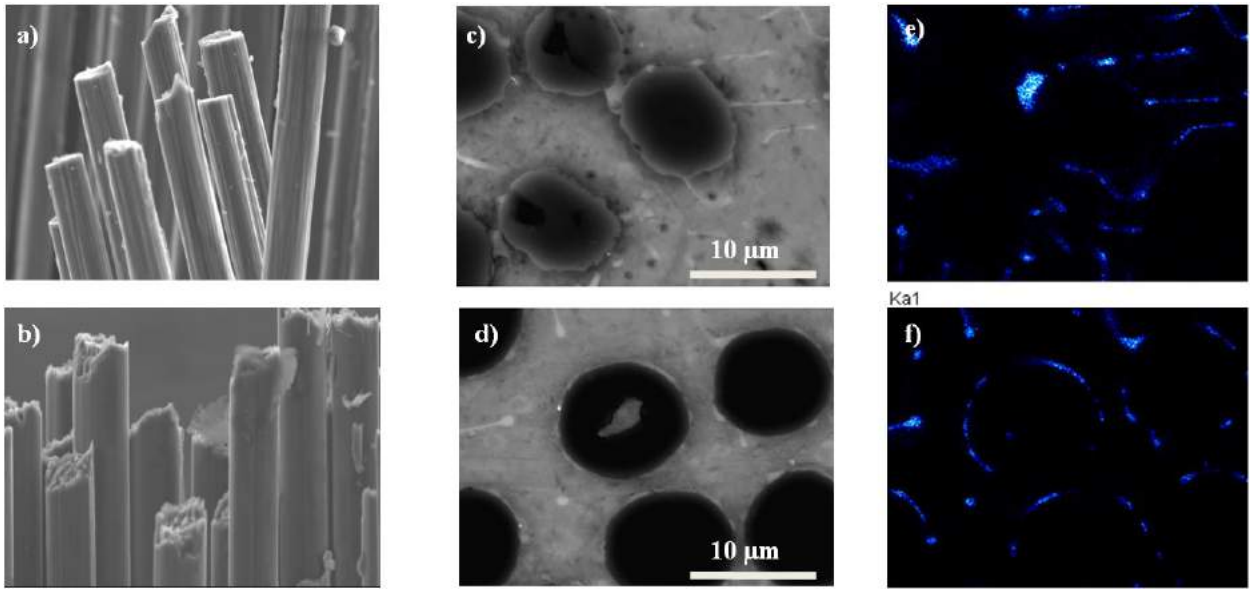

Figure 3. SEM images of the C-fibers and microstructures of samples ST, SG: a) T300; b) Granoc; c) microstructure of ST MMC; d) microstructure of SG MMC; e, f) EDS silicon (Si) element maps.

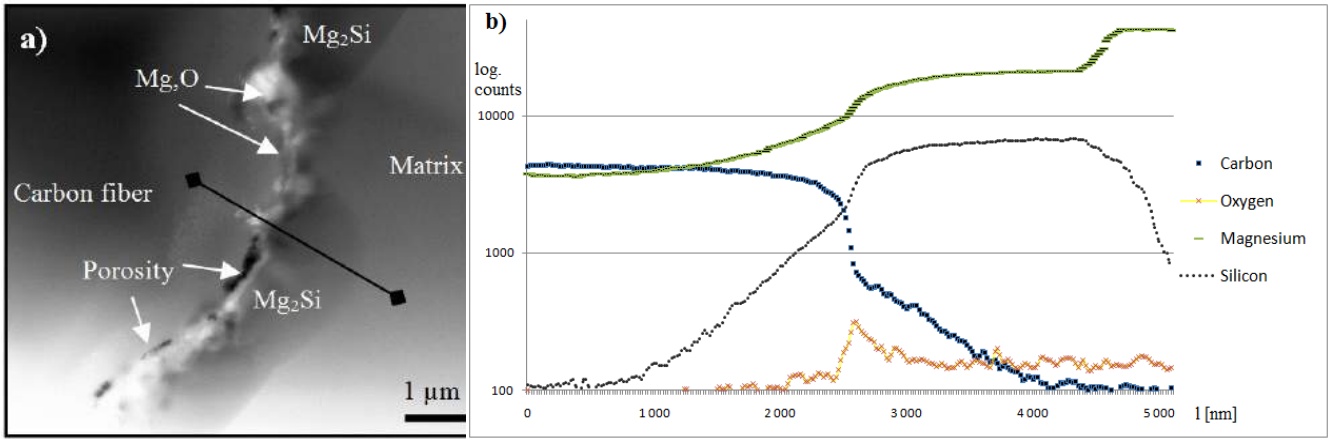

Figure 4. Interface characterization of the SG sample: a) STEM bright field image of the interface, b) EDS line scan of the interface

EDS map shown in Fig. 5 using STEM reveals formation of continuous (Mg, O) layer at the interface in sample ST. This area is without Mg_2Si phase at the interface. Another interface area was investigated with TEM. The electron diffraction of the visibly interface layer is a ring diffraction indicating presence of polycrystalline grains. From the dark field image on Fig. 6d at higher magnification, it is evident that this area consists of crystalline nano-grains of different orientations. The diffraction lines suggest presence of the MgO phase with reflections (111), (200), (220), (222) etc., according to 01-075-1525 PDF file. Next to the MgO layer, Mg_2Si phase (Fig.6c) is present with zone axis [00-1].

Feldhoff et al. in their study [2] mentioned also formation of MgO passivating interlayers between carbon fiber and matrix. This MgO layer can be formed as incorporation of oxygen during the manufacturing processes of the carbon fibers itself. Beronska et al. [1], [9] reported presence of polycrystalline zone of nanometric crystals composed of Mg and O in Mg/C (T-1100 fiber) composite and Hung. et al., Deng et al. [7, 8] reported MgO nanoparticles formation at the interface of SiC particles in Mg MMC alloy systems.

According to literature [2], [7], [8], [10], formation of this oxide layer is questionable. It can be formed due to oxidation of melted Mg during the infiltration process, or the formation of oxides directly on the carbon surface can result from the surface oxidation of the carbon.

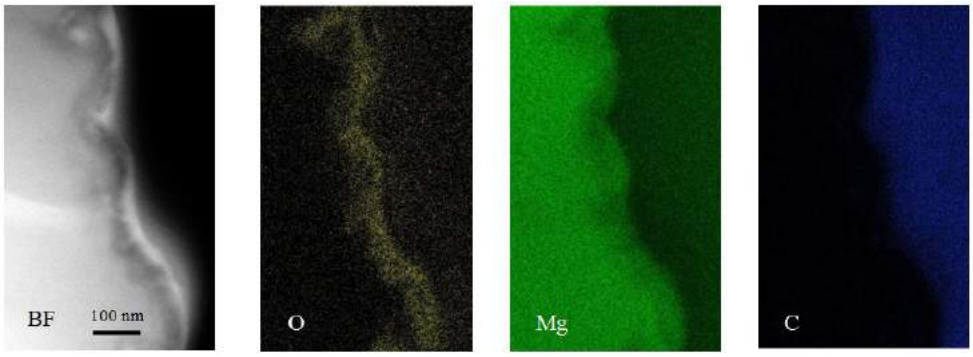

Figure 5. STEM bright field image and EDS chemical map of elements: O, Mg and C.

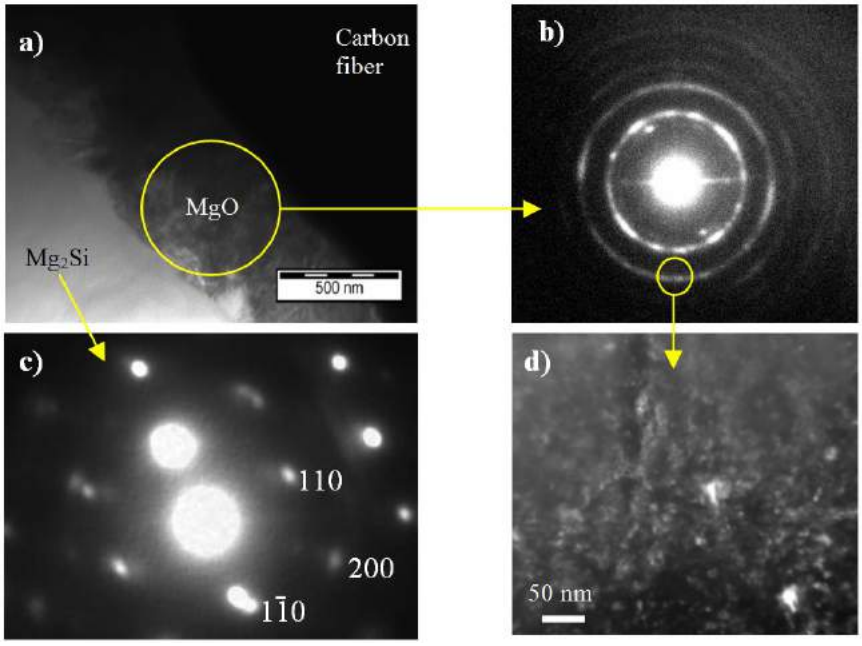

Figure 6. TEM investigation of the interface in case of sample ST: a) Mg_2Si/MgO/C interface; b) SAED pattern of nanocrystaline MgO; c) SAED pattern of Mg_2Si; d) dark field image of MgO area

4. Conclusion

Manufacturing of the carbon fiber/MgSi MMC through pressure assisted infiltration method for various carbon fibers is reported in this study. Microstructural analysis of the interface itself and description of TEM specimen preparation using support slotted grids is also presented in this work.

GPI technology offers controllable settings for preparation of carbon fiber composites. The fibers were successfully infiltrated with molten MgSi alloy.

Within microstructure for both used C-fibers, there are larger Mg_2Si areas presented in composite matrix and thin Mg_2Si layer on the interface between carbon fibers and Mg matrix. The Mg_2Si layer is more consistent in the composite with Granoc carbon fibers.

MgO interfacial layer was detected in both samples between carbon fiber and matrix (or Mg_2Si phase). This oxide layer is undesirable and degrades interface consistency.

SiC was not observed on the interface. The parameters of the GPI were not sufficient and the oxide layer of MgO also could prevent the reaction.

The presented support slotted grid technique for preparation of TEM specimens appeared as efficient and reliable procedure.

Acknowledgements

This work was supported by Slovak Foundation VEGA Grant 2/0158/16, VEGA Grant 2/0172/16, VEGA Grant 2/0144/17 and by Grant APVV-14-0936. Some results were acquired using infrastructure built during the projects ITMS 26240120006/ ITMS 26240120020.

REFERENCES

[1] N. Beronska, K. Iždinský, P. Štefanik, S. Kúdela Jr., T. Dvorák, F. Simančík, Z. Hájovská, A. Rusnák, The microstructure and thermal expansion of Mg/C composite prepared by gas pressure infiltration, Kovove Mater. 53, 2015, 451-458,

[2] A. Feldhoff, E. Pippel, J. Wolterdorf, Interface Engineering of Carbon-Fibre Reinforced Mg-Al Alloys, Advanced engineering materials 2000, 2, No. 8

[3] ZHANG Yunhe, WU Gaohui, Comparative study on the interface and mechanical properties of T700/Al and M40/Al composites, Rare Metals, Vol. 29, No. 1, Feb 2010, p. 102.

[4] ZHANG Yunhe, WU Gaohui, Interface and thermal expansion of carbon fiber reinforced aluminium matrix composites, Trans. Nonferrous Met. Soc. China, 20(2010), 2148-2151.

[5] D.V. Sridhara Rao, K. Muraleedhara, C. J. Humphreys, TEM specimen preparation techniques, Microscopy: Science, Technology, Applications and Education, Formatex 2010.

[6] W. Haiming, L. Yaojun, D. N. Seidman, J. M. Schoenung, I. J. van Rooyen, E. J. Lavernia, An Efficient and Cost-Effective Method for Preparing Transmission Electron Microscopy Samples from Powders, Microsc. Microanal. 21, 1184-1194, 2015.

[7] Y. P. Hung, J. C. Huang, K. J. Wu, Chi Y. A. Tsao, Strengthening and Toughness of AZ61 Mg with Nano SiO_2 Particles, Materials Transactions, Vol. 47, No. 8 (2006), pp. 1985-1993.

[8] K. K. Deng, J. C. Li, J. F. Fan, X. J. Wang, K. Wu, B. S. Xu, Interfecial Characteristic of as-Deformed SiCp-Reinforced Magnesium Matrix Composite, Acta Metall. Sin., 2014, 27(5), 885-893.

[9] N. Beronska, K. Iždinský, P. Štefanik, S. Kúdela Jr., F. Simančík, I. Vávra, Z. Križanová, Structure and thermal expansion behaviour of Al/C composites reinforced with unidirectionally aligned continuous high modulus C fibers, Kovove Mater. 49, 2011, 427-436.

[10] A. Kleine, J. Hemptenmacher, H.J. Dudek, K.U. Kainer, G. Kruger, J. Mater. Sci. Lett., 1995, 14, 358.

ISSN 1847-7917

Implementacija aditivne tehnologije u medicini

Iva NAKIĆ, David IŠTOKOVIĆ, Mladen PERINIĆ, Goran CUKOR
Sveučilište u Rijeci, Tehnički fakultet/ University of Rijeka, Faculty of Engineering, Vukovarska 58, 51000 Rijeka, Hrvatska/Croatia

E-mail: nakic.ivaa@gmail.com, david.istokovic@riteh.hr mladen.perinic@riteh.hr goran.cukor@riteh.hr

Keywords
Additive manufacturing
Skull reconstruction
Stereolitography
3D model
Implant

Ključne riječi
Aditivna proizvodnja
Rekonstrukcija lubanje
Stereolitografija
3D model
Implantat

Implementation of additive technology in medicine

Original scientific paper

Abstract: More and more advances in technology connect multiple scientific areas, such as mechanical engineering and medicine. In cases where drawings, technical documentation or computer models are not available, access to reverse engineering. An example is medicine where uses of additive methods made a usable 3D model. Additive production directly builds an object from a digital 3D model by adding layered material. The aim of this work is to convert data from a CT (*Computerized Tomography*) system into a CAD/CAM system and to use an additive process stereolitography to create a physical object. The CT scan of the damaged human skull was saved as a DICOM (*Digital Imaging and Communications in Medicine*) format, which is unique to medical applications. Using software programs, a series of 2D image data transforms into a digital 3D model that is stored as STL (*Standard Triangulation Language*) format. Since the STL format is a raw unstructured triangulated surface that surrounds the CAD model, it does not satisfy the function. Smoothing the surface by interpolating a raw unstructured triangulated surface into the curve results in an acceptable skull appearance. So obtained a digital 3D skull model is approaching reconstruction in such a way that an implant that replaces the damaged part is created of the existing non-damaged part. Finally, the skull and implant procedure is performed by stereolithography. The end result is satisfactory and the implant with slightly modifications is ready to use.

Izvorni znanstveni članak

Sažetak: Sve većim napretkom tehnologije dolazi do povezivanja više znanstvenih područja, kao što su u ovom slučaju strojarstvo i medicina. U slučajevima kada nisu dostupni crteži, tehnička dokumentacija ili računalni modeli pristupa se reverznom inženjerstvu. Primjer je medicina gdje se uz pomoć aditivnih postupaka izrađuje iskoristivi 3D model. Aditivna proizvodnja izravno gradi objekt iz digitalnog 3D modela dodavanjem materijala sloj po sloj. Cilj ovog rada je konvertirati podatke iz CT (engl. *Computerized Tomography*) sustava u CAD/CAM sustav te služeći se aditivnim postupkom stereolitografije izraditi fizički objekt. CT snimak oštećene ljudske lubanje spremljen je kao DICOM (engl. *Digital Imaging and Communications in Medicine*) format, koji je svojstven za medicinsku primjenu. Korištenjem softverskih programa, niz 2D slikovnih podataka transformira se u računalni 3D model koji se pohranjuje kao STL (engl. *Standard Triangulation Language*) format. Obzirom da je STL format mreža trokuta koja okružuje CAD model, kao takav ne zadovoljava funkciju. Zaglađivanjem površine pomoću interpolacije mreže trokuta u krivulje dolazi se do prihvatljivog izgleda lubanje. Tako dobivenim računalnim 3D modelom lubanje pristupa se rekonstrukciji na način da se od postojećeg zdravog dijela izrađuje implantat koji će nadomjestiti oštećeni dio. Na kraju se vrši postupak izrade lubanje i implantata postupkom stereolitografije. Krajnji rezultat je zadovoljavajući te je implantat uz male dorade spreman za upotrebu.

1. Uvod

Sve većim napretkom tehnologije rastu i zahtjevi suvremenog društva. Teži se većoj fleksibilnosti pri razvoju i proizvodnji tvorevina, visokoj kvaliteti, uz istovremeno skraćenje vremena i sniženje troškova. Kako bi se zahtjevi mogli zadovoljiti dolazi do povezivanja više znanstvenih područja. U ovom radu su to strojarstvo i medicina, dva važna područja ljudske djelatnosti. Jedno takvo područje koje odgovara na kompliciranе zahtjeve suvremene proizvodnje je aditivna

proizvodnja. Kod aditivne proizvodnje objekt se gradi izravno iz digitalnog 3D modela dodavanjem materijala sloj po sloj. Na taj način nestaje ograničenje po pitanju kompliciranе geometrije, isto su tako dodatni alati sve manje potrebni. Danas se aditivnim postupcima izrađuje različita paleta proizvoda te se područja primjene kreću od strojarstva, automobilske industrije, aeroindustrije, umjetnosti pa sve do medicine i stomatologije. U slučajevima kada nisu dostupni crteži, tehnička dokumentacija ili računalni modeli pristupa se reverznom inženjerstvu.

U teorijskom dijelu rada riječ je općenito o povratnom ili reverznom inženjerstvu te aditivnoj proizvodnji, definirano njihovo značenje, faze procesa te područja primjene. Prikazan je pregled postupaka aditivne proizvodnje te je dodatno provedena analiza onog postupka koji će se primijeniti i u eksperimentalnom dijelu. Detaljnije je provedena analiza aditivne proizvodnje unutar područja medicine, materijali koji se u tu svrhu koriste te ograničenja i daljnji razvoj. Na konkretnim primjerima uspoređeni su klasični i aditivni postupci.

U eksperimentalnom dijelu rada detaljno je opisana pretvorba podataka iz CT-a u računalni 3D model koristeći besplatan programski paket *Slicer* i probnu verziju *Optical RevEng*-a. U suradnji s tvrtkom Izit d.o.o. koja je omogućila korištenje računalnog programa *Geomagic Design X*, napravljena je rekonstrukcija lubanje kako bi se dobio implantat što je i cilj ovog rada. Za kraj je još prikazan postupak izrade lubanje i implantata odabranim aditivnim postupkom stereolitografije pomoću 3D printera *Form 2* u vlasništvu Zavoda za industrijsko inženjerstvo i management Tehničkog fakulteta u Rijeci.

2. Primjena aditivne tehnologije u medicini

Reverzno inženjerstvo (engl. *Reverse engineering,* RE) definira se kao proces umnožavanja ili rekonstrukcije postojećeg dijela, sklopa ili gotovog proizvoda, u slučajevima kada nisu dostupni crteži, tehnička dokumentacija ili računalni model.

Za razliku od klasičnog inženjeringa gdje se kreće od ideje, njene razrade i transformacije u konačan proizvod, ovdje se kreće s gotovim proizvodom koji se kroz proces 3D digitalizacije prevodi u CAD model.

Proces RE sastoji se od dva osnovna koraka:

1. digitalizacije (skeniranje ili slični postupak) fizičkog objekta
2. 3D modeliranja dijela na osnovu prije dobivenih podataka

Nakon toga modelom se može upravljati uz pomoć uobičajenih CAD aplikacija te ih se na kraju može i proizvesti aditivnim metodama ili CNC strojnom obradom kako je prikazano na slici 1. Prednost korištenja RE je u tome što smanjuje troškove i skraćuje vrijeme potrebno proizvodu da izađe na tržište. [1,2]

Aditivna proizvodnja (engl. *Additive manufacturing*, AM) je formalni pojam za ono što se nekad nazivalo brzom proizvodnjom prototipova (engl. *Rapid Prototyping,* RP). Princip svih aditivnih procesa izrade je isti i sastoji se od sljedećih faza: [4]

1. Izrada CAD modela (I-DEAS, Catia, SolidWorks, Pro/Engineer…)
2. Pretvaranje CAD modela u STL ili AMF standardnu datoteku
3. Virtualno rezanje datoteke na slojeve (engl. *slicing*)
4. Izrada objekta na AM stroju sloj po sloj
5. Naknadna obrada (ovisno o AM postupku)

2.1. Primjena AM postupaka

U mnogim granama industrije koristi se AM. Na slici 2. prikazani su rezultati istraživanja *Wohlers* 2012. godine gdje su vidljiva područja primjene i koliki im udio pripada. Najveći udio zauzimaju proizvodi široke potrošnje te elektronika, npr. sport, tekstilna industrija, igračke itd. Zatim je tu automobilska industrija gdje se izrađuju dijelovi ovjesa, izrada kalupa za odljevke itd.

Figure 1. Reverse engineering process
Slika 1. Proces povratnog inženjerstva [3]

Treća po redu je medicina, gdje je AM primjenjiva kod pripreme i planiranja složenih operacija, kod izrade implantata, proteza i ortoza, a razvijaju se i prema proizvodnji matičnih stanica, odnosno pokušaju 3D tiskanja organa.

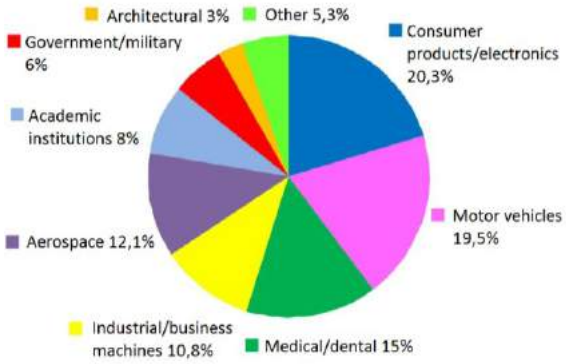

Figure 2. Fields of application of additive manufacturing
Slika 2. Područja primjene aditivne proizvodnje [5]

Medicina je područje gdje svakom novom inovacijom mogu biti spašeni novi životi, a AM tehnologija potiče doktore, znanstvenike i proizvođače medicinskih pomagala na brži rad, temeljitije ispitivanje novih proizvoda te s time omogućiti bolju zdravstvenu skrb. U usporedbi s tradicionalnim metodama liječenja 3D tehnologija je u suvremenu medicinu donijela znakovita poboljšanja. [6]

Najčešće primjene AM postupaka u medicini su: [6]

- istraživanje novih medicinskih uređaja
- predklinička ispitivanja
- proizvodnja medicinske opreme
- izrada demonstracijskih modela
- izrada realnih modela za obuku i vježbu kompliciranih zahvata
- ortopedija i protetika

Tijelo svake osobe je jedinstveno. Zbog toga su implantati, ortopedija i proizvodi za stomatološku upotrebu tako izazovan proces. Za takve potrebe savršeno su prilagođene pojedinačne i male serije proizvoda koje su ekonomične i brze za proizvodnju te koje zadovoljavaju najviše standarde kvalitete u smislu materijala i metoda obrade. Zbog toga je AM tehnologija sve raširenija u sektorima medicine i stomatologije jer može zadovoljiti postavljene zahtjeve. [7]

Biomedicinsko inženjerstvo je jedna od grana inženjerstva s najbržim širenjem. Inovacije koje se pritom proizvode, imaju za cilj poboljšati zdravlje i kvalitetu života – razvoj umjetnih organa, poboljšanje tehnologije oslikavanja koja liječnicima omogućuje preciznije preglede nego dosad pa sve do tehnologije praćenja pacijenata na daljinu. Dolazi do spajanja inženjerskih znanja s primijenjenim znanjima iz prirodnih znanosti poput kemije, biologije i fizike.

2.2. Materijali u medicini

Jedan od najvećih problema pri korištenju medicinskih pomagala izrađenih od različitih materijala, npr. metala, stakla, polimera, itd., je odbacivanje stranog tijela od strane ljudskog organizma. Zbog toga je veoma važno istražiti materijale koje tijelo neće odbaciti, tj. koji će se uspješno implementirati. Tu se onda pojavljuju biokompatibilni materijali koji se sve češće primjenjuju u medicinske svrhe. Njihovo istraživanje je skupo i potrebno je okupiti inženjere materijala, kemijske inženjere, kemičare, biologe, kako bi se istražili i izradili. [8]. Materijali koji se koriste unutar živih bića moraju zadovoljiti određene kriterije i imati sljedeća svojstva:[9]

- Biokompatibilnost
- Netoksičnost
- Izdržljivost
- Visoka čvrstoća i žilavost

2.3. Podjela AM postupaka

AM postupci mogu se podijeliti prema: vrsti materijala za potrebnu izradu, izvoru energije, postupku oblikovanja sloja i gotovom obliku proizvoda.

Table 1. Division of additive procedures
Tablica 1. Podjela aditivnih postupaka [11]

State of starting material	Process	Material preparation	Layer creation technique	Typical materials
Liquid	SLA	Liquid resin in a vat	Laser scanning/light projection	UV curable resin, ceramic suspension
	MJM	Liquid polymer in jet	*Ink-jet* printing	UV curable acrylic plastic, wax
	RFP	Liquid droplet in nozzle	On-demand droplet deposition	Water
Filament / Paste	FDM	Filament melted in nozzle	Continuous extrusion and deposition	Thermo-plastics, waxes
	Robo-casting	Paste in nozzle	Continuous extrusion	Ceramic paste
	FEF	Paste in nozzle	Continuous extrusion	Ceramic paste
Powder	SLS	Powder in bed	Laser scanning	Thermo-plastics, waxes, metal powder, ceramic
	SLM	Powder in bed	Laser scanning	Metal
	EBM	Powder in bed	Electron beam scanning	Metal
	LMD	Powder injection through nozzle	On-demand powder injection and melted by laser	Metal
	3DP	Powder in bed	Drop-on-demand binder printing	Polymer, metal, ceramic, other powders
Solid sheet	LOM	Laser cutting	Feeding and binding of sheets with adhesives	Paper, plastic, metal

Ti faktori utječu na završnu kvalitetu površine, dimenzijsku preciznost, mehanička svojstva, vrijeme i cijenu izrade proizvoda. [10] U tablici 1. prikazana je podjela aditivnih postupaka.

2.4. Stereolitografija

Kod ove tehnologije koristi se podloga sa tekućim fotopolimerom, tzv. smolom i UV laser kako bi se izradio model sloj po sloj. Svaki se sloj izrađuje na način da se skrućuje samo onaj dio UV osjetljivog fotopolimera u tekućem stanju kojeg obasja vođeni laserski snop te se spaja sa čvrstim slojem ispod njega. Kako se koji sloj skrutne, tako se radna platforma pomakne za tu debljinu prema dolje, obično od 0,025 mm do 0,15 mm. Smola ponovno prekrije model i ponavlja se postupak. Nakon izrade 3D modela, model se čisti od preostale smole, a zatim se dodatno učvršćuje u UV komori. Slika 3. prikazuje postupak stereolitografije. [12]

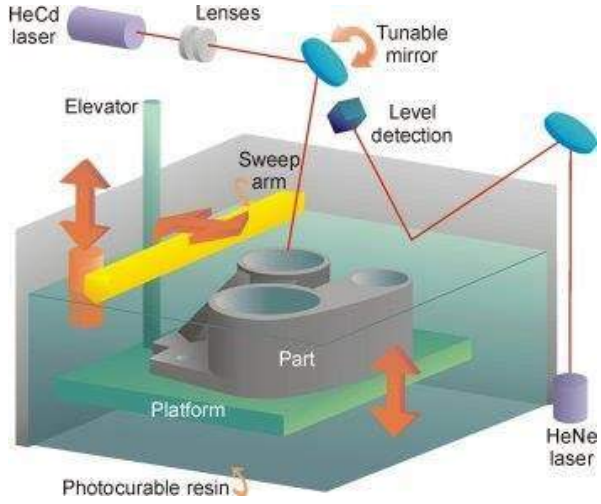

Figure 3. Stereolitography (SLA)
Slika 3. Stereolitografija (SLA) [12]

2.5. Ograničenja AM postupaka za medicinske primjene

Iako nema sumnje da su medicinski modeli korisna pomagala kod rješavanja kompleksnih kirurških problema, postoje brojni nedostaci u postojećim tehnologijama aditivnih metoda vezani uz njihovu upotrebu za generiranje medicinskih modela. Dio razloga je to što su aditivne metode izvorno dizajnirane za rješavanje problema u širem smislu područja razvoja proizvodnje, a ne specifično za rješavanje medicinskih problema. Stoga se razvoj tehnologije usredotočio na rješavanje problema proizvođača umjesto problema liječnika i kirurga. Međutim, nedavna i buduća poboljšanja u tehnologiji aditivnih metoda mogla bi otvoriti vrata mnogo širem rasponu primjena u medicinskoj industriji. Ključna pitanja koja mogu promijeniti ove nedostatke u prednosti korištenja AM uključuju:

- brzinu
- troškove
- točnost
- materijale
- jednostavnost korištenja

Analizom ovih problema može se odrediti koje bi tehnologije mogle biti najpogodnije za medicinske primjene, kao i kako se te tehnologije mogu razviti u budućnosti kako bi bolje odgovarale za te primjene.

Izrada modela aditivnih metoda često može trajati dan ili više. Zbog toga što se medicinski podaci moraju segmentirati i obraditi prema anatomskim značajkama, priprema podataka može u stvari potrajati dulje od vremena izgradnje AM-a. Osim toga, proces segmentacije zahtijeva određenu vještinu i razumijevanje anatomije. To znači da se medicinski modeli mogu učinkovito uključiti samo u kirurške zahvate koji uključuju dugoročno planiranje i ne mogu se koristiti, na primjer, kao pomagala za brzu dijagnozu i liječenje u hitnim operacijama.

Za proizvodnju medicinskih proizvoda koji su spomenuti ranije, troškovi stroja nisu jednako važni kao i neki drugi faktori. Za usporedbu, svrha medicinskih modela za dijagnozu, kirurško planiranje i razvoj protetike je da se optimizira vrijeme planiranja kirurga i da se poboljša kvaliteta, učinkovitost i efikasnost. Što su strojevi, materijali i operativni troškovi niži, biti će prikladniji za više medicinskih modela.

Mnogi AM postupci se poboljšavaju kako bi se stvorile preciznije komponente. Međutim, mnoge medicinske aplikacije trenutačno ne zahtijevaju visoku točnost jer su podaci iz 3D sustava znatno manje točni od AM strojeva u koje ulaze. To ne znači da korisnici u medicini ne bi trebali biti zadovoljni. Kako CT i MRI tehnologije postaju sve točnije i sofisticiranije, tako će zahtjevi za AM postati izazovniji.

Samo nekoliko AM polimernih materijala klasificirano je kao sigurno za transport u operacijsku salu, a još manje njih je kvalificirano za postavljanje unutar tijela. Općenito su uređaji koji pružaju najprikladnija svojstva materijala i najskuplji uređaji. Sustavi na bazi praha također su nešto teži za implementirati zbog potencijalnih problema s onečišćenjem. To ograničava raspon aplikacija korištenih za medicinske potrebe. [13]

3. Rekonstrukcija lubanje

Cilj eksperimentalnog dijela rada je konvertirati podatke iz CT (engl. *Computerized Tomography*) sustava u CAD/CAM sustav te služeći se aditivnim postupkom stereolitografije izraditi fizički objekt. CT snimak oštećene ljudske lubanje dobiven je iz Kliničkog bolničkog centra Sušak, Rijeka.

Dobiveni CT snimak spremljen je kao DICOM (engl. *Digital Imaging and Communications in Medicine*) format. To je standardan format koji se koristi diljem svijeta za pohranu, razmjenu i prijenos medicinskih slika. To uključuje definiciju formata datoteka (ime ustanove u

kojoj je izvršen pregled, ime pacijenta, datum, vrijeme, rezolucija slike, itd.) i mrežni protokol za komunikaciju. Na taj način dva uređaja mogu mrežno izmjenjivati podatke o pacijentu preko TCP/IP (engl. *Transmission Control Protocol/ Internet Protocol*) protokola. S obzirom da se informacije grupiraju u podatkovne setove, snimke se ne mogu pomiješati ili zamijeniti. [14]

3.1. 3D Slicer

3D Slicer je besplatan softverski program za analizu, obradu i 3D vizualizaciju medicinskih slika. Izgrađen je tijekom dva desetljeća uz pomoć podrške Nacionalnih instituta za zdravstvo i zajednice u razvoju diljem svijeta. Jednostavan je za korištenje liječnicima, istraživačima, ali i široj javnosti. Podrška je za multidisciplinarnu snimku, uključujući MRI, CT, US, nuklearnu medicinu i mikroskopiju. Mogućnost prikaza više organa, od glave do pete. *3D Slicer* sadrži više od 100 modula za segmentaciju slike, registraciju i 3D vizualizaciju medicinskih slika. Moduli se mogu implementirati u *C++*, *Python*, *Matlab*. [15]

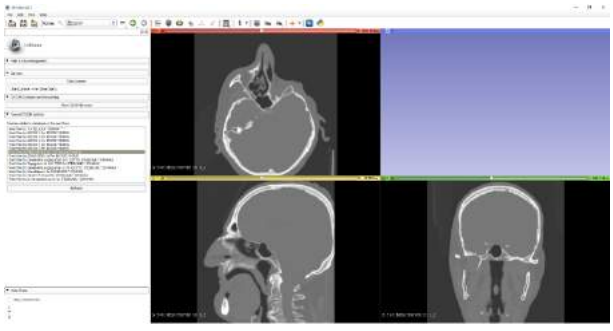

Figure 4. View the user interface in 3D Slicer
Slika 4. Prikaz korisničkog sučelja u 3D Slicer-u

Uz pomoć njega moguće je niz 2D slikovnih podataka transformirati u računalni 3D model. Na slici 4. prikazano je korisničko sučelje. Jedan prozor predviđen je za 3D preglednik, dok su ostala tri preglednici za presjeke ravnina. U anatomiji čovjeka koriste se tri zamišljene ravnine:

- središnja (medijalna) ili sagitalna (engl. sagittal) – žuti prozor
- čeona (frontalna) ili koronalna (engl. coronal) – zeleni prozor
- poprečna ili transverzalna (engl. axial) – crveni prozor

Pomoću modula *Volume Rendering* dobije se prikaz 3D modela te se od ponuđenih predložaka prikaza odabire *MR-Default* kojim se prikazuju samo kosti lubanje. Prikaz je potrebno izoštriti. Rezanjem volumena ostavlja se samo onaj dio koji je potreban za daljnju upotrebu kao što je vidljivo na slici 5. U svim prozorima preglednika pojavljuje se okvir s osima koje pomicanjem određuju područje interesa.

Figure 5. Crop to region of interest
Slika 5. Odrezivanje do željenog volumena

Pomoću modula *Editor* određuje se struktura lubanje. Ovdje je potrebno medicinsko znanje kako bi se preciznije izdvojila željena anatomija glave, tj. lubanja. Izrađeni model pohranjuje se kao STL datoteka.
Obzirom da je dobiveni STL format mreža trokuta koja okružuje CAD model, kao takav ne zadovoljava funkciju. Potreban je još jedan korak prije same rekonstrukcije, a to je zaglađivanje površine pomoću interpolacije mreže trokuta u krivulje kako bi se došlo do prihvatljivog izgleda lubanje. Taj korak će se odraditi u računalnom softveru *Optical RevEng*-u. STL datoteke opisuju samo geometriju površine trodimenzionalnog objekta bez ikakvog prikaza boje, teksture ili drugih uobičajenih atributa CAD modela. Može biti spremljena u ASCII formatu, ali se češće koristi binarni zapis.

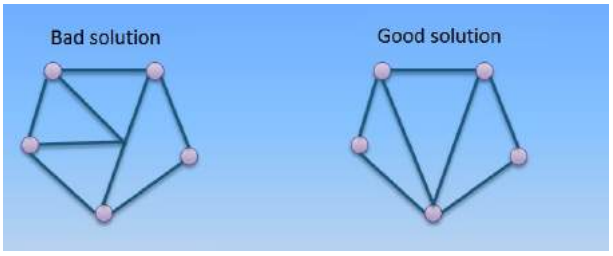

Figure 6. Triangulation conventions
Slika 6. Konvencije pri triangulaciji [16]

STL datoteka opisuje sirovu nestrukturiranu trokutastu (trianguliranu) površinu uobičajenim jedinicama i vrhovima (pravilo desne ruke) trokuta pomoću trodimenzionalnog kartezijevog koordinatnog sustava. Prilikom izvoza u STL format, moraju se poštovati pravila konvencije pri triangulaciji, tj. spremanja trokuta kako je prikazano na slici 6. [16]

3.2. Optical RevEng

Optical RevEng korisnicima omogućuje vizualizaciju i transformaciju podataka iz oblaka točaka i uvezenih 3D formata (3DS, STL, OBJ, DXF, itd.) u 3D poligonske mreže za izradu, analizu, dizajn, itd. Posjeduje snažne alate za brzo i precizno stvaranje čistih poligonskih modela iz neobrađenih podataka skeniranja, također i alate za uređivanje poligoniziranih modela. Učitani STL model prikazan na slici 7. podvrgava se postupku

Repairing kako bi se uklonile neželjene greške poput sitnih komponenti koje nisu vezane za lubanju ili vrhova šiljaka koji nisu spojeni u trokute. Potrebno je ponavljati postupak sve dok greške u potpunosti ne nestanu.

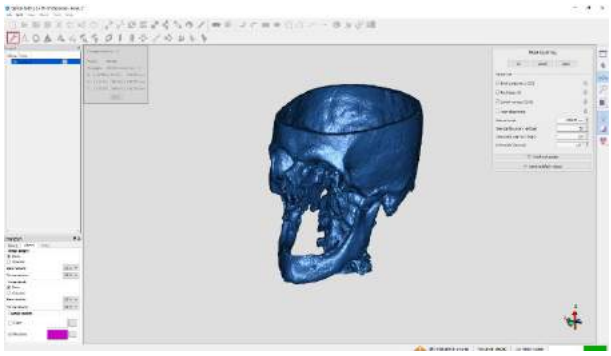

Figure 7. Optical RevEng
Slika 7. Optical RevEng

Uklanjanjem prethodno navedenih grešaka dolazi do otvaranja neželjenih rupa na modelu. Odabirom opcije *Hole filling* otvara se izbornik u kojem postoje različiti načini zatvaranja rupa. Postoji više modula označavanja rupe, kao što je označavanje cijele rupe, zatim povlačenjem linija od ruba do ruba parcijalno zatvaranje rupe, itd. Isto tako postoji više načina popunjavanja rupe, kao što je ravna površina, izbočena površina, itd.
Nakon zatvaranja svih rupa, opcijama *Denoising* i *Smoothing* zaglađuje se površina. Opcijom *Denoising* se uz pomoć iteracija mreža trokuta pretvara u krivulje. Iteracija se provela 5 puta uz jačinu 1,7. Opcijom *Smoothing* se definiranjem vrijednosti svojstva osjetljivosti i svojstva zaštite zaglađuje i poboljšava površina. Transformacija je vidljiva na slici 8. Poslije svakog koraka provodi se početni postupak *Repairing*. Konačni model se ponovo sprema kao STL datoteka.

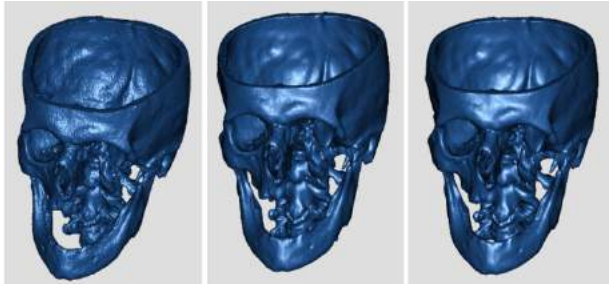

Figure 8. 3D mode – after Denoising – after Smoothing
Slika 8. 3D model – nakon Denoising – nakon Smoothing

3.3. Geomagic Design X

Geomagic Design X je softverski program predviđen za 3D skeniranje i reverzno inženjerstvo. Namijenjen je za pretvaranje podataka 3D skeniranja u visoko kvalitetne CAD modele. Omogućuje brzu obradu oblaka točaka, poligonizirane mreže, površina i solida, sve u jednoj aplikaciji. Brza i precizna interpolacija ulaznih podataka, brza isporuka rezultata i povećanje produktivnosti u dizajnu i inženjerskom tijeku rada. [17]
S obzirom da je cilj rekonstrukcije nadomjestiti oštećeni dio, to će se napraviti zrcaljenjem zdravog dijela lubanje. Za to je prvo potrebno odabrati novu ravninu presjeka klikom na *Plane* gdje postoji više načina odabira ravnine, ali za ovaj slučaj uzima se *Pick Multiple Points*. Odabiru se točke kako bi se njihovom aritmetičkom sredinom dobila ravnina potrebna za nastavak, slika 9.

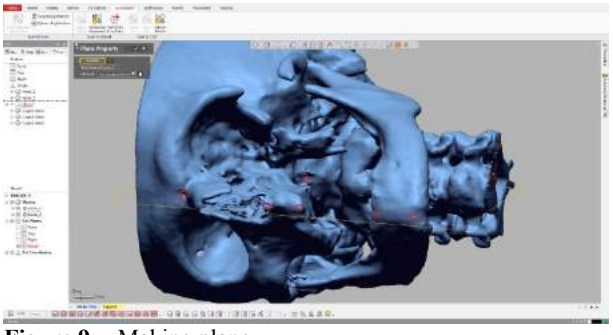

Figure 9. Making plane
Slika 9. Izrada ravnine

Opcijom *Split* i odabirom prije definirane ravnine odrezuje se oštećena polovica. Ponovnim odabirom definirane ravnine i opcijom *Mirror* zrcali se originalna polovica.
Sljedeći korak je kopirati početni ulazni *Mesh*, isključiti vidljivost odrezane originalne polovice te usporediti koliko novi zrcaljeni dio odstupa od originala lubanje. Na slici 10. kopirani *Mesh* je sada žute boje, a prethodno zrcaljeni dio je roze boje te se vidi njihova razlika.

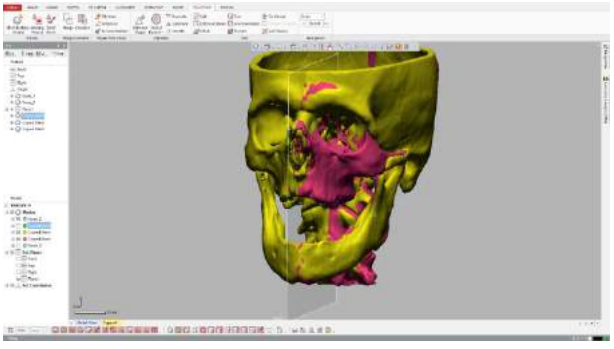

Figure 10. Comparison with the original state
Slika 10. Usporedba s postojećim stanjem

Zrcaljeni dio dosta odstupa od originala te ih je potrebno poravnati, tj. namjestiti jedan na drugi. Naredbom *Align Between Scan Data* koristiti će se metoda na temelju izbora točaka. Kao referentni element uzima se original (žuta boja), a kao pomični element uzima se zrcaljeni dio (roza boja).
Potrebno je odabrati dovoljan broj točaka, prikazano na slici 11, ali ne prevelik kako ne bi došlo do još većih

odstupanja. Problem može predstavljati uloga čovjeka, tj. osobe koja odabire točke jer je njihov izbor proizvoljan, a i potrebno je pogoditi isto mjesto na oba dijela. Proces je iterativan, što znači da se ponavlja dok god se ne postigne približna točnost.

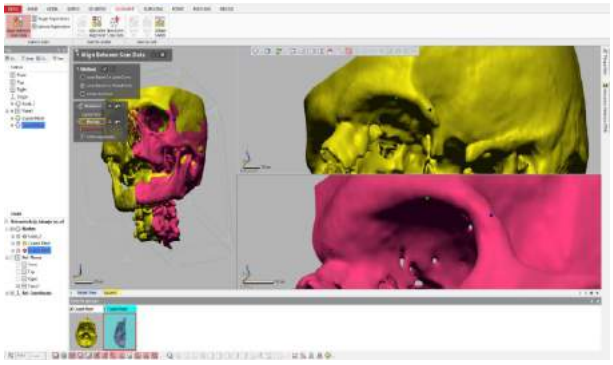

Figure 11. Alignment with the point selection method
Slika 11. Poravnanje uz metodu izbora točaka

Jednom kad je proces poravnanja gotov, slijedi rezanje zrcaljene polovice na manji dio kako bi se dobio potrebni implantat. Isključi se vidljivost originalnog dijela, uz pomoć označene ikone *Paint Brush* proizvoljno se određuje dio koji se želi ukloniti te se on jednostavno izbriše, slika 12. Ako je potrebno postoji i još jedna naredba za namještanje. To je *Datum Match* gdje se kao pomični element odabire zrcaljeni dio te se ručno uz pomoć x, y, z osi namješta na original.

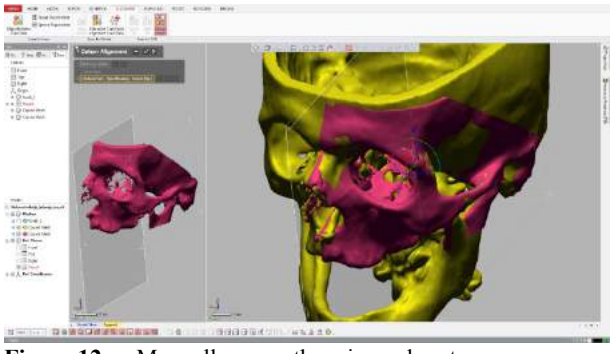

Figure 12. Manually move the mirrored part
Slika 12. Ručno pomicanje zrcaljenog dijela

Nakon namještanja, ponovo se pristupa procesu rezanja zrcaljenog dijela. Proces se ponavlja tako dugo dok se ne dobije prihvatljiva veličina implantata. Paralelno se uključuje i isključuje vidljivost originala kako bi se vidjelo pravo stanje. S obzirom da se dio rezao, pojavile su se neželjene rupe na njemu. Njih će se zatvoriti uz pomoć naredbe *Fill Holes*.
Tako zatvorenom implantatu promijenjena je boja u crnu, radi lakšeg prepoznavanja koraka u samom procesu izrade. Predzadnji korak je na mjestima spojeva ova dva elementa napraviti nalijegajuću površinu, tj. udubljenja na implantatu kako bi što bolje „sjeo" na svoje mjesto. Opcijom *Boolean* odabire se metoda rezanja (ponuđene su metoda spajanja, rezanja i križanja). Kao *Tool Mesh*, odnosno dio koji će napraviti rezanje, koristi se lubanja (žuta boja), a kao *Target Mesh*, odnosno dio na kojem će se izrezivat, koristi se implantat (crna boja). Na slici 13, vidi se implantat i njegovi izrezani, odnosno udubljeni vrhovi (mjesta na kojima naliježe na lubanju).

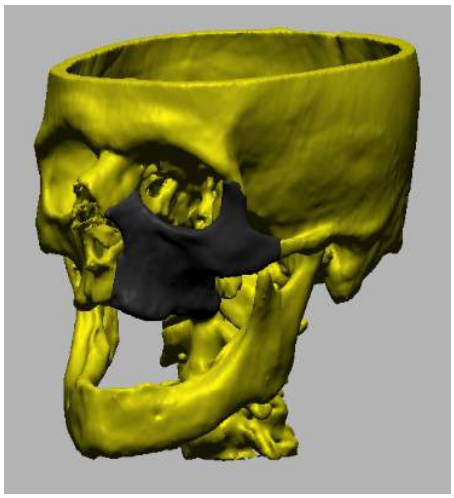

Figure 13. Final look
Slika 13. Završni izgled

3.4. Izrada lubanje i implantata

Nakon pretvorbe podataka iz CT snimke oštećene ljudske lubanje u računalni 3D model (STL format) i kasnijom njenom rekonstrukcijom stvoreni se uvjeti za izradu fizičkog modela. Aditivnim postupkom stereolitografije biti će izrađeni lubanja i implantat.
S obzirom da je njena stvarna veličina prevelika za radni prostor printera, lubanja se skalira na 65% ukupnog volumena. Ručno se okreće i naginje radi što boljih uvjeta samog printanja. Postavljaju se potpornji uz parametre gdje je njihova gustoća 0,9, a prihvatna točka 0,55 mm. Kao materijal je odabrana siva smola koja je savršena za opću svrhu prototipova i dizajn te za sitne detalje. Debljina sloja je 0,05 mm. Potrebna količina smole iznosi 208,01 mL. Broj slojeva koji je potreban za izradu lubanje je 2741, a vrijeme printanja iznosi 19 sati i 16 minuta, slika 14.
Za izradu implantata vrijedi isti postupak. Implantat se također skalira na 65% ukupnog volumena, a ostali parametri su jednaki kao i za lubanju. Koristi se prozirna smola u količini od 10,29 mL. Debljina sloja je 0,025 mm, a broj slojeva iznosi 1389. Vrijeme printanja iznosi 4 sata i 35 minuta.
Rekonstruirana lubanja spojena je s implantatom preko nalijegajućih površina koje su definirane u prethodnim programima. Krajnji rezultat je zadovoljavajući te je implantat uz manje dorade spreman za upotrebu. Postoji odstupanje na predjelu gornje vilice koje se može riješiti dodatnim namještanjem u *Geomagic Design X*-u.

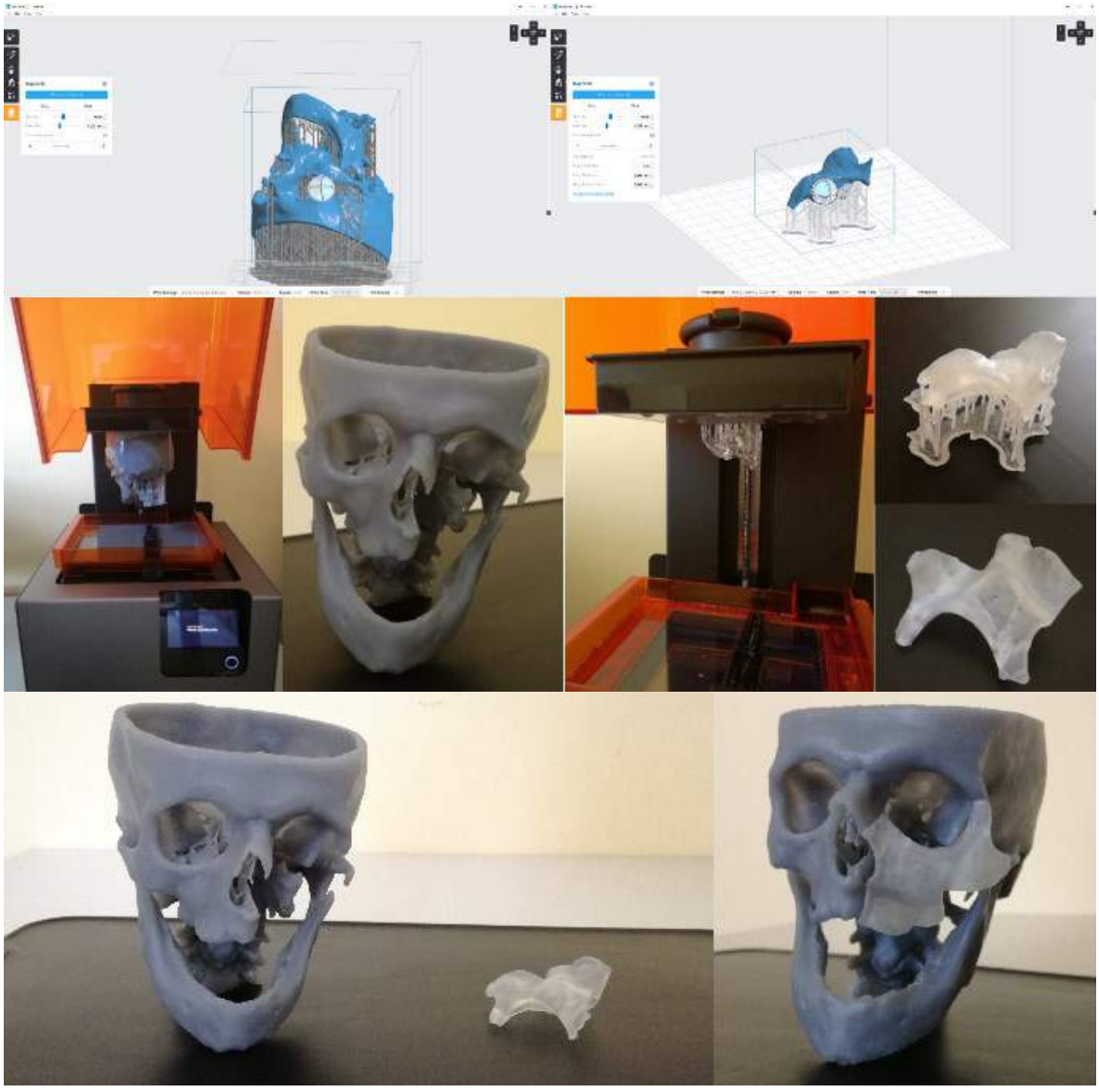

Figure14. Making skulls and implants - the ultimate model
Slika 14. Izrada lubanje i implantata - konačan model

4. Zaključak

Cilj ovog rada bio je konvertirati podatke iz CT sustava u CAD/CAM sustav te služeći se aditivnim postupkom stereolitografije izraditi fizički objekt. Kako aditivna proizvodnja ima široko područje primjene, tako se u ovom primjeru htjelo pokazati povezanost medicine i tehnike. Biomedicinsko inženjerstvo je jedna od grana inženjerstva s najbržim širenjem te su AM postupci jedan od važnijih alata. Dosadašnja rješenja više ne zadovoljavaju brzinom izrade i svojom preciznošću te je potreba za razvojem novih tehnologija sve veća.
U slučajevima kada nisu dostupni crteži, tehnička dokumentacija ili računalni modeli pristupa se reverznom inženjerstvu, kao što je i ovdje bio slučaj. CT snimak oštećene ljudske lubanje spremljen je kao DICOM format, koji je svojstven za medicinsku primjenu. Korištenjem softverskih programa, niz 2D slikovnih podataka transformirao se u računalni 3D model te je daljnjim postupcima napravljena rekonstrukcija, odnosno od postojećeg zdravog dijela dobiven je implantat koji je u mogućnosti nadomjestiti oštećeni dio. Rezultat je prihvatljiv, izrađeni implantat vrlo dobro naliježe na originalni dio lubanje. Postoji mala nepravilnost u predjelu gornje vilice koje se mogu riješiti dodatnim namještanjem u *Geomagic Design X*-u.
Ovo je bio pokazni primjer na jednom stvarnom modelu gdje se uz veću suradnju i povezanost s medicinskom strukom mogu proizvesti iskoristiva rješenja. Potrebno je proširivati znanja i više ulagati u istraživanje ovih

postupaka. Iako ima mnogo prednosti, još se uvijek o tome priča kao o fenomenu i iznimkama.

Zahvale/Acknowledgements

Rad je financijski podržan potporom Sveučilišta u Rijeci, ugovor broj 13.09.1.2.14
This work was financially supported by the University of Rijeka, Croatia, contract number 13.09.1.2.14.
Rad je financijski podržan potporom Sveučilišta u Rijeci, ugovor broj 13.09.1.2.10.
This work was financially supported by the University of Rijeka, Croatia, contract number 13.09.1.2.10.

Reference/References

[1] Perinić, M.: „Reverzno inženjerstvo", predavanje iz kolegija „Računalna simulacija proizvodnih procesa", Rijeka, 2016.

[2] S Interneta, http://www.izit.hr/usluge/povratno-inzenjerstvo-reverse-engineering/, 20.6.2017.

[3] S Interneta, http://likesuccess.com/img5610925, 21.6.2017.

[4] Pilipović, A.: „Osnovni pojmovi, definicije i podjela postupaka aditivne proizvodnje i prototipova", s Interneta, http://www.hok.hr/cehovi/3dprintanje, 25.6.2017.

[5] Godec, D.: „Značaj aditivnih postupaka proizvodnje tvorevina u suvremenom razvoju i proizvodnji", s Interneta, http://www.hok.hr/cehovi/3dprintanje, 25.6.2017.

[6] S Interneta, http://www.izit.hr/primjena/medicina/, 4.7.2017.

[7] Rovelo, P.: „Additive Manufacturing in the medical and dental technology industries", s Interneta, https://3dprintingindustry.com/news/additive-manufacturing-medical-dental-technologyindustries-80348/, 4.7.2017.

[8] Bartolo, P.; Bidanda, B.: „Bio – Materials and Prototyping Applications in Medicine", Springer, New York, 2008

[9] S Interneta, https://www.scribd.com/doc/125530395/Materijali-u-Medicini, 5.7.2017.

[10] Pilipović, A.; Pilipović, J.: „Aditivna proizvodnja", Polimeri, Vol.33 No.3-4, 135.-142. str., Zagreb, 2012.

[11] Guo, N.; Ming, C.L.: „Additive manufacturing; technology, applications and resarch needs", Front. Mech. Eng. 215.-243. str., 2013.

[12] S Interneta, http://anaruzic.wixsite.com/3dprinteri/vrste, 26.6.2017.

[13] Gibson, I.; Rosen, D.; Stucker, B.: „Additive Manufacturing Technologies", Springer, New York, 2015.

[14] S Interneta, https://en.wikipedia.org/wiki/DICOM, 30.6.2017.

[15] S Interneta, https://www.slicer.org/, 30.6.2017.

[16] Perinić, M.: „CAD/CAPP/CAM", predavanje iz kolegija „CAD/CAPP/CAM", Rijeka, 2017.

[17] S Interneta, http://www.topomatika.hr/Geomagic_design-x-RE.html, 3.7.2017.

ISSN 1847-7917

EBSD of aluminium powder compacts - preparation method for observation in dependence on powder size

Ľubomír OROVČÍK[1)]***, Martin NOSKO***[1)] ***and Alica ROSOVÁ***[2)]

1) Institute of Materials & Machine Mechanics, Slovak Academy of Sciences Dúbravská cesta 9, 845 13 Bratislava, **Slovakia**
2) Institute of Electrical Engineering, Slovak Academy of Sciences Dúbravská cesta 9, 841 04 Bratislava, **Slovakia**

author_ummsorov@savba.sk

Keywords
aluminium
grain size
index rate

Original scientific paper
Abstract: For successful EBSD analysis, the most important is preparation of sample surface which assures index-able Kikuchi patterns. In case of hard materials, it is sufficient to remove top surface layer with residual strain induced by polishing which could be done by standard metallographic procedures with final oxide polishing suspension. However, depending on the type of material, it is necessary to adapt sample preparation method. The aim of the work is to reveal effects of different types of preparation methods of aluminium prepared by powder metallurgy on the quality of Kikuchi pattern in dependence on the size of aluminium powder particles. Effect of polishing, polishing and large-beam Ar ion milling and focused Ga ion beam is analysed.

1. Introduction

The investigation of microstructure and alloy composition in material engineering is an interesting and important subject leading to improving their properties. Nowadays, Electron Backscattered Diffraction (EBSD) technique is steadily gaining popularity as a tool used for materials characterization at the micro-scale. EBSD is used for the investigation of crystalline sample microstructure, morphology, phase, and texture in crystalline samples [1]. Aluminum prepared by powder metallurgy route (PM) is one of the main candidates for material selection in different industries due to its excellent mechanical behavior, design easiness, high strength to weight ratio and manufacturability [2], [3] and [4]. Moreover, more than 80 years PM aluminium components are used in automobile industries and for light weight construction [5]. In case of EBSD techniques, the quality of measured surface is very important. It is necessary to remove scratches and surface layer affected by local stresses during classical preparation route by grinding and polishing. In case of conventional bulk materials (steel, titanium, copper, zinc, etc.) without important volume of oxides between grains, sufficiently strain-free surface could be reached by standard metallographic procedures with or without final oxide polishing suspension (OPS) technique. However, if material contains inner oxides, (usually materials manufactured via PM route) the preparation method depends on their amount since it decreases conductivity of material [6] and [7] leads to the decrease of index rate in EBSD. The preparation method depends on grain size (influenced by original powder particle size), process of powder manufacturing (e.g. milling or spraying) and compaction technique (hot extrusion, ECAP, forging, etc.). Therefore, it is necessary to adapt the sample preparation method respecting the above mentioned factors. Generally, lower grain size material requires more demanding sample preparation.
In case of EBSD observation of soft materials prepared by PM as aluminium or magnesium with grain size < 9 μm it is necessary to use polishing and different types of ion milling to remove surface with residual stresses appearing after classical preparation route which negatively influences quality of the Kikuchi pattern. The aim of this work is to reveal the effect of the preparation techniques on the quality of the EBSD measurement in dependence on the grain size of the PM aluminium produced through direct extrusion.

2. Material and methods of samples preparation

For this study, aluminium powders of different particle size (250 μm and 9 μm) were hot direct extruded at 450°C [8]. To study an effect of the preparation methods, all EBSD maps of cross-sections were acquired after grinding and polishing using automatic machine PRESI Mecatech 334 without additional etching. To remove deformation layer after mechanical grinding and polishing, final polishing step was performed by Oxide

Polishing Suspensions - Type S (OP-S). OP-S is especially suited for polishing of very ductile metals like refractory metals, aluminium, titanium, tungsten, copper and other materials. For lower grain size of aluminium, the surface was additionally modified by Ar ion milling with a GATAN PIPS II machine using 6kV voltage and etching time of 60 min and focused ion beam (FIB) milling performed by double-beam scanning microscope FEI Quanta 3D 200i using 30 keV Ga ions (the beam current of 1 nA) [6].

EBSD analysis was carried out using scanning electron microscope (SEM, Jeol JSM-7600F) equipped by EBSD detector (Oxford, NordlysNano, UK). In this particular set-up, the tilt of the sample was 70° with working distance of 25mm and magnification 1500x. The EBSD patterns were taken at locations of a square grid with 320 × 225 x 0,2 μm using electron accelerating voltage of 15 kV and current of approximately 12 nA. HKL Channel5 evaluation software was used to evaluate crystallographic misorientation. A noise reduction after EBSD was not performed to show and demonstrate index rate after different methods of sample preparation.

3. Results

There are differences in quality of surface in case of compacts manufactured from 250 μm powder size prepared by classical preparation route - grinding and polishing without OP-S shown in fig. 1a and using final OP-S polishing step (fig. 1c). The final OP-S polishing has removed scratches and revealed grains and grain boundaries by surface etching. Moreover, it has enhanced quality of Kikuchi pattern (fig. 1d in comparison to fig. 1b). The reason is that OP-S as chemical-mechanical polishing completely removes top surface layer containing scratches and deformations produced in preceding preparation steps. In previous research performed at IMMM SAS focused on EBSD observation of aluminium bulk materials, the index rate of 86% was gained for samples prepared by classical preparation route and 94% if final polishing by OP-S was used. Observation parameters were identical (15kV current 12nA, Aperture 1).

As mentioned in introduction, in case of aluminium powder compacts, the preparation is more difficult and strongly depends on powder particle size. Therefore, in case aluminium compacts made of lower particle size (<9 μm), volume ratio of oxides (oxides boundaries) in inner structure is higher. In process of hot extrusion the deformation of relatively small aluminium particles does not occur and the fragmentation of fine surface oxides as in for example larger particles (>9 μm) [6], [7] and [8] does not take place.

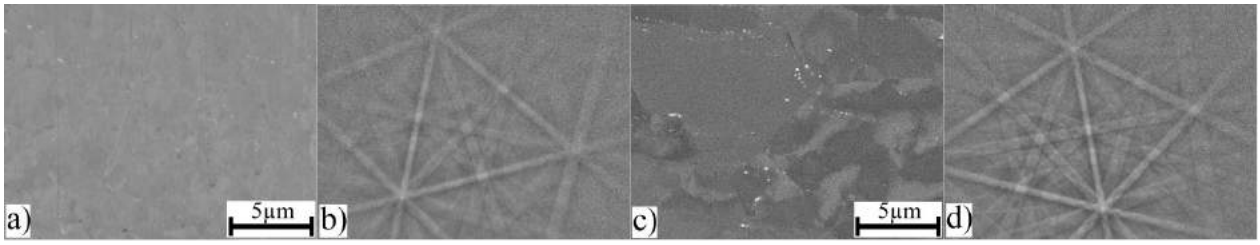

Figure 1. Microstructure and gained Kikuchi patterns of compacted aluminium powder made from 250 μm particles a) and b) classical preparation route and c) and d) classical preparation route with final OP-S polishing.

All Euler EBSD maps of the extruded compacts made using 250 μm powder in fig. 2a, (longitudinal direction) and in fig 2b (transverse direction) show differences in grain size. Index rate is 88% in case of longitudinal direction and 81% in case of transverse direction due to different density of grain and sub-grain boundaries. The un-indexed points (showed as green in fig. 2a and 2b) mainly present grain boundaries. The grain boundaries contain oxide layers of different thickness. As visible in top right corner marked in fig. 2b by red rectangle – rectangle, it illustrates technical limitations of observation in the case of smaller grain size due to sample preparation or chosen step size during data gathering. To obtain better index rate in case of lower grain size it is necessary to adapt suitable preparation process or to change observation parameters as gun voltage, gun current or step size due to possible overlapping of the Kikuchi pattern close to grain border which makes it impossible for proper evaluation [1], [9]. Moreover, different working distance could also help to enhance the indexation of the Kikuchi pattern.

.

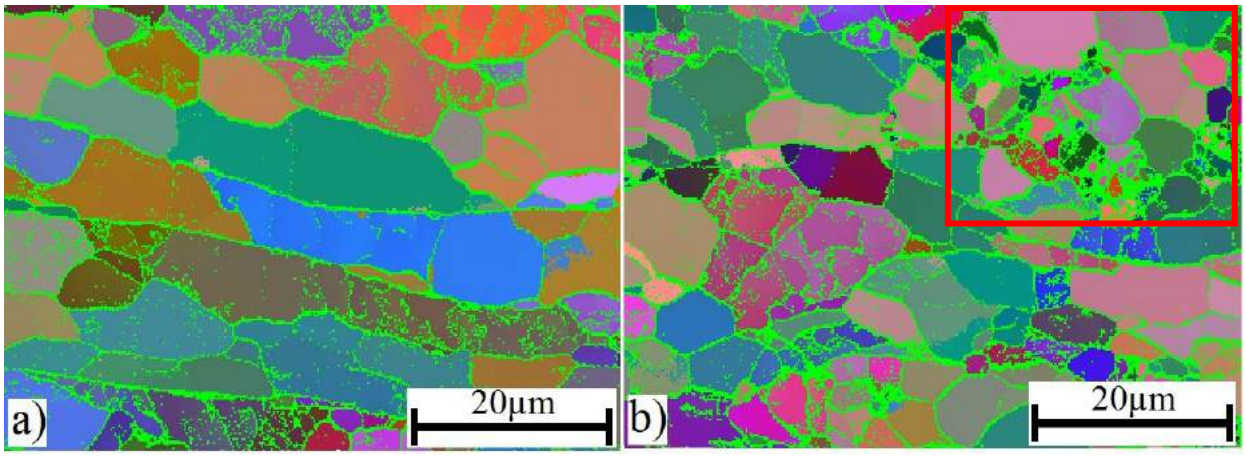

Figure 2. EBSD maps in Euler contrasts without noise reduction in a) longitudinal cross-section along to hot extrusion direction and b) transversal cross-section .

In fig.3, there is presented difference in dependence on preparation methods for 9 μm powder particle size. Figs 3a, b show microstructure and Kikuchi pattern after mechanical grinding and polishing. In fig. 3 c, d, there are microstructure and Kikuchi pattern after additional OPS. Fig. 3e, f, and 3g, h reveal effect of additional Ar ion milling and Ga focused ion beam milling, respectively. As can be seen in fig.3 a (grinding and polishing without final OP-S), the quality of surface is comparable with that obtained for 250 μm powder compact (fig. 1a), but quality of Kikuchi pattern is worse (compare figs. 1b and 3b). The same effect is also observed after polishing with final OP-S (compare figs. 1d and 3d). Improvement of surface quality is assured after preparation performed by Ar ion milling (fig. 3 e,f) due to removal of the residual surface stresses. In case of FIB technique, the quality of Kikuchi pattern is decreased probably due to damaging the material surface by Ga beam and implantation of the Al powder compacts by Ga. On the other hand, the FIB milling increased the index rate of Kikuchi patterns. In case of lower grain size e.g. 1 μm this method can be more effective than ion milling [6].

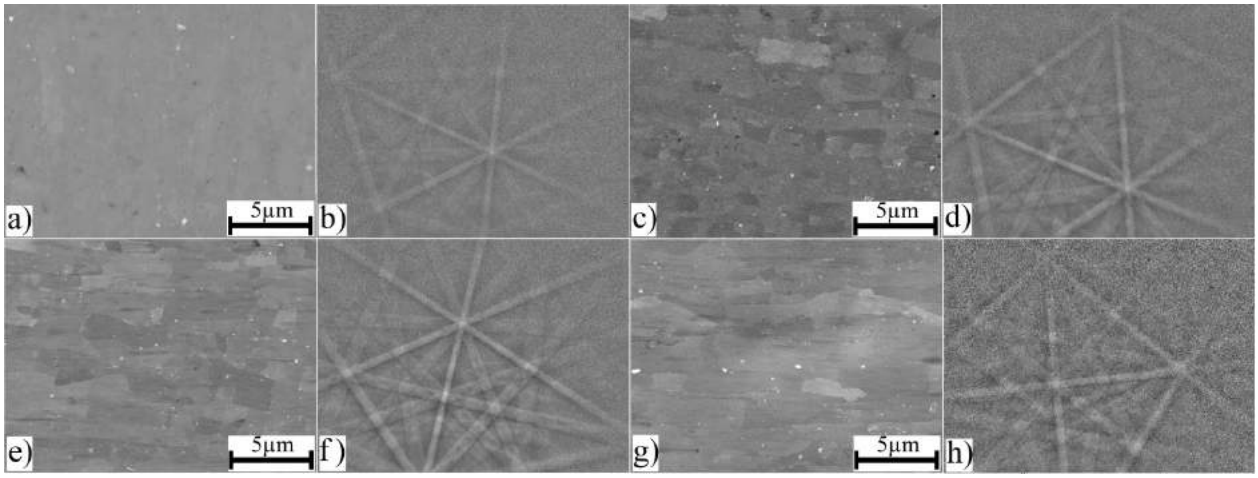

Figure 3. Microstructure of compacted aluminium powder made from 9 μm powder ; a) classical preparation route, c) classical preparation route with final OP-S step, e) with additional ion milling on PIPS II and g) via FIB. b), d), f) and h) are corresponding gained intensity of Kikuchi patterns.

Euler EBSD maps of PM compacts for 9 μm powder size in the longitudinal cross-section are shown in fig.4 in dependence on preparation method. Effect of polishing process with final OP-S polishing is shown in fig. 4a and after ion milling in fig.4b. Index rate is 54% for samples prepared with OP-S and 56% for additional ion milling applied. It suggests that in case of lower powder size, additional ion milling helps to remove surface residual stresses and to improve indexation.

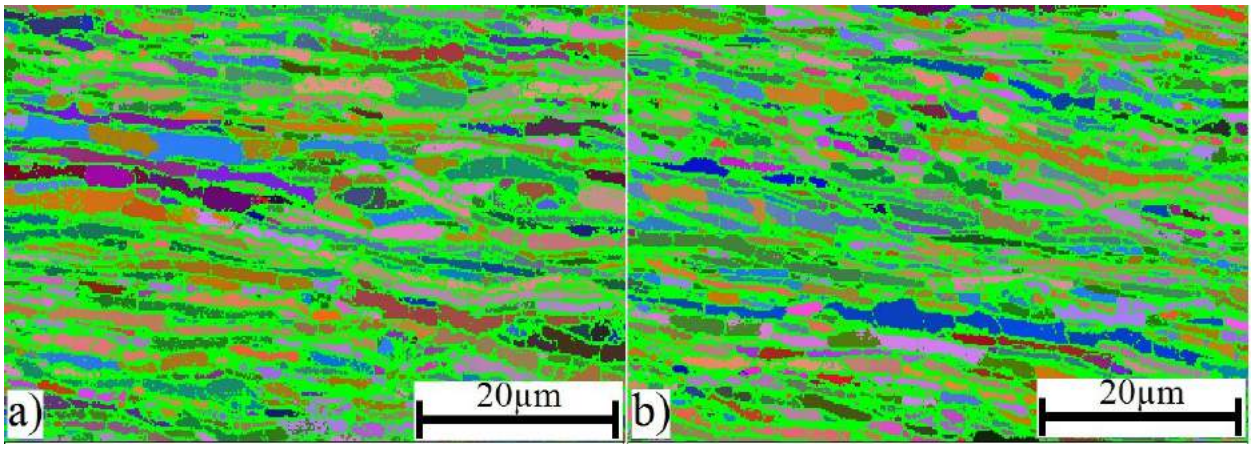

Figure 4. EBSD maps in Auler contrast band a) polishing surface with OP-S b) by Ion milling

4. Conclusion

- Effects of different sample surface preparation were observed on extruded compacts made using Al powders with particle size of 250 and 9 μm.
- In the case of 250 μm extruded compact, different index rates of 88% in longitudinal cross-section and 81% in transversal cross-section was observed after OP-S final polishing due to different grain boundary density.
- In case of compacts with powder particle size < 9 μm, it is necessary to adapt preparation technique using Ar ion beam milling to improve quality of measured surface and quality of Kikuchi pattern as well.
-

Acknowledgements

This work was supported by Slovak Foundation VEGA Grant 2/0158/16, VEGA Grant 2/0172/16, VEGA Grant 2/0144/17 and by Grant APVV-14-0936. Some results were acquired using infrastructure built during the projects ITMS 26240120006/ ITMS 26240120020.

REFERENCES

[1] Dingley D., (2004), *Progressive steps in the development of electron backscatter diffraction and orientation imaging microscopy*, Journal of Microscopy - Oxford Vol. 213, p 214-224

[2] Kah P., Rajan R., Martikainen J., Suoranta R., (2015), *Investigation of weld defects in friction-stir welding and fusion welding of aluminium alloys*, International Journal of Mechanical and Materials Engineering No 10, p 26

[3] Cical E., Duffet G., Andrzejewski H., Grevey D., Ignat S., (2005), *Hot cracking in Al-Mg-Si alloy laser welding–operating parameters and their effects*, Materials Science and Engineering A 395, p 1-9

[4] Kim J., Lim H., Cho J., Kim C., (2008), *Weldability during the laser lap welding of Al 5052 sheets*, Archives of Materials Science and Engineering No 31, p 113-116

[5] Lakshminarayanan A.K., Balasubramanian V., Elangovan K., (2007), *Effect of welding processes on tensile properties of AA6061 aluminium alloy joints*, The International Journal of Advanced Manufacturing Technology No 40, p 286-296

[6] Balog M., Krizik P., Nosko M., Hajovska Z., Riglos M.V.C., Rajner W., Liu D.-S., Simancik F., (2014) *Forged HITEMAL: Al-based MMCs strengthened with nanometric thick Al_2O_3* skeleton, Materials Science and Engineering A 613, p 82-90

[7] Balog M., Poletti C., Simancik F., Walcher M., Rajner W., (2011) *The effect of native Al_2O_3 skin disruption on properties of fine Al powder compacts*, Journal of Alloys and Compounds 509S, p S235-S238

[8] Krizik P., Balog M., Bajana O., Riglos M. V. C., Svec P. Sr., (2017) *Warm Pressing of Al Powders: An Alternative Consolidation Approach*, Chapter Light Metals, Part of the series The Minerals, Metals & Materials Series, p 463-469

[9] Britton T.B., Maurice C., Fortunier R., Driver J.H., Day A.P., Meaden G., Dingley D.J., Mingard K., Wilkinson A.J., (2010) *Factors affecting the accuracy of high resolution electron backscatter diffraction when using simulated patterns,* Ultramicroscopy No.110 p. 1443-1453

ISSN 1847-7917

Modeling and Optimization of Tensile Strength of ABS Parts Manufactured by the Fused Deposition Modeling Process

Ivan PEKO [1)]***, Jure KROLO*** [1)],
Petra BAGAVAC [1)]***, Stefan ĐURIĆ*** [2)],
Nikola KOSTIĆ [2)], ***Andrej BAŠIĆ*** [1)]
1) University of Split, Faculty of Electrical Engineering, Mechanical Engineering and Naval Architecture, Department for Production Engineering
Sveučilište u Splitu, Fakultet elektrotehnike, strojarstva i brodogradnje, R. Boskovica 32, 21 000 Split, Croatia
2) University of Kragujevac, Faculty of Engineering
Univerzitet u Kragujevcu, Fakultet inženjerskih nauka
Sestre Janjić 6, 34 000 Kragujevac, Serbia

ipeko@fesb.hr
jkrolo@fesb.hr
pstrizak@fesb.hr
stefandjuric992@gmail.com
nikollakg93@gmail.com
abasic@fesb.hr

Keywords
Fused Deposition Modeling
Tensile Strength
Cost
Modeling
Optimization

Ključne riječi
Taložno očvrćivanje materijala
Vlačna čvrstoća
Trošak
Modeliranje
Optimizacija

Original scientific paper

Abstract: In the last two decades additive manufacturing (AM) technology has been emerged as a powerful fabrication method to obtain finished components within a short span of time, without any tooling requirements and minimal human interface. Fused Deposition Modeling (FDM) is one of the most used AM techniques. It has an ability to produce a complex functional geometries with a good properties. Properties mainly depend on process parameters and can be improved by setting parameters at appropriate levels. In this paper, mathematical models for prediction of ultimate tensile strength (UTS) and cost were developed. Process parameters whose influence was analyzed are top and bottom surface layers number, fill spacing and layer resolution. Experiments were conducted on specimens manufactured from Acrylonitrile butadiene styrene (ABS) material. Design Expert software and ANOVA analysis were used for mathematical modelling and optimization and based on that process parameters that lead to maximal tensile strength and minimal cost were defined. Thus obtained results will have practical meaning for users involved in FDM additive manufacturing process.

Izvorni znanstveni rad

Sažetak: U posljednja dva desetljeća tehnologija aditivne proizvodnje (AM) se istaknula kao moćna metoda izrade za dobivanje gotovih komponenata u kratkom vremenu, bez potrebnih alata i uz minimalno učešće čovjeka. Taložno očvršćivanje materijala (FDM) je jedan od najčešće korištenih postupaka aditivne proizvodnje. Uz pomoć njega se mogu proizvesti kompleksni funkcionalni geometrijski oblici s dobrim svojstvima. Svojstva uglavnom ovise o parametrima samog procesa i mogu biti poboljšana postavljanjem parametera na odgovarajuće nivoe. U ovome radu razvijeni su matematički modeli za predviđanje vlačne čvrstoće (UTS) i troškova. Parametri procesa čiji utjecaj je analiziran su broj nanesenih slojeva materijala na početku i na kraju izrade, razmak između slojeva i rezolucija slojeva. Eksperimenti su provedeni na uzorcima izrađenim iz akrilonitril-butadien stirel (ABS) materijala. Za matematičko modeliranje su primjenjeni Design Expert softver i ANOVA analiza i temeljem toga su definirani parametera procesa kojima se postiže maksimalna vlačna čvrstoća i minimalni trošak. Tako dobiveni rezultati će imati praktičan značaj za korisnike uključene u FDM postupak aditivne proizvodnje.

1. Introduction

Additive manufacturing (AM) is relatively new technology used to fabricate three dimensional computer aided designed (CAD) component by building it in layers of material. Today on the global market exist several different AM processes. These processes differ mainly according to the type of material used in production process and a manner in which the layers of material apply and join together. Among all available AM processes the Fused Deposition Modeling (FDM) is one of the most popular due to its lower production costs, simple manipulation and higher strength of fabricated components. In FDM process parts are built by applying polymer wire material in a molten state to the moveable platform according to computer controlled paths (x-y plane). Extruded material quickly solidifies at a room temperature and thereby generates the first layer of component. After generating the first layer the building platform moves down by the thickness of the new layer (z axis) and furtherly next layer applies. Building process is repeated until a complete part is generated. If some complex geometric parts should be created then it is required a supporting material structure. Once the model is built a supporting structure can be easily removed by melting in water of fracturing. Also built parts can be

further processed by conventional machining operations such as turning, milling or grinding. Materials that are mainly used in this process are plastics as ABS, PLA, PC, PP, PE-HD, PE-LD etc.[1][2][3]. Parameters of FDM process differently affect the properties of build parts. To analyze their effects and to find values that lead to optimal responses many authors conducted a comprehensive researches. Sood et al. [4] made an extensive study to understand the effect of five important FDM parameters such as layer thickness, part build orientation, raster angle, raster width and air gap on the compressive stress of test specimens. They also developed a statistically validated predictive equations using artificial neural network approach and regression analysis and found optimal parameter settings through quantum-behaved particle swarm optimization (QPSO). Raut et al. [5] investigated the effect of the built-up orientation on the mechanical properties and total cost of the FDM parts. Considered responses were mechanical and bending strength . The specimens were prepared at three different orientations (0°, 45°, 90°) and in three different axes with the axis of rotation parallel to the larger length of the specimen and perpendicular to the other two sides. Onwubolu et al. [6] analyzed the influence of layer thickness, part orientation, raster angle, raster width and air gap on tensile strength of test specimens. Mathematical models relating the response with the process parameters were developed using group method of data handling (GMDH). Optimal process parameters that lead to maximized tensile strength were defined through application of differential evolution (DE) algorithm. Panda et al. [7] performed experiments to analyze the impact of layer thickness, orientation, raster angle, raster width and air gap on tensile, flexural and impact strength. Response surface methodology (RSM) was used for mathematical modeling and bacterial foraging optimization algorithm (BFOA) for finding optimal process parameters settings. Mohamed et al. [8] studied the influence of layer thickness, air gap, raster angle, build orientation, road width and number of contours using Q-optimal response surface methodology. Their effects on build time, feedstock material consumption and dynamic flexural modulus were critically examined. Mathematical models were formulated to describe a functional relationship between the processing conditions and the process quality characteristics. ANOVA technique was employed to check the adequacy and significance of mathematical models and furtherly optimal setting of process parameters were determined. Nidagundi et al. (9) performed parametric optimization of ultimate tensile strength, surface roughness, dimensional accuracy and manufacturing time using Taguchi method and ANOVA. Input process parameters that were considered were layer thickness, orientation angle and fill angle. Validation of optimal conditions was conducted by making verification experiment. Panda et al. [10] carried out performance modelling of FDM parts using two soft computing (SC) methods such as multi-gene genetic programming (MGGP) and general regression neural network (GRNN). Proposed SC models predict compressive strength of fabricated specimens in terms of input process parameters, layer thickness, orientation and raster angle. The predictions of compressive strength by mathematical models were evaluated against the data generated in experimental study. Liu et al. [11] considered three responses that characterize the mechanical properties of FDM parts, tensile strength, flexural strength and impact strength. As significant factors that contribute to the strength of a FDM product were identified deposition orientation, layer thickness, deposition style, raster width and raster gap. The influences of input parameters on responses were analyzed by the use of ANOVA analysis. Finally, based on the gray relational analysis, process parameters values that optimize mechanical properties of built parts were obtained. Except these mentioned, there is also a large number of other research papers dealing with modeling and optimization of FDM parts properties related with various input process parameters.

In present article experiments were conducted on samples fabricated from ABS material. ABS parts are sufficiently resistant to heat, chemicals and moisture and that enables FDM parts to be used for prototyping, functional testing and installation. It was analyzed the influence of input process parameters, top and bottom surface layers number, fill spacing and layer resolution on ultimate tensile strength and cost. Mathematical modelling and optimization were performed using regression analysis (RA) and Design Expert software.

2. Experimental procedure

In order to optimize FDM process and develop mathematical models design of experiments (DOE) method was utilized. Usually, DOE method is followed by analysis of variance (ANOVA) and regression analysis (RA). These mathematical models should be able to predict process output responses based on some influential input parameters. In this paper, DOE was prepared using D-Optimal response surface design [12]. D-optimal design is very often used because offers the possibility of process optimization. Furthermore, selection of both numerical and categorical factors are possible. In order to optimize FDM process, influence of fill spacing, layer resolution and number of top and bottom surface layers on built samples maximal tensile strength and material cost are investigated. Numerical factors, in this case, are top and bottom surface layers number in range from 3 to 15 and fill spacing in range from 2 mm to 15 mm. The categorical factor is layer resolution and it is varied on three levels, 70 μm, 200 μm and 300 μm. Main aim is to optimize process and to develop mathematical models which will be enabled to predict the cost of material for desired ultimate tensile

strength (UTS) of built samples. The second goal is to find optimal parameters to produce FDM samples with good mechanical properties and lower cost. Utilizing DOE and D-Optimal design experimental plan is created by means of ''Design Expert'' software (Table 1). Fixed input parameters are: building material: ABS, print mode: custom, print strength: strong, print pattern: cross, outer walls: 1.

Table 1. Design of experiment and results
Tablica 1. Dizajn eksperimenata i rezultati

Simulation	Top and bottom surface layers number	Fill spacing [mm]	Layer resolution [μm]	UTS [MPa]	Cost [€]
1	6	8.50	200	9.74	1.14
2	10	2.00	300	10.94	1.06
3	3	7.39	300	6.19	0.69
4	15	15.00	70	17.61	1.59
5	15	15.00	200	12.45	1.39
6	15	9.62	300	8.42	0.97
7	8	15.00	300	9.50	1.00
8	8	15.00	300	8.97	1.00
9	15	2.00	70	20.30	2.22
10	9	8.50	70	12.83	1.28
11	9	8.50	300	10.17	1.13
12	3	8.50	70	8.49	1.02
13	6	2.00	70	14.82	1.84
14	15	2.00	200	11.70	1.49
15	3	15.00	70	6.83	0.73
16	9	2.81	200	12.38	1.60
17	3	15.00	200	7.69	0.79
18	15	15.00	200	9.82	1.37
19	15	15.00	70	17.67	1.57
20	10	2.00	300	11.83	1.05
21	15	9.62	300	8.88	0.96
22	3	2.00	200	8.52	1.19

According to experimental plan, 22 experiments should be performed. As shown in Tab. 1, AM machine was set to build part with top and bottom surface layer number 3, 6, 8, 9, 10 and 15, values of fill spacing are 2 mm, 2.81 mm, 7.39 mm, 8.50 mm, 9.62 mm and 15 mm. Finally, layer resolutions are 70 μm, 200 μm and 300 μm. Experimental work was conducted on a CubePro (3D Systems) additive manufacturing machine (Fig. 1a). Test specimens were generated according to standard HRN EN ISO 527:2012 (Fig. 1b). Building material was applied in layers in z axis (Fig. 1c). Furthermore, ultimate tensile strength evaluation was performed on universal testing machine ''Instron 8801'' (Fig. 2a).

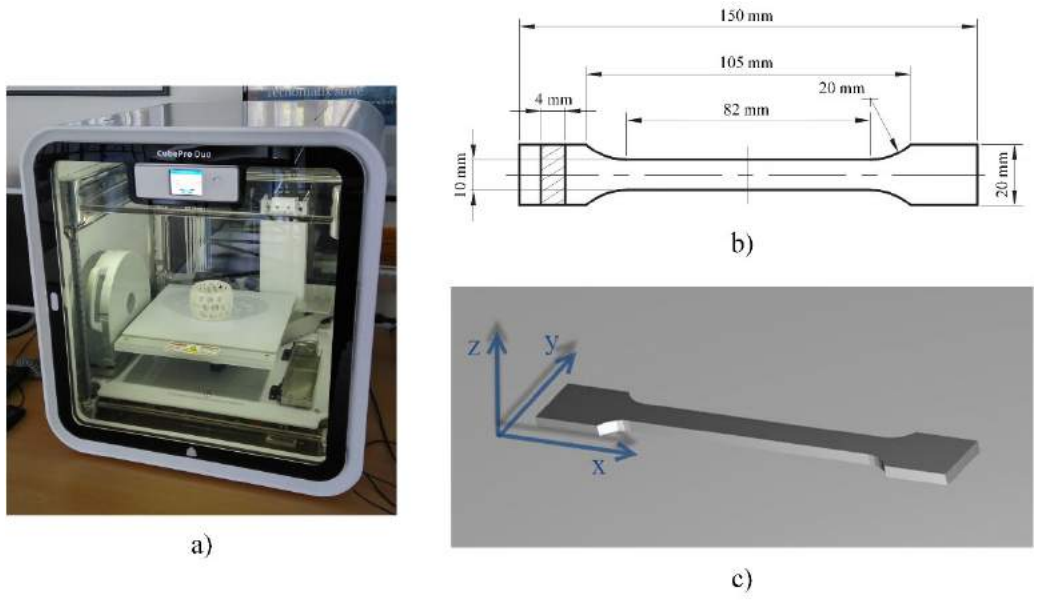

Figure 1. a) CubePro additive manufacturing machine, b) Test specimen dimensions, c) Building direction
Slika 1. a) CubePro uređaj za aditivnu proizvodnju, b) Dimenzije ispitnog uzorka, c) Smjer izrade

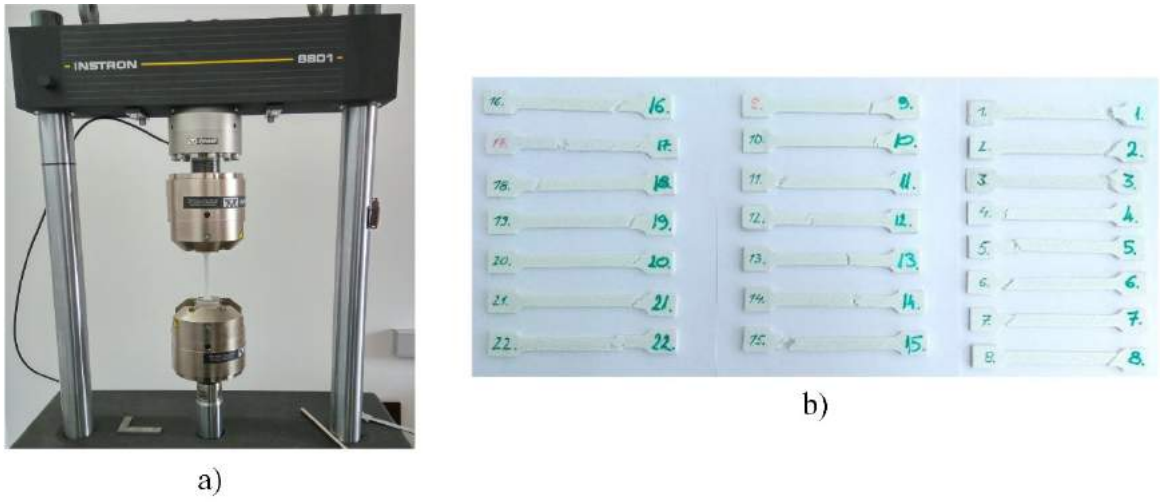

Figure 2. a) Universal tensile testining machine ''Instron 8801'', b) 22 samples after tensile testing
Slika 2. a) Univerzalna kidalica ''Instron 8801'', b) 22 uzorka nakon vlačnog testa

3. Results and analysis

After experiments, obtained results for the ultimate tensile strength are in the range from 6.19 MPa to 20.30 MPa, while samples material cost is in the range from 0.69 € to 2.22 €. In order to create mathematical models, RA and ANOVA are performed by means of Design-Expert software. According to analysis three quadratic mathematical models were proposed, one for each categorical factor (Table 2). Also, ANOVA indicates that all three parameters have an influence on UTS. R-Squared, Adj R-Squared, Pred R-Squared and Adeq Precision in this case are 0.9371, 0.9056, 0.8139 and 18.455, respectively. Three mathematical models for each categorical factor predict UTS based on input fill spacing and surface layers number are presented in Table 2. For further notice, surface layers number will be denoted as A model term, while fill spacing will be denoted as B model term.

Table 2. Mathematical models for UTS
Tablica 2. Matematički modeli za vlačnu čvrstoću (UTS)

Layer resolution	Mathematical models	Eq.
70 µm	$UTS = 4.35429 + 1.82541 \cdot A - 0.14126 \cdot B - 0.053183 \cdot A^2$	(1)
200 µm	$UTS = 5.74949 + 1.26549 \cdot A - 0.14126 \cdot B - 0.053183 \cdot A^2$	(2)
300 µm	$UTS = 5.13681 + 1.15089 \cdot A - 0.14126 \cdot B - 0.053183 \cdot A^2$	(3)

Figure 3. in continuation is a graphical representation of the influence of top and bottom surface layers number and fill spacing value on UTS for each layer resolution (70 µm, 200 µm and 300 µm).

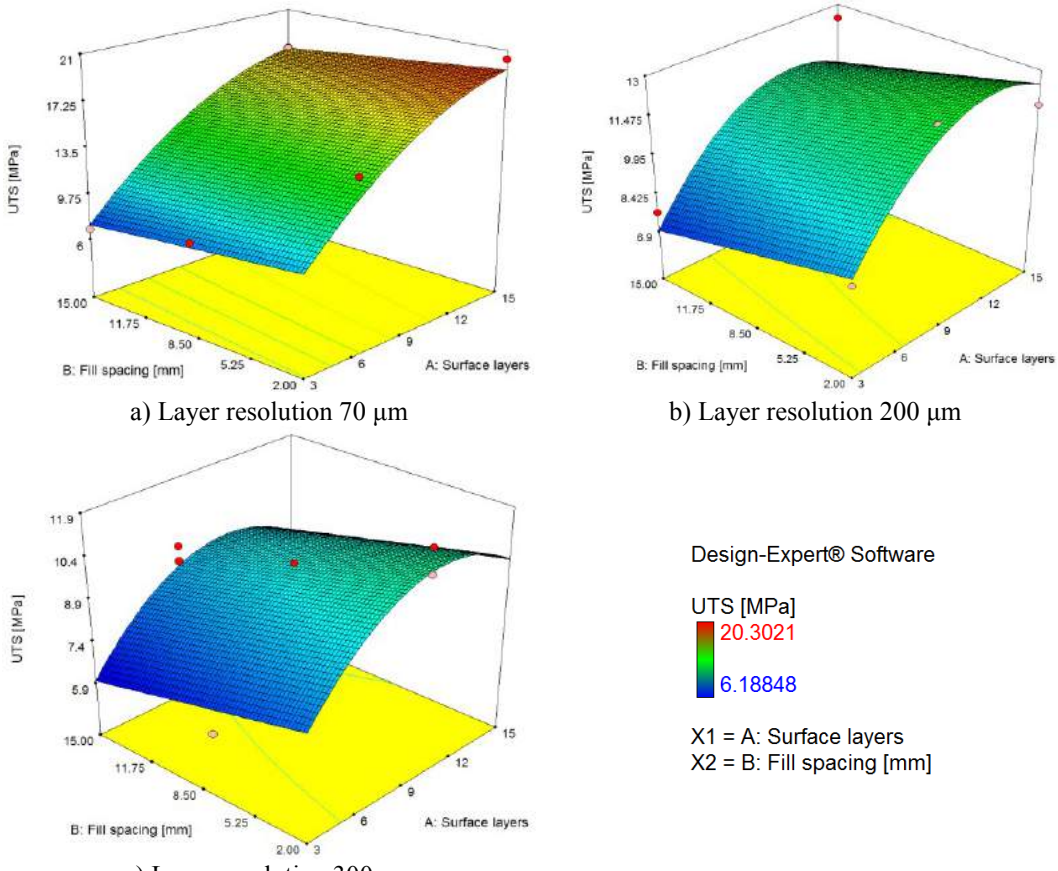

Figure 3. Influence of fill spacing and top and bottom surface layers number on ultimate tensile strength for three different layers resolution (70 µm, 200 µm and 300 µm)
Slika 3. Utjecaj razmaka između slojeva i broja nanesenih gornjih i donjih slojeva materijala na vlačnu čvrstoću za tri različite rezolucije slojeva (70 µm, 200 µm and 300 µm)

Generally, the higher number of surface layers increase UTS, while the higher value of fill spacing decrease UTS, (Figure 3). For samples produced with layer resolution 70 µm influence of surface layers number of the sample on UTS is more pronounced than the influence of fill spacing, (Figure 3a). However, the influence of fill spacing on UTS is more pronounced for samples produced with layer resolution 200 µm and 300 µm than for those with 70 µm layer resolution, (Figure 3b and 3c). However, for samples produced with layer resolution 200 µm and 300 µm and one chosen fill spacing in range from 2 mm to 15 mm, a number of surface layers between 12 and 15 provide similar results in UTS. Overall, lowest values of UTS are for layer resolution 300 µm, while highest are for layer resolution 70 µm.

Statistical analysis was also done and for material cost evaluation and also three linear mathematical models were proposed, one for each categorical factor, (Table 3). Also, ANOVA indicates that all three parameters have the influence on cost. R-Squared, Adj R-Squared, Pred R-Squared and Adeq Precision in this case are 0.9117, 0.8573, 0.7255 and 17.257, respectively. Three mathematical models for each categorical factor predict material cost based on input fill spacing and surface layers number are presented in Table 3.

Table 3. Mathematical models for cost evaluation
Tablica 3. Matematički modeli za procjenu troška

Layer resolution	Mathematical models	Eq.
70 μm	$Cost = 1.36282 + 0.068244 \cdot A - 0.057569 \cdot B$	(4)
200 μm	$Cost = 1.12455 + 0.039034 \cdot A - 0.024704 \cdot B$	(5)
300 μm	$Cost = 0.85449 + 0.014560 \cdot A - 1.87306 \cdot 10^{-3} \cdot B$	(6)

Figure 4. in continuation is graphical representation of influence of top and bottom surface layers number and fill spacing value on cost of the specimens for each layer resolution.

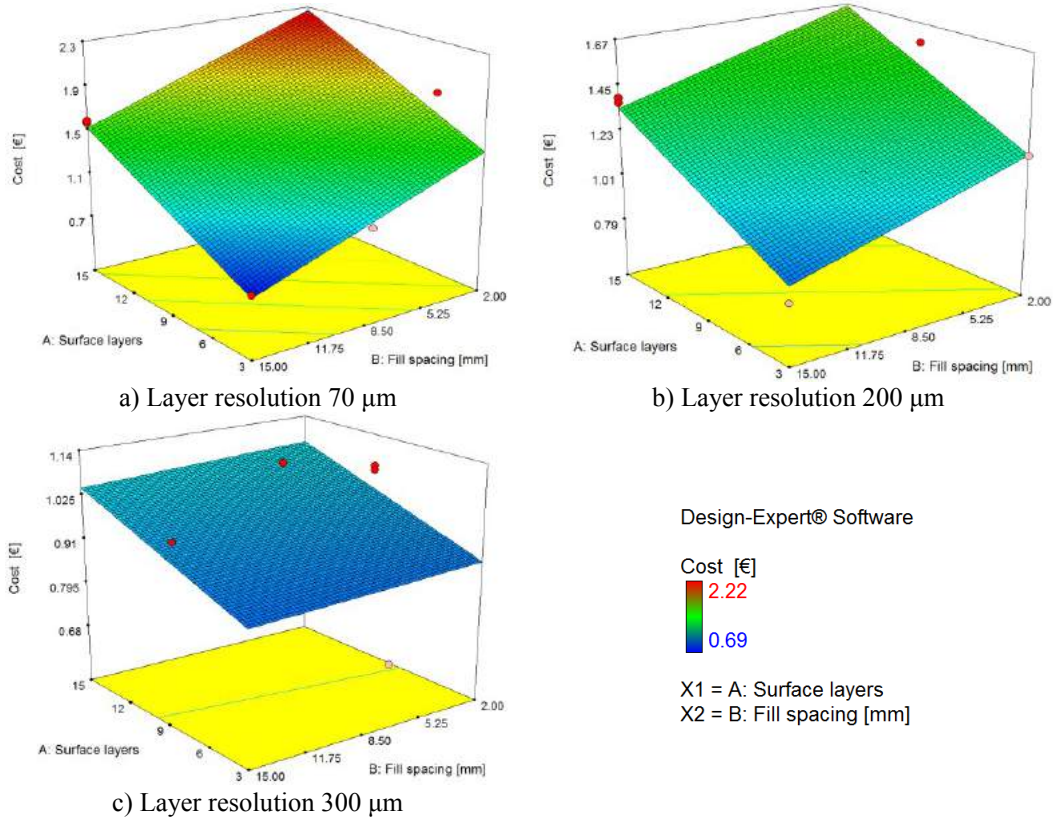

a) Layer resolution 70 μm

b) Layer resolution 200 μm

c) Layer resolution 300 μm

Figure 4. Influence of fill spacing and top and bottom surface layers number on material cost for three different layers resolution (70 μm, 200 μm and 300 μm)

Slika 4. Utjecaj razmaka između slojeva i broja nanesenih gornjih i donjih slojeva materijala na trošak materijala za tri različite rezolucije slojeva (70 μm, 200 μm and 300 μm)

According to the results for layer resolution 70 μm and 200 μm both fill spacing and surface layers number have great influence on the material cost, (Figure 4a and 4b). Fill spacing decrement and surface layers number increment results with the material cost increase. However, for samples with layer resolution 300 μm, the influence of fill spacing on samples cost is not that pronounced as for samples with layer resolutions 70 μm

and 200 μm, (Figure 4c). As expected highest cost (2.22 €) have samples with layer resolution 70 μm, 15 surface layers and fill spacing 2 mm, but this samples also have higher UTS (20.30 MPa). On the other hand lowest cost (0.69 €) have sample produced with 300 μm layer resolution, 3 surface layers and 7.39 mm fill spacing. Furthermore, according to the results as already was mentioned highest values of UTS have samples with 70 μm layer resolution, while lowest have samples with 300 μm. Influence of fill spacing, for samples with 70 μm layer resolution, is much less pronounced on the UTS than on the material cost of the same samples.

Thus, authors of this work found that optimization of the process could be performed in order to find which parameters are better to produce samples with good mechanical properties, but also with reduced price. Utilizing Design-Expert software package and D-Optimal response surface methodology optimization of the process was performed. According to optimization results samples produced with 11 surface layers, fill spacing 15 mm and layer resolution 70 μm will have UTS 15.79 MPa and their cost will be 1.24 €.

According to this results, it is possible to produce samples which have 77.8 % of maximal UTS (20.3 MPa) obtained in this research, but these samples also cost 45.9 % less than those with the maximal value of UTS (2.22 €).

4. Conclusion

In the present work an attempt has been made to study the effect of three processing parameters, layer resolution, fill spacing and surface layers number on tensile strength and cost of FDM built parts. The experimental results were used to establish a mathematical relationship between tensile strength and cost (output) and process parameters. Mathematical models were validated by using statistical measures. Effect of factors and their interactions were explained using response surface plots. Also, the models were proven to be effective for further analysis to define the process parameters values that lead to optimal combination of tensile strength and cost. According to that, desirability analysis was performed and it was found out the process parameters settings that result in minimal cost and maximal tensile strength should be 11 surface layers, fill spacing 15 and layer resolution 70 μm. Future research will take into consideration other mechanical properties of FDM built parts and their modeling and optimization procedures.

5. Acknowledgement

This work has been fully supported by Croatian Science Foundation under the project Innovative Smart Enterprise – INSENT (1353).

REFERENCES

[1] Peko, I., Bajić, D., Veža, I., (2015), *Selection of additive manufacturing process using the AHP method*, International Conference ''Mechanical Technologies and Structural Materials'', Split, Croatia

[2] Dandgaval, O., Bichkar, P., (2016), *Rapid prototyping technology-study of fused deposition modeling technique*, International Journal of Mechanical and Production Engineering, Vol. 4, Iss. 4, pp. 44-47.

[3] Novakova Marcincinova, L., Novak Marcincin, J., (2012), *Applications of rapid prototyping fused deposition modeling materials*, Annals of DAAM for 2012 and Proceedings of the 23rd International DAAM Symposium, Vol. 23, No.1, DAAM International, Vienna, Austria

[4] Sood, A. K., Ohdar, R. K., Mahapatra, S. S., (2012), *Experimental investigation and empirical modeling of FDM process for copmpressive strength improvement*, Journal of Advanced Research, Vol. 3, pp. 81-90.

[5] Raut, S., Jatti, V. S., Khedkar, N. K., Singh, T. P., (2014), *Investigation of the effect of built orientation on mechanical properties and total cost of FDM parts*, Procedia Matreials Science, Vol. 6, pp. 1625-1630.

[6] Onwubolu, G. C., Rayegani, F., (2014), *Characterization and Optimization of Mechanical Properties of ABS Parts Manufactured by the Fused Deposition Modelling Process*, International Journal of Manufacturing Engineering, Volume 2014, Article ID 598531

[7] Panda, S. K., Padheee, S., Sood, A. K., Mahapatra, S. S., (2009), *Optimization of fused deposition modelling (FDM) process parameters using bacterial foraging technique*, Intelligent Information Management, Vol. 1, pp. 89-97.

[8] Mohamed, O. A., Masood, S. H., Bhowmik, J. L., (2016), *Mathematical modeling and FDM process parameters optimization using response surface methodology based on Q-optimal design*, Applied Mathematical Modelling, Vol. 40, Iss. 23-24, pp. 10052-10073.

[9] Nidagundi, V. B., Keshavamurthy, R., Prakash, C. P. S., (2015), *Studies on Parametric Optimization for Fused Deposition Modelling Process*, Materialstoday: Proceedings, Vol. 2, Iss. 4-5, pp.1691-1699.

[10] Panda, B. N., Bahubalendruni Raju, M. V. A., Biswal, B. B., (2015), *A general regression neural network approach for the evaluation of compressive strength of FDM prototypes*, Neural Computing and Applicationa, Vol. 26, Iss. 5, pp. 1129-1136.

[11] Liu, X., Zhang, M., Li, S., Si, L., Peng, J., Hu, Y., (2017), *Mechanical property parametric appraisal of fused deposition modeling parts based on the gray Taguchi method*, The International Journal of Advanced Manufacturing Technology, Vol. 89, Iss. 5, pp. 2387-2397.

[12] Vinayagamoorthy, R., Rajeswari, N., Vijayshankar, S., Balasubramanian, K., (2014), *Drilling Performance Investigations on Hybrid Composites by Using D-Optimal Design*, International Review of Mechanical Engineering, Vol. 8, No. 5, pp. 952-961.

ISSN 1847-7917

Residual stress determination by neutron diffraction in low-carbon steel wires with accumulated shear deformation

***Massimo ROGANTE*[1)], *Pavol MIKULA*[2)], *Pavel STRUNZ*[2)], *Anatoliy ZAVDOVEEV*[3)]**

1) Rogante Engineering Office, I-62012 Civitanova Marche, **Italy**
2) Nuclear Physics Institute ASCR v.v.i., 25068 Řež near Prague, **Czech Republic**
3) Paton Electric Welding Institute of NAS, Bozhenko n. 11, 03680 Kiev, **Ukraine**

main@roganteengineering.it

Keywords

Residual stresses
Neutron diffraction
Steel
08G2S GOST 1050
Shear deformation

Scientific paper

Abstract: Modern methods of severe plastic deformation (SPD) currently allow obtaining the ultrafine-grained (UFG) structure nearly in any material. In the manufacturing process of wire with UFG structure, a main restriction is the continuous drawing scheme in which this process occurs, thus it is important to consider the factors affecting the drawing efficiency. Despite the data on SPD steels such as strength, plasticity and conductivity, obtained by classical methodologies, further investigations are needed: a key information is the residual stresses (RS) status, and RS determination is an essential issue to improve knowledge of SPD effects.

In this work, 15 wires samples made of low-alloyed quality structural steel Grade 08G2S GOST 1050 with accumulated shear deformation - as result of rolling with shear of the metal ingot and conventional wire drawing - have been investigated by neutron diffraction (ND). Results provide substantial data helping to evaluate the effect of shear deformation on RS of the considered steel, as well as additional support to complement the information already achieved by using the other characterization methodologies. Knowledge of the RS status can help developing a low-carbon wire drawing technology with needed manufacturability and efficiency, playing a decisive role in the debugging of material selection and engineering design requirements.

1. Introduction

Contemporary approaches of SPD consent to get the UFG structure almost in several materials, and to produce a wire with UFG involves a continuous drawing scheme. A typical volume of orders, e.g., is calculated in tons by weight and in tens of thousands of kilometres by length. SPD, hence, should take place while drawing using special dies without reduction of process efficiency. In this case, it is very essential to take into account the parameters affecting the drawing efficiency while developing the technology, based on the SPD process. These factors include, e.g., the speed of wire passage through the die, the required number of passes and the method of alternation of dies with shear and a standard round shape dies. Optimization of these parameters will permit creating a low-carbon wire drawing technology with required manufacturability and efficiency. Shear deformation is in the base of SPD methods: SPD leads to significant grain refinement, thus it allows achieving enhanced properties [1]. Besides SPD materials combines unique complex of properties such as high strength with maintain level of plasticity.

Previous studies have shown the effect of SPD on low-carbon steel properties [2-5]. In particular, structural and physico-mechanical properties changes of low-carbon steel were examined. On example of rolling with shear [2], it was shown that shear deformation induces micro-pore healing during the consequent process of cold drawing.

This feature reflects on metal's density and conductivity. These data are in good agreement with the microstructural analysis already carried out by small angle neutron scattering (SANS) on low-carbon steel

Symbols/Oznake

d_{hkl}	- lattice spacing, nm -	θ_{hkl}	- diffraction angle, degrees -
$d_{0,hkl}$	- unstressed lattice spacing, nm -	λ	- neutron wavelength, Å -
		K	- electrical conductivity, Sm m/mm^2 -
	Greek letters/Grčka slova		
ε_{hkl}	- lattice strain -	σ	- stress, MPa -

wires subjected to consequent rolling with shear and cold drawing. The saturation of micro-inhomogeneities (SANS scattered objects size) accumulation for rolling with shear metal was registered instead of standard rolling metal. Those results are closely correlated with the curves of the electrical conductivity (see Figures 1 and 2).

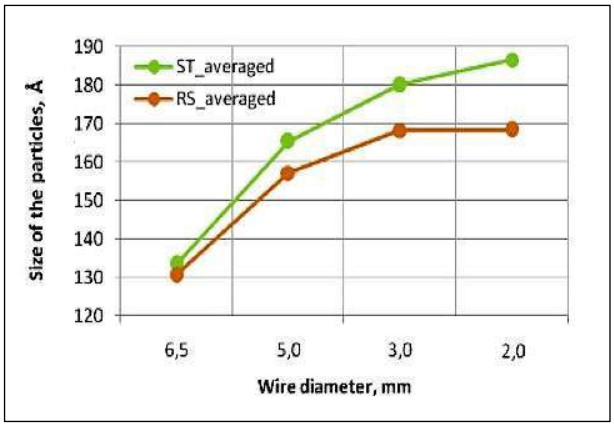

Figure 1. Graphs of the particle size distribution from the wire diameter, for averaged size of the particle [6].

Despite the amount of data on SPD steels such as strength, plasticity, conductivity, further investigations are needed. One of the key information is the RS status, and RS determination is an essential issue to improve knowledge of SPD effects. Last development of continuous SPD is drawing with shear technology (DShT), which includes shear deformation [7-8].

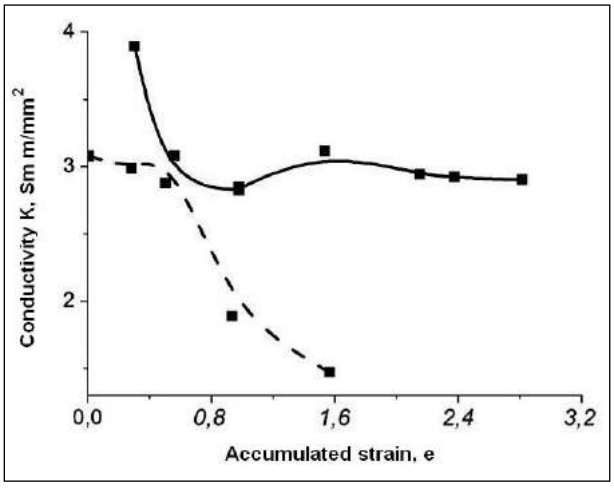

Figure 2. Electrical conductivity vs. accumulated strain (deformation of drawing): rolling with shear with cold drawing (solid line) and standard rolling with cold drawing (dotted line).

The results obtained by adopting neutron techniques in materials analysis have often proved their strong support for better understanding of material's characteristics and behaviour [9-11]. In this connection, the main objective of the present work has been to evaluate the effect of shear deformation on the RS status in these wires.

2. Materials and method

For this experiment, 15 wires samples have been investigated, made of low-alloyed quality structural steel Grade 08G2S GOST 1050 with accumulated shear deformation, as result of rolling with shear of the metal ingot and conventional wire drawing. Table 1 reports the chemical composition of the steel.

Table 1. Chemical composition of low-alloyed structural steel grade 08G2S GOST 1050

element	C	Mn	Si	S	P	Cr	Ni	Cu	N2
wt %	0,08	1,87	0,82	0,020	0,022	0,02	0,02	0,02	0,007

2.1.

A schematic representation of the samples is reported in Figure 3.

These samples are 10 cm in length, and they are subdivided as follows:

- *Wires with accumulated shear deformation of 8%*
  1. initial non deformed ∅ 5.1 mm
  2. shear def. (8%) ∅ 4.65 mm
  3. shear def. (8%) + drawing def. (9.3%) ∅ 4.65 mm
  4. shear def. (8%) + drawing def. (16.6%) ∅ 4.46 mm
  5. shear def. (8%) + drawing def. (23.2%) ∅ 4.28 mm
- *Wires with accumulated shear deformation of 16.6%*
  6. initial non deformed ∅ 5.35 mm
  7. shear def. (16.6%) ∅ 4.65 mm
  8. shear def. (16.6%) + drawing def. (9.3%) ∅ 4.65 mm
  9. shear def. (16.6%) + drawing def. (16.6%) ∅ 4.46 mm
  10. shear def. (16.6%) + drawing def. (23.2%) ∅ 4.28 mm
- *Wires with accumulated shear deformation of 23%*
  11. initial non deformed ∅ 5.57 mm
  12. shear def. (23%) ∅ 4.65 mm
  13. shear def. (23%) + drawing def. (9.3%) ∅ 4.65 mm

14. shear def. (23%) + drawing def. (16.6%) ∅ 4.46 mm
15. shear def. (23%) + drawing def. (23.2%) ∅ 4.28 mm.

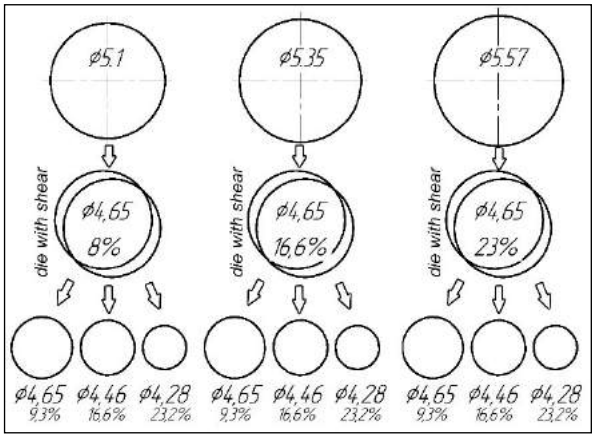

Figure 3. Scheme of drawing for a model experiment. Percentage shows the reduction degree.

TKSN-400 facility of CANAM NPL infrastructure was used for the measurement. The samples were positioned for measurement of axial and radial component of the strain. Due to the size of the samples, the measurement was carried out only in the centre of the wires. The peak positions and their widths were determined by fitting Gaussian curve to the measured strongest diffraction peak from the (310) plane for each sample. From the 2θ peak positions, the strains were calculated by using Eq. 1:

$$\varepsilon_{hkl} = \frac{d_{hkl} - d_{0,hkl}}{d_{0,hkl}} = \frac{\Delta d_{hkl}}{d_{0,hkl}} = -\cot\theta_{hkl}\Delta\theta_{hkl} \quad (1)$$

obtained by differentiating d in Eq. 2 (Bragg law) with respect to θ:

$$2d\sin\theta = \lambda \ . \quad (2)$$

Then, stresses were calculated from the measured strains by using Eq. 3.

$$\sigma_x = \frac{E_x}{(1-2\nu)(1+\nu)}\left[(1-\nu)E_x + \nu\left(E_y + E_z\right)\right] \quad (3)$$

For stress calculation from the measured strains, it was assumed that in the centre of the wire hoop strain is the same as radial strain.
Using this assumption, radial and axial stresses were calculated using the procedure described in [12].

3. Results and discussion

Fig. 4 shows a wire sample during the preliminary measurements.
In these preliminary tests, each wire sample was placed with its axis in vertical position, and a 2 mm wide slit and

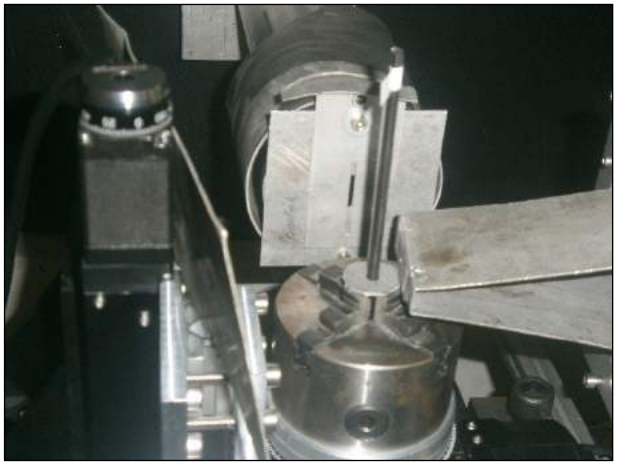

Figure 4. Wire sample during the preliminary measurements.

a hole having a diameter of 3 mm were used respectively for the incident and the diffracted beam.

Concerning the successive full tests, Figure 5 shows the measured (310) peaks for the radial direction, related to samples 6 to 10.

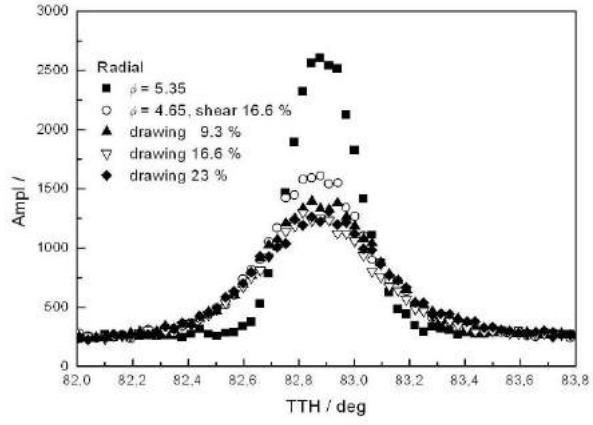

Figure 5. Measured 310 peaks for the radial direction, related to samples 6 to 10

Figure 6 and 7 report respectively the resulting axial and radial RS for all the investigated samples.

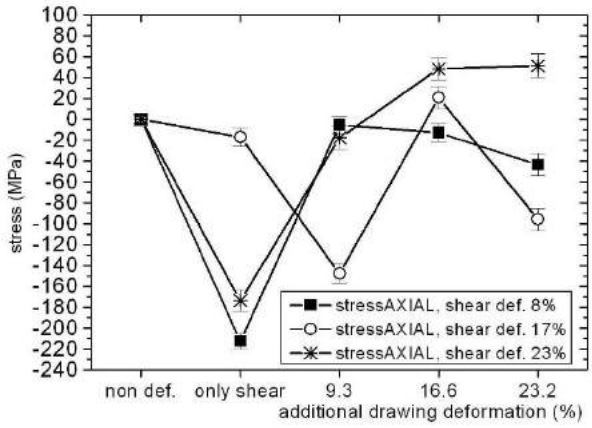

Figure 6. Resulting axial RS for all the investigated samples.

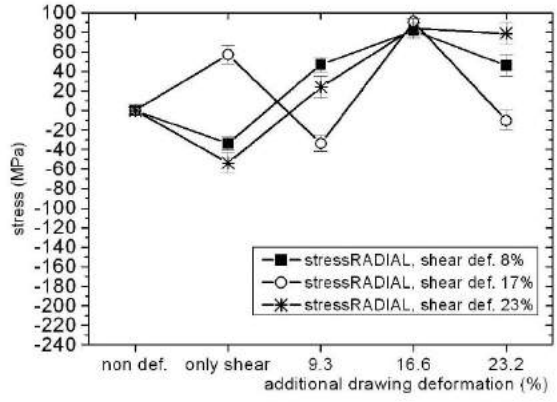

Figure 7. Resulting radial RS for all the investigated samples.

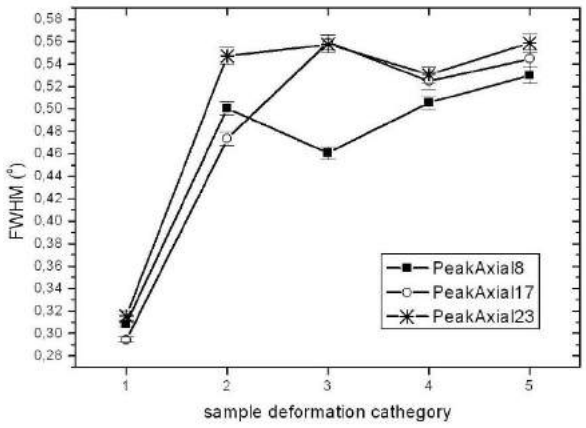

Figure 8. FWHM of the measured diffraction peaks 310 for the axial direction for all the investigated samples.

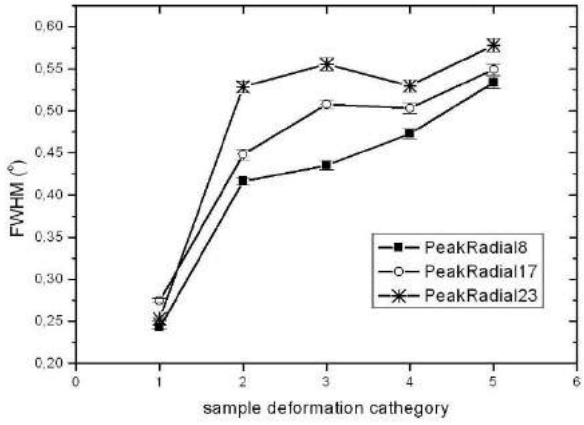

Figure 9. FWHM of the measured diffraction peaks 310 for the radial direction for all the investigated samples.

For 8% and 23% shear deformation, the stressing by shear causes a large increase of axial RS (about 200 MPa in compression). These relevant RS significantly decreases after subsequent drawing deformation. In case of 23% shear deformation, the subsequent larger drawing deformations even lead to appearance of tensile axial RS. 8% and 23% shear deformation also cause certain compressive radial RS in the range of 40÷50MPa. After subsequent drawing deformation, the radial component of the RS decreases and becomes gradually tensile RS.
Surprisingly, 17% shear deformed sample does not cause the same behaviour: in fact, the axial RS does not appear after shearing and radial RS is in the range of 50÷60MPa in tension. Further development of the stresses with increasing drawing deformation has no clear trend.
Full width at half maximum (FWHM), i.e. width of the measured diffraction peaks (in this case, 310) measured between those points on the y-axis which are half the maximum amplitude, were also evaluated. Figures 8 and 9 report respectively the resulting FWHM for the axial and the radial directions for all the investigated samples.

The peak width and shape supply information related to imperfections of the crystal structure, i.e. about the grain size and dislocation densities. In this simple analysis, we have qualitatively assessed the evolution of these imperfections with subsequent deformation steps. FWHM increases, as expected, with the intensity of deformation, as shown in Figure 9. The largest increase occurs during the shearing step, and the subsequent drawing further gradually adds an amount of imperfections (dislocations and/or amount of grain boundaries, due to the grain refinement).

4. Conclusions

ND results have provided substantial data helping to evaluate the effect of shear deformation on RS of low-carbon steels (and, in particular, of the low-alloyed quality structural steel Grade 08G2S GOST 1050), as well as additional support to complement the information already achieved by using the other characterization methodologies.

Knowledge of the RS status can help developing a low-carbon wire drawing technology with needed manufacturability and efficiency, and can play a decisive role also in the debugging of material selection and engineering design requirements.

Acknowledgements

Financial supports through MŠMT project No. LM2015056 and infrastructural project No. LM2015074 (Experimental nuclear reactors LVR-15 and LR-0) projects, and from EU's NMI3-II (FP7) Grant number 283883, are acknowledged. Dr. M. Vrána, Dr. B. Michalcova, Dr. P. Januš are acknowledged for their help in the neutron experiment. Dr. E. Pashinska and PhD-student A. Maksakova are acknowledged for their help in the deformation experiment carried out in the frame of the economic contract #13-13 "Wire drawing technology to improve ductility without the use of the heat treatment" - RPC "Donix".

REFERENCES

[1] Estrin Y., Vinogradov A., (2013), *Extreme grain refinement by severe plastic deformation: A wealth of challenging science*, Acta Materialia 61, p. 782-817 Great Britain

[2] Pashinska E., Varyukhin V., Myshlaev M., Zavdoveev A., (2014), *Formation of Structure and Properties of Low Carbon Steel Under Rolling with Shear and Cold Drawing*, Advanced Engineering Materials 16 (1), p. 26-32 Germany

[3] Zavdoveev A., Pashinska E., Dobatkin S., Varyukhin V., Belousov N., Glazunov F., Maksakova A., (2014), *Structure and properties of low-carbon steel at twist extrusion*, Emerging Materials Research 4, p. 89-93 Great Britain

[4] Pashinska E., Varyukhin V., Dobatkin S., Zavdoveev A., (2013), *Mechanisms of structure formation in low-carbon steel at warm twist extrusion*, Emerging Materials Research 2 (3), p. 138-143 Great Britain

[5] Pashinska E., Maksakova A., Zavdoveev A., Tkachenko V., *Influence of drawing with shear technology on the structure and properties of low-carbon wire*, MTMS2014, Split

[6] Len A., Zavdoveev A., Maksakova A., Pashinska E., Varyukhin V., Káli Gy., (2015), *SANS study of nanoscale structure of low-carbon steel after rolling with shear*, ECNS2015 Book of Abstracts, Zaragoza, Spain

[7] Pashinskaya E.G., Varyukhin V.N., Maksakova A., Maksakov A.I., Tolpa A.A., Zavdoveev A., *Effect of the technique of drawing with shear on the structure and the properties of low-carbon wires*, arXiv:1408.0125 [cond-mat.mtrl-sci], p. 1-5

[8] Rogante M., Zavdoveev A., (2016), *Filo d'acciaio a basso contenuto di carbonio: caratteristiche e dipendenza dalla deformazione per trafilatura*, Tecnologie del Filo 1, p. 30-34 Italy

[9] Rogante M., (2008), *Applicazioni Industriali delle Tecniche Neutroniche*, AITN2008, Civitanova Marche, Italy

[10] Rogante M., Mikula P., Vrána M., (2011), *Residual stresses assessment in coated materials: complementarity between Neutron and X-ray techniques*, Key Engineering Materials 465, p. 259-262 Switzerland

[11] Rogante M., Rosta L., (2005), *Nanoscale characterisation by SANS and residual stresses determination by neutron diffraction related to materials and components of technological interest*, Proc. SPIE 5824, p. 294-305 U.S.A.

[12] Hutchings M.T., Withers P.J., Holden T.M., Lorentzen T., (2005), *Introduction to the characterization of residual stress by neutron diffraction*, Boca Raton, Florida, U.S.A.

ISSN 1847-7917

Feasibility study for PIXE and neutron beam techniques on fishing nets made of polymeric materials

***Massimo ROGANTE*[1)], *Imre KOVÁCS*[2)], *Emilio NOTTI*[3)], *Antonello SALA*[3)], *Zoltán SZŐKEFALVI-NAGY*[2)]**

1) Rogante Engineering Office, I-62012 Civitanova Marche, **Italy**
2) Wigner Research Centre for Physics, Institute for Particle and Nuclear Physics, H-1121 Budapest, **Hungary**
3) ISMAR, Largo Fiera della Pesca, 60125 Ancona, **Italy**

main@roganteengineering.it

Keywords

Fishing nets
Polymers
PIXE
Neutron techniques
SANS
Spectrometry

Scientific paper

Abstract: External milli-beam particle induced X-ray emission spectroscopy (PIXE) has been adopted as non-destructive technique to investigate two fishing net samples made of polymeric materials. The primary goal of this study has been to create indications to advance the correct technological and material description of the objects providing scientific data for further and more comprehensive comparative analyses.
PIXE has supplied quantitative data related to major and trace elements (e.g., S, K and Ca) in order to recognize the constitutive mixtures and to supply information on the near-surface elemental composition complementary to the data characteristic for the bulk. The obtained results give an important contribution to complete the data achieved by using the classical methodologies, being useful also to set up a classification according to the chemical composition.
Considerations are reported, furthermore, concerning the possible investigation of these kind of fishing tools by using neutron beam techniques (NBT), and in particular small angle neutron scattering (SANS).

1. Introduction

Various categories of polymeric materials, after long periods under the combined influence of thermo-mechanical and weathering actions, meet ageing and consequent deterioration. A contribution to ageing is also in their chemical composition, which combines long organic molecules (i.e. the polymers) with additives that supply the material with the required characteristics of resistance to temperature, plasticity and workability. The material loses these features if the chemical bonds between the different components are broken and the additives migrate. The very subtle but however important chemical signatures significantly affect the physical properties and hence performance. Ropes, e.g., are frequently used in the industrial sector (e.g., construction) and in various other activities (e.g., fishing and sailing ships). A rope may consists of a hierarchy of fibres, as shown in Figure 1.
The interesting scale is usually 5 nm: nylon is a semi-crystalline polymer, made of crystallized lamellas piled up uniformly, linked up by amorphous zones.
The rupture of a fishing net or of a rope can be followed by problematical consequences, sometimes devastating, hence a complete characterization of these tools is necessary to advance products and safety levels.
The progress in diagnostics of these materials is directly dependent on the adoption of successful evaluation methods of damages due to the ageing process, in order to determine the relationship between defects characteristics and macroscopic functional properties.

Symbols/Oznake

Conc.	- concentration, %m/m -	*LOD*	- limit of detection, %m/m -
dia	- diameter, nm -	*Rtex*	- resultant linear mass density, g/1000m -

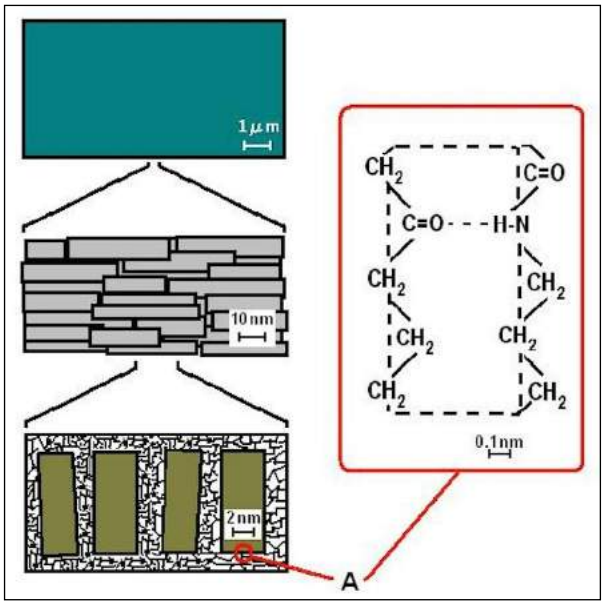

Figure 1. Scheme of the hierarchy of fibres of a rope.

Spectroscopic analyses (e.g., Fourier transform infrared, near-infrared and Raman spectroscopy) are typically adopted as routine testing for quality control and failure analysis and, generally, to investigate polymers and clarify problems associated to their production [1].

The netting materials used to make fishing gears are typically described in terms of their mesh size and shape and the thickness, number, tenacity and material type of the twines from which they are made. For instance, it is spoken of 120 mm, 5 mm double, high tenacity polyethylene (PE) diamond mesh netting.

These variables are important since they help determining the mechanical, engineering and fishing performance of the fishing gears they make up. They can affect the longevity of the gear, the ease of handling on deck, the fuel efficiency of the fishing operation, the fish behavioural reactions and the selective performance of the fishing gear.

Chemical analysis of polymeric materials and, in this case, of fishing net has become, recently, an important tool based on the determination of major- and trace elements.

2. Investigated objects and their conventional tests

Basically, netting panel for fishing gears is characterized by twine mechanical resistance and elongation. Such tests are commonly deployed by using stress/strain test machines. Despite the results coming from strength/strain tests is the nominal stiffness or the nominal traction resistance, as the material commonly used is the same, potential differences between different stock of netting are generally negligible. For this reason, netting panels are more often described in terms of density vs. diameter section - see Figure 2 [2]. The leakage of interest by end-users of specific properties of netting materials make manufacturers less interested in testing and reporting the performances and properties of their nettings [3].

Some specific test tool has been conceived, nevertheless, focusing at the properties of a netting panel, tested not as a single twine, but applying a force system to the entire netting. A prototype instrument, named resistance to opening and deflection meter (ROD-m) was designed by CNR-ISMAR, Ancona, and described in [4]. ROD-m reproduces a system of force which is symmetric along two horizontal and perpendicular axes.

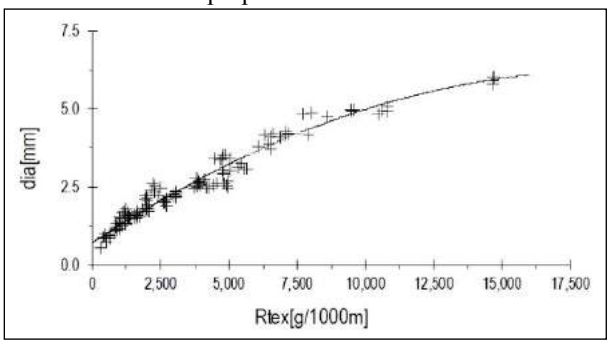

Figure 2. Empirical relationship among mesh twine thickness parameters: diameter (dia) and resultant linear mass density (Rtex). Experimental data are knotless polyamide netting materials [2].

Two different samples of new (not used) fishing nets made of polymeric materials have been investigated, in the present work (see Figure 3), which are adopted in the bottom trawl fisheries.

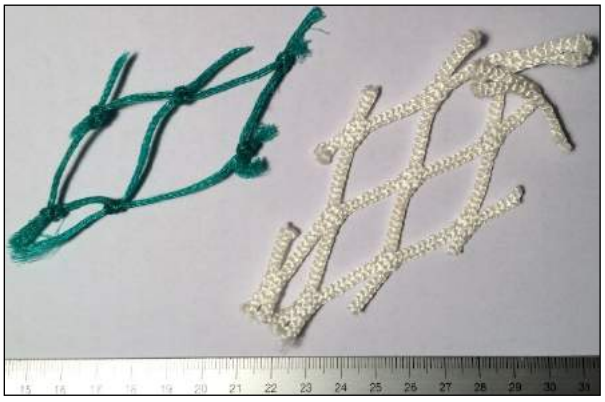

Figure 2. The investigated network samples.

Their characteristics are described as follows:

Sample 1

- material: high density polyethylene (rope diameter 3.5 mm), used in the front parts of the network body.
- colour: white

- Sample 2
- - material: high density polyethylene (rope diameter 1.8 mm), used in the front parts network body.
- - colour: green

3. Experimental method and results

Particle induced X-ray emission (PIXE) is an X-ray emission spectroscopy technique, which can be applied as non-destructive, simultaneous elemental analysis of samples and objects. Bombardment of the target by high energy ion, usually proton of MeV energy, creates inner shell ionisations. Outer shell electrons drop down and fill the inner shell vacancies. When an inner shell vacancy is filled, an x-ray photon of energy characteristic for the target atom is emitted [5]. An energy dispersive detector is applied to measure the emitted characteristic x-rays, the x-ray spectrum is analysed off-line and the characteristic x-ray intensities are converted to elemental concentrations [6-7]. The sensitivities are in the range of 50-1000 ppm, they vary with the elements and depend also on the matrix composition [8]. Since size of the proton beam on the target can be as small as 0.8-3 mm, small spots and selected particularities can be analysed on the samples. The PIXE technique can be successfully in several fields such as life sciences [9], as well as in art conservation, geology and archaeology [10, 11].

The measurements of the present experiment have been carried out by using the 5MV Van De Graaff accelerator of the Institute of Particle and Nuclear Physics of the Wigner Research Centre, Hungarian Academy of Sciences. The elemental composition of the base material could be determined in the upper 10 μm thick layer of the studied objects. Spot measurements were carried out on these objects, and no beam scanning was performed. The properly collimated proton beam of 2.5 MeV energy was extracted from the evacuated beam pipe to air through a 7.5 micrometre thick Kapton foil. A target-window distance of 10 mm was selected for the measurements, therefore the resulting beam diameter was ≅1.5 mm. The characteristic X-rays were collected by an Amptek X-123 spectrometer. The SDD type detector of 25 mm^2×500 μm active volume was positioned at 135 degree with respect to the beam direction. The energy resolution was 130 eV for the Mn-Ka line. A beam of 2.5 MeV protons was adopted with currents around 2 nA, with measurement times varying in the range 600-1800 s. Figure 4 shows the fishing net sample 2 during the PIXE investigation

PIXE has been used for quantitative analysis and it allowed identifying and quantifying trace elements on the surface of the considered samples, determining their distribution and supplying data complementary to those from other investigations techniques. The results of the PIXE investigation of sample 1 are reported in Table 1.

Figure 4. The fishing net sample 2 during the PIXE investigation.

Table 1. Results of the PIXE investigation of sample 1.

Element/	Conc. (%m/m)/	Error (%)/	LOD (%m/m)/	#
S	18.7	23.9	4.1	Y
K	22.2	9.4	2.3	Y
Ca	51.1	2.9	1.4	Y
Ti	1.4	55.4	1.1	?
Mn	1.8	22.8	0.4	?
Fe	4.3	11.0	0.3	Y
Cu	0.3	64.3	0.2	Y
Zn	0.2	95.7	0.3	?
Notes: #) The last column is a decision on the presence of that element in the spectrum. Y: present at level of quantization; N: not present at LOD; ?: may be present near LOD levels				

The results of the PIXE investigation of sample 2 are reported in Table 2.

Table 2. Results of the PIXE investigation of sample 2.

Element/	Conc. (%m/m)/	Error (%)/	LOD (%m/m)/	#
S	16.4	13.0	2.2	Y
K	8.1	6.6	1.1	Y
Ca	55.2	1.1	0.5	Y
Ti	1.6	15.2	0.4	?
Mn	0.2	48.3	0.2	?
Fe	14.9	2.4	0.3	Y
Cu	2.9	7.9	0.2	Y
Zn	0.7	22.8	0.2	?
Notes: #) The last column is a decision on the presence of that element in the spectrum. Y: present at level of quantization; N: not present at LOD; ?: may be present near LOD levels				

The obtained results are helpful for the identification of the compositional details, and they can be interpreted also as possible indications to create copies of the major

element compositions, as well as to make comparisons with analogue nets from different manufacturers.

4. The integrity of fishing nets and their nano- and micro-structure

In order to advance the considered fishing tools, studies of correlations should be carried out, between the evolution of the nano- and micro-structure and different chemical or physical ageing fishing nets and ropes made of polymeric materials. Neutrons represent an increasingly substantial probe for exploring and modifying the internal nano features of materials throughout an extensive range of disciplines in engineering, chemistry, physics and medicine. They are able to reveal significant properties and allow the monitoring of key nanoscale parameters helpful to evaluate the origin of structural failure. Such assessment conversely enhances the quality of manufacturing processes. This is all primarily due to the uniqueness of neutrons, which probe the bulk of a specimen in contrast to X-ray techniques which are typically surface-sensitive. Neutrons, thus, can give a substantial contribution to solve complex problems connected with the analyses of polymers. A wide range of other materials can be investigated, e.g. plastics, metals, composites, ceramics, nanomaterials, shape memory alloys, semi-crystalline systems, biomedical and pharmaceutical materials, fibres, glasses, gradient materials, membranes and multilayer structures. The applications of NBT are also concerning various new industrial sectors [12, 13] where the Rogante Engineering Office has developed special procedures using neutron measurements data particularly for industrial applications.

SANS, as well as other NBT, is a solution tool able to answer key industrial questions as well as provide in a non-destructive way, the fundamental information to develop the design, manufacture and maintenance phases. SANS-monitoring serves to characterize materials on the nano and microscopic level, also detecting cohesion breaking leading to internal surface growth and fracture.

The fundamental principles of the analysis of nanoscopic defects in solids (e.g., atomic clusters formed by precipitation and micro-phase inclusions) were designed in the early period of small-angle X-ray scattering (SAXS) and SANS techniques [14-16]. SANS, averaging over a macroscopic sample volume, provides information with high enough statistical accuracy to determine void sizes and their distributions in porous media. Such averaging also investigates particle agglomeration and the evolution of pores during the sintering process. A SANS analysis of polymers can be related to the bulk structure, specifically observing nano-pores and nano-micro cracks and their grouping in the matrix of the polymer.

The invisible total internal surface of these defects can be assessed, and leads to material fracture during loading. The structure of macromolecules in solution can be studied by exploiting the hydrogen→deuterium isotopic substitution for polymer or solvent, which supplies a high contrast in scattering between the polymer and the surrounding medium. Industrial polymers, when protonated, can be investigated in the bulk material (e.g., in polymeric networks) since in this case the coherent scattering length density of the material allows determining the contrast of some structural defects [17].

For a SANS investigation, the samples should be washed with solutions containing various detergents or acids. These solutions can be deuterated, as above mentioned, in order to assure a good contrast with the polymer, revealing thus a characteristic peak of the piling up of the crystalline lamellas. A nano- and micro-scale investigation of the considered polymeric fishing nets, performed in the planning phase by NBT, would improve the knowledge and design of these tools, and assist in overcoming the methodological limitations of conventional analyses. Thereby giving additional information for forecasting the behaviour of materials. SANS would permit materials' characterization at atomic and nano-scale level and offer existing technologies an essential contribution of precise structural methods [12, 13]. This information can give essential support in improving the quality and durability of these fishing tools.

NBT can be used also to characterise the nano-composite morphology of polymers with added inorganic nanoparticles, to optimize this addition in order to better study the interaction between nanoparticles and polyamide units [18] and to enhance the performances of the final products.

In consideration of the described peculiarities of neutrons, NBT could be taken into consideration as a part of the improvement process of fishing nets, since this technology has been used in various polymer investigations, obtaining information complementary to those achieved by using other techniques and relevant to the main features of the nano- and micro-structure. The SANS data can be applied not only to improve material's properties, but also to enhance the precision in the control and prediction of functional properties, which strongly depend on the size, extent of defects and their total area.

5. Conclusions

PIXE has been successfully adopted to investigate fishing nets, supplying in a non destructive way useful data on major and trace constitutive elements.

The feasibility of a neutron investigation of these fishing nets has been considered, furthermore, to complete the information achievable by the methodologies usually adopted in this case. A possible application of NBT to the various materials, in fact, has already moved their

industrial applicability for polymer investigation forward. SANS therefore, can be considered to be useful industrial tool for micro-scale polymer analysis sectors. This technique, in the present case, can supply significant data on basic parameters connected with degradation, fracture and other phenomena, allowing also a more reliable material lifetime assessment.

REFERENCES

[1] Rogante M., Rosta L., Heaton, M.E., (2013), *Neutron beam measurement of industrial polymer materials for composition and bulk integrity*, Measurement Science and Technology 24, 105601 (8pp) United Kingdom

[2] Sala A., Brčić J., Conides A., De Carlo F., Klaoudatos D., Grech D., Lucchetti A., Mayans A., Notti E., Paci N., Salom S., Sartor P., Sbrana M., Soler I., Spedicato M.T., Virgili M., (2013), *Technical specifications of Mediterranean trawl gears (myGears)*, Final project report, financed by the European Commission through the Framework service contract for Scientific Advice and other services for the implementation of the Common Fisheries Policy in the Mediterranean: Contract MARE/2009/05-Lot 1, p. 519

[3] O'Neill F.G., Kynoch R.J., Blackadder L., Fryer R.J., Eryaşar A.R., Notti E., Sala A, (2016), *The influence of twine tenacity, thickness and bending stiffness on codend selectivity*, Fisheries Research 176, p. 94-99 United Kingdom

[4] Sala A., O'Neill F.G., Buglioni G., Lucchetti A., Palumbo V., Fryer R.J., (2007), *Experimental method for quantifying resistance to the opening of netting panels*, ICES Journal of Marine Science 64, p. 1573-1578 United Kingdom

[5] Johansson T.B., Akselsson R., Johansson S.A.E., (1970), *X-ray analysis: elemental trace analysis at the 10^{-12} g level*, Nuclear Instruments and Methods 84, p. 141-143 United Kingdom

[6] Maenhaut W., Malmqvist K.G., (2002), *Particle-induced X-ray emission analysis*, Handbook of X-ray Spectrometry 2nd ed., p. 719–810 U.S.A.

[7] Mandò P.A., Przybyłowicz W.J., (2009), *Particle-Induced X-ray Emission (PIXE)*, Encyclopedia of Analytical Chemistry, John Wiley & Sons, p. 47 U.S.A.

[8] Gyódi I., Demeter I., Hollós-Nagy K., Kovács I., Szőkefalvi-Nagy Z., (1999), *External-beam PIXE analysis of small sculptures*, Nuclear Instruments and Methods in Physics Research B 150, p. 605-610 United Kingdom

[9] Szőkefalvi-Nagy Z., (1994), *Applications of PIXE in the Life Sciences*, Biological Trace Element Research 43-45/1, p. 73-78 Germany

[10] Rogante M., Horváth E., Káli G., Kasztovszky Z., Kis Z., Kovács I., Maróti B., Rosta L., Szőkefalvi-Nagy Z., (2015), *Neutronenuntersuchungen an einer Zink-Lampe unbekannten Ursprungs von der Archäologischen Sammlung der Academia Georgica Treiensis (Italien)*, Restaurierung und Archäologie Bd. 8, p. 45-53 Germany

[11] Rogante M., Kovács I., Rosta L., Stortoni E., Szőkefalvi-Nagy Z., (2015), *PIXE investigation of Roman metal archaeological objects from the Municipium Tifernum Mataurense area (S. Angelo in Vado, Italy)*, Nuclear Instruments and Methods in Physics Research Section B: Beam Interactions with Materials and Atoms 363, p. 156-160 United Kingdom

[12] Rogante M., (2008), *Applicazioni Industriali delle Tecniche Neutroniche*, AITN2008, Civitanova Marche, Italy

[13] Rogante M., Rosta L., (2005), *Nanoscale characterisation by SANS and residual stresses determination by neutron diffraction related to materials and components of technological interest*, Proc. SPIE 5824, p. 294-305 U.S.A.

[14] Guinier A., Fournet G., (1955), *Small -angle scattering of X-rays*, John Wiley & Sons, Ltd, New York., U.S.A.

[15] Marshall W., Lovesey S., (1971), *Theory of thermal neutron scattering*, Clar Press, Oxford, United Kingdom

[16] Schelten J., Hendricks R.W., (1977), *Recent developments in X-ray and neutron small angle scattering instrumentation and data analysis*, Journal of Applied Crystallography 11, p. 297-324 United Kingdom

[17] Rogante M., Lebedev V.T., (2007), *Microstructural characterization of polymeric materials by small angle neutron scattering*, Polymer Engineering and Science 47/8, p. 1213-1219 U.S.A.

[18] Vaia R.A., Maguire J.F., (2007), *Polymer nanocomposites with prescribed morphology: going beyond nanoparticle-filled polymers*, Chemistry of Materials 19, p. 2736-2751 U.S.A.

ISSN 1847-7917

Neutrons for Materials Research

László ROSTA[1)]***, Massimo ROGANTE***[2)]
1) Wigner Research Centre for Physics of the Hungarian Academy of Sciences, H-1525 Budapest, **Hungary**
2) Rogante Engineering Office, I-62012 Civitanova Marche, **Italy**
rosta.laszlo@wigner.mta.hu
main@roganteengineering.it

Keywords
Neutrons
Non-destructive testing
Materials research
Cultural Heritage

Ključne riječi
Klj.riječA
Klj.riječB
Klj.riječC
Klj.riječČ

Review paper
Abstract: Neutron methods constitute an essential and unique part of the science tool kit for exploiting information about the properties and behaviour of matter at the atomic and molecular level – this indispensable in order to design novel materials, devices, drugs and solve complex engineering problems. Neutrons can probe structure and dynamics of matter from mesoscale to nanoscale and from seconds to nanoseconds. Intense neutron beams are produced in nuclear reactors or accelerator based neutron sources. In Europe 9 neutron source centres provide access to about 150 various neutron spectrometers for materials research. The Budapest Neutron Centre (BNC) is one of these 9 facilities, it operates 15 experimental stations. BNC is the research organisation for the open access utilisation in science and technology development for the 10 MW Budapest Research Reactor (BRR), a unique infrastructure of this kind in the Central European region. Industrial applications of neutron techniques, which offer unique possibilities for non-destructive testing of materials and structural components, have been pioneered by the BNC and by the Rogante Engineering Office (REO) in various industrial sectors. BNC makes part of the SINE2020 EU network/project to promote these applications. The interaction of neutrons with matter has three major ways: 1) Imaging by passing neutron beams through objects – this is called neutron radiography and tomography; this can reveal internal parts or hidden objects inside bulky materials. 2) Absorption of neutrons by nuclear reaction with atoms of studied materials – radiative capture via (n,γ) reaction; this technique gives information on the elemental composition of objects. 3) Week interaction with atoms – changing in the trajectory and velocity of neutrons passing through solid or liquid materials – neutron scattering (elastic or inelastic); measuring intensity variation of scattered neutrons from the sample reveal information on microstructure. The uncharged neutron penetrates deeply in materials and with extreme sample environments and the combination of the techniques can provide complex information and in-situ studies on engineering materials. The neutron experimental capabilities of BNC are presented and examples are given for lifetime management, quality assurance problems of materials, technology development for industry and unveiling secrets of archaeological objects.

1. Introduction - the neutron

In order to design novel materials, devices and drugs, scientists are increasingly exploiting information about the properties and behaviour of matter at the atomic and molecular level. This information is acquired using advanced techniques, X-rays, electrons, photons, and ***neutrons*** are suitable probes of the micro-structure of the matter, and neutron methods constitute an essential and unique part of the science tool kit.

Neutrons can probe structure and dynamics of matter from mesoscale to nanoscale and from seconds to nanoseconds. Neutrons have distinct properties *for materials research*:
- Large penetration into the bulk of materials,
- Suitable wavelength/energy range
- Isotope sensitivity, spin/magnetic scattering

Symbols/Oznake

$\hbar$	- Planck's constant, $m^2 \times kg/s$		
	-	**Greek letters/Grčka slova**	
k	- wave vector, 1/Å	λ	- neutron wavelength, Å
	-		-
m	- mass of neutron, g	v	- velocity of neutron, m/s
	-		-

Thus, neutrons provide unique possibilities for ***non-destructive*** testing of materials and structural components. Figure 1 shows the energy scale of neutrons.

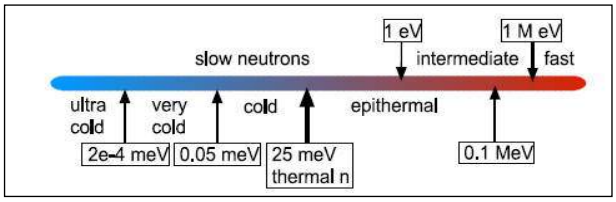

Figure 1. Energy scale of neutrons.

Intense neutron beams are produced in nuclear reactors - e.g., the Budapest Research Reactor (BRR), see Figure 2 - or accelerator based neutron sources.

Figure 2. The 10 MW BRR, the largest research infrastructure in Central-Europe.

In Europe 9 neutron source centres provide access to about 150 various neutron spectrometers for materials research. The BNC operates 15 experimental stations.

2. Interaction of neutrons with matter

There are three major ways/techniques to get information with neutrons on materials properties and internal topology of objects:

1. Imaging by passing neutron beams through objects, this technique is the neutron radiography and tomography.

In this technique the „Drawing with radiation" is realised. Radiography is a direct imaging technique, where the visual representation of an object is obtained non-destructively by detecting the modification of an incident beam as it passes through the matter. Figure 3 shows the principle set-up of radiography experiment.

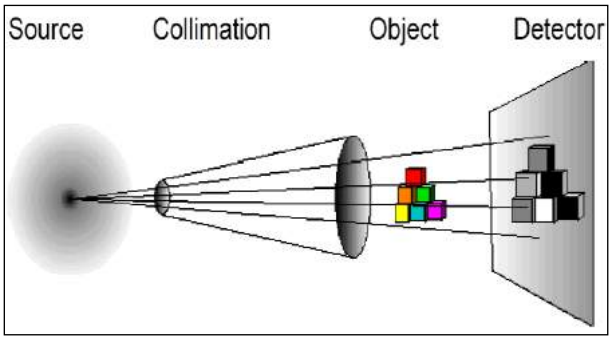

Figure 3. Transmission of neutron or X-ray beam through an object provides a contrast image in the detector.

Neutrons penetrate deep into bulk materials (metals, alloys, stones etc.), so radiography transforms invisible radiation into visible images.

2. Absorption of neutrons by nuclear reaction with atoms of studied materials, this called radiative capture – (n,γ) reaction.

In (n,γ) reactions: captured neutrons induce emission of gamma rays. Figure 4 shows the principle of this process. This technique is useful for the determination of elemental composition of materials.

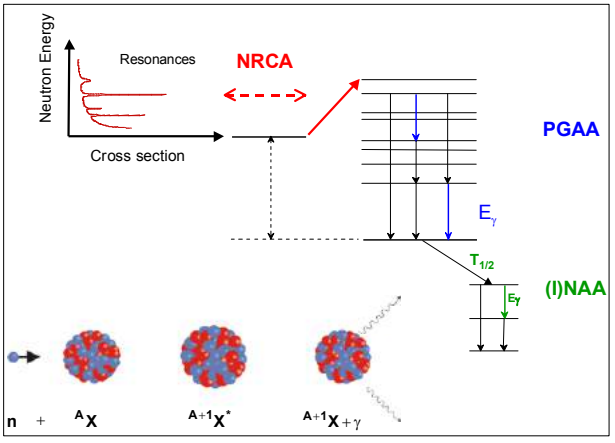

Figure 4. Neutron-gamma reaction scheme. By neutron radiative capture activation, a gamma cascade is produced, each element/isotope has its own characteristic gamma emission spectrum.

3. Week interaction with atoms – changing in the trajectory and velocity of neutrons passing through solid or liquid materials, this process is called neutron scattering (elastic or inelastic).

This interaction is based on that distinct particle properties of neutrons, which influence the experimental scattering results. Neutrons have nearly no electrical properties: "no" electrical charge, "no" electrical dipole momentum. Neutrons mainly obey nuclear interactions. However, their magnetic moment couples to the local magnetic field of magnetic atoms and ions. Neutrons with the mass ***m*** and a velocity ***v*** (for thermal neutrons ***v***

~ 2000 m/s) have a De Broglie wavelength λ and a wave vector $\boldsymbol{k}$ (or often denoted as $\boldsymbol{q}$).

$$mv = \hbar k = h / \lambda \quad (1)$$

The wavelength is in the order of tenths of nanometres, and it is comparable to atomic distances, similarly to x-rays. Figure 5 shows the scheme of a scattering set-up.

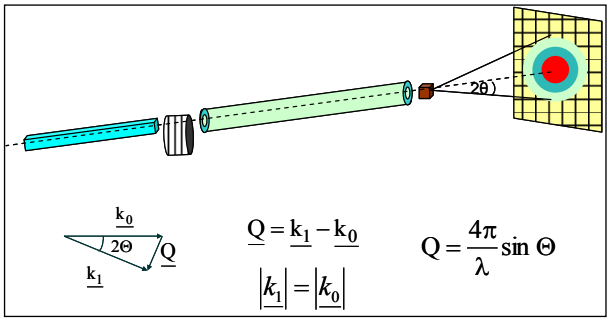

Figure 5. Neutron scattering scheme. Measuring intensity variation of scattered neutrons from the sample as a function of the wavelength and the scattering angle reveal information on microstructure by reconstructing a model of structural arrangements in real space.

Comparing with other scattering methods, the special features of neutrons are explained as below.

In the case of ***light scattering*** (e.g. laser spectroscopy) photons of typical energy of 10 eV (500 nm wavelength) interact with the matter through an electromagnetic interaction described as the polarizability of the scattering kernels. Relatively large assemblies of atomic structures and a wide range of energies (but in a very limited reciprocal space) can be studied.

X-rays with typical energy of 10 000 eV ($0.1 < \lambda < 0.5$ nm) interact with the electron shell of the atoms and in this way the atomic scattering length scales with the atomic (isotopic) number, i.e. the heavier of an atom in a material the larger is the scattering cross section characteristic for this substance. Due to the very suitable wavelength scale of X-ray photons comparable to atomic distances, X-ray techniques are essential for a versatile range of investigation of materials structures. Because of the weak interaction of X-rays with light elements (e.g. hydrogen), X-ray scattering has, however, strong limitations in the study of organic materials.

Neutrons have typical energies in the range from neV to hundreds of meV ($0.01 < \lambda < 5$ nm). The interaction is of nuclear nature and varies from isotope to isotope. The atomic scattering length can be positive or negative. For example light water (H_2O) or heavy water (D_2O) have neutron scattering length as -0.165 and +1.92 barn, respectively. This enables neutron experiments to use the contrast variation technique, i.e. distinguish for example between organic atomic-molecular fragments in mixture solutions of light and heavy water.

3. The Budapest Neutron Centre facilities for materials research

The BNC is a consortium of the *Wigner Research Centre for Physics* and the *Centre for Energy Research*. Both research centres with their staff over 400 persons each are part of the research network of the Hungarian Academy of Sciences and they have become important national hubs of their research fields including the jointly operated BNC as the largest research infrastructure in the country [1]. BNC's mission is to operate and provide research services by the neutron experimental stations at the BRR, which is the largest neutron research facility in Central Europe. At 10 MW power the reactor provides a maximum thermal neutron flux of 2.2×10^{14} n/cm^{2}s and a fast neutron flux of 1×10^{14} n/cm^{2}s in the core. The reactor has 10 horizontal beam tubes (eight radial and two tangential). At one of the tangential beam tubes a cold neutron source (CNS) has been installed. Three neutron guides transport neutrons to the measurement site in the guide hall adjacent to the reactor building. The neutron guides have bi-spectral nature, i.e. they can provide neutrons both with thermal or cold spectra [2].

The scheme of the neutron instruments at BRR are presented in Figure 6.

The most important instruments are described below.

SANS - Small Angle Neutron Scattering Diffractometer

The Yellow Submarine covers a Q-range from 0.003 to 0.5 Å^{-1} allowing probing structures at length scales from 5 Å to 1400 Å. The instrument is installed on the curved neutron guide No.2, with 4×4 cm^2 cross-section, made from supermirrors. It has a wide range of applications from studies of chemical aggregation, defects in materials, surfactants, colloids, ferromagnetic correlations in magnetism, alloy segregation, polymers, proteins, biological membranes and macromolecules.

PSD - Neutron diffractometer

The instrument is installed on the tangential thermal channel No. 9 (see Figure 7), with 10^6 cm^{-2}s^{-1} neutron flux at the sample position. It is a 2-axis diffractometer equipped with a linear position sensitive detector system. The detector assembly is mounted on the diffractometer arm and it spans a scattering angle range of 25° at a given detector position. The entire diffraction spectrum can be measured in five steps.

The neutron diffractometer is suitable for atomic structure investigations of amorphous materials, liquids and crystalline materials where the resolution requirements are not very high.

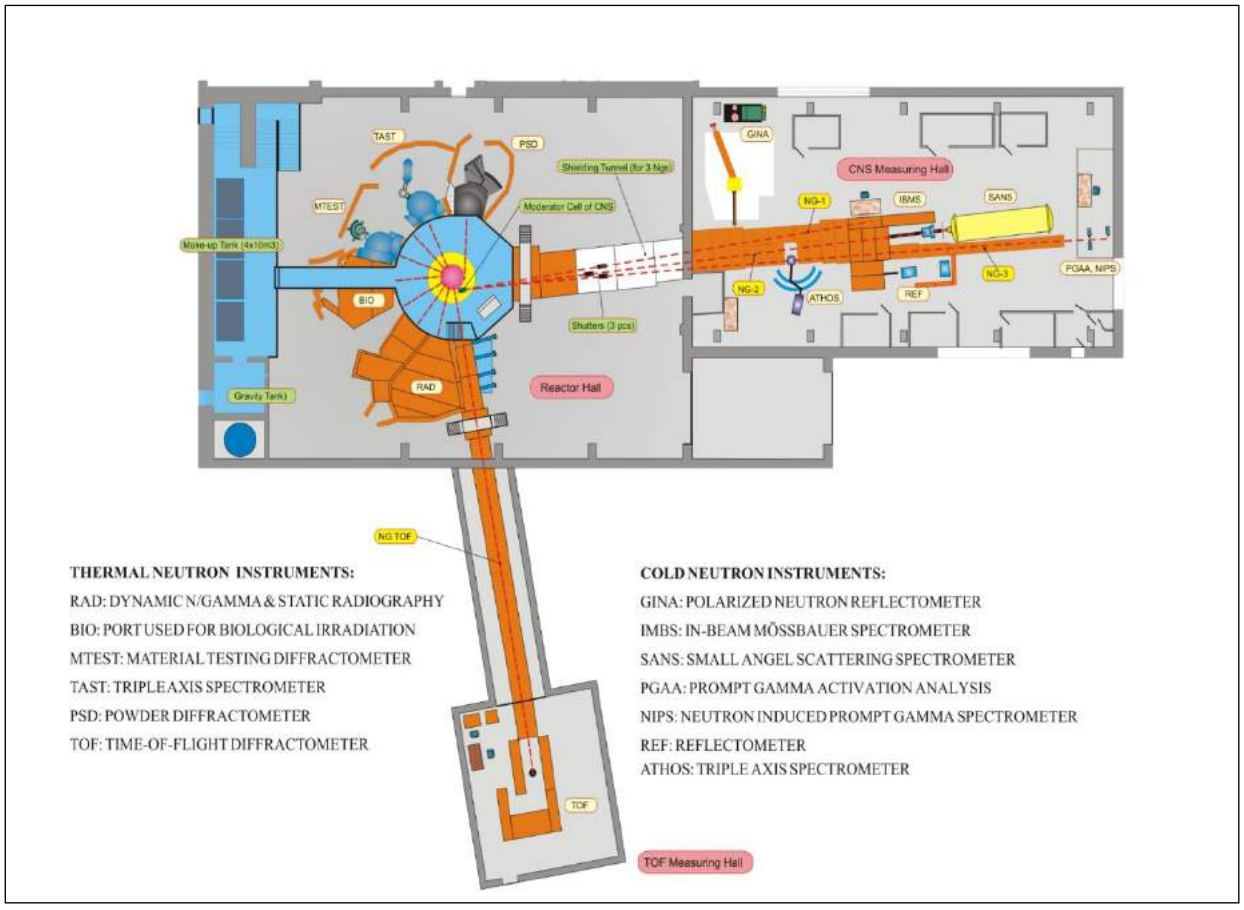

Figure 6. Layout of the BNC instrument suit in the Reactor Hall and the neutron guide halls (TOF – thermal neutrons, and the Cold Measuring Hall).

Figure 7. The PSD Diffractometer at the BRR.

High Resolution TOF Powder Diffractometer

The instrument has been installed on a radial thermal neutron beam in a new guide-hall. Full diffraction spectrum can be recorded within a variable bandwidth with high resolution or with high intensity at conventional resolutions. In high resolution mode the very short (10μs) neutron pulse and the 25m total flight path allows us to obtain a diffractogram with an accuracy of 10^{-3}Å in a single measurement on poly-crystalline materials, while in low resolution mode liquid diffraction can be performed at good neutron intensity up to 15 $Å^{-1}$ scattering vector. The diffractometer is suitable for determination of single and polycrystalline structure, strain analysis-, texture- and phase analysis.

PGAA - Prompt Gamma Activation Analysis

It provides non-destructive element analysis of samples by observing prompt gamma-rays from neutron capture from the irradiated sample. Before the beam enters to the experimental area, the beam is divided by suitable collimators. The thermal-equivalent neutron fluxes at the PGAA sample positions to 7.7×10^{7} cm^{-2} s^{-1}, while at the NIPS position it is 2.5×10^{7} cm^{-2} s^{-1}, where a neutron tomograph (NORMA) is installed. The beams can be collimated from 2×2 cm^2 down to 5mm^2. All chemical elements can be observed, with accuracy varying between 0.1 ppm to 1000 ppm. The most sensitive elements are H, B, Cl, Cd, Nd, Sm, Eu and Gd. Measurements of radiative capture of Isotopes and neutron tomography can also be performed [3].

RAD - thermal neutron imaging facility

The RAD thermal neutron imaging facility is served by a Cd-covered pin-hole-type collimator located at the No 2. radial horizontal channel, inside the biological shielding. The imaging device can be moved parallel to the beam axis on a rail system. Its closest and farthest measurement positions (see Figure 8) are used for dynamic (DNR at 209 cm from beam port, to prefer intensity) and for static (SNR at 282 cm from beam port, to prefer beam quality) imaging, respectively.

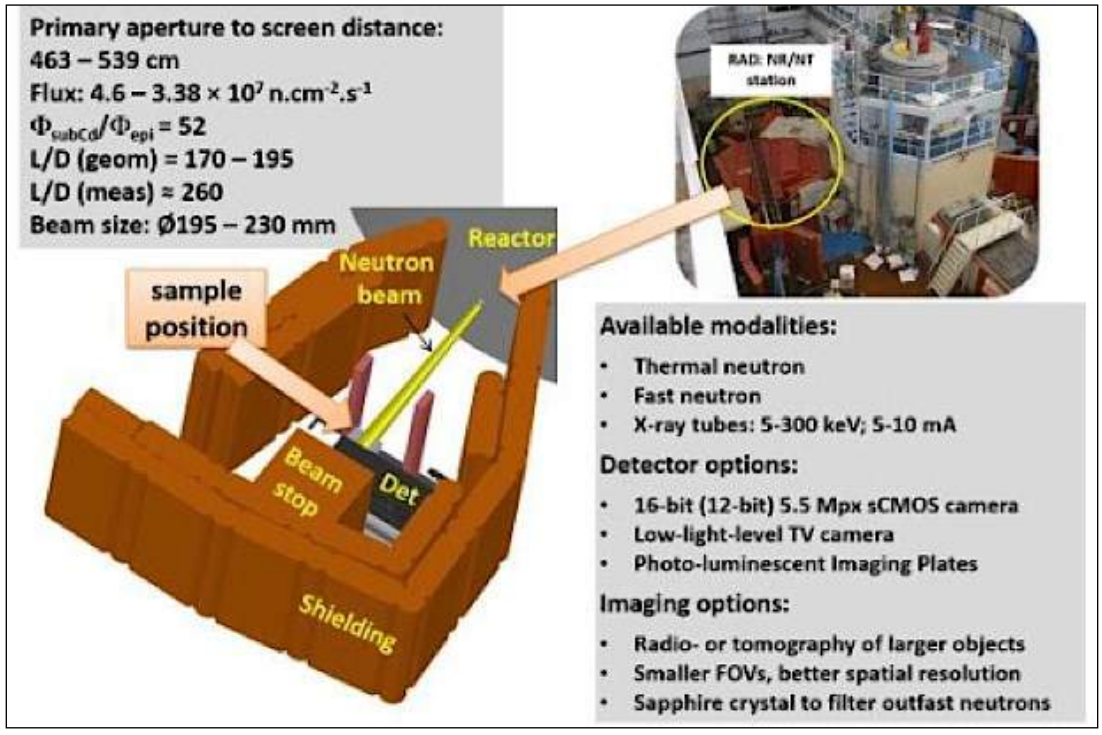

Figure 8. The RAD neutron imaging station at the BRR thermal neutron beamline No. 2.

The measured L/D ratios are around 260, which are reasonably good values for a traditional imaging beamline. The beam diameter is adjustable up to a maximum of 230 mm at the SNR position. The thermal neutron fluxes at the two positions are 4.64×107 $cm^{-2}s^{-1}$ and 3.38×107 $cm^{-2}s^{-1}$, respectively. The beam has a neutron-to-gamma ratio of 1.72×105 $cm^{-2}mR^{-1}$ and a cadmium ratio of 3.3. The thermal to epithermal flux measured by the cadmium covered and bare gold monitor method is about 51. The gamma-ray intensity is about 8.5 Gy/h. The RAD facility is also equipped with a set of X-ray generator tubes, covering the energy range between 5□300 keV with max. 10 mA current, for dual beam imaging. A massive, motorized sample manipulator with maximum load up to 250 kg, and a smaller one up to 5 kg are available to position the investigated objects. The RAD station has an up-to-date digital imaging equipment. The facility is able to carry out radiographic or tomographic imaging based on scintillation screens; for neutron imaging, scintillation screens with resolutions of 50-450 μm; for X-ray imaging, intensifying screens with resolutions of 100-200 μm. To make the instrument more flexible it is possible to set larger or smaller fields of view with respective lower or higher spatial resolutions. The static radiography and tomography are accomplished by an Andor Neo 5.5 sCMOS 2560×2160 px camera. In the light-tight optical box, three different optics can be used (computer-controlled interchangeable lenses with 50 mm, 105 mm and 300 mm fixed focal lengths) coupled to the digital camera, as shown in. Real-time radiography can be done by means of a low-light-level TV camera (640×480 px) with a light sensitivity of 10^{-4} lux. The imaging cycle of this camera is 40 ms (25 Hz), making possible the high-frame rate imaging, resulting in a video file. A zoom optics coupled to this camera provides inherently a variable field of view. The two cameras can be used as alternatives in the light-tight camera box. A mirror placed at 45 degree reflects the light towards the camera [4].

4. Examples of case studies for materials research

Neutron beam methods are essential tools for the investigation of very practical problems in materials science [5-7]. Below some examples of imaging, elemental analysis and structural investigations by neutron beam techniques are outlined.

Neutron imaging (radiography and/or tomography) can play a crucial role in quality assurance for industrial products especially of high security importance. In Figure 9 a high resolution image of a turbine blade is shown. In case of aircraft engines each blade of the rotor is inspected by neutron radiography. The engine operates at higher temperature than the melting point of the superalloy of the blade, thus cooling by internal channels is essential. As a part of the manufacturing procedure internal fins are produced and their perfect transmission ability is to be controlled, thus neutron imaging is applied to avoid eventual defects in these cooling channels.

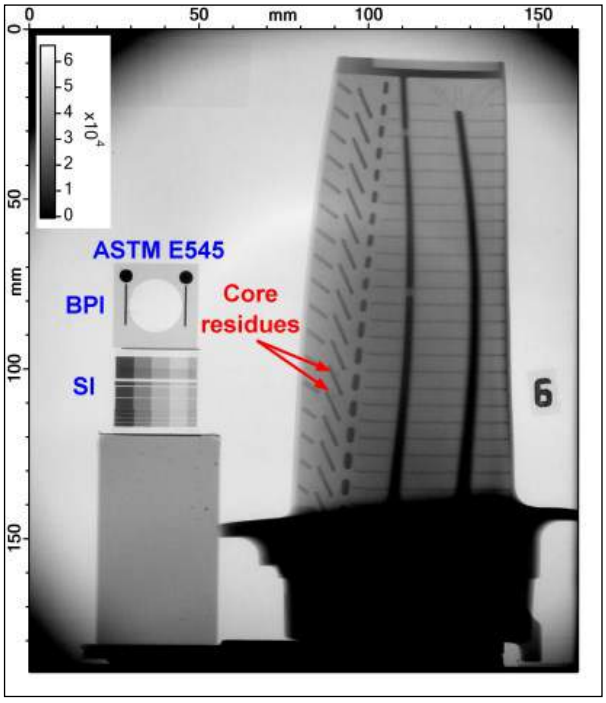

Figure 9. Turbine blade inspected by neutron radiography for the defect analysis of the internal cooling channels of the device.

Figure 10 shows another application: the internal part of a step-motor is visualised and a parallel measurement by ***PGAA reveals the main elemental compositions***, which correspond to the compositions of the motor along the axis. The dominant elements as Cu, Fe, B, H at the different parts are seen.

In the next example present that ***SANS investigations*** revealed life-time prolongation features of tungsten wires used in lighting industry. From sintered W bars wires are drawn and the presence of a small amount of potassium (0.5%) improves the quality of wires at high temperature usage. The presence of potassium filled bubbles is responsible for blocking grain-size growth, thus the quality of the wire is improved. The structure of bubbles follows the macroscopic deformation of the wire. As a consequence of oriented macroscopic strain induced by wire drawing the bubbles are oriented parallel to the wire axis. This is shown in Figure 11, where 2D SANS patterns represent the anisotropy of the bubbles [8]. By matching and unifying the scattered intensities in a wide scattering vector range at different neutron centres (Figure 12), we have concluded that the potassium bubbles are not the only reason of the small angle range scattering. This "additional" scattering is not influenced by the annealing temperature; it originates in the micrometre sized oriented cracks along the wires. The existence of these always presumed, but never seen cracks has been finally demonstrated experimentally [9].

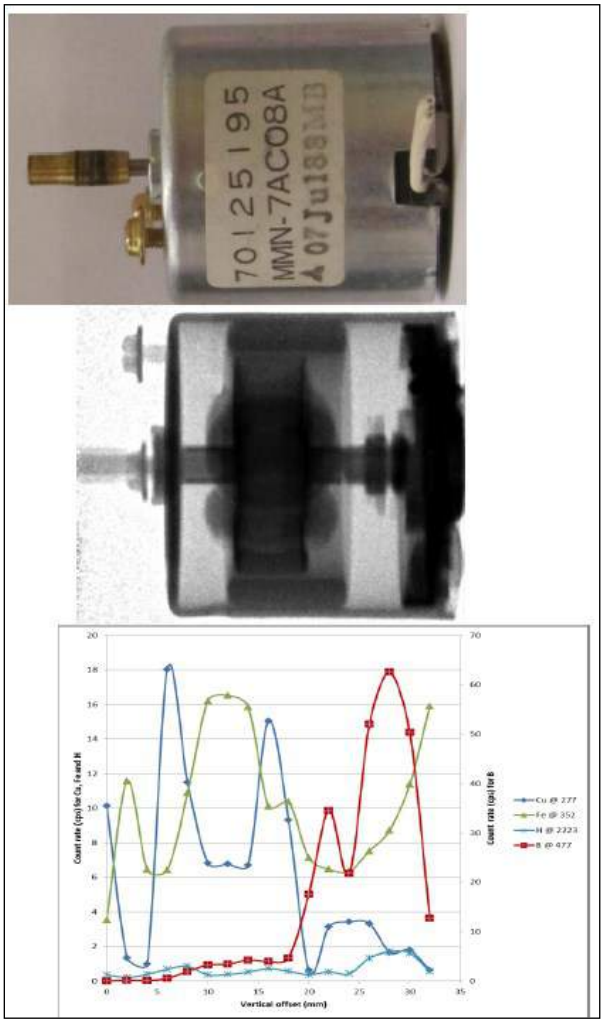

Figure 10. Combination of radiography with elemental analysis on a step-motor.

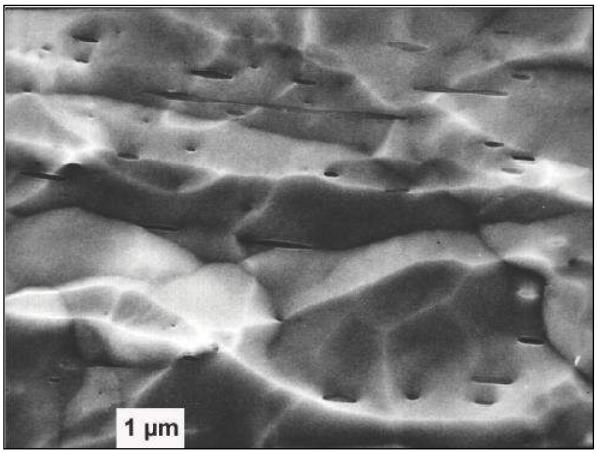

Figure 11. Electronmicroscopy image of W wire with elongated boubles.

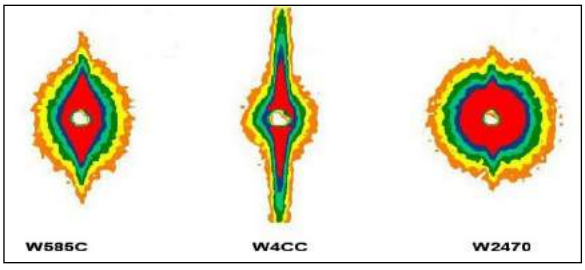

Figure 12. 2D SANS maps of W wire samples after different drawing and tempering stages.

Figure 13 shows the SANS curve measures for various potassium bubble sizes.

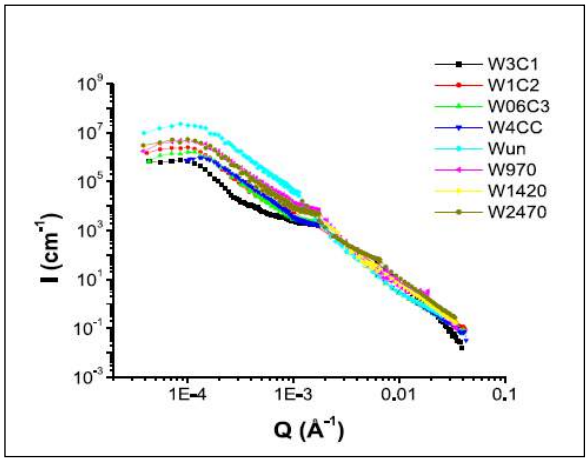

Figure 13. SANS curve measures for a wide range of bubble sizes in the range 1-1500 nm.

Figure 14 is related to another example of SANS investigation, carried out by the REO at the BNC and concerning polymer cement concretes [10].

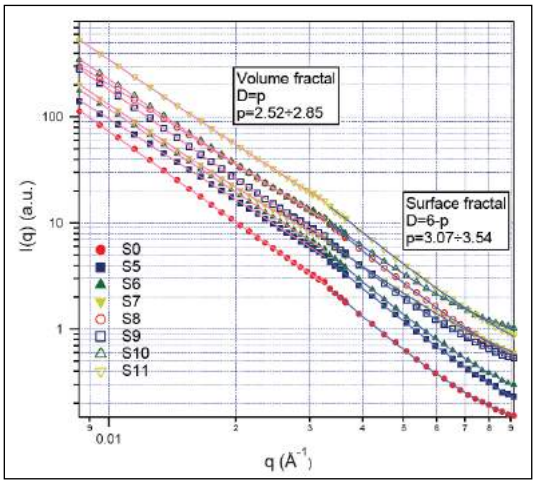

Figure 14. SANS curve measures for different polymer cement concrete samples.

Different PCC specimens made of Portland cement with added γAl_2O_3 and redispersible dry polymer RDP were investigated. The objective of the measurement was to verify the assumption that these polymers change the concrete's structure when the binding agent and water forms the cement stone that joints the particles together to make a monolith. Key parameters of the material (e.g., porosity, fractal dimensions and size distribution) at nanoscale level.

The deep penetration of thermal neutrons into the bulk of material makes ***neutron diffraction a powerful tool for the residual strains*** measurement by the high precision determination of lattice parameters and such non-destructive validation plays an important role in engineering sciences. For a series of "standard metal" samples a worldwide Round Robin test was performed; here we used the cold neutron triple axis spectrometer ATHOS in order to validate the followed procedure with our instrumental setup. ATHOS is an instrument with high flexibility and a relatively big sample table for investigation industrial samples. A vertically focusing PG monochromator provides continuously changeable wavelength, the detector is 200×200 mm position sensitive delay line type detector. The Round Robin sample was VAMAS Aluminium Ring & Plug Aluminium Ring & Plug Set. Figure 15 shows the experimental setup and the scheme for measuring radial and hoop stresses.

For stress measurement we used the 111 reflection using a gauge volume determined by the incident beam 20×3mm (HxW) and by the outgoing beam 20×3mm (HxW) at the detector direction. At the 111 reflection we used the wavelength of 0.33 nm giving us the 90 deg scattering angle. The measured strain data fit well to the results measured elsewhere of the Round Robin series. Figure 16 shows the strain distribution for hoop strains.

It is seen that the strain fits well on the negative side of sample position, while on the positive side the fit is rather

poor due to longer beam path in the sample well corresponding to the peak intensity weakening.

Figure 15. The experimental setup for measuring the strain distribution.

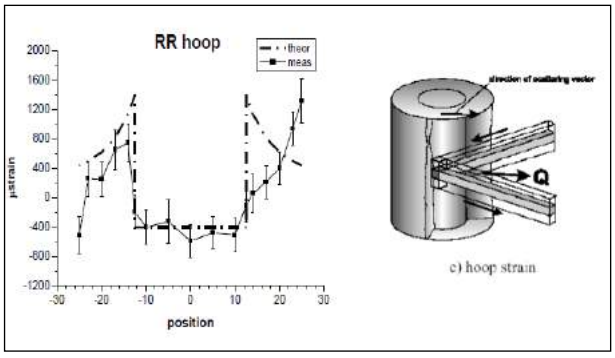

Figure 16. The measured and calculated hoop strain in the Aluminium Ring & Plug Set.

Figures 17 and 18 are related to another example of neutron diffraction application, carried out by the REO at the BNC and concerning a new and a used (25000 hours) Inconel 738 turbine blade [5].

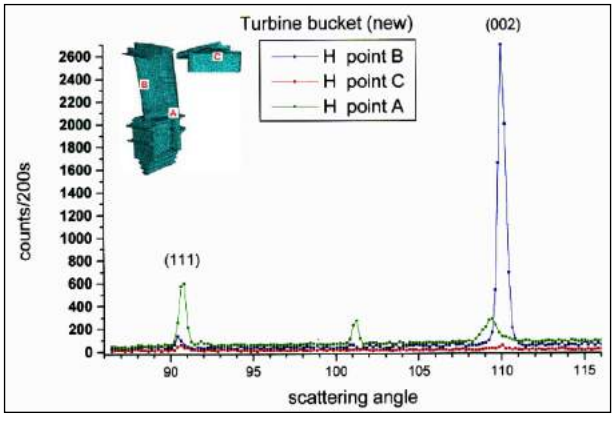

Figure 17. Turbine blade (new). Diffraction spectrum.

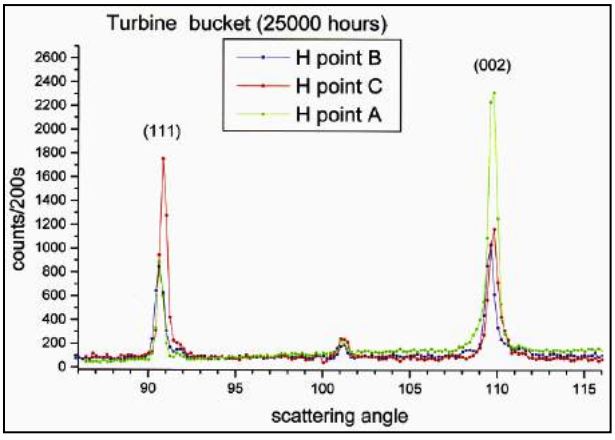

Figure 18. Turbine blade (25000 hours). Diffraction spectrum.

By comparing both spectra, different interplanar distances are indicated between the new and the old blade, showing a strain status. During the exercise, the crystallinity is growing; near the Ni peaks, the satellites indicate some phase decompositions, such effect depending on temperature and stress. These satellites are much lower in the new bucket. The present study has shown the possibility of following the blade's ageing.

The combination of various neutron techniques proved itself to be very useful for non-invasive characterisation of objects of ***Cultural Heritage*** [11]. A complex experimental work was performed at the BNC to reveal features of the mankind's known earliest iron objects. 5000-year-old Egyptian iron beads have been found to be made from hammered pieces of meteorites [12]. The nature and origin of humankind's earliest iron artefacts has been a matter of debate for over a century. This discovery not only demonstrates successful nuclear analytical methodology to uncover trace elements after complete corrosion, but also proves that already in the fourth millennium BC metalworkers had mastered the smithing of meteoritic iron, an iron-nickel alloy much harder and more brittle than the more commonly worked copper. Nine small beads securely dated to circa 3200 BC, from two burials in Gerzeh, northern Egypt. It highlights that these beads were made from meteoritic iron, shaped by being careful hammered into thin sheets before being rolled into tubes. The iron beads were strung into a necklace together with other exotic minerals such as lapis lazuli, gold and carnelian, revealing the status of meteoritic iron as a special material on a par with precious metal and gem stones. Figure 19 shows a neutron image of an iron bead.

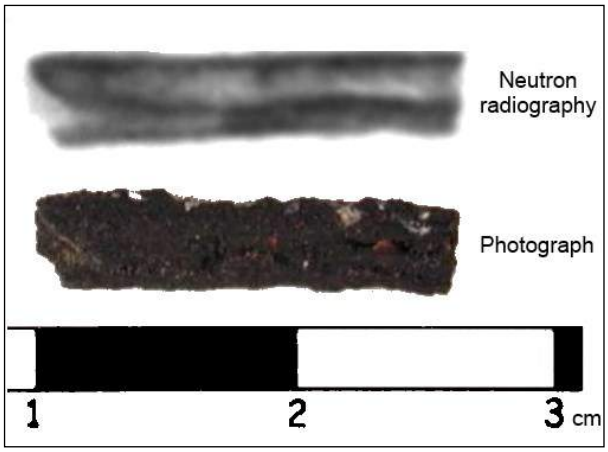

Figure 19. Neutron image of one of the iron beads, its in-side view and photo.

Using various neutron techniques at BNC – complemented by X-ray spectroscopy analysis – the ability to determine the nature of material even after complete corrosion of the iron metal has been demonstrated. In contrast to former investigations of the beads which involved only surface analysis, taking advantage of the deep penetration but non-invasive nature of the neutron techniques used, the authors were now able to get a more detailed insight into material features. PGAA, ND and NR reviled features such as the elemental composition, crystal/amorphous structure and the internal topology of the beads, respectively. Particle induced X-ray emission has also complemented to the full understanding of compositional data showing that the beads were made from meteoritic iron.

Acknowledgements

The SINE2020 project (H2020-INFRADEV-1-2014-1 65400) is acknowledged for the financial support and dissemination efforts provided for promoting the industrial applications of neutrons.

REFERENCES

[1] Rosta L., Baranyai R., (2011), *Budapest Research Reactor – 20 years of international operation*, Neutron News 22, p. 31-36 U.S.A.

[2] Rosta L., (2002), *Cold Neutron Research Facility at BNC*, Applied Physics A 74, S52 Switzerland

[3] Szentmiklósi L., et al., (2016), *Fifteen years of success: user access programs at the Budapest prompt-gamma activation analysis laboratory*, Journal of Radioanalytical and Nuclear Chemistry, 309, p. 71–77 Switzerland

[4] Kis Z., Szentmiklósi L., Belgya T., Balaskó M., Horváth L.Z., Maróti B., (2015), *Neutron based imaging and element-mapping at the Budapest Neutron Centre*, Physics Procedia 69, 40–47 Great Britain

[5] Rogante M., Rosta L., (2005), *Nanoscale characterisation by SANS and residual stresses determination by neutron diffraction related to materials and components of technological interest*, Proc. SPIE 5824, p. 294-305 U.S.A.

[6] Rogante M., Rosta L., (2010) *Forged components and possibilities of their investigation by neutron techniques*, Strojarstvo: Journal for Theory and Application in Mechanical Engineering 53 (4), p. 277-285 Croatia

[7] Rogante M., (2008), *Industrial Applications of Neutron Techniques*, AITN2008, Civitanova Marche, Italy

[8] Len A., Harmat P., Pépy G., Rosta L., (2002), *SANS Investigation of Potassium Morphology in Bubble Inclusions of Sintered Tungsten*, Applied Physics A 74, S1418-S1420 2.231 Switzerland

[9] Rosta L., Len A., Pépy G., Harmat P., (2012), *Nano-scale Morphology of Inclusions in Tungsten Wires - a Complex SANS Study*, Neutron News 23, p. 13-16 U.S.A.

[10] Rogante M., Domanskaya I.K., Gerasimova E.S., Len A., Rosta L., Székely N.K., Vladimirova E., (2017), *Nanoscale investigation of Polymer Cement Concretes by Small Angle Neutron Scattering*, Science and Engineering of Composite Materials 24(1), p. 67-72 Germany

[11] Hnatowitz V., Kasztovszky Zs., Kucera J., Macková A., Rosta L., (2016), *Neutron beam analytical methods*, Nuclear Physics for Cultural Heritage, EPS 2016, p. 23-29 Great Britain

[12] Rosta L., Belgya T., Káli Gy., Kasztovszky Zs., Kis Z., Kovács I., Maróti B., Szentmiklósi L., Szőkefalvi-Nagy Z., Jambon A., Rehren Th., (2013), *Proof of the Meteoritic Origin of Mankind's Earliest Iron Artefacts through Neutron and X-ray Analysis*, Hungarian archaeology e-journal, Winter, p. 5 Hungary

ISSN 1847-7917

Numeričko modeliranje i simulacija kontroliranog ohlađivanja toplo valjanog čelika

Božo SMOLJAN[1], Dario ILJKIĆ[1], Sunčana SMOKVINA HANZA[1], Lovro ŠTIC[1], Andrej BORIĆ[1], Bojan SENČIĆ[2] and Robert VERTNIK[2]

1) Zavod za materijale, Sveučilište u Rijeci - Tehnički fakultet
Department of Materials Science and Engineering, University of Rijeka - Faculty of Engineering
Vukovarska 58, 51000 Rijeka, **Croatia**
2) Štore Steel d.o.o.,
Železarska cesta 3, SI-3220 Štore, **Slovenia**

smoljan@riteh.hr
darioi@riteh.hr
suncana@riteh.hr
lstic@riteh.hr
aboric@riteh.hr
bojan.sencic@store-steel.si
robert.vertnik@store-steel.si

Ključne riječi
Matematičko modeliranje
Mehanička svojstva
Kontrolirano ohlađivanje
Valjanje

Keywords
Mathematical modelling
Mechanical properties
Controlled cooling
Rolling

Izvorni znanstveni rad

Sažetak: Razvijen je numerički model kontroliranog ohlađivanja toplo valjanih čeličnih šipki. Razvijeni numerički model opisuje promjenjivo temperaturno polje, razvoj mikrostrukture te tvrdoću čeličnih šipki tijekom ohlađivanja na klupi za ohlađivanje.
Numerički model promjenjivog temperaturnog polja temelji se na metodi konačnih volumena. Algoritam za predviđanje tvrdoće i mikrostrukture čeličnih šipki temelji se na stvarnom kemijskom sastavu. Čelične šipke se posebnim slaganjem na klupi za ohlađivanje kontrolirano hlade.
Numerički model i računalni program eksperimentalno su verificirani u stvarnim industrijskim uvjetima proizvodnje šipki izrađenih iz niskolegiranog čelika. Numerički je model verificiran usporedbom tvrdoća dobivenih simulacijom i eksperimentalno izmjerenih tvrdoća.

Numerical modelling and simulation of controlled cooling of hot rolled steel

Original scientific paper

Abstract: Numerical model of controlled cooling of steel hot rolled bars was developed. Numerical model of controlled cooling describes a transient temperature field, microstructure evolution and hardness of steel bars during their cooling in cooling beds.
The numerical model of transient temperature field is based on control volume method. The algorithm for prediction of hardness and microstructure distribution in steel bars is based on real chemical composition. The controlled cooling is performed by special placement of hot rolled bars on cooling beds.
Numerical model and computer program was experimentally verified in real industrial manufacturing of low-alloyed steel bars. The verification of developed numerical model was performed by comparison of simulated hardness with experimentally evaluated results.

1. Uvod

Istraživanja u vezi numeričke simulacije ohlađivanja čeličnih uzoraka prioritetna su istraživanja u simulaciji toplinske obrade čelika [1, 2]. Rezultati ohlađivanja čelika ovise o geometriji čeličnog uzorka, karakterističnim fizikalnim svojstvima ohlađenog čelika te o načinu ohlađivanja. Značajna fizikalna svojstva uključena u proces ohlađivanja su specifični toplinski kapacitet čelika, koeficijent toplinske vodljivosti čelika, gustoća čelika i koeficijent prijelaza topline okoline čeličnog uzorka. Ove varijable mogu se procijeniti inverznom metodom, na osnovi postignutih rezultata ohlađivanja i na osnovi kvalitativne analize krivulje ohlađivanja [2, 3, 4, 5].
U razvijenom računalnom programu za simulaciju, tvrdoća se u različitim točkama obratka procjenjuju na temelju TTT dijagrama i termokinetičkih jednadžbi za procjenu kinetike mikrostrukturnih pretvorbi.

Oznake/Symbols

c	- specifični toplinski kapacitet, $Jkg^{-1}K^{-1}$ - specific heat capacity		**Grčka slova/Greek letters**
k	- kinetički parametar - kinetic parameter	α	- koeficijent prijelaza topline,$Wm^{-2}K^{-1}$ - heat transfer coefficient
T	- temperatura, K - temperature	λ	- koeficijent toplinske vodljivosti, $Wm^{-1}K^{-1}$ - coefficient of heat conductivity
V	- volumen, m^3 - volume	τ	- vrijeme, s - time
X	- transformirani dio mikrostrukture - transformed part of microstructure	ρ	- gustoća, kgm^{-3} - density
n	- eksponent deformacijskog očvršćivanja - strain-hardening exponent		**Indeksi/Subscripts**
t	- vrijeme, s - time	f	- medij za kaljenje - quenchant
$t_{8/5}$	- vrijeme ohlađivanja od 800 do 500 °C, s - time of cooling from 800 to 500 °C	M	- broj koraka ohlađivanja od 800 do 500 °C - number of time steps during the cooling from 800 to 500 °C
ρ	- gustoća, kgm^{-3} - density	s	- površina - surface

2. Matematičko modeliranje prijenosa topline

Promjena temperature u izotropnom krutom tijelu može se opisati Fourierovim zakonom:

$$\frac{\delta(c\rho T)}{\delta t} = div(\lambda\, grad T) \tag{1}$$

gdje je λ/$Wm^{-1}K^{-1}$ koeficijent toplinske vodljivosti, ρ/kgm^{-3} gustoća, a c/$Jkg^{-1}K^{-1}$ specifični toplinski kapacitet.

Karakteristični granični uvjet je:

$$-\lambda \left.\frac{\delta T}{\delta n}\right|_s = \alpha(T_s - T_f) \tag{2}$$

gdje je α/$Wm^{-2}K^{-1}$ koeficijent prijelaza topline okoline tijela, T_s/K temperatura površine, a T_f/K temperatura okoline tijela.

Za izradu modela promjene temperaturnog polja, fizikalna svojstva uključena u model moraju biti dosljedna postignutim rezultatima. Ulazni podaci bi trebali biti procijenjeni u skladu s eksperimentalnim rezultatima [6, 7].

Izraz 1 može se riješiti metodom konačnih volumena [8-10]. Primjerice, promjena temperaturnog polje u izotropnom krutom tijelu može se definirati pomoću 2-D metode konačnih volumena [8]:

$$T_{ij}^1\left(\sum_{m=1}^{2} b_{I(i+n)j} + \sum_{m=1}^{2} b_{Ji(j+n)} + b_{ij}\right) =$$

$$= \sum_{m=1}^{2}\left(b_{I(i+n)j} T_{(i+k)j}^1 + b_{Ji(j+n)} T_{i(j+k)}^1\right) + b_{ij} T_{ij}^0 \tag{3}$$

$i = 1,2,...,i_{max}$, $\quad j = 1,2,...,j_{max}$,

$n = 2 - m, \quad k = 3 - 2m$

gdje je T_{ij}^0/K temperatura na početku vremenskog koraka Δt/s, T_{ij}^1/K temperatura na kraju vremenskog koraka Δt/s, $b_{ij} = (\rho_{ij} c_{ij} \Delta V_{ij})/\Delta t$, ΔV_{ij}/m^3 je volumen kontrolnog volumena, $b_{I(i+n)j} = W_{I(i+n)j}^{-1}$ i $b_{Ji(j+n)} = W_{Ji(j+n)}^{-1}$, gdje su varijable $W_{I(i+n)j}$ i $W_{Ji(j+n)}$ toplinski otpori za x os. Primjerice, $W_{I(i+n)j}$ je toplinski otpor između volumena ij, te volumena $(i\text{-}1)j$ za $n = 0$ i za $n = 1$, dok je $W_{I(i+n)j}$ jednak toplinskom otporu između volumena ij i $(i+1)j$. Nomenklatura je jednaka i za y os.

Vrijeme ohlađivanja od temperature T_{start} do neke određene temperature, za pojedini volumen u uzorku, određuje se kao zbroj temperaturnih koraka:

$$t_M = \sum_{m=1}^{M} \Delta t_m \tag{4}$$

gdje je M broj temperaturnih koraka do određene temperature.

3. Matematičko modeliranje tvrdoće i sastava mikrostrukture

Prema adicijskom pravilu, kinetika neizotermičkih pretvorbi pri kontinuiranom ohlađivanju može se opisati kao zbroj malih prirasta izotermičkih pretvorbi.
Na slici 1 shematski je prikazana procjena mikrostrukture na osnovi krivulje ohlađivanja i izotermičkog TTT dijagrama. Na slici 1 temperaturni raspon je podijeljen u seriju malih koraka. Ako su vremenski intervali Δt_i dovoljno maleni, može se pretpostaviti da su u svakom vremenskom koraku vrijede izotermički uvjeti pretvorbi. Pretpostavljeno je da se u svakom vremenskom koraku dogodi pretvorba jednaka onoj u izotermičkom TTT dijagramu pri istoj temperaturi i s istim mikrostrukturnim sastavom.

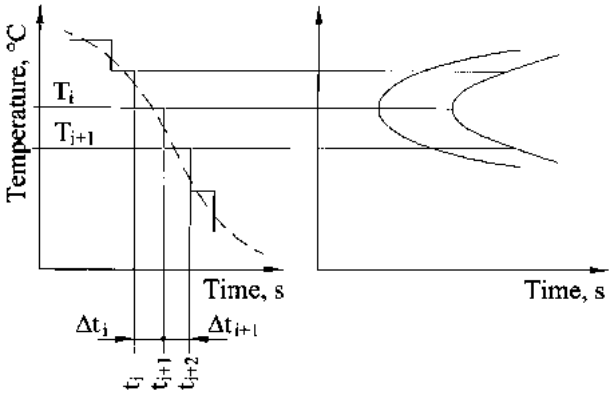

Slika 1. Određivanje mikrostrukturnog sastava i mehaničkih svojstava iz krivulje ohlađivanja i izotermičkog TTT dijagrama

Figure 1. Prediction of microstructure composition and mechanical properties from cooling curve and IT diagram

Izotermički TTT dijagram za čelik EN 42CrMo4 prikazan je na slici 2a.
Kada se koriste TTT dijagrami za kontinuirano ohlađivanje, tvrdoća se može procijeniti ucrtavanjem krivulje ohlađivanja u takav dijagram [11]. Ovo je vrlo jednostavna i često korištena metoda. Tvrdoća u različitim točkama uzorka također se može procijeniti pretvorbom izračunatog vremena ohlađivanja, $t_{8/5}$ u tvrdoću, koristeći TTT dijagram za kontinuirano ohlađivanje. Razlika između stvarnog kemijskog sastava čelika i propisanog kemijskog sastava čelika za koji je izrađen TTT dijagram za kontinuirano ohlađivanje također se mora uzeti u obzir. U ovom slučaju ta se razlika uzima u obzir korištenjem izraza 5 do 9. TTT dijagram za kontinuirano ohlađivanje čelika EN 42CrMo4 prikazan je na slici 2b.
Transformirani dio mikrostrukture, X pri nekoj temperaturi T, za vrijeme t, može se izračunati Avramijevom izotermičkom jednadžbom:

$$X = 1 - \exp(-k \cdot t^n) \tag{5}$$

Za potrebe numeričke analize pomoću računala kinetiku raspada austenita praktično je proučavati Avramijevom izotermičkom jednadžbom definiranom u inkrementalnom obliku. Deriviranjem Avramijeve jednadžbe, slijedi:

$$\frac{dX}{dt} = \exp(-k \cdot t^n) \cdot n \cdot k \cdot t^{n-1} \tag{6}$$

a izlučivanjem vremenske komponente iz izraza 6, slijedi da je:

$$\frac{dX}{dt} = n \cdot k^{\frac{1}{n}} \cdot \left(\ln \frac{1}{1-X} \right)^{1-\frac{1}{n}} \cdot (1-X). \tag{7}$$

Izraz 7 može se zapisati u inkrementalnom obliku, a volumni udio transformiranog austenita ΔX, u vremenskom intervalu Δt_i, na temperaturi T_i može se izračunati na sljedeći način:

$$\Delta X_{(N)} = n \cdot k^{\frac{1}{n}} \cdot \left(\ln \frac{1}{1-X_{(N-1)}} \right)^{1-\frac{1}{n}} \cdot \left(1-X_{(N-1)}\right) \cdot \Delta t_{(N)}. \tag{8}$$

Kinetički parametri k i n iz izraza 8 mogu se odrediti inverzno korištenjem podataka iz izotermičkih TTT dijagrama. Kada se koriste izotermički TTT dijagrami, u skladu sa Scheillovim adicijskim pravilom, karakteristična mikrostrukturna pretvorba je završena onda kada je transformirani dio mikrostrukture, X jednak jedan [11, 12]:

$$\int_0^t \frac{dt}{\tau(X_0, T)} = 1 \tag{9}$$

gdje $\tau(X_0, T)$ predstavlja vrijeme izotermičke pretvorbe za $X = X_0$ pri temperaturi T, a t predstavlja ukupno vrijeme transformacije. Vrijeme izotermičke transformacije, τ može se ili izračunati termokinetičkim jednadžbama ili odrediti pomoću izotermičkog TTT dijagrama [12].

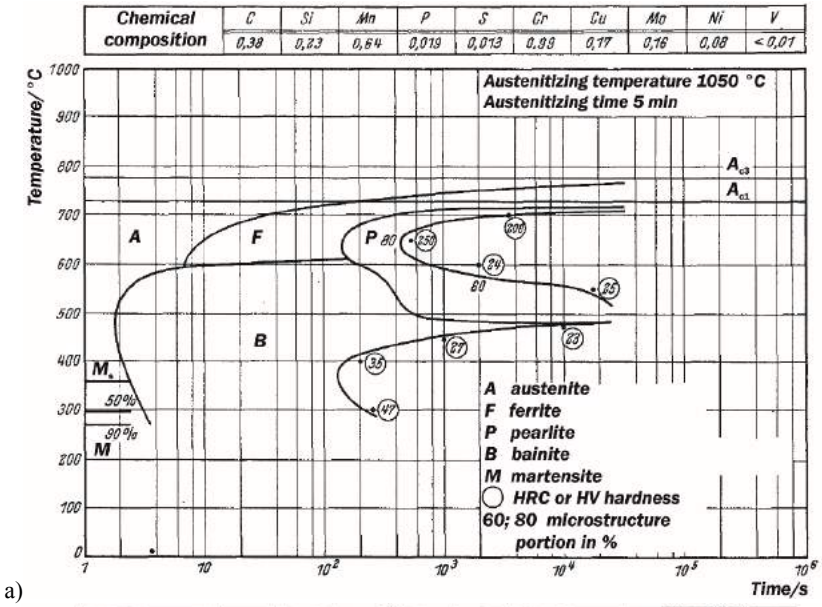

a)

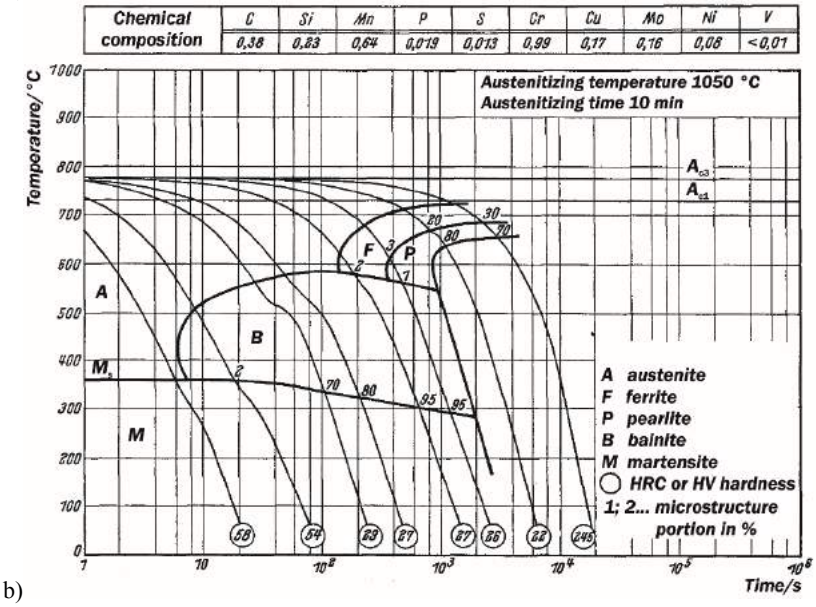

b)

Slika 2. TTT dijagram za čelik EN 42CrMo4, a) izotermički b) dijagram za kontinuirano ohlađivanje [13]
Figure 2. a) IT diagram for steel EN 42CrMo4. b) CCT diagram for steel EN 42CrMo4 [13]

Tablica 1. Krivulje ohlađivanja čeličnih šipki promjera 60 mm i duljine 6000 mm

Table 1. Cooling curves of steel bar with dimension of 60 mm diameter and 6000 mm length

1		2		3	
Temperatura/°C	Vrijeme/s	Temperatura/°C	Vrijeme/s	Temperatura/°C	Vrijeme/s
920	0	924	0	926	0
892	34	913	26	890	52
841	110	880	57	847	87
797	136	849	86	820	121
758	190	805	150	780	167
733	224	736	245	751	206
				726	241
Tvrdoća = 298 HB		Vrijeme kašnjenja = 76 s		Vrijeme kašnjenja = 115 s	

4. Eksperiment

Eksperiment je proveden na čeličnim šipkama promjera 60 mm i duljine 6000 mm, izrađenim od čelika EN 42CrMo4. Kemijski sastav čelika EN 42CrMo4 je: 0,42 %C, 0,26 %Si, 0,84 %Mn, 0,013 %P, 0,034 %S, 1,07 %Cr, 0,22 %Mo, 0,19 %Ni, 0,01 %V.
U tablici 1 prikazani su rezultati izmjerenih krivulja ohlađivanja proučavanih čeličnih šipki promjera 60 mm i duljine 6000 mm. U tablici 1, prvi stupac (1) prikazuje slučaj ohlađivanja jedne šipke, a ostala dva stupca (2 i 3) prikazuju slučajeve zajedničkog ohlađivanja složenih čeličnih šipki.
Temperatura je mjerena M90R-1 pirometrom, čiji se temperaturni interval mjerenja kreće u rasponu od 700 °C do 2000 °C, s vremenom odaziva od 0,5 s.

5. Primjena

Razvijeni model primijenjen je u računalnoj simulaciji ohlađivanja šipki promjera 60 mm i duljine 6000 mm. Šipke su od čelika EN 42CrMo4, kemijskog sastava 0,42 %C, 0,26 %Si, 0,84 %Mn, 0,013 %P, 0,034 %S, 1,07 %Cr, 0,22 %Mo, 0,19 %Ni, 0,01 %V.
Napravljena je numerička simulacija za slučaj zasebnog ohlađivanja jedne šipke, te za slučajeve zajedničkog ohlađivanja dviju šipki. Početna temperatura čeličnih šipki, T_{start} je 920 °C. Za slučaj zajedničkog ohlađivanja dviju šipki vrijeme kašnjenja, t_{lag} je 76 s. Temperatura zraka, T_{air} je 30 °C. Raspodjela tvrdoće i mikrostrukturnog sastava procijenjena je numeričkom simulacijom korištenjem softvera BS-QUENCHING [8]. Raspodjela tvrdoće i mikrostrukture različito složenih šipki prikazani su na slikama 3-12.

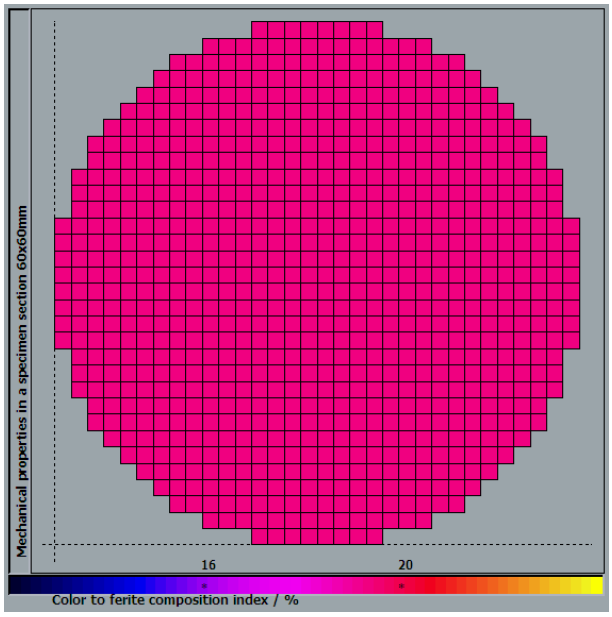

Slika 4. Raspodjela ferita u čeličnoj šipki nakon ohlađivanja
Figure 4. Distribution of ferrite of steel bar after cooling

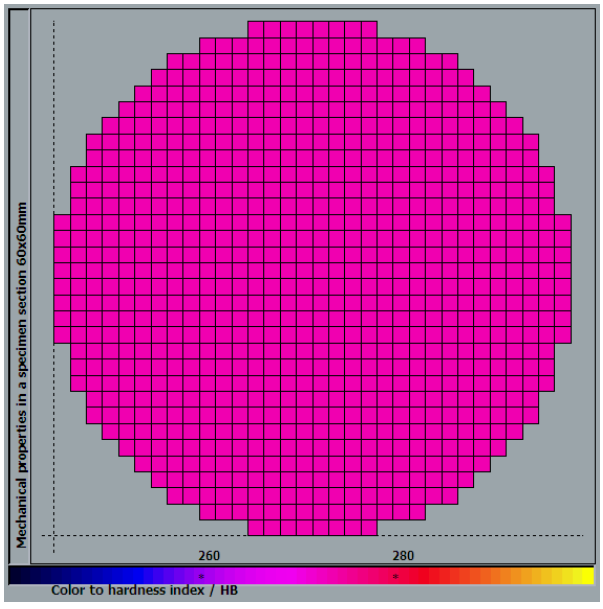

Slika 3. Raspodjela tvrdoće u čeličnoj šipki nakon ohlađivanja
Figure 3. Distribution of hardness of steel bar after cooling

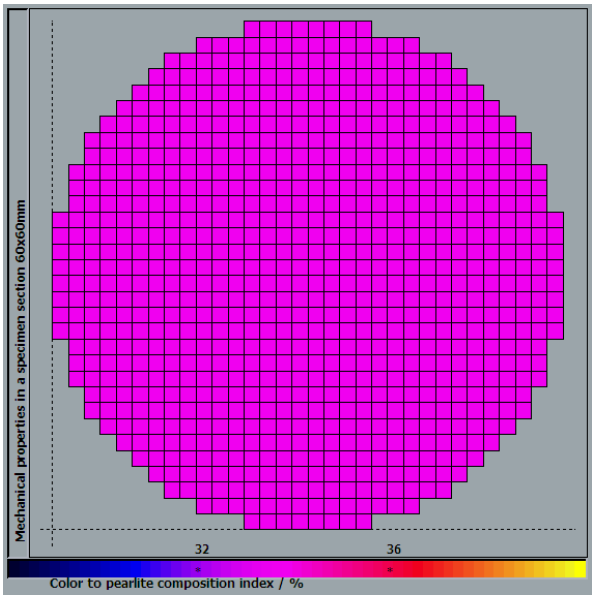

Slika 5. Raspodjela perlita u čeličnoj šipki nakon ohlađivanja
Figure 5. Distribution of pearlite of steel bar after cooling

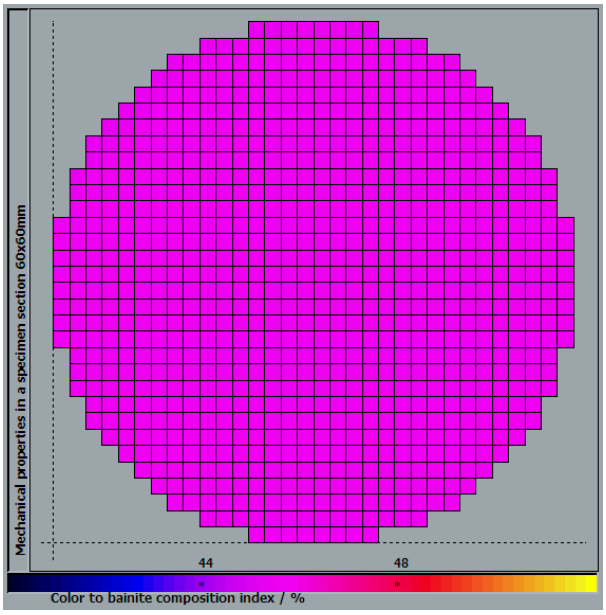

Slika 6. Raspodjela bainita u čeličnoj šipki nakon ohlađivanja
Figure 6. Distribution of bainite of steel bar after cooling

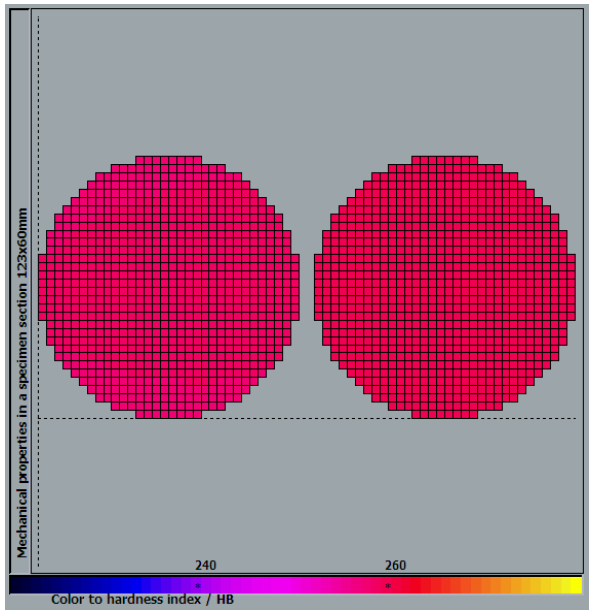

Slika 8. Raspodjela tvrdoće u dvije složene čelične šipke nakon ohlađivanja
Figure 8. Distribution of hardness of two packed steel bar after cooling

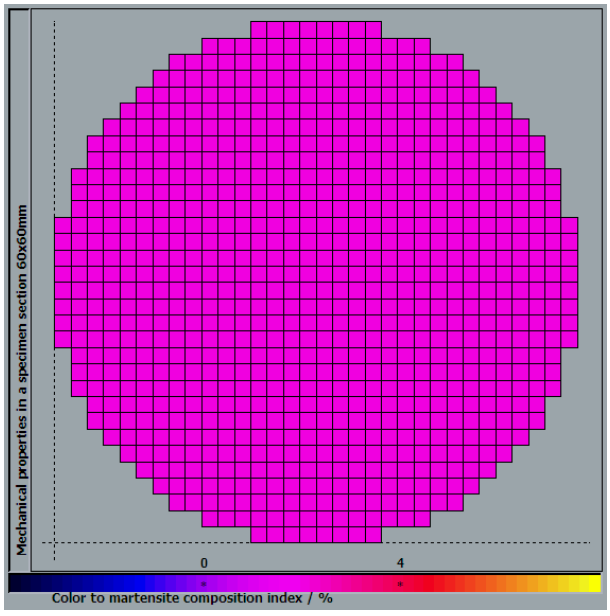

Slika 7. Raspodjela martenzita u čeličnoj šipki nakon ohlađivanja
Figure 7. Distribution of martensite of steel bar after cooling

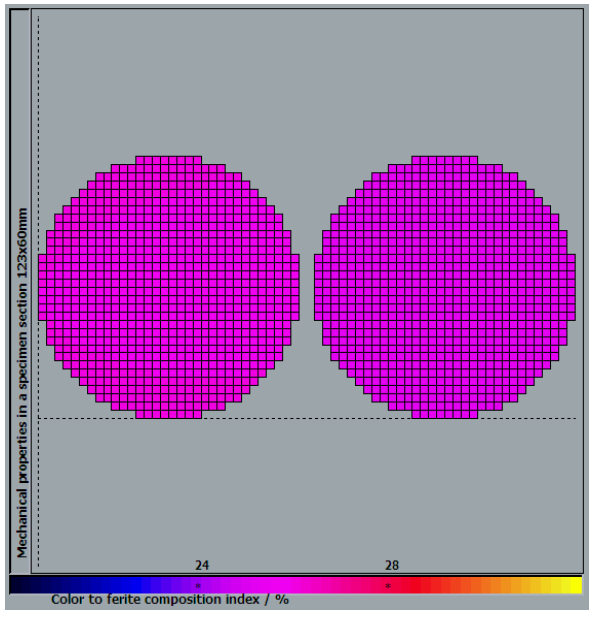

Slika 9. Raspodjela ferita u dvije složene čelične šipke nakon ohlađivanja
Figure 9. Distribution of ferrite of two packed steel bar after cooling

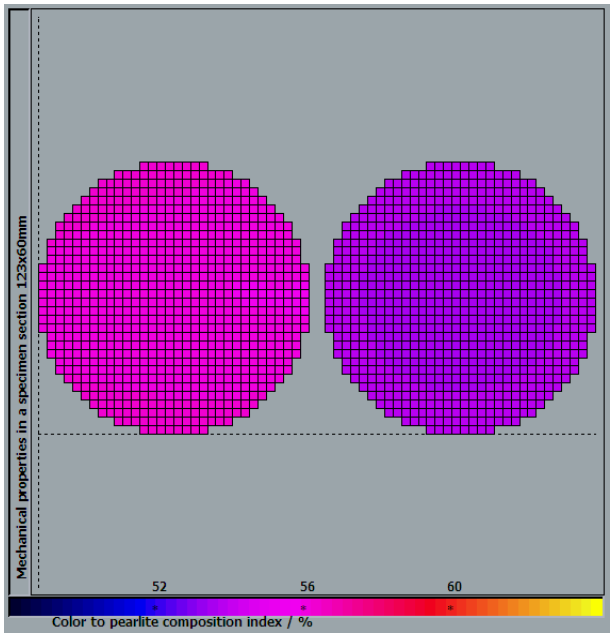

Slika 10. Raspodjela perlita u dvije složene čelične šipke nakon ohlađivanja
Figure 10. Distribution of pearlite of two packed steel bar after cooling

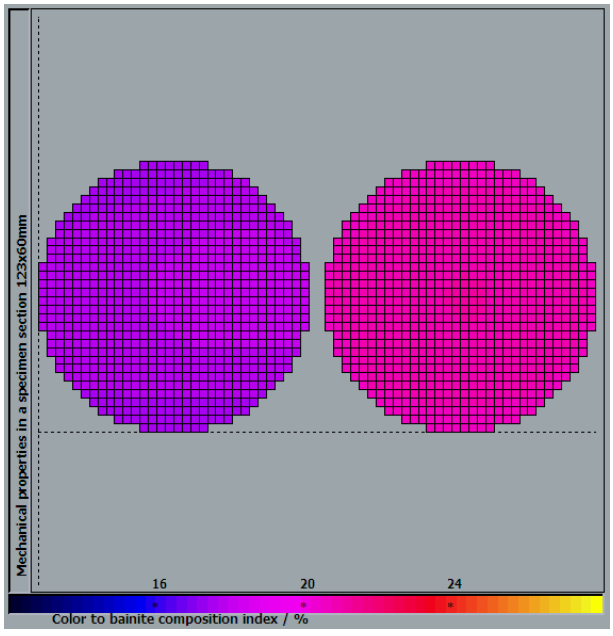

Slika 11. Raspodjela bainita u dvije složene čelične šipke nakon ohlađivanja
Figure 11. Distribution of bainite of two packed steel bar after cooling

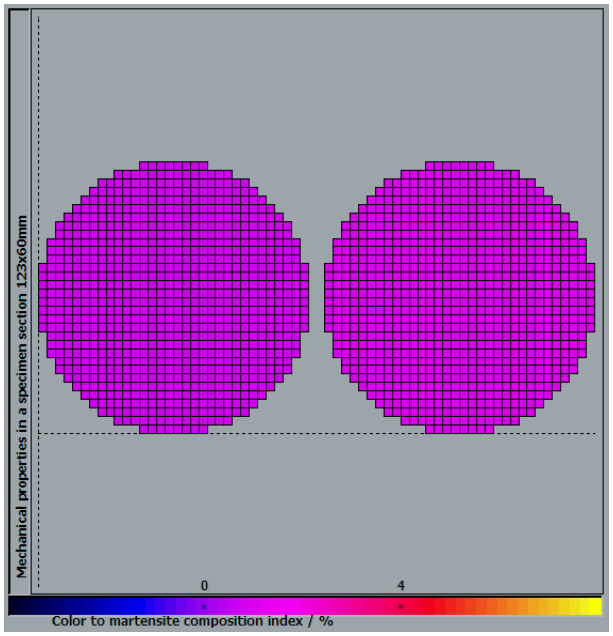

Slika 12. Raspodjela martenzita u dvije složene čelične šipke nakon ohlađivanja
Figure 12. Distribution of martensite of two packed steel bar after cooling

6. Zaključak

Razvijeni numerički model kontroliranog ohlađivanja čeličnih šipki na klupi za ohlađivanje sastoji se od predviđanja promjenjivog temperaturnog polja, razvijanja mikrostrukture i tvrdoće čeličnih šipki tijekom ohlađivanja na klupi za ohlađivanje.

Numerički model prijelaza topline temelji se na metodi konačnih volumena. Algoritam za predviđanje tvrdoće i mikrostrukture u čeličnim šipkama temelji se na TTT dijagramima za kontinuirano ohlađivanje čelika i uzimaju u obzir stvarni kemijski sastav čelika.

Razvijeni numerički model verificiran je usporedbom tvrdoća dobivenih simulacijom s tvrdoćama dobivenim nakon eksperimenta.

Razvijeni model primijenjen je u dva slučaja kontroliranog ohlađivanja različito složenih toplo valjanih šipki na klupi za ohlađivanje. U slučaju zajedničkog ohlađivanja dviju složenih šipki postignuta je prikladnija tvrdoća s minimalnim udjelom bainita i martenzita.

Na osnovi postignutih rezultata može se zaključiti da bi razvijeni softver mogao biti dobro rješenje za predviđanje promjenjivog temperaturnog polja, mikrostrukturnog sastava i raspodjele tvrdoće pri optimizaciji proizvodnje toplo valjanih čeličnih šipki.

Potpora

Ovaj rad je sufinancirala Hrvatska zaklada za znanost projektom 5371.
Ovaj rad je sufinanciralo Sveučilište u Rijeci, broj potpore 13.09.1.1.02.

LITERATURA

[1] Just E., "Verguten—Werkstoffbeenflussung durch Harten und Anlassen", VDI, Bericht, Vol. 256, (1976), pp. 124-140.

[2] Smoljan B., Iljkić D., Senčić B., Vertnik R., Numerical model of controlled cooling of steel hot rolled bars. Proceedings of the HEAT TREAT 2017, (2017) in print.

[3] Liščić B., System for Process Analysis and Hardness Prediction When Quenching Axially-Symmetrical Workpieces of Any Shape in Liquid Quenchants, Materials Science Forum, Vol. 638-642, (2010), pp. 3966-3974.

[4] Felde I., Réti T., Evaluation of Cooling Characteristics of Quenchants by Using Inverse Heat Conduction Methods and Property Prediction, Materials Science Forum, Vol. 659, (2010), pp. 153-158.

[5] Smoljan B., The Calibration of the Mathematical Model of Steel Quenching. Proceedings of the 5th World Seminar on Heat Treatment and Surface Engineering IFHT'95, in: M. Salehi (Ed.), Isfahan, Iran, pp. 709-715, (1995).

[6] Bhadeshia H., Material Factors, in Handbook of "Residual Stress and Deformation of Steel", G. Totten, M. Howes, T. Inoue (eds.), ASM International, (2002).

[7] Smoljan B., Iljkić D., Computer Modeling of Mechanical Properties and Microstructure of Quenched Steel Specimen. Proceedings of the 5th International Conference on Thermal Process Modeling and Computer Simulation, 16-18 June 2014, Orlando, USA.

[8] Smoljan B., Numerical simulation of as-quenched hardness in a steel specimen of complex form, Communications in Numerical Methods in Engineering, 14/1, pp. 277-285, (1998).

[9] Patankar S., "Numerical Heat Transfer and Fluid Flow", McGraw Hill Book Company, (New York, 1980).

[10] Holman J.P., "Heat transfer", McGraw Hill Book Company, (1986).

[11] "Heat Treating", Vol. 4, ASM Handbook, ASM International, 1991.

[12] Smokvina Hanza S., "Mathematical modeling and computer simulation of microstructure transformations and mechanical properties during steel quenching", Doctoral Thesis, Department of Materials Science and Engineering, Faculty of Engineering, University of Rijeka, (2011) (in Croatian).

[13] Rose A., et al. "Atlas zur Wärmebehandlung der Stahle". Teil II. Max-Planck-Institut für Eisenforschung und Werkstoffausschuss des Vereins Deutscher Eisenhüettenleute, (Düsseldorf, 1954).

ISSN 1847-7917

Effect of sample dimensions and fusing temperature on coating/base material structure obtained by flame spraying

Katica ŠIMUNOVIĆ, Sara HAVRLIŠAN, Tomislav ŠARIĆ, Ilija SVALINA, Roberto LUJIĆ and Goran ŠIMUNOVIĆ

University of Osijek, Mechanical Engineering Faculty in Slavonski Brod, Trg I. Brlic-Mazuranic 2, 35000 Slavonski Brod, **Croatia**

Sveučilište u Osijeku, Strojarski fakultet u Slavonskom Brodu, Trg I. Brlić-Mažuranić 2, 35000 Slavonski Brod, **Hrvatska**

katica.simunovic@sfsb.hr
sara.havrlisan@sfsb.hr
tomislav.saric@sfsb.hr
ilija.svalina@sfsb.hr
roberto.lujic@sfsb.hr
goran.simunovic@sfsb.hr

Keywords

Coatings
Flame spraying
Fusing
NiBSi alloy

Ključne riječi

NiBSi legure
Prevlake
Topli postupak naštrcavanja pomoću plinskog plamena

Original scientific paper

Abstract: Flame sprayed Ni-based self-fluxing alloys are frequently used for repairing worn out parts in many industrial applications thus prolonging the service life of products. In practice, these alloys are used in sprayed and fused state. The main purpose of fusing (at temperatures higher than 1000 ^{o}C) is the densification of the coating after spraying and forming the metallurgical bond between the coating and base material. In order to investigate the influence of the fusing temperature on the structure of coating/base material system, but taking into account the dimensions of samples, two different NiBSi alloys were flame sprayed and simultaneously fused on the previously heat treated medium-carbon steel. The conclusion is drawn that the microstructure is influenced not only by high fusing temperature, but also by dimensions of the samples.

Znanstveni rad

Sažetak: Legure nikla s dodatkom bora i silicija naštrcane pomoću plinskog plamena često se primjenjuju za produljenje vijeka trajanja istrošenih dijelova u mnogim industrijama. U praksi se primjenjuju u naštrcanom i pretaljenom stanju da bi se dobila bolja gustoća prevlake (odnosno uklonila poroznost) i postigla metalurška veza između prevlake i podloge. S ciljem istraživanja utjecaja temperature pretaljivanja (iznad 1000 ^{o}C) na mikrostrukturu sustava prevlaka/podloga, ali uzimajući u obzir i dimenzije uzoraka, na čelik prethodno poboljšan, naštrcane su dvije vrste NiBSi legura pomoću plinskog plamena s istovremenim pretaljivanjem. Zaključeno je da je visoka temperatura pretaljivanja utjecala na promjenu strukture podloge, uz nezanemariv utjecaj i dimenzija uzoraka.

1. Introduction

Flame spraying is a thermal spray technology that uses heat energy of flame (mainly acetylene-oxygen) to melt the powder or wire thus forming the coating on the base material. The main purpose of applying this technology is to maintain and repair worn out parts and to prolong the service life. It is an effective and economic deposition technology since many coatings and base materials can be used.

Flame sprayed Ni-based self-fluxing alloy coatings are frequently applied to protect steel parts [1, 2] against wear and corrosion. Mostly, low carbon steels have been used as base materials, but also medium-carbon and alloyed steels (e.g. stainless steels).

Among medium-carbon steels, some authors investigated coated carbon steel containing app. 0.5 % C which is frequently used in hardened, quenched and tempered condition in practice. In the paper [3], AISI 1045 steel with 0.45 % C is flame sprayed with Ni-based alloy modified by CeO_2 and La_2O_3 and then laser remelted. The authors have mainly focused on the sliding wear properties and structure of the coating and dilution in the interface zone. The same base material (SAE 1045) is used in investigation [4] (although the authors have stated 0.15 % C), where the authors applied design of experiment methodology to investigate sliding wear of plasma and flame sprayed Ni-based self-fluxing alloy coatings. The authors [5] have applied the AISI 1050 steel base material (but using the term "low carbon steel") flame sprayed with Ni-based self-fluxing alloy and added WC particles, focusing their research on sliding wear resistance and microstructure of worn out coating. Ni-based self-fluxing alloy modified by rare earth elements or oxides (Ce, La_2O_3 and CeO_2) was deposited onto 1045 steel base material to investigate the sliding wear in [6-8], where the emphasis was put on wear tracks on the coating [6] and microstructure of the coating and coating/base material interface [7, 8]. By the use of EDS mapping, the authors have made conclusion about

diffusion of chemical elements from the coating to the base material and vice versa [7]. In addition, the authors [8] have stated that the coating/base material interface thickness is increased by the addition of CeO_2.

Abrasive wear resistance of flame and HVOF sprayed Ni-based self-fluxing alloy coatings with added WC+Co was investigated in [9]. Ck 45 steel was used as a base material and the authors examined the structure of the coatings and adhesion strength. The authors [10] also used AISI 1045 steel coated with NiCrBSi alloy with added $B_{13}C_2$ to have more borides precipitated during flame spraying.

Erosion resistance of Ni-based self-fluxing alloy coatings was investigated in [11-13], where the normalized carbon steel with 0.45 % C was used as a base material. The authors have given the directions to select the appropriate coating resistant to erosive wear. AISI 1050 carbon steel was used as a reference material in a hardened and quenched state to investigate erosive wear and compare it with surface engineering treated state (boronising, nitriding and thermal spraying) in the paper [14].

The authors [15] have noticed that the martensitic structure was formed from ferrite and cementite in the interface of AISI 1050 steel and flame sprayed and laser remelted NiCrBSi coating. These authors investigated laser surface alloying process too and mentioned a very important property of the base material - thermal conductivity (W/mK) that can influence on the structure of heat-affected zone. For the base materials with higher thermal conductivity, hardening in the interface can occur because of faster conduction of heat. These authors also made conclusion that the chemical composition of the base material can affect the microstructure of the coating. For the base material with 0.5 % C a higher hardness of the coating can be obtained due to formation of carbides in the coating, when comparing to the same laser alloyed coating but deposited onto the stainless steel (lower carbon content).

According to the review of recent literature it can be concluded that there are not so many investigations taking into consideration flame spraying of Ni-based self-fluxing alloy coatings onto the previously heat-treated base material (e.g. the authors [16] highlighted using SAE 1045 steel as a base material without any heat treatment). A similar is valid generally for all thermal spray technologies when depositing Ni-based self-fluxing alloy coatings. However, some authors used heat-treated base material, but focusing their investigation on fatigue and cracking properties [17-21]. Furthermore, the authors mainly focused on the microstructure of the coating and less often on the coating/base material interface as well as base material. In some papers, the base material is not even specified, confirming that a majority of investigators is focused only on the properties of the coating.

Therefore, the main aim of this study is to highlight the influence of high fusing temperature as well as sample size on the microstructure of completely coating/base material system. This paper presents a more detailed analysis of medium-carbon steel/Ni-based self-fluxing alloy coatings system, previously investigated in [22, 23]. After introductory section where the problem is defined and papers presenting investigations of flame sprayed NiBSi coatings on 0.5 % carbon steel are analysed, the sections describing the flame spraying procedure and metallographic examination follow. Finally, the results are analysed and discussed and the conclusions are drawn.

2. Experimental procedure

Two different Ni-based self-fluxing alloy powders (Table 1) were flame sprayed onto the previously heat-treated base material C45 (carbon steel with 0.45 % C), which chemical composition is shown in Table 2. The powder NiCrBSi+WC is a composite powder with 60 % of hard WC particles and 40 % NiCrBSi matrix powder.

Prior to flame spraying the base material samples of hardness 176 HV30 were hardened (temperature 840 °C; time 15 minutes), water quenched and then tempered (temperature 600 °C; time 30 minutes, air-cooling). A small laboratory furnace (power 3000 W, max. temperature 1150 °C) was used for heat treatment. After tempering, the tempered martensite microstructure of base material (Figure 1) was obtained with an average hardness of 30.3 HRC (320 HV30). For flame spraying, Castolin trade mark Eutalloy Super Jet acetylene-oxygen torch (acetylene pressure 50000 Pa, oxygen pressure 200000 Pa) was used where the sprayed powders were simultaneously fused, Figure 2, to obtain dense coatings as well as metallurgical bond between the base material and applied coating. The following terms for this procedure can be found: hot flame spraying, flame spraying with simultaneous fusion (fusing), one-step flame spraying and fusing, spray and fuse, thermal spray welding

Table 1. The chemical composition of powders, wt., % [23]
Tablica 1. Kemijski sastav prašaka, maseni udio, % [23]

	NiCrBSi	NiCrBSi+WC
Cr	15	7
B	3.2	3
Si	4.4	4.5
Fe	0.7	5.8
C	0.7	0.1
W	-	-
Ni	balanced/ostalo	balanced/ostalo

As compared to cold flame spraying where the temperature of the base material is app. 200 °C, in hot flame spraying high fusion temperature of app. 1000 °C for Ni-based self-fluxing alloys can significantly affect the base material. The fusing can be carried out subsequent to flame spraying and this procedure is called two-step flame spraying and fusing or remelting. The

flame torch or laser can be used for remelting as well as heat treatment in furnace or by induction [1, 2].

Table 2. The chemical composition of base material – steel C45 [23]
Tablica 2. Kemijski sastav osnovnog materijala – čelik C45 [23]

Chemical Element/ Kemijski element	C	Si	Mn	S	P	Fe
wt. (%)/Maseni udio (%)	0.45	0.26	0.74	0.032	0.027	balanced/ostalo

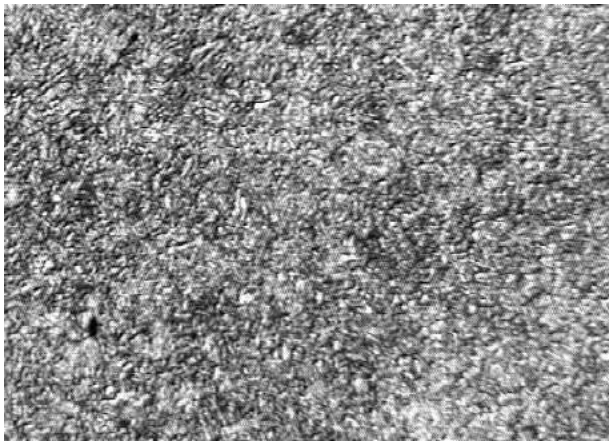

Figure 1. Microstructure of heat treated C45 steel (250:1; etching: nital) [23]
Slika 1. Mikrostruktura osnovnog materijala – čelik C45 (250:1; nagrizanje nital) [23]

Having in mind one of the goals of the paper, two different sizes of steel samples were used for flame spraying and fusing (18x18x18 mm and 75x25x12.5 mm), Figure 2. For small 18x18x18 mm sample, time of spraying and fusing was app. 1 minute (NiCrBSi coating of 0.3 mm thickness; 3 passes), or 1.5 minute (NiCrBSi+WC coating of 0.5 mm thickness; 4 passes). For big 75x25x12.5 mm sample, time of spraying and fusing was app. 4.5 minutes (NiCrBSi coating of 0.3 mm thickness; 3 passes), or 6.5 minutes (NiCrBSi+WC coating of 0.5 mm thickness; 4 passes). Since the big samples were present within the group of samples in the investigation [24], where the Taguchi design was conducted (combining three different base materials, three coatings and three thicknesses) to investigate the cracking resistance, two different thicknesses appear in this study.

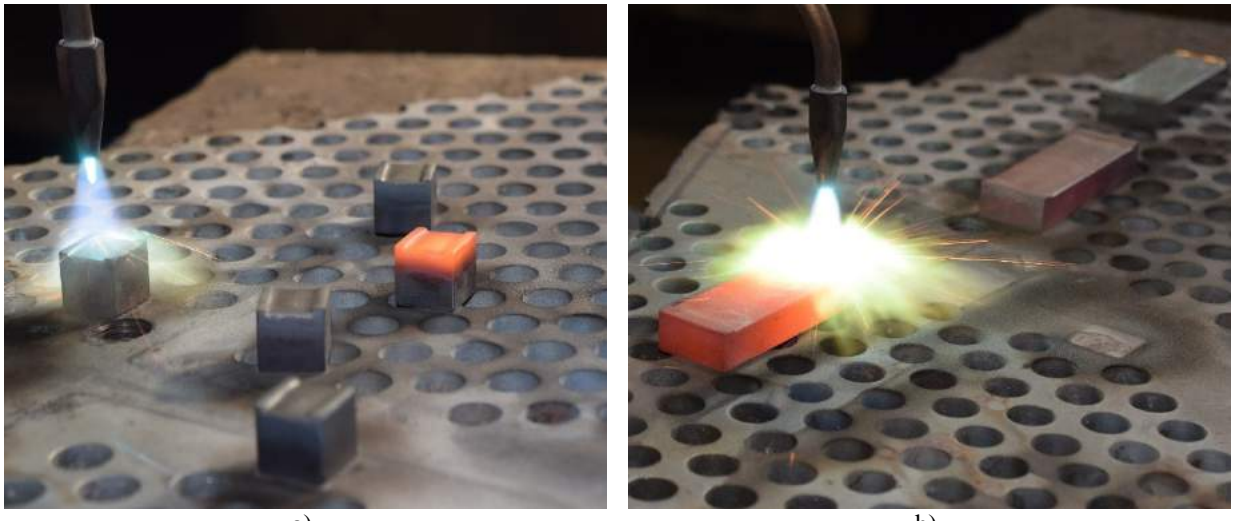

a) b)

Figure 2. Flame spraying and fusing using samples of a) 18x18x18 mm, b) 75x25x12.5 mm
Slika 2. Topli postupak naštrcavanja pomoću plinskog plamena a) uzorak 18x18x18 mm, b) uzorak 75x25x12.5 mm

After flame spraying and fusing, the big samples were cut to dimension 25x25x12.5 mm to be suitable for metallurgical examination. The samples are then prepared by grinding, polishing and etching (nital).
In the following text the terms "small sample" and "big sample" will be used for original sprayed samples of dimensions 18x18x18 mm and 75x25x12.5 mm, respectively, while the term "sample cut from big sample" will be used for cut samples of dimensions 25x25x12.5 mm.

3. Result analysis and discussion

Tables 3 and 4 present the microstructure of the systems NiCrBSi coating/C45 base material and NiCrBSi+WC/C45 base material, for small sample (18x18x18 mm) and sample cut from big sample (25x25x12.5 mm), respectively.

Table 3. C45 steel base material + NiCrBSi coating (0.3 mm thickness)

Tablica 3. Osnovni materijal – čelik C45 + NiCrBSi prevlaka (debljine 0.3 mm)

	Small sample	**Sample cut from big sample**
Coating/base material interface	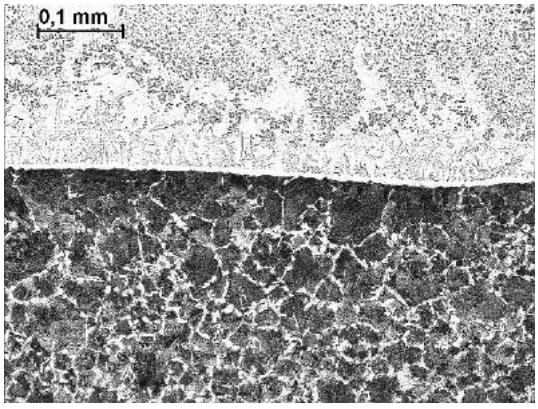	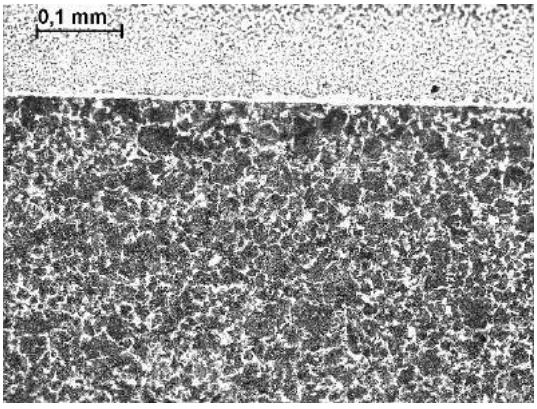
1 mm from coating/base material interface	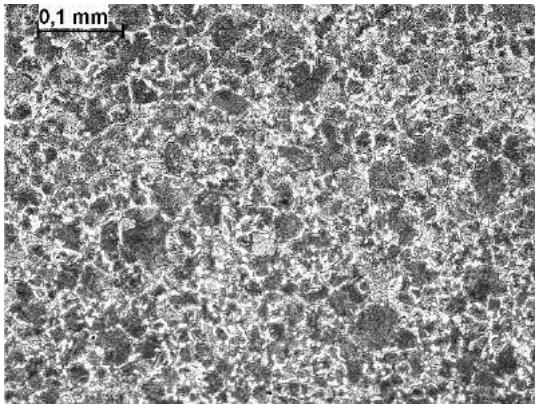	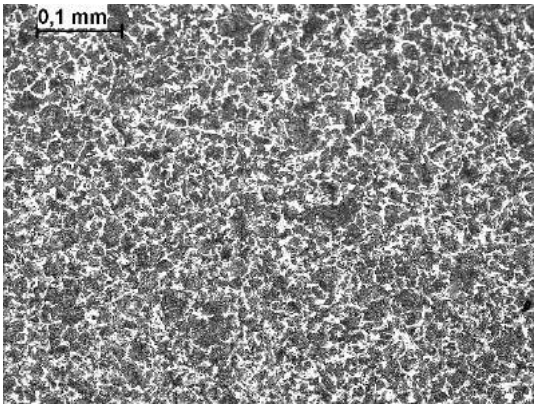
2 mm from coating/base material interface	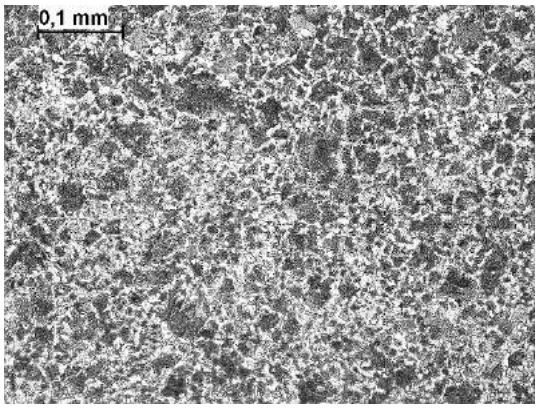	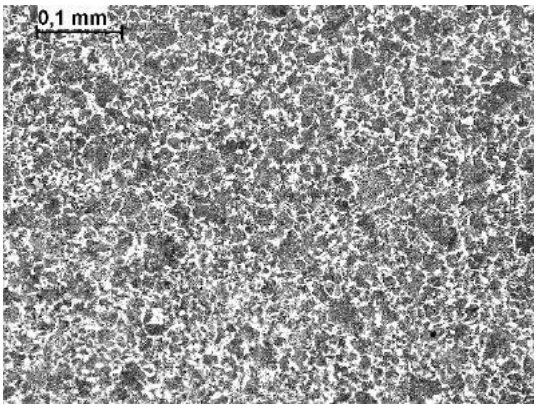
5 mm from coating/base material interface	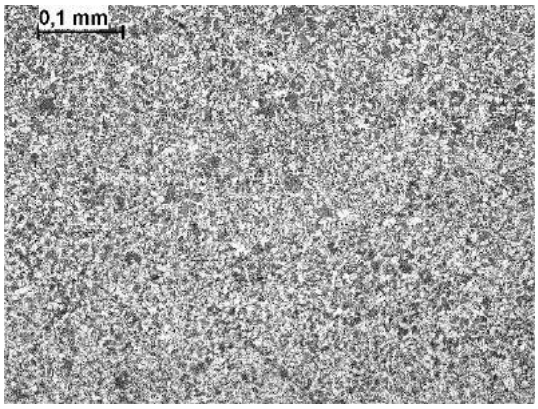	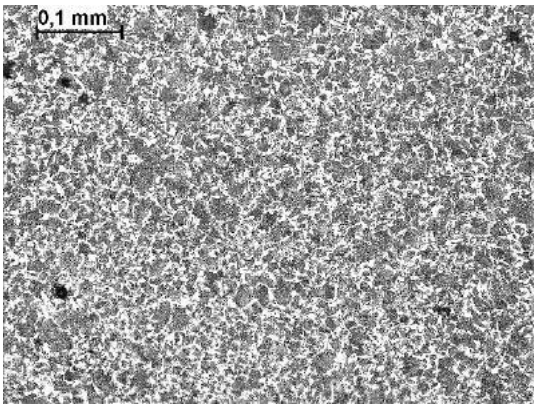

Table 3 continued. C45 steel base material + NiCrBSi coating (0.3 mm thickness)

Tablica 3 nastavak. Osnovni materijal – čelik C45 + NiCrBSi prevlaka (debljine 0.3 mm)

	Small sample	Sample cut from big sample
8 mm from coating/base material interface	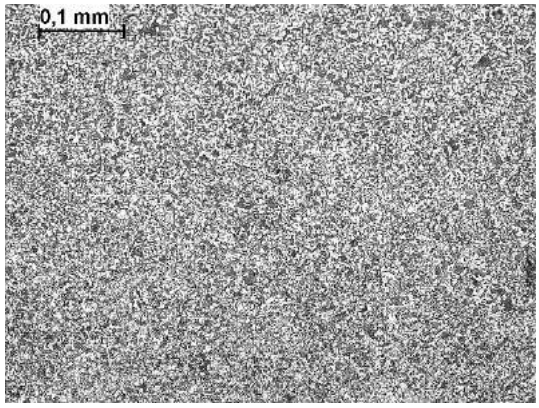	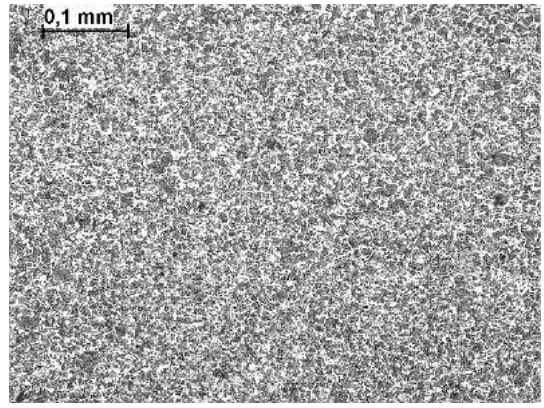
Base material remote to coating	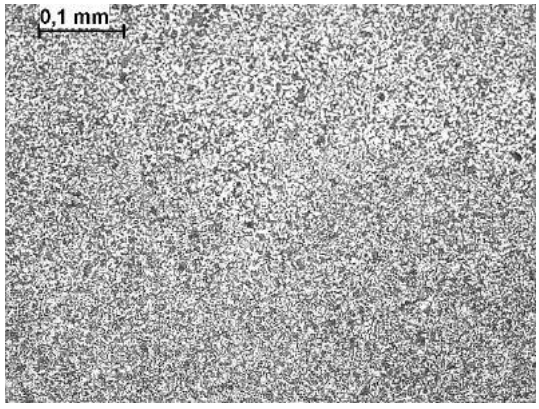	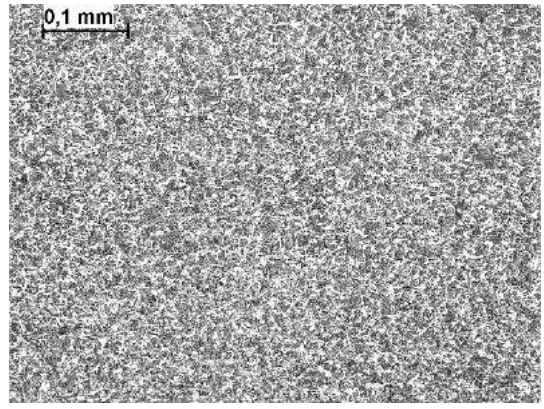

By the analysis of pictures (obtained by the use of light optical microscope Leica DM 2500M at proper magnifications defined on the pictures), in Table 3, the pearlite-ferrite structure of base material is visible for both samples, i.e. the original martensitic structure of base material present prior the flame spraying and fusing (Figure 1) turned to pearlite and ferrite due to high temperature for fusing NiCrBSi alloy coatings (about 1000 ^{o}C). At this temperature carbon steel is in austenitic region. As mentioned above in the introductory section, the authors [15] claimed that martensitic structure was obtained in the interface zone. In the present study, coarser grains of base material are noticed in the interface due to longer exposure to heat input. This is more pronounced in small samples, probably due to concentrated heat input.

In addition, it is visible that there is a heat-affected zone for both types of samples, but it is wider for samples cut from big sample because the big samples were warmed up completely during the flame spraying and fusing (see Figure 2 b). Small samples have a narrower heat-affected zone in the base material (between 2 and 5 mm from interface) since they did not warmed up through the entire thickness (see Figure 2 a).

The similar conclusions are valid for the samples coated with NiCrBSi+WC coating (Table 4). However, due to longer heating (thicker coating), the sample cut from big sample has coarser grains through the entire thickness.

Finally, when considering the coatings of system presented in Table 3, it can be seen that the structure of the NiCrBSi coating near to base material in small sample is different (dendritic) than the structure of the coating on the sample cut from big sample. Because of faster cooling, the formation of precipitates was not possible near the base material when comparing to sample cut from big sample. As to the NiCrBSi+WC coating (Table 4), many coarse WC particles are visible in a NiCrBSi matrix.

Table 4. C45 steel base material + NiCrBSi+WC coating (0.5 mm thickness)

Tablica 4. Osnovni materijal – čelik C45 + NiCrBSi+WC prevlaka (debljine 0.5 mm)

	Small sample	Sample cut from big sample
Coating/base material interface	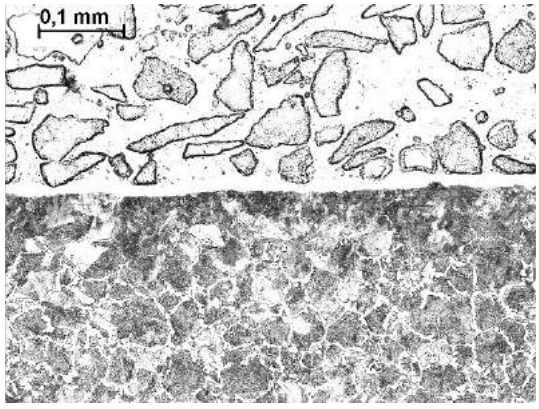	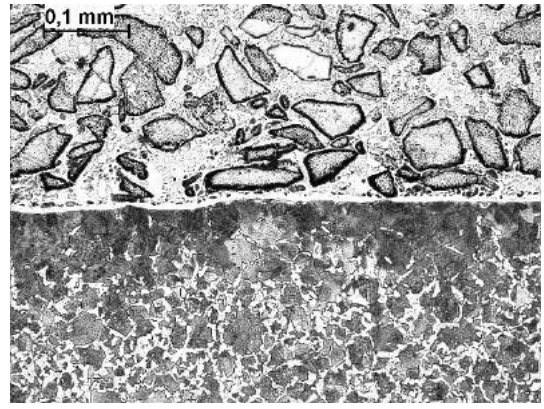
1 mm from coating/base material interface	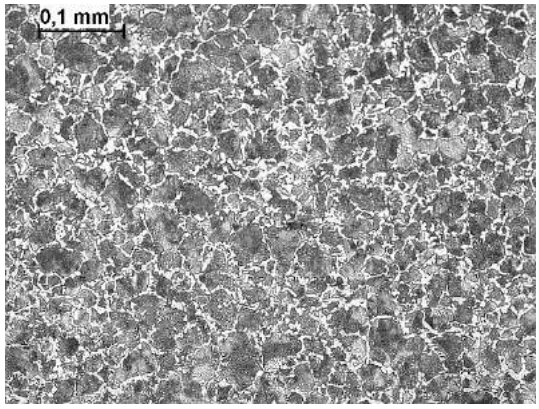	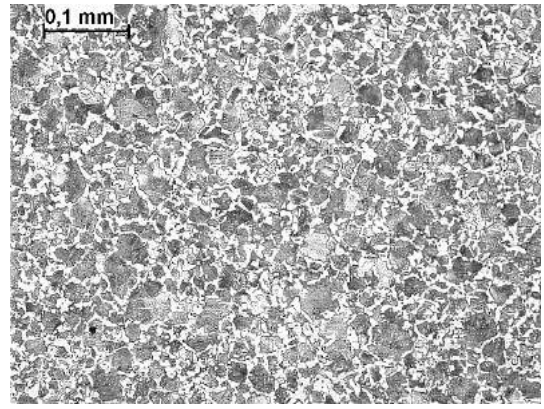
2 mm from coating/base material interface	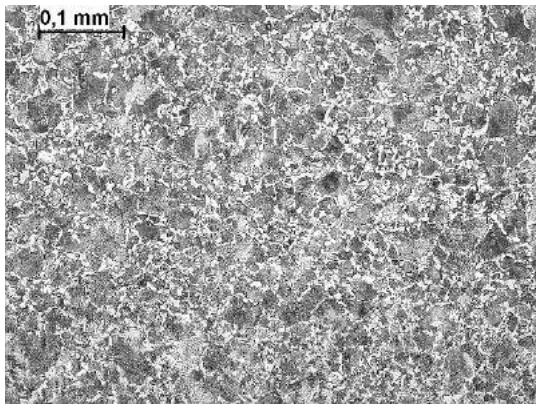	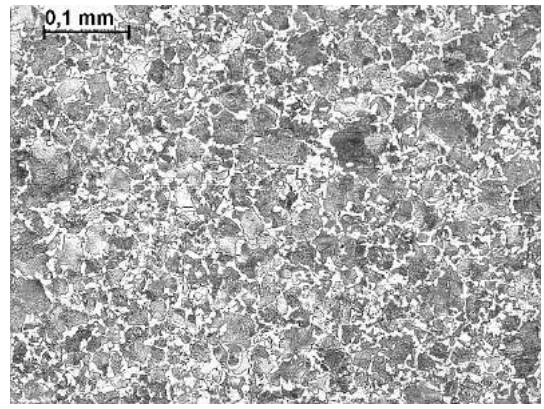
5 mm from coating/base material interface	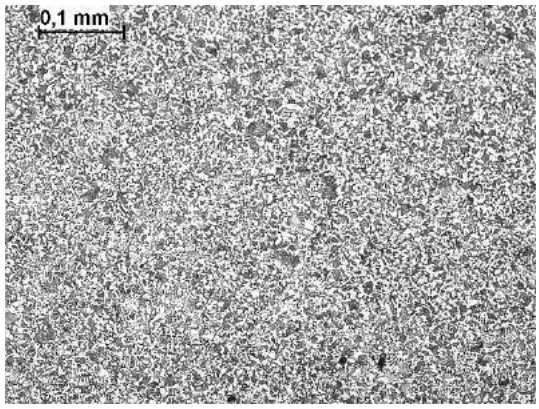	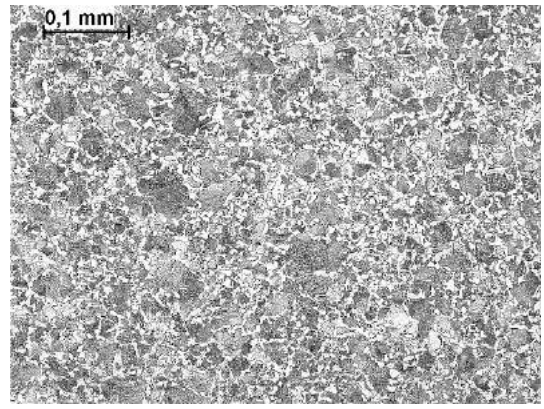

Table 4 continued. C45 steel base material + NiCrBSi+WC coating (0.5 mm thickness)

Tablica 4 nastavak. Osnovni materijal – čelik C45 + NiCrBSi+WC prevlaka (debljine 0.5 mm)

	Small sample	Sample cut from big sample
8 mm from coating/base material interface	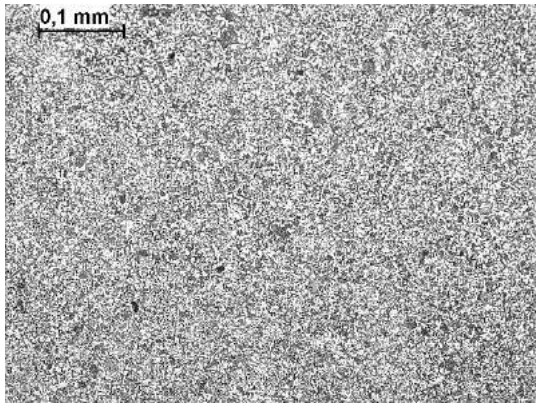	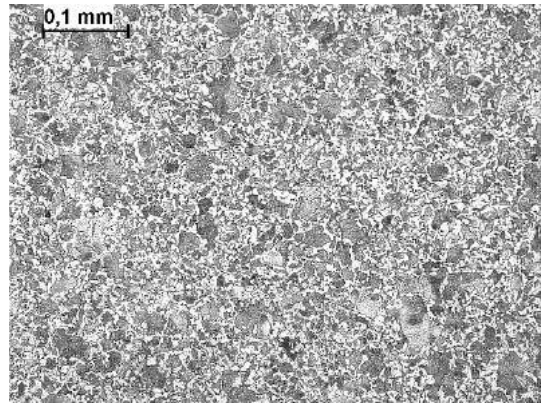
Base material remote to coating	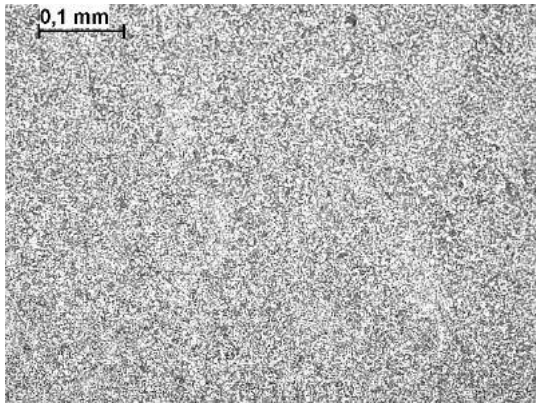	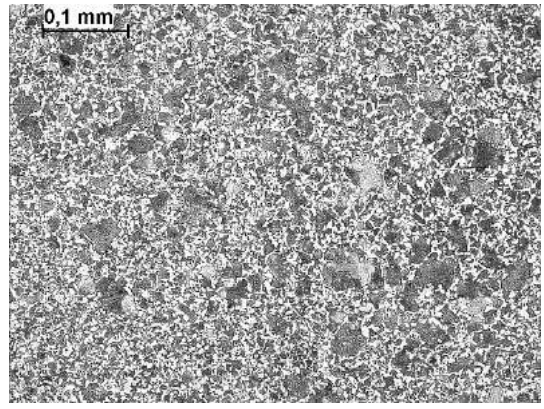

4. Conclusion

As stated in section Introduction, the investigators mainly focused their research on the microstructure of the coating, eventually coating/base material interface and less often on the base material. Moreover, a small amount of investigations is carried out by the use of heat-treated steel with app. 0.5 % C considered in this study. Finally, one should be aware of the sample size. In this paper a conclusion has been made that the sample size can have an influence on the microstructure of the coating/base material system because of different heating times and warming up for small and big samples.

REFERENCES

[1] Šimunović, K., Šarić, T., Šimunović, G., (2014), *Different Approaches to the Investigation and Testing of the Ni-Based Self-Fluxing Alloy Coatings-A Review. Part 1: General Facts, Wear and Corrosion Investigations*, Tribology Transactions 57 No. 6, p 955-979

[2] Šimunović, K., Šarić, T., Šimunović, G., (2014), *Different Approaches to the Investigation and Testing of the Ni-Based Self-Fluxing Alloy Coatings-A Review. Part 2: Microstructure, Adhesive Strength, Cracking Behavior, and Residual Stresses Investigations*, Tribology Transactions 57 No. 6, p 980-1000

[3] Wang, K. L., Zhang, Q. B., Sun, M. L., Wei, X. G., Zhu, Y. M., (2001), *Rare Earth Elements Modification of Laser-Clad Nickel-Based Alloy Coatings*, Applied Surface Science 174, Nos. 3-4, p 191-200

[4] Rodriguez, J., Martin, A., Fernandez, R., Fernandez, J. E., (2003), *An Experimental Study of the Wear Performance of NiCrBSi Thermal Spray Coatings*, Wear 255, p 950-955

[5] Sari, N. Y., Yilmaz, M., (2008), *Improvement of Wear Resistance of Wire Drawing Rolls with Cr-Ni-B-Si+WC Thermal Spraying Powders*, Surface and Coatings Technology 202 No.13, p 3136-3141

[6] Zhang, Z., Wang, Z., Liang, B., (2009), *Wear Characterization of Thermal Spray Welded Ni-Cr-B-Si-RE Alloy Coatings*, Journal of Materials Processing Technology 209 No. 3, p 1368-1374

[7] Zhang, Z., Wang, Z., Liang, B., (2010), *Microstructure and Dry-Sliding Wear Behavior of Thermal Sprayed and Fused Ni-Based Coatings with*

the Addition of La_2O_3, Tribology Letters 37 No. 2, p 141-148

[8] Zhang, Z., Wang, Z., Liang, B., Dong, H. B., Hainsworth, S. V., (2007), *Effect of CeO_2 on the Microstructure and Wear Behavior of Thermal Spray Welded NiCrWRE Coatings*, Wear 262 Nos. 5-6, p 562-567

[9] Miranda, J. C., Ramalho, A., (2001), *Abrasion Resistance of Thermal Sprayed Composite Coatings with a Nickel Alloy Matrix and a WC Hard Phase. Effect of Deposition Technique and Re-Melting*, Tribology Letters 11 No. 1, p 37-48

[10] Shieh, Y. H., Wang, J. T., (1993), *Alloying and post-heat-treatment of thermal-sprayed coatings of self-fluxing alloys*, Surface and Coatings Technology 58, p 73-77

[11] Kulu, P., Pihl, T., (2002), *Selection Criteria for Wear Resistant Powder Coatings under Extreme Erosive Wear Conditions*, Journal of Thermal Spray Technology 11 No. 4, p 517-522

[12] Kulu, P., Hussainova, I., Veinthal, R., (2005), *Solid Particle Erosion of Thermal Sprayed Coatings*, Wear 258 Nos. 1-4, p 488-496

[13] Kulu, P., Halling, J., (1998), *Recycled Hard Metal-Base Wear-Resistant Composite Coatings*, Journal of Thermal Spray Technology 7 No. 2, p 173-178

[14] Sari N. Y., Yilmaz, M., (2006), *Investigation of Abrasive + Erosive Wear Behaviour of Surface Hardening Methods Applied to AISI 1050 Steel*, Materials and Design 27 No. 6, p 470-478

[15] Kwok, C. T., Man, H. C., Cheng, F. T., (2001), *Cavitation Erosion-Corrosion Behaviour of Laser Surface Alloyed AISI 1050 Mild Steel using NiCrSiB*, Materials Science and Engineering A 303, Nos.1-2, p 250-261

[16] Yu, H. L., Zhang, W., Wang, H. M., Yin, Y. L., Ji, X. C., Zhou, K. B., (2016), *Comparison of Surface and Cross-Sectional Micro-Nano Mechanical Properties of Flame Sprayed NiCrBSi Coating*, Journal of Alloys and Compounds 672, p 137-146

[17] Voyer, J., Kreye, H., (2003), *Determination of Cracking Resistance of Thermal Spray Coatings during Four-Point Bend Testing using an Acoustic Emission Technique*, Journal of Thermal Spray Technology 12 No. 3, p 416-426

[18] Hernandez, L., Oliveira, F., Berrios, J. A., Villalobos, C., Pertuz, A., Puchi Cabrera, E. S., (2000), *Fatigue Properties of a 4340 Steel Coated with a Colmonoy 88 Deposit Applied by High-Velocity Oxygen Fuel*, Surface and Coatings Technology 133-134, p 68-77

[19] Puchi-Cabrera, E. S., Berrios-Ortiz, J. A., Da-Silva, J., Nunes, J., (2003), *Fatigue Behavior of a 4140 Steel Coated with a Colmonoy 88 Alloy Applied by HVOF*, Surface and Coatings Technology 172 Nos. 2-3, p 128-138

[20] La Barbera-Sosa, J. G., Santana, Y. Y., Villalobos-Gutierrez, C., Chicot, D., Lesage, J., Decoopman, X., Iost, A., Staia, M. H., Puchi-Cabrera, E. S., (2013), *Fatigue Behavior of a Structural Steel Coated with a WC-10Co-4Cr/Colmonoy 88 Deposit by HVOF Thermal Spraying*, Surface and Coatings Technology 220, p 248-256

[21] Oliveira, F., Hernandez, L., Berrios, J. A., Villalobos, C., Pertuz, A., Puchi Cabrera, E. S., (2001), *Corrosion-Fatigue Properties of a 4340 Steel Coated with Colmonoy 88 Alloy, applied by HVOF Thermal Spray*, Surface and Coatings Technology 140 No. 2, p 128-135

[22] Šimunović, K., Slokar, Lj., Havrlišan, S., (2017), *SEM/EDS Investigation of One-step Flame Sprayed and Fused Ni-Based Self-Fluxing Alloy Coatings on Steel Substrates*, Philosophical Magazine 97 No. 4, p 248-268

[23] Šimunović, K., Kladarić, I., Krumes, D., (2008), *Investigation of Substrate Microstructure after Flame Spraying and Fusing*, Strojarstvo 50 No. 4, p 209-216

[24] Šimunović, K., Šarić, T., Šimunović, G., Lujić, R., (2008), *Optimisation of Tribomechanical Systems using Taguchi Experimental Design*, Proceedings of the Eight International Conference on Advanced Manufacturing Systems and Technology (AMST 08) / Elso Kuljanić, ed., Udine: CISM International Centre for Mechanical Sciences, p 629-640

ISSN 1847-7917

Development and optimization of surface roughness predictive models in turning super duplex stainless steel by using artificial intelligence methods

Mario VEIĆ, Dražen BAJIĆ
Sonja JOZIĆ
Faculty of Electrical Engineering, Mechanical Engineering and Naval Architecture, University of Split
Ruđera Boškovića 32, 21000 Split, Republic of Croatia
Fakultet elektrotehnike, strojarstva I brodogradnje, Sveučilište u Splitu
Ruđera Boškovića 32, 21000 Split, Republika Hrvatska

mario.veic@fesb.hr
dbajic@fesb.hr
sonja.jozic@fesb.hr

Keywords
Super duplex stainless steel
ANFIS
Genethic algorithm
Response surface method
Surface roughness

Ključne riječi
Super duplex nehrđajući čelik
ANFIS
Genetski algoritam
Metoda odzivne površine
Površinska hrapavost

Original scientific paper

Abstract: Super duplex stainless steels are alloys that have good corrosion resistance properties and are intended for applications in corrosive environments. Due to their chemical composition and microstructure providing high strength and thermal resistance as well as high ductility, the machinability of these alloys is difficult, resulting in longer production cycles and higher costs in terms of more frequent replacement of tools. In this paper the machinability of the superduplex EN 1.4410 was investigated in the machining process without using a cooling and lubricating medium. Experimental data were generated using the range of selected input parameters and correspondingly analyzed surface roughness as output data. Predictive and mathematical models were developed that were used in the optimization process to minimize the surface roughness. The influence of input parameters on surface roughness was analyzed and the optimum values of the input parameters were obtained using the genetic algorithm. The accuracy of developed predictive models was analyzed using different sets of experimental data. Developed predictive models could be in practice used by operators while selecting optimal processing parameters to achieve the surface roughness value requested by the constructor.

Originalni znanstveni rad

Sažetak: Super dupleks nehrđajući čelici su legure koje imaju dobro svojstvo otpornosti na koroziju te su namijenjene za primjene u korozivnim okolinama. Zbog njihovog kemijskog sastava i mikrostrukture koja osigurava visoku čvrstoću i toplinsku otpornost kao i visoku duktilnost, strojna obradivost ovih legura je otežana, što za posljedicu ima duže proizvodne cikluse i veće troškove u pogledu češće zamjene alata. U ovom radu istraživana je obradivost superdupleks čelika oznake EN 1.4410 u postupku obrade tokarenjem bez korištenja sredstva za hlađenje i podmazivanje. Eksperimentalni podaci su generirani pomoću odabranog raspona vrijednosti ulaznih parametara te odgovarajuće analizirane izlazne veličine površinske hrapavosti. Razvijeni su prediktivni i matematički modeli koji su korišteni u postupku optimiranja s ciljem minimizacije veličine površinske hrapavosti. Analizirani su utjecaji ulaznih parametara obrade na površinsku hrapavost te su primjenom genetskog algoritma dobivene optimalne vrijednosti ulaznih parametara. Analizirana je točnost razvijenih prediktivnih modela korištenjem različitih skupova eksperimentalnih podataka. Razvijeni prediktivni modeli bi u stvarnoj praksi mogli koristiti operaterima pri odabiru optimalnih parametara obrade s ciljem ostvarivanja zahtijevane površinske hrapavosti od strane projektanta.

1. Introduction

Stainless steel or corrosion-resistant steel is an iron alloy containing at least 10.5% chrome (modern stainless steels containing up to 30% chromium), unlike ordinary steel that is rapidly oxidized to the air if it is not in some way corrosion-protected. Unlike other materials that are mainly classified by chemical composition, corrosion-resistant steels are more often classified according to the microstructure. Microstructure of stainless steel can be ferrite, martensite and austenitic, so there are ferrite, martensite and austenitic stainless steels. There is also a group having a structure composed of approximately 50% austenite and 50% ferrite. These are duplex stainless steels which have better properties of austenitic and ferrite steels. Today duplex steels are applied in many places due to their superior corrosion resistance and very good mechanical properties. Due to the high ferrite content they are ferromagnetic, they have higher thermal conductivity and lower thermal expansion than austenitic steels. In places where high resistance to puncture corrosion is required, the choice of austenitic steel is more appropriate. Because of the relatively high strength,

duplex steels are the optimal choice for structures exposed to corrosion, where their remarkable combination of corrosion resistance and mechanical properties is highlighted. Duplex steels have a much larger stretching limit (about 425 MPa) versus austenitic (about 210 N / mm2). Their hardness is also higher and, accordingly, abrasion wear resistance. Most new steel duplexes have good toughness and ductility. Because of the large fraction of the ferritic phase, the temperature drops rapidly from a tough to a fragile area, similar to ferrite stainless steels. The temperature range of their application is limited to -40 ° C or 315 ° C due to the numerous microstructure precipitates that can be isolated at a relatively low temperature, which have a poor influence on corrosion resistance and mechanical properties. First stainless duplex steel was manufactured in Sweden in 1930 and has been successfully applied in the paper industry as a replacement for austenitic stainless steel that is sensitive to intercrystalline corrosion. At the same time, the first duplex cast was manufactured in Finland. After the Second World War, more intensive application of crushed and casted duplex alloys in the process industry begins. The first duplex steels (duplexes of the first generation) do not have a well-balanced chemical composition and generally do not contain nitrogen. Such steels are difficult to weld and have poorer mechanical properties and corrosion resistance compared to later developed duplexes in which nitrogen is an indispensable legal supplement. The division of the second-generation steel duplex was based on the resistance of the duplex of steel to perforated corrosion by the Pitting Resistance Equivalent Number (PREN).

2. Literature review

Super and hyper duplex steels contain more elements which provide them with an effective sum value of more than 40. The basic elements in duplex steel are chrome and nickel, and also a very important role in the formation of microstructures are still nitrogen, molybdenum, copper, manganese, silicon and tungsten. An increased percentage of molybdenum increased their corrosion resistance. They have great application as construction materials [1]. Super duplex stainless steels are extremely corrosion-resistant alloys intended for applications in corrosive environments such as sea water. Because of their chemical composition and microstructure, which ensures high strength and thermal resistance as well as high ductility, the machinability of these alloys is poor, resulting in longer production cycles and higher costs in terms of more frequent tool replacement.

Oliveira Junior [6] investigated the turning process of SAF 2507 alloy in order to analyze the influence of machining process on corrosion resistance in practical applications. The results of the experiments show that using PVD coated tools at high pressure cooling achieves a longer tool life, a satisfactory surface finish quality, and high corrosion resistance of machined material after machining process.

Rajaguru [2] was investigating the machining of superduplex steel by using tools with different types of coatings. Process characteristics such as tool wear, cutting force, cutting temperature, and integrity of the machined surface are analyzed. Tool wear analysis has shown that the [MT-TiCN]Al_2O_3 coating tool provides relatively good wear resistance due to high MT-TiCN hardness and Al_2O_3 oxidation stability. TiN- [MT-TiCN]Al_2O_3 coatings are exposed to relatively high cutting force values. TiOCN-Al_2O_3-TiCN-[MT-TiCN] -TiN coating provides less cutting forces due to high TiOCN hardness and of their lower friction coefficient. AlTiN coating generates the highest temperature due to high friction and low thermal conductivity. [MT-TiCN] -Al_2O_3 coating provides lower surface roughness due to increased resistance to abrasion wear of cutting edges. Finally, it can be concluded that the [MT-TiCN] -Al_2O_3 coating provides relatively good performance in terms of tool wear, cutting force, cutting temperature and surface integrity compared to other used coatings.

In his research, Paiva [3] used three types of PVD coatings: Al50Cr50N, Al60Cr40N, and Al50Cr50N/ Ti95Si5N, which were applied to a carbide tool. Analyzing the wear mechanisms of used tools, it has been shown that in all types of coatings is the dominant adhesive wear. Due to the more favorable chemical composition, the Al50Cr50N / Ti95Si5N coating provides less friction and consequently less tool wear.

Kumar [4] analyzed the impact of machining parameters on the tool wear during turning experiment of super duplex stainless steel SAF 2507 with uncoated carbide tool. The process was carried out under dry conditions, wet processing and using gaseous carbon dioxide. Carbon dioxide has a beneficial effect as a coolant, which ensures less tool wear.

Ahmed [5] has studied the wear mechanisms of uncoated and coated carbide tools during the turning experiment of SAF 2507 alloy. The results of the experiments show that the dominant mechanism of tool wear is adhesive wear for all the tools used and that AlTiN coating provides better process characteristics compared to CVD TiCN + Al_2O_3 coatings and uncoated tools in the sense of a significant reduction in the formation of the built-up edge.

Dhanachezian [7] investigated machinability of the austenitic stainless steel AISI 316L and SDSS 2507 by using tools coated with Ti-AlN PVD coatings. The results of the experiments show that higher cutting forces, poor quality of the treated surface and higher wear of tools occur in the machining of super duplex stainless steel. It is also concluded that more preferred forms of separate particles occur during the processing of austenitic stainless steel. In the end, it can be concluded that the super duplex stainless steel 2507 is an extremely difficult material for machining.

In this paper, the machinability of the super duplex stainless steel EN 1.4410 will be investigated in terms of obtaining satisfactory quality of treated surface. By performing experiments on the chosen range of input parameter limits, will be developed predictive Neural Networks (ANFIS) models and also mathematical models that will enable optimization of response variables and input parameters. Comparative analysis will determine the accuracy of each developed predictive model.

3. Eksperimental work

The experimental work was obtained at the Laboratory of Machine Tools at the Faculty of Electrical Engineering, Mechanical Engineering and Naval Architecture in Split. The aim was to obtain measurement results that will enable mathematical modeling for the selected output value of surface roughness *Ra* in the turning process. Experiments were carried out on the universal lathe machine PRVOMAJSKA RAŠA under dry conditions, figure 1. As tool holder was used from "PROMAX" manufacturer and cutting insert "Partizan". The workpiece material is super duplex stainless steel 1.4410 according to EN 10028-7: 2007. **Figure 1** shows the preparation of workipece material with dimensions ø50x250mm. Measurements of the surface roughness were used by the device of the manufacturer Mitutoyo, **Figure 2**. The aim of experimental study of this paper is developing the appropriate mathematical models that would describe the output value of the process depending on the input processing parameters. In the next chapter by processing of experimental data will develop mathematical models describing the dependence of the observed output value on particular input processing parameter.

Figure 1. *Turning of super duplex steel*

Figure 2. *Surface roughness measuring device*

4. Developing the predictive models of surface roughness

4.1. Mathematical modeling of surface roughness

The results of the experiments were used to develop a mathematical surface roughness model using regression analysis. The surface roughness equation is modeled using the response surface method (RSM), which consists of a series of statistical techniques that are useful in analyzing a problem in which the response is dependent on several variables to optimize the response itself. For the calculation of regression constants and parameters, the central composite (CCD) second order test plan was used in the Design Expert software package. The number of experimental points required in second-order trial plans is determined by the following expression:

$$N= 2^k +n_o+n_a \quad (1)$$

where are:

2^k – the number of experiments in the basic points

n_o – number of repeat experiments at the middle level

n_a – number of experiments on the central axes

Optimization implementation in Design Expert requires application of limit input parameters, whose values have been adopted on thebasis of the manufacturer's recommendation and physical limitations of the machine, as well as the testing of the test experiment, as shown in **Table 1.**

Table 1*. Input parameters physical values*

Input parameters	Unit of measure	Lower bound	Upper bound
Feedrate	mm/rev	*0.063*	*0.224*
Cutting speed	m/min	*28*	*45*
Cutting depth	mm	*1*	*2*

According to the above expression, the number of experimental points required for k = 3, but = 6, to = 6 is N = 20. In the next chapter, **Table 3** shows all input parameters of the experiment and the corresponding response surface roughness.

Impact of input parameter on response can be found by variance analysis (ANOVA). Variance analysis is a comparison procedure of multiple samples, each sample being the basic set. After examining the significance of the coefficients of the second order model, a final mathematical model of surface roughness was obtained: Dependence diagrams of the mathematical model of surface roughness on the processing input parameters are shown in **Figures 3, 4** and **5**.

$$Ra = -7{,}97119 + 20{,}55505 \cdot f_n + 0{,}24488 \cdot v_c + 4{,}33502 \cdot a_p - 0{,}14249 \cdot f_n \cdot v_c + 0{,}12422 \cdot f_n \cdot a_p - 0{,}00235294 \cdot v_c \cdot a_p - 45{,}69440 \cdot f_n^2 - 0{,}00311973 \cdot v_c^2 - 1{,}34708 \cdot a_p^2$$

where are:

- Ra – surface roughness,
- v_c – cutting speed,
- a_p – cutting depth.
- f_n – feedrate,

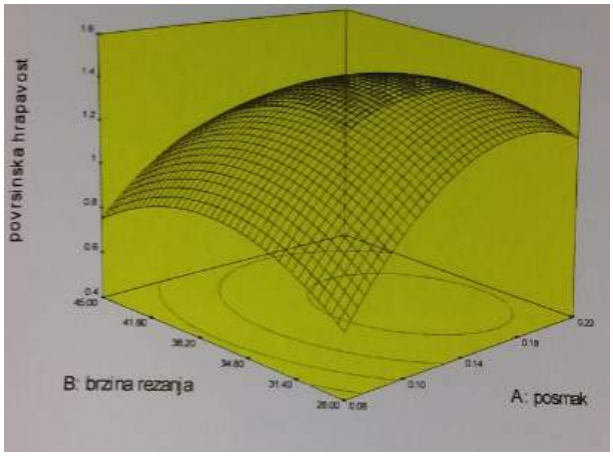

***Figure 3**. Surface roughness dependence of federate and cutting speed*

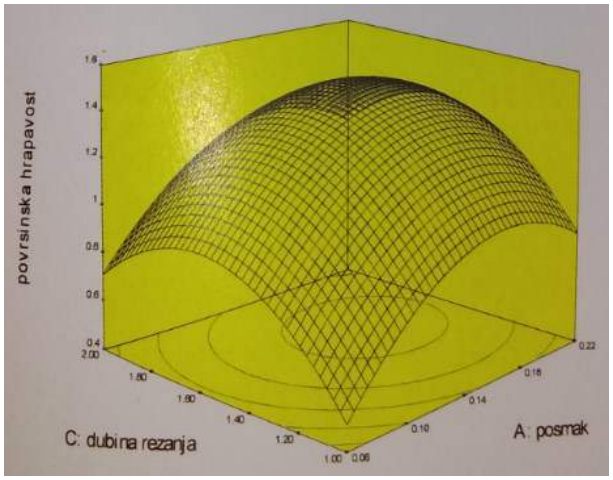

***Figure 4.** Surface roughness dependence of federate and cutting depth*

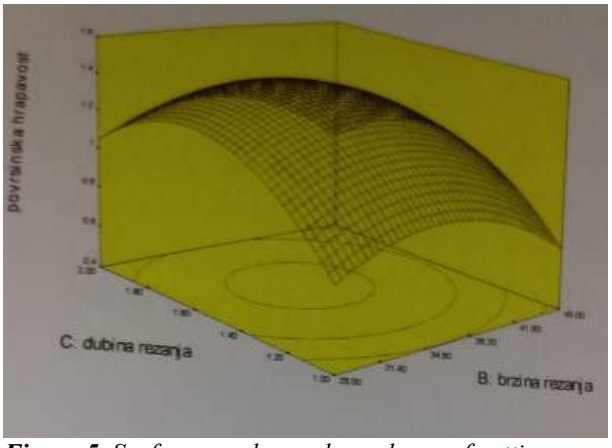

***Figure 5**. Surface roughness dependence of cutting depth and cutting speed*

4.2. ANFIS predictive model

ANFIS (engl. *Adaptive neuro fuzzy inference system*) is an artificial intelligence method that implies a hybrid approach to combining artificial neural networks and FIS (Fuzzy Interference System) systems, which are typically used to approximate unfamiliar functions. The result is a system that allows the use of well-known algorithms for learning artificial neural networks, which can't be used in fuzzy systems, while retaining the ability to use fuzzy logic and inconceivable conclusions. Prior to implementing this method, it is necessary to make experimental data sharing on learning, testing, and validation sets. Then starts working with the Matlab software package. Creating a fuzzy system provides an automatic structure of the ANFIS network. ANFIS networks are generated with differences in fuzzy logic systems, generated by differences in membership functions, by the number of affiliation functions for each input variable and the value type for the output variable. [8] Considering the results obtained by the validation of the generated ANFIS networks, **Gauss2mf linear membership function** was chosen (**Figure 6**), which had the lowest validation error.

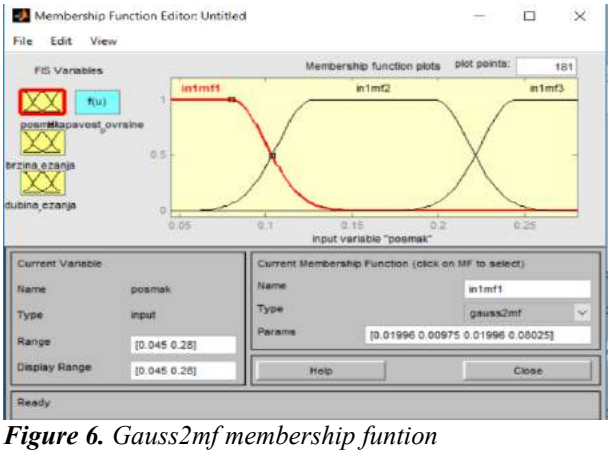

***Figure 6.** Gauss2mf membership funtion*

For the SUGENO fuzzy locking system (**Figure 7),** three input values and one output value are defined. Each input value generates three linear Gauss2mf membership functions, and the output value is also generated by the linear Gauss2mf function. By generating a fuzzy logic system, the ANFIS network structure shown in **Figure 8** and the "if-then" rules shown in **Figure 9** and **Figure 10** are automatically generated.

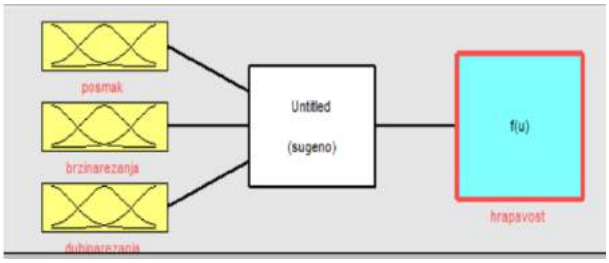

Figure 7. SUGENO FIS surface roughness model

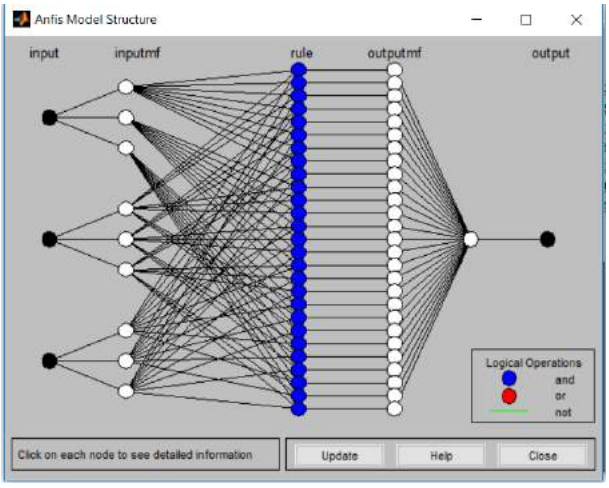

Figure 8. Structure of ANFIS network

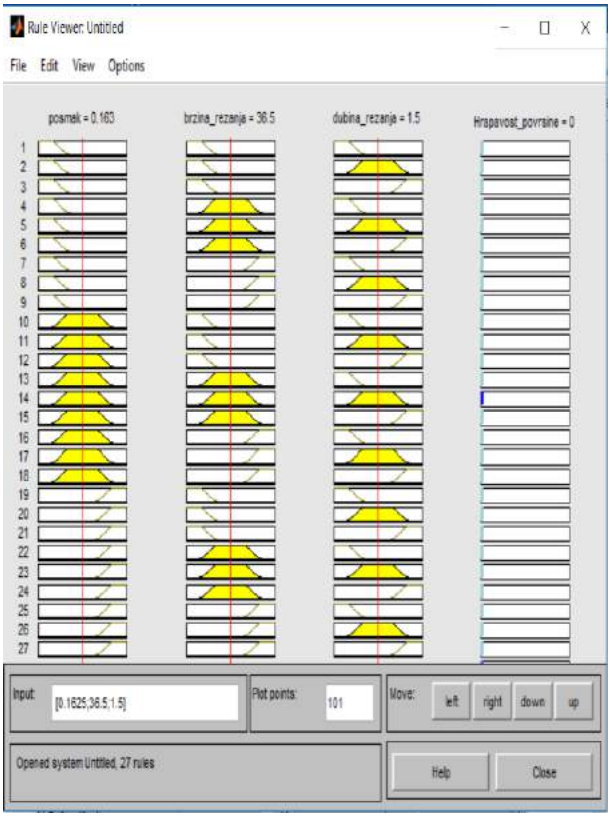

Figure 9. Created fuzzy rules

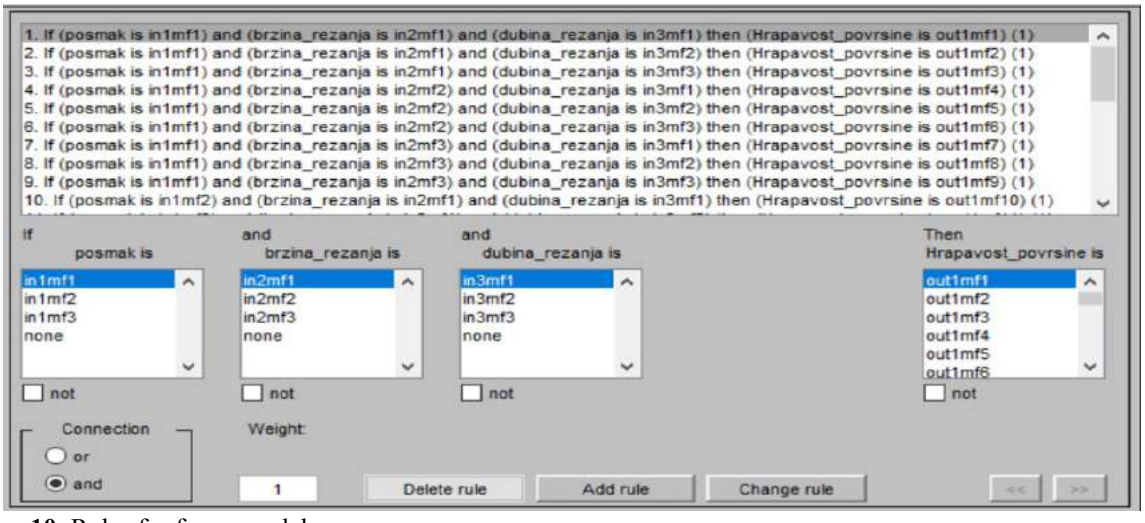

Figure 10. Rules for fuzzy model

After generating the fuzzy logic system and structure of the ANFIS network and the if-then rules follows the train of the ANFIS network hybrid algorithm, which takes place over 100 cycles (epochs) and the result can be seen on the graph in **Figure 11**. The ANFIS training network error is 0.0075593. After training the ANFIS network, then follows the test procedure for the network. An error of 0.058022 was found when testing the ANFIS network, as shown in **Figure 12**. After testing the ANFIS network, the validation of the trained ANFIS network is provided. During validation of ANFIS network there was obtained 0.051512 validation error, **Figure 13**.

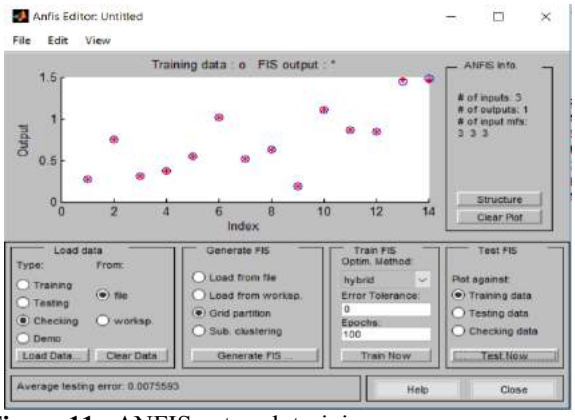

Figure 11. ANFIS network training

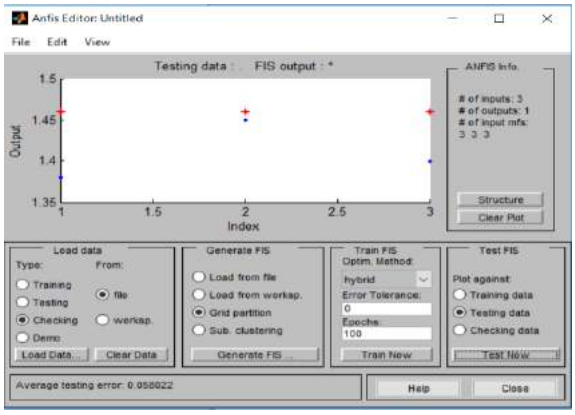

Figure 12. ANFIS network testing

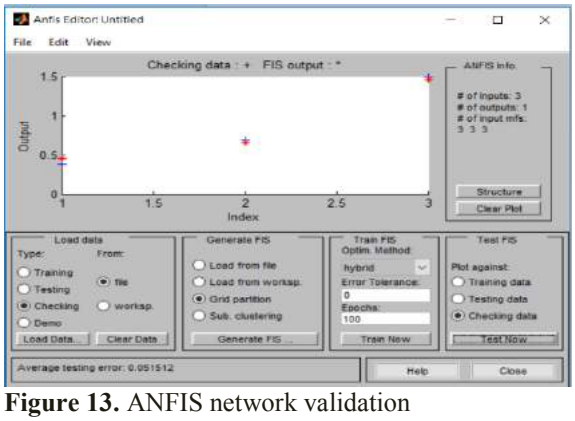

Figure 13. ANFIS network validation

Analog to variance analysis, ANFIS predictive surface roughness dependence diagrams on input processing parameters are shown in **Figures 14, 15 and 16**.

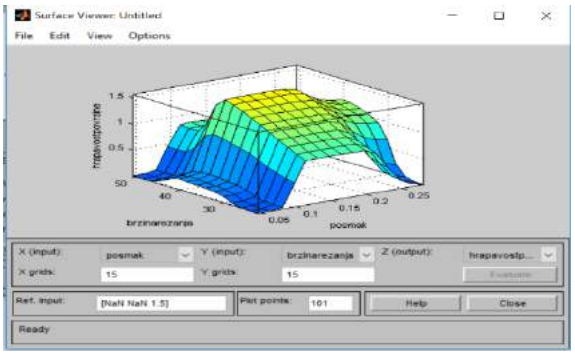

Figure 14. Surface roughness dependence of cutting speed and feedrate

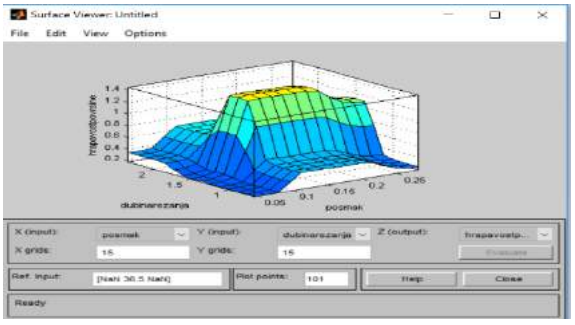

Figure 15. Surface roughness dependence of cutting depth and feedrate

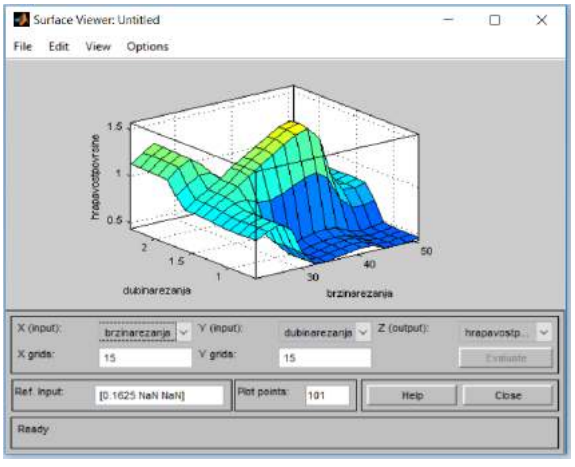

Figure 16. Surface roughness dependence of cutting speed and cutting depth

5. Comparative accuracy analysis of developed predictive models

In order to evaluate the performance index of the learning algorithm in solving the selected task, it is necessary to define measure accuracy. By using a measure of accuracy for typical learning tasks it is possible to compare the applied algorithm with other learning algorithms. To compare predicted and measured surface roughness values, a statistical approach will be used to determine the root mean square error according to the expression:

$$RMSE = \sqrt{\frac{1}{N}\sum_{i=1}^{N}(M_i - P_i)^2} \quad (2)$$

Where are:
M_i – measured value
P_i – predicted value
N - number of measurements
The statistical error of surface roughness values predicted by response surface method and ANFIS based learning database method are shown in **Table 2**, and a graphical comparison of the accuracy of developed predictive models in **Figure 17**.

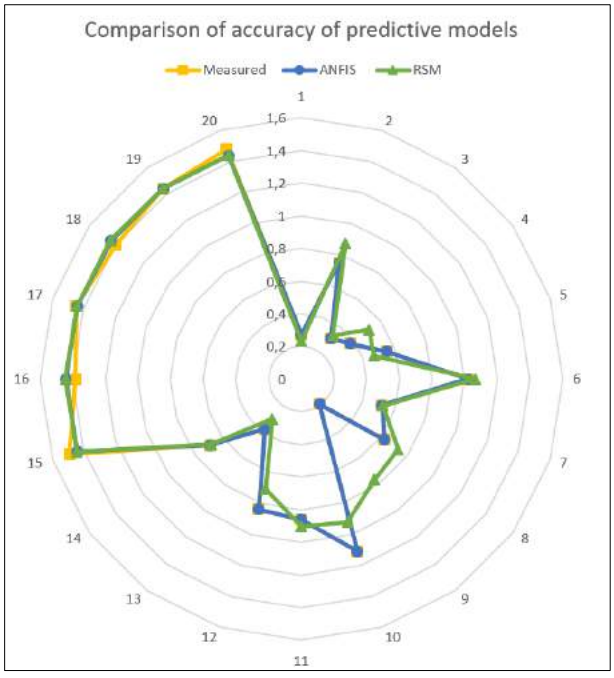

Figure 17. Comparison of the accuracy of developed predictive models

Table 2. Results of conducted experiments and comparison of accuracy of predictive models

f_n *[mm/rev]*	v_c *[m/min]*	a_p *[mm]*	*Ra* Measured	RSM Predicted	RMSE (%) RSM	ANFIS Predicted	RMSE (%) ANFIS
0.063	28	1	0.27	0.2317	0.856	0.27	0
0.224	28	1	0.75	0.873	2.750	0.749997	6.7082e-05
0.063	45	1	0.31	0.3305	0.458	0.309999	2.2361e-05
0.224	45	1	0.37	0.5161	3.266	0.370001	2.2361e-05
0.063	28	2	0.55	0.4674	1.847	0.549998	4.4721e-05
0.224	28	2	1.02	1.0631	0.963	1.019995	1.1180e-04
0.063	45	2	0.52	0.5262	0.138	0.519999	2.2361e-05
0.224	45	2	0.63	0.7318	2.276	0.629999	2.2361e-05
0.045	36.5	1.5	0.19	0.7602	12.75	0.190001	2.2361e-05
0.28	36.5	1.5	1.11	0.9223	4.197	1.11	0
0.1435	22.2	1.5	0.86	0.9024	0.948	0.86	0
0.1435	50.8	1.5	0.84	0.7068	2.978	0.839	2.23e-05
0.1435	36.5	0.66	0.38	0.3024	1.735	0.38	0
0.1435	36.5	2.34	0.69	0.6817	0.185	0.69	0
0.1435	36.5	1.5	1.49	1.4426	1.059	1.44	1.1180
0.1435	36.5	1.5	1.38	1.4426	1.059	1.44	1.3416
0.1435	36.5	1.5	1.45	1.4426	1.059	1.44	0.2236
0.1435	36.5	1.5	1.4	1.4426	1.059	1.44	0
0.1435	36.5	1.5	1.44	1.4426	1.059	1.44	0
0.1435	36.5	1.5	1.48	1.4426	1.059	1.44	0.8944

6. Optimization of processing parameters

It is necessary to determine the optimum processing parameters to achieve the minimum cutting time with required surface quality. In order to determine the optimum processing parameters, the equation for predicting the production time and the surface roughness equation will represent the objective functions, which includes the limitations of the input processing parameters.

Surface roughness equation:

$$Ra = -7{,}97119 + 20{,}55505 \cdot f_n + 0{,}24488 \cdot v_c + 4{,}33502 \cdot a_p - 0{,}14249 \cdot f_n \cdot v_c + 0{,}12422 \cdot f_n \cdot a_p - 0{,}00235294 \cdot v_c \cdot a_p - 45{,}69440 \cdot f_n^2 - 0{,}00311973 \cdot v_c^2 - 1{,}34708 \cdot a_p^2 \quad (3)$$

Cutting time equation, according to [9]:

$$CT = \frac{\pi \cdot D \cdot L}{1000 v_c \cdot f_n} \quad (4)$$

where are:

CT - cutting time

D – workpiece diameter: D = 50 mm.

To find optimal solutions, a multi-criteria optimization technique was used with an evolutionary genetic algorithm. The members of the population are vectors of independent variables. During the implementation of the genetic algorithm the population size does not change. The initial population is the one with which the algorithm starts and is randomly generated. After a certain number of iterations, the process stops if the best member of the current population is the solution closest to the optimum. Using the MATLAB program package and introducing the equation for processing (4) and surface roughness (3), optimal processing parameters were obtained, as shown in **Table 3**.

Table 3. Optimal values of processing parameters

Feedrate [mm(rev]	0.045
Cutting speed [m/min]	26.93
Cutting depth [mm]	0.66
Ra [μm]	0.30

L - machining length: L= 30 mm

7. Conclusion

This paper presents the development of predictive surface roughness models in the super duplex steel turning process under dry conditions. Input parameters are feedrate, cutting speed, and cutting depth. Based on the 20 experiments that were carried out, surface roughness prediction models were developed using the response surface method, variance analysis and ANFIS predictive method, and the following conclusions were derived:

- By analyzing the diagrams obtained by regression analysis, it can be concluded that the feedrate has the greatest influence on the roughness of the treated surface. Determination coefficient of mathematical model is R^2 = 0.97. It can be concluded that the model is representative because it explains 97% of the deviations resulting from the processing parameters.
- 15 sets of experimental data were used for training of the ANFIS network, while 3 sets of data were used to test the developed network. Two sets of data are used for validation of ANFIS network.
  The average accuracy of the ANFIS model validation is 94.9%, indicating the possibility of applying this model when predicting surface roughness for other set of input data.
- Analyzing **Figure 17**, it can be concluded that both predictive models well describe the observed process, given the small differences in predicted and measured surface roughness values. By analyzing the accuracy of the developed models, it can be concluded that the ANFIS model is more precise since it achieves a maximum root mean square error of 1.3%, compared to the value of 12.75% for variance analysis, as can be seen from **Table 2**.
- Based on the developed predictive models and the process of multi-criteria optimization and knowing the advantages and limitations of these processes, it is possible to finally achieve a more productive process based on further development and application of the artificial intelligence methods and development of an intelligent production system.

REFERENCES

[1]. Židov B.: "*Ispitivanje nehrđajućih čelika – diplomski rad*", FSB Zagreb, 2012.

[2]. Rajaguru J, Arunachalam N.: "*Coated tool performance in Dry turning of Super Duplex Stainless Steel*", Procedia Manufacturing ,601-611, 2017.

[3]. Jose Mario F. Paiva, Fred L. Amorim, Paulo C. Soares Jr., Stephen C. Veldhuis, Luciano A. Mendes, Ricardo D. Torres: "*Tribological Bbehaviour of superdupleks stainless steel against PVD hard coatings on cemented carbide*", International Journal of Advanced Manufacturing, Springer-Verlag London, 2016.

[4]. K. Senthil Kumar, J.S. Senthilkumaar: "*Morphology when machining super duplex stainless steel in gas cooled enviroment*", International Journal of Engineering and Technology (IJET), India, 2013.

[5]. Yassmin Seid Ahmed, Jose Mario Paiva, Danielle Covelli, Stephen Clarence Veldhuis: "*Investigation of coated cutting tool performance during machining of superduplex stainless steels through 3D wear evaluations*", Coatings, 2017.
[6]. Carlos Ancelmo de Oliveira Junior, Anselmo Eduardo Diniz, Rodnei Bertazzoli: "*Corelating tool wear, surface roughness and corrosion resistance in the turning process of super duplex stainless steel*", Brazilian Society of Mechanical Sciences and Engineering, 2013.
[7]. Dhanachezian M, Tinesh T, Steven Niketan Paul, Inian Roy: "*Study of machinability characteristics for turning austenitic (316L) and super duplex (2505) stainless stell using PVD-TiAlN nano-multilayer inserts*", ARPN Journal of Engineering and Applied Sciences, 2016.
[8]. Jyh-Shing, Roger Jang: "*ANFIS: Adaptive network-based fuzzy interference system*", IEE Transactions on Systems, Manufacturing and Cybernetics, California, 1993.
[9]. Petkovic D., Radovanovic M.: "*Using genethic algorithm for optimization of turning machining process*", Journal of Engineering Studies and Research,2013.

ISSN 1847-7917

Effect of pH on corrosion of CuAlMn alloy in 0.9% NaCl solution

Ladislav VRSALOVIĆ[1)], ***Marko MATULIĆ***[1)], ***Stjepan KOŽUH***[2)], ***Ivana IVANIĆ***[2)] and ***Mirko GOJIĆ***[2)]

1) University of Split, Faculty of Chemistry and Technology, Ruđera Boškovića 35, 21000 Split, Croatia

2) University of Zagreb, Faculty of Metallurgy, Aleja narodnih heroja 3, 44103 Sisak, Croatia

ladislav@ktf-split.hr, kozuh@simet.hr, marko.matulic13@gmail.com, iivanic@simet.hr, gojic@simet.hr

Keywords

CuAlMn-alloy
NaCl solution
corrosion
polarization
SEM/EDS

Ključne riječi

CuAlMn-legura
NaCl-otopina
korozija
polarizacija
SEM/EDS

Original scientific paper

Abstract: This paper presents the results of corrosion investigation of cast CuAlMn alloy in 0.9 % NaCl solution at 37 °C and pH = 3.4, 5.4 and 7.4. Investigations were performed by open circuit potential measurements, linear and potentiodynamic polarization measurements. After polarization measurements, electrode surfaces were investigated by optical microscope and also with SEM/EDS analysis. Results of polarization measurements have shown that the corrosion current density of CuAlMn alloy was decreased and the values of polarization resistance were increased with the increasing in pH. Optical microscopy surface examination of the CuAlMn alloy, after the polarization investigations, revealed the grain boundaries within the alloy as well as damages on the surface of the electrodes due to the uniform corrosion of the alloy. The EDS analysis determined the chemical composition at certain sites on the surface of the samples.

Izvorni znanstveni rad

Sažetak: U radu su prikazani rezultati korozijskih ispitivanja lijevane CuAlMn legure u 0.9% NaCl otopini pri 37 °C i pH = 3.4, 5.4 i 7.4. Ispitivanja su provedena mjerenjem potencijala otvorenog strujnog kruga, mjerenjima linearne i potenciodinamičke polarizacije. Nakon polarizacijskih mjerenja površine elektroda su ispitane optičkim mikroskopom a također i SEM/EDS analizom. Rezultati polarizacijskih mjerenja su pokazali da povećanjem pH otopine dolazi do smanjenja vrijednosti gustoće korozijske struje i povećanja vrijednosti polarizacijskog otpora. Pregledom površine CuAlMn legure optičkim mikroskopom nakon polarizacijskih ispitivanja vidljiva su granica zrna unutar legure kao i oštećenja površine elektroda koje su posljedica opće korozije legure. EDS analizom utvrđen je kemijski sastav na pojedinim mjestima na površini uzoraka

1. Introduction

Shape memory alloys (SMA) are a family of metallic alloys with the remarkable ability to switch from one crystallographic structure to another through a change in temperature or applied stress [1-3]. The uniqueness of shape memory alloys lies in their ability to switch from one crystalline structure to another by a diffusionless transformation. The interchangeable crystalline forms are austenite and martensite [4]. The reason the alloy attains a particular phase at a given temperature is because the alloy continuously tries to attain thermodynamic equilibrium. As such, the alloy tries to attain the phase which makes it thermodynamically stable at a given temperature. If such alloys are plastically deformed at one temperature, they will completely recover their original shape on being raised to a higher temperature. In recovering their shape the alloys can produce a displacement or a force as a function of temperature.

Among many alloy systems which exhibit shape memory effect, Ni–Ti, Cu–Al–Ni and Cu–Zn–Al shape memory alloys have been studied extensively [5-8].

The Ni–Ti shape memory alloys in particular are used extensively in many engineering and biomedical applications. Nevertheless, the low transformation temperatures (-100 to 100 °C) and excessive production cost of NiTi alloys render their usage for many applications impractical, particularly for high temperature usage. Copper-based shape memory alloys, on the other hand, are easier to produce and process and are also less expensive. But most Cu–Al–Ni and Cu–Zn–Al polycrystalline shape memory alloys are brittle and cannot, therefore, be cold worked.

However, it has been reported in recent studies that Cu-Al-Mn alloys with low aluminium contents show good ductility because their parent phase with L2 structure possesses comparatively a lower degree of order [9, 10]. This feature could well be useful for the shape memory alloys to exhibit better pseudoelasticity.

Electrochemical experiments were conducted in a three-electrode cell using a potentiostat (PAR M273A). Corrosion investigations were performed in double-jacketed glass corrosion cell, equipped with platinum sheet as a counter electrode and saturated calomel electrode (SCE) as reference electrode. The evaluation of corrosion behaviour of CuAlNi alloy in 0.9% NaCl solution were performed by open circuit potential measurements (E_{OC}) in 60 min time period, followed by linear polarization measurements in the potential region of ±20 mV around corrosion potential with the scanning rate of 0.2 mV s^{-1}. Potentiodynamic polarization measurements was performed in the potential region of −0.250 V from open circuit potential to 1.500 V with the

Symbols/Oznake

E_{oc}	- open circuit potential, V - potencijal otvorenog strujnog kruga	*SCE*	- saturated calomel electrode - zasićena kalomel elektroda
i_{corr}	- corrosion current density, μAcm^{-2} - gustoća korozijske struje	*wt.%*	- maseni postotak, - weigh percentage
E_{corr}	- corrosion potential, V - korozijski potencijal	*at.%*	- atomski postotak - atomic percentage
R_p	- polarization resistance, Ωcm^2 - polarizacijski otpor		

scanning rate of 0.5 mV s^{-1}. The surface morphology of the samples after potentiodynamic measurements was examined in detail by optical microscope Olympus GX 51, and with scanning electron microscope Tescan Vega TS 5136 MM. The quantitative analysis of the elements on the electrode surface was determined by energy dispersive spectroscopy (EDS).

2. Electrochemical measurements

The open circuit potential changes for studied CuAlMn electrodes in 0.9% NaCl solution of different pH values is shown in Figure 1.

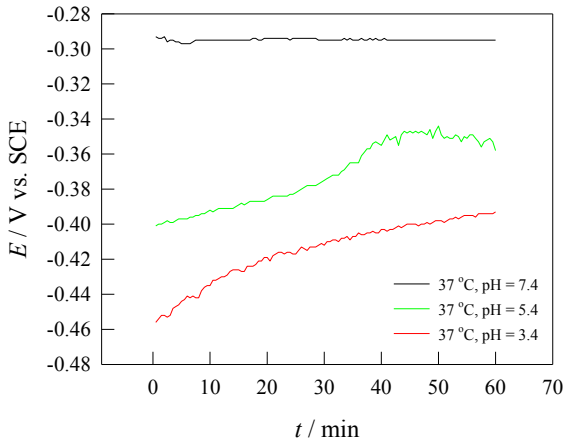

Figure 1. Open circuit potential measurement for CuAlMn alloy in 0.9% NaCl solution of different pH values.

Slika 1. Mjerenje potencijala otvorenog strujnog kruga za CuAlMn leguru u 0.9% NaCl otopini pri različitim vrijednostima pH otopine

The steady state is reached within 60 minutes of electrode immersion in the electrolyte. It can be seen that lowering pH values of NaCl solution leads to changes of E_{oc} to the negative direction. So the most negative E_{oc} of CuAlMn alloy was obtained in 0.9% NaCl solution pH = 3.4.

After open circuit potential measurements the linear polarization measurements were performed, in the potential region of ±20 mV around E_{OC} and the results were shown in Figure 2.

Polarization resistance (R_p) represents the resistance of metal to corrosion, and is defined by the slope of the polarization curve near the corrosion potential, by the equation (1):

$$R_p = \frac{\Delta E}{\Delta i} \ (\Omega \ \text{cm}^2) \qquad (1)$$

The values of corrosion resistance for the CuAlMn samples were shown in Table 1. From the Figure 2 it can be seen that lowering the pH values of NaCl solution leads to decrease the slopes of the polarization curves, resulting in lower values of R_p, which means lower resistance of CuAlMn alloy to corrosion.

Right after linear polarization measurements, potentiodynamic polarization measurements were performed in wide range of potential, from -0.250 V from E_{oc} to 1.5 V, and the obtained curves are shown in Figure 3.

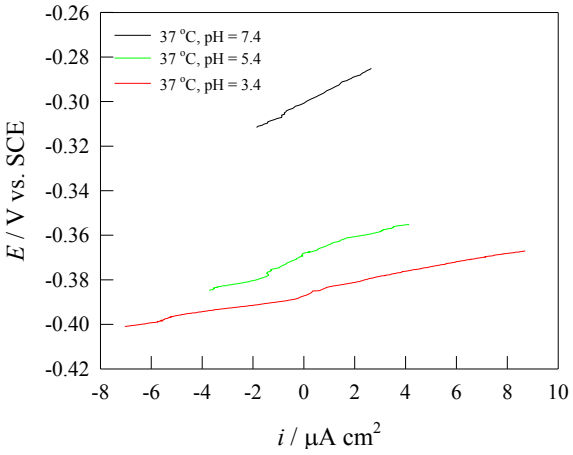

Figure 2. Linear polarization curves for CuAlMn alloy, in 0.9% NaCl solution of different pH values.

Slika 2. Krivulje linearne polarizacije za CuAlMn leguru u 0.9% NaCl otopini različitih pH vrijednosti

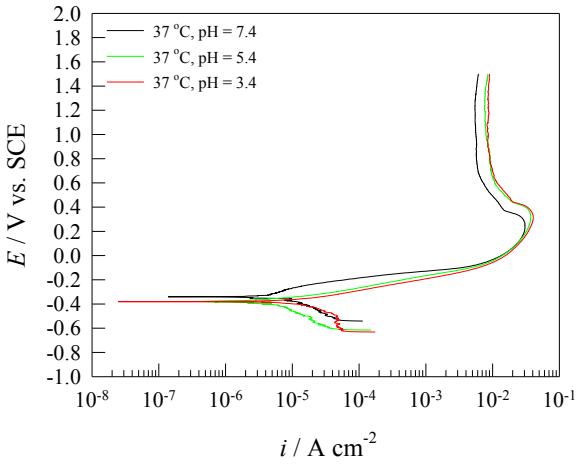

Figure 3. Potentiodynamic polarization curves of CuAlMn alloy in 0.9%NaCl solution of different pH values

Slika 3. Potenciodinamičke polarizacijske krivulje za CuAlMn leguru u 0.9% NaCl otopini različite pH vrijednosti

Potentiodynamic polarisation curve is composed of two branches: cathodic branch, which is the result of occurring cathodic reaction and the anode part which is the result of occurring the anodic reaction, in this case alloy dissolution. Cathodic parts of polarisation curves should reflect hydrogen evolution reaction due to deaeration of the solution with Ar, 20 minutes before immersion of electrode in electrolyte, as well as slow deaeration during investigation. Anodic parts of the curve describe corrosion of CuAlMn alloy and can be divided into different regions. First region is the apparent Tafel region in which dissolution of Cu and Al from the alloy surface occurs, accompanied by formation of complexes ($CuCl_2^-$) that diffuses from the surface of the electrode in a solution [11,12]. After first region anodic current density reach its maximum value and start to decrease which can be explained by the formation of the surface corrosion products which contains different chloride and oxide compounds, for example cuprous chloride (CuCl) and cuprous oxide (Cu_2O), as well as aluminium oxide/hydroxide (Al_2O_3/$Al(OH)_3$ and manganese oxide (MnO_2). As the corrosion product forms on the CuAlMn surface, the anodic reaction will be controlled by mass transfer process and for this reason the active dissolution of metals from the surface is reduced [13]

From the Figure 3 it can be seen that lowering the pH of the solution leads to an increase the anodic current density and also to shift the corrosion potential to negative values.

Corrosion parameters obtained from polarization measurements are presented in Table 1:

Table 1. Corrosion parameters obtained from polarization measurements

Tablica 1. Korozijski parametri određeni iz polarizacijskih mjerenja

pH	i_{corr} (μA cm^{-2})/	E_{korr} (V)/	R_p (kΩcm^2)
7.4	4.34	-0.320	5.950
5.4	4.97	-0.373	4.422
3.4	8.91	-0.389	2.272

From the Table 1 it is obvious the negative effect of reducing the pH of the NaCl solution on the corrosion stability of CuAlMn alloy, which is manifested by the reduction of the polarization resistance values and the increase the values of corrosion current density

3. Surface investigations

After polarization measurements corroded alloy surfaces were investigated by optical microscope (Figure 4). Images of CuAlMn alloy after polarization measurements reviled significantly damage surface due to intense corrosion process.

Detail surface morphology was examined by scanning electron microscope equipped with energy dispersive spectroscope (EDS), and the results are shown in Figure 5 and 6.

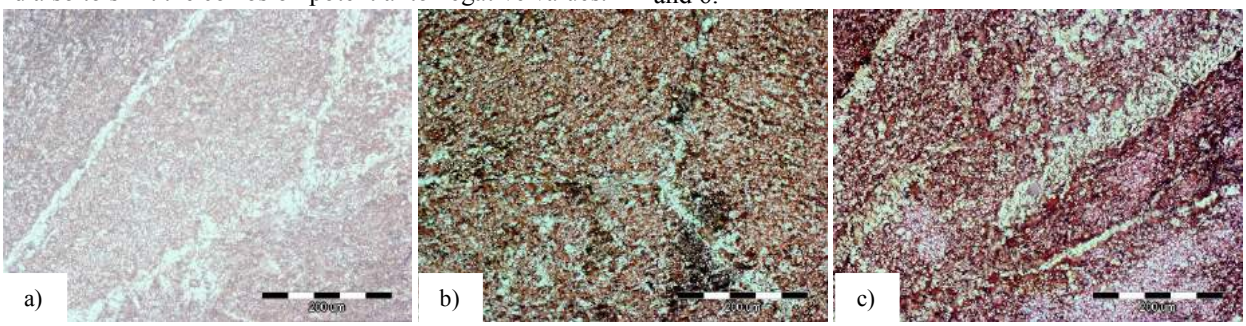

Figure 4. Optical micrograph of CuAlMn shape memory alloy after polarization measurements in 0.9% NaCl solution pH = 7.4 (a), pH = 5.4 (b) and pH = 3.4 (c)

Slika 4. Snimke površine legure CuAlMn optičkim mikroskopom nakon polarizacijskih ispitivanja u 0.9% NaCl otopini pH = 7.4 (a), pH = 5.4 (b) i pH = 3.4 (c)

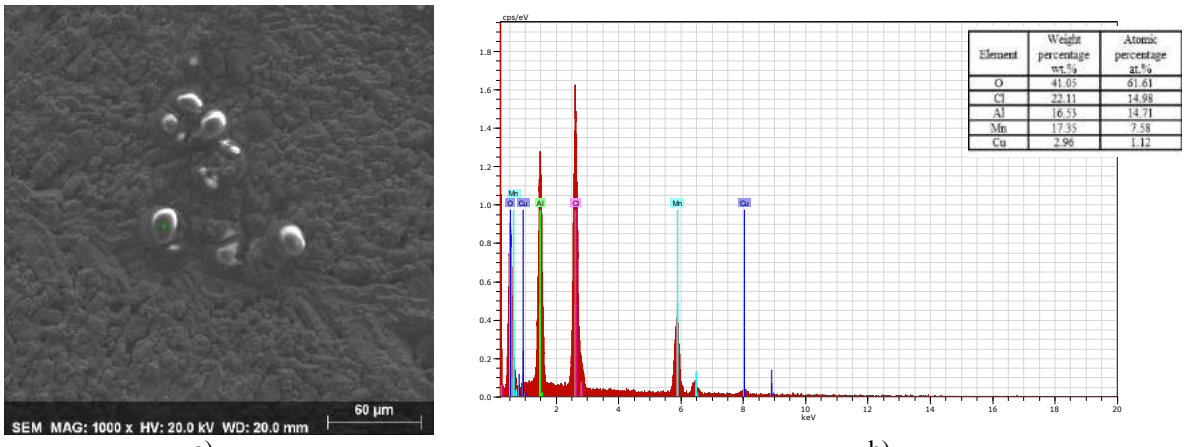

Figure 5. SEM images of CuAlMn alloy surface after polarization measurements in 0.9% naCl solution (T = 37 °C, pH = 5.4) (a) and EDS analysis for marked position on surface (b)

Slika 5. SEM snimka površine CuAlMn legure nakon polarizacijskog mjerenja u 0.9% NaCl otopini (T = 37 °C, pH = 5.4) (a) i EDS analiza za označenu poziciju na površini (b)

Surface damages as well as partially undissolved corrosion products are clearly visible at the figure 5 a). EDS analysis confirmed that the corrosion products are rich in O, Cl, Al and Mn, with the small quantities of Cu, which could corresponds to aluminium oxides, hidroxides and oxychloride complexes, as well as manganese oxide and chloride with the small quantities of copper oxide and chloride.

The matrix around the corrosion products consist mostly of copper (Fig 6) which is the main element in alloy.

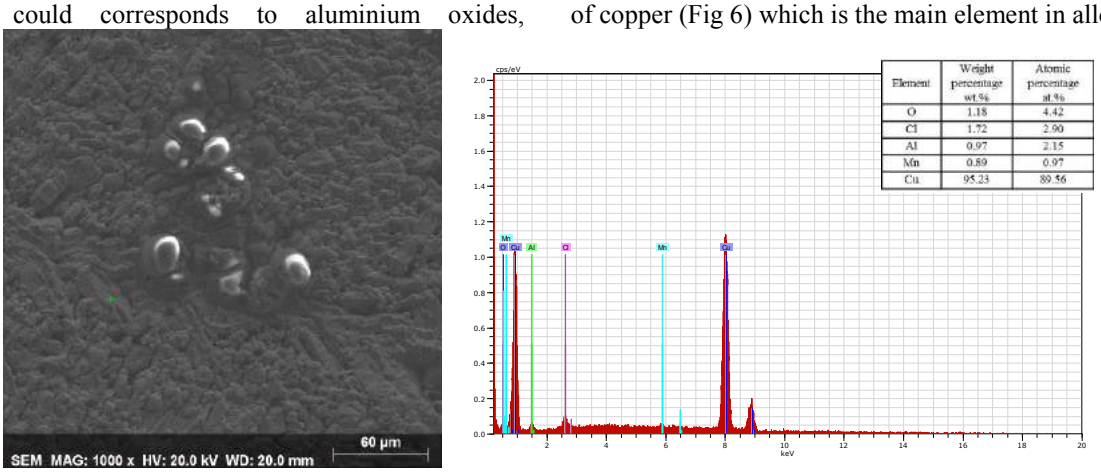

Figure 6. SEM images of CuAlMn alloy surface after polarization measurements in 0.9% naCl solution (T = 37 °C, pH = 5.4) (a) and EDS analysis for marked position on surface (b)

Slika 6. SEM snimka površine CuAlMn legure nakon polarizacijskog mjerenja u 0.9% NaCl otopini (T = 37 °C, pH = 5.4) (a) i EDS analiza za označenu poziciju na površini (b)

4. Conclusions

- Lowering pH values of 0.9% NaCl solution leads to changes of E_{oc} of CuAlMn alloy to the negative direction.
- Polarization measurements were shown that decreasing pH values of 0.9% NaCl solution leads to reduction of the polarization resistance values and the increase the values of corrosion current density
- Optical and SEM images of CuAlMn alloy after polarization measurements reviled significantly damage surface due to intense corrosion process.
- EDS analysis confirmed that the corrosion products are rich in O, Cl, Al and Mn, with the small quantities of Cu, while the matrix around the corrosion products consist mostly of copper.

Acknowledgements

This work has been fully supported by Croatian Science Foundation under the project IP-2014-09-3405.

REFERENCES

[1] Memory alloys (Part II): Clasification, Production and Application, Kem. Ind., 63, p 331-344

[2] Gojić M., Vrsalović L., Kožuh S., Kneissl A., Anžel I., Gudić S., Kosec B., Kliškić M., (2011), *Electrochemical and microstructural study of Cu-l-Ni shape memory alloy*, J. Alloys Compd., 509, p 9782-9790

[3] Lagoudas C. D., (2008), *Shape memory alloys modelling and engineering applications*, Springer, Spring Street, New York, USA.

[4] Ivanić, I., Gojić, M., Kožuh, S., (2014), *Shape memory alloys (Part I): Significant properties*, Kem. Ind., 63, p 323-330

[5] Kneissl A. C., Unterweger E., Bruncko M, Lojen G., Mehrabi K., Scherngell H., (2008), *Microstructure and Properties of NiTi and CuAlNi Shape Memory Alloys*, MJoM, 14, p 89-101

[6] Figuera N., Silva T. M., Carmezim M. J., Fernandes J. C. S., (2009), *Corrosion behaviour of NiTi alloy*, Electrochim. Acta, 54, p 921-926

[7] Ivanić I, Kožuh S., Kosel F., Kosec B., Anžel I, Bizjak M., Gojić M. (2017), *The influence of heat treatment on the microstructure and mechanical properties of aluminium bronze*, Engneering Faiure Analysis, 77, p 85-92

[8] Datta S., Bhunya A., Banerjee M. K., (2001), *Two way shape memory lost in CuZnAl alloy*, Materials Science and Engineering A, 300, p 291-298

[9] Mallik U. S., Sampath V., (2008), *Effect of alloying on microstructure and shape memory characteristics of Cu–Al–Mn shape memory alloys*, Materials Science and Engineering A, 481–482, p 680–683

[10] Kumar P., Jain A. K., Hussain S., Pandey A., Dasgupta R., (2015), *Changes in the properties of Cu-Al-Mn shape memory alloy due to quaternary addition of different elements*, Revista Materia, 20, p 284-292

[11] Gomez de Salazar J. M., Soria A., Barrena M. I. (2005), *Corrosion behaviour of Cu-based shape memory alloys, diffusion bonded*, Journal of Alloys and Compounds, 387, p 109-114.

[12] Benedeti A.V., Sumodjo P. T. A., Nobe K. Cabot P. L., Proud W. G., (1995), *Electrochemical studies of copper, copper –aluminium and copper-aluminium-silver alloys: impedance results in 0.5M NaCl*, Electrochim. Acta 40, p 2657-2668.

[13] Saud S. N., Hamzah E., Abubakar T., Bakhsheshi-Rad H. R., (2015), *Correlation of microstructural and corrosion characteristics of quaternary shape memory alloys Cu-Al-Ni-X (X = Mn or Ti)*, Trans. Nonferrous Met. Soc.China, 25, p 1158-1170.

ISSN 1847-7917

Weldability of S460M high strength low-alloyed steel

Anatoliy ZAVDOVEEV[1)], Valeriy POZNIAKOV[1)], Massimo ROGANTE[2)], Sergey JDANOV[1)], Andrey MAKSIMENKO[1)]

1) Paton Electric Welding Institute of NAS, Bozhenko n. 11, 03680 Kiev, **Ukraine**
2) Rogante Engineering Office, I-62012 Civitanova Marche, **Italy**

main@roganteengineering.it

Keywords

High strength low-alloyed steel
Welded joints
Construction
Gas metal arc welding

Scientific paper

Abstract: Structural steels with yield strength of 460MPa (S460M) and higher are used in the construction of bridges, buildings and wind turbine towers, as well as in the manufacture of metal structures for rail freight transport. The use of high-strength rolled stock allows up to 80% decrease of the total metal content in structures in comparison with the products of St3 and 09G2S. In the constructions made of low-alloy steels of such strength class, it becomes a relevant issue the study of their weldability. It is known that in the welding process a metal heat affected zone (HAZ) undergoes structural transformations that lead to changes in mechanical properties. In this regard, this article examines the impact of thermal welding cycles on properties and structure of the metal HAZ, particularly the resistance to cold cracking. It justified, also, the choice of welding consumables for steel grade S490 strength, and the changes in the mechanical properties of welded joints are analysed.

1. Introduction

The development of modern constructions and energy industries puts force on new demands for metal ware in the case of their steel intensity and increasing of reliability[1-8]. This effect could be reached by adopting new high strength steels with yield stress more than 390MPa. Structural steel of such class of strength is used in building industry, bridge construction, wind energy for wind tower and also for metal ware of railway transport[1,6]. The application of high strength steels gives opportunity to reduce the overall weight up to 80% (Figure 1) in comparison with steels of 300MPa strength (for instance, st.3, 09G2S - former USSR GOST, approximately S300 grade according to the EN10025-4 norm)[5]. In the modern industry, to develop steels with improved mechanical characteristics (increased level of strength), two approaches are used.

The first consist in the application of alloying elements, i.e. increased strength value of steel. This method, nevertheless, leads to significant rise in price of manufactured rods.

An alternative path for the alloying procedure is thermal mechanical cold processing (TMCP). Such kind of steel is high strength low alloyed (HSLA) steel grade S460M (490MPa level of strength, EN:10025-4), micro-alloyed with Nb and V. It has the following mechanical properties: YS > 460 MPa; UTS = 540÷720 MPa; δ_5 > 18 %; KCV_{-40} > 27 J/cm^2. These mechanical characteristics of the S460M steel are conditioned by refined structure, obtained by TMCP. During a construction employing HSLA steels, the problem of their weldability arises [3]. A number of definitions for weldability exists, but in our consideration we hold with the following one: weldability is the ability of welded metal to form monolithic joints with equal properties. It is commonly known that during a welding process, the HAZ metal is subjected to the influence of high temperature (up to the melting point in fusion line), thus structural changes occur, resulting in changes of mechanical properties [4]. In this connection, in the current work we are considering the effect of thermal cycle of welding (TCW) on structure and properties of HAZ metal of S460M steel.

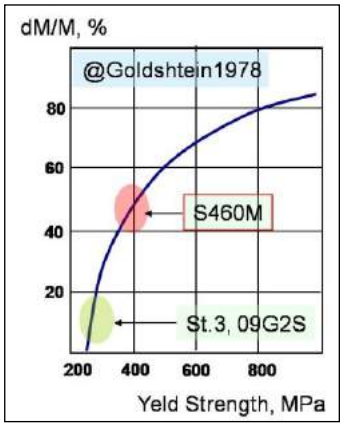

Figure 1. Steel intensity changes vs. strength grade.

2. Materials and method

For the experiments, the structural steel S460M was selected having a thickness of 16 mm. The chemical composition is reported in Table 1 and the mechanical properties in Table 2.

Symbols/Oznake

YS	- Yield Stress, MPa	$W_{6/5}$	- Cooling rate (600÷500ºC range), ºC/s
UTS	- Ultimate Tensile Stress, MPa	δ_5	- Elongation for failure, %
HAZ	- Heat affected zone	KCV_{-40}	- Impact toughness at −40ºC (Charpy test), J/cm^2
Ua	- Voltage of arc	Iw	- Welding current, A-
Vw	- Welding speed, m/h		

Table 1. As received steel S460M: chemical composition, wt.%

C	Si	Mn	Cr	Ni	V	Nb	Al	S	P
0.15	0.23	1.3	0.09	0.019	0.01	0.05	0.025	0.013	0.017

Table 2. As received steel S460M: mechanical properties

σ_T, MPa	σ_B, MPa	δ_5, %	ψ, %
480	600	27	58

For the criterion of TCW, the cooling rate ($W_{6/5}$) was chosen of heated up to 1300 ºC metal in the temperature range of 600÷500 ºC (interval of minimum equilibrium of austenite).

Based on the research results, the cooling rates were determined at which the HAZ metal strength, ductility and toughness indexes decrease in comparison with the regulated requirements for welded joints. The change in the mechanical properties in relation to the HAZ metal cooling rate in the 600÷500 °C temperature range was studied with 120×12×12 mm model samples, which were heat-treated in accordance with welding thermal cycles at the MCP-75 unit [9]. The heat treatment process was the following. The samples, crossed by current were firstly heated to temperatures in the range 1200÷1300 ºC, which are typical for the coarse grain heat affected zone (CGHAZ) of welded joints. The heating rate was in the range 150÷170 ºC/s, which corresponds to the conditions of metal heating in the zone of thermal influence during arc welding processes. The samples were held at such temperature for approximately 2 seconds, then they were forcedly cooled.

For a static tensile test of the steel, cylindrical samples (3 for each cooling rate) with a 6 mm diameter of the working part of were mechanically manufactured (type II in accordance with GOST 6996-96, equal to ISO 6892:1998 norm). The tests were carried out at ambient temperature.

For impact toughness determination, the Charpy impact tests were carried out at the temperatures of +20, −20 and −40 °C (type IX GOST 6996-96, i.e. 10×10×55 mm with V-notch, according to the ASTM A370 norm).

The welding process was carried out via different types of consumables and modes, as reported in Table 3.

The shield metal arc welding (SMAW) of the S460M steel joints was carried out with the UONI-13/55 and FOX EV-50 4.0 mm electrodes using the following modes: Iw = 160–170 A; Ua = 24–25 V; Vw = 8.5–9 m/h. For the gas metal arc welding (GMAW) the solid wires Sv-08G2S and G3Si1 and the 1.2 mm diameter powder wire of Megafil 821R were used. The welding process was carried out in a gas mixture of 82% Ar + 18% CO_2 at the following modes:

- when using wire of solid cross-section: Iw = 170–190 A; Ua = 26–28 V; Vw = 12 m/h
- when using powder wire: Iw = 220–240 A; Ua = 28–30 V; Vw = 15 m/h.

Table 3. Welding consumables characteristic.

Consumable	Type	C, %	Si, %	Mn, %
Fox ev 50*	electrode	0.08	0.4	1.2
G3Si1*	wire	0.08	0.7	1.3
Megafil 821R*	Powder wire	0.05	0.5	1.3
Uoni 13/55**	electrode	0.04	0.7	1.5
Sv-08G2S**	wire	0.08	0.7	1.8
Note: * and **: see correspondences in Table 4				

3. Results and discussion

Structure and mechanical properties of as received metal are the following. Thermomechanically hardened steel S460M (strength class 440MPa) was manufactured according to the EN 10025-4:2007 norm at the Mariupol metallurgical plant, Ukraine. Due to the thermo-mechanical rolling and controlled cooling in the temperature range of 900÷700 ºC (TMCP) in S460M steel, a ferrite-pearlite, banded structure with a Vickers hardness of 195HV is formed (see Figure 2).

A slight contamination was observed, with non-metallic inclusions such as silicates, alumino-silicates, sulphides and oxysulfide. The fracture toughness of the S460M steel is significantly higher than the standard values of $KCV_{-40} \geq 34$ J/cm^2 even at a test temperature of −60 ° C ($KCV_{-60} = 76$ J/cm^2).

The dependencies characterizing the changes in the strength and ductility parameters in the simulated metal of the HAZ of S460M steel under the influence of TCW are shown in Figures 3 and 4.

The results indicate that with the change in the cooling rate from 3 to 25 ºC/s in the temperature range 600÷500 ºC ($W_{6/5}$) the indices of the HAZ metal strength increase in comparison with the initial state, namely YS from 490 to 810 MPa and UTS from 600 to 1000 MPa.

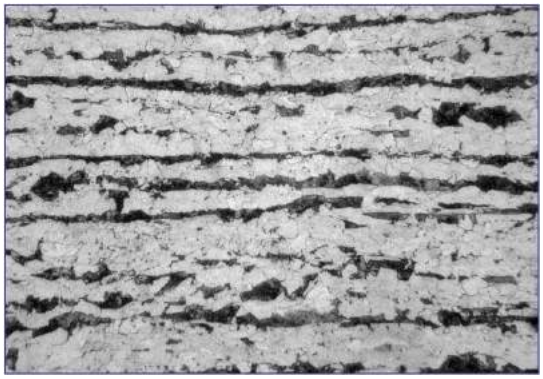

Figure 2. Microstructure of as received S460M steel (×500).

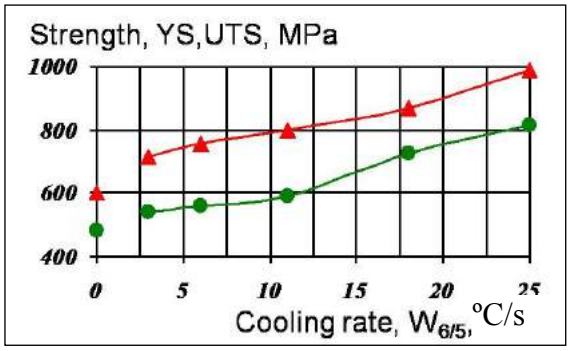

Figure 3. Yield (green) and ultimate tensile (red) strength in dependence of cooling rate for the S460M steel.

At the same time, the plastic properties of the simulated HAZ metal deteriorate in comparison with the initial state. This is especially true concerning the indices of relative elongation, which are reduced by 2.5 times, while the relative elongation is reduced by 15–20%.

In the impact bending tests of samples with a V-notch, the impact toughness of the S460M steel HAZ metal decreases with respect to the base metal (see Figure 5). The most significant decrease in the KCV values is from 4 to 9 times in the samples that cooled at the rate $W_{6/5}$ = 3 ºC/s (from 111 to 33 J/cm^2 at the test temperature of +20 ºC, from 109 to 15 J/cm^2 at the temperature of −20 ° C and from 95 to 10 J/cm^2 at a temperature of −40 °C). With an increase in the cooling rate to 10 ºC/s, they increase to KCV_{-40} = 27 J/cm^2, then they decrease somewhat and at $W_{6/5}$ = 25 °C/s they result: KCV_{+20} = 50 J/cm$_2$; KCV_{-20} = 30 J/cm^2; KCV_{-40} = 20 J/cm^2 (for comparison of the impact toughness of the S460M steel at test temperatures in the range from +20 ° C to −40 ° C are within 95−110 J/cm^2).

Such changes in the mechanical properties of the S460M steel HAZ metal are due to various structural transformations in the range of the studied cooling rates. This is evidenced by the results of metallographic studies, which showed that a structure consisting of different morphological forms of ferrite and a small amount of perlite is formed in the CGHAZ metal of the S460M steel at a cooling rate of $W_{6/5}$ = 3 ºC/s (Figure 6).

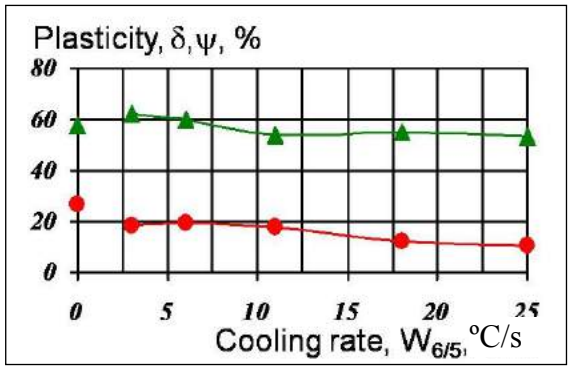

Figure 4. Relative reduction (green) and relative elongation (red) in dependence of cooling rate for the S460M steel.

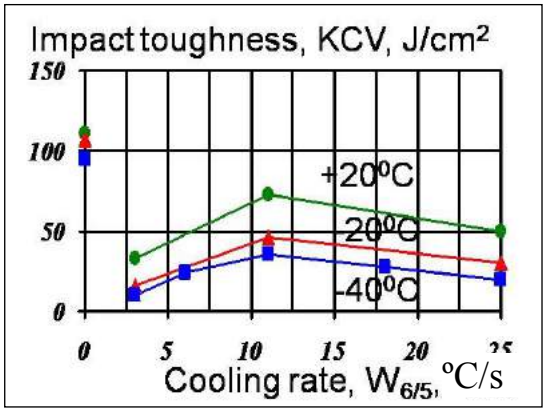

Figure 5. Impact toughness in dependence of cooling rate for the S460M steel.

The hardness of such metal is 240 HV, and the bands of its structure, as observed before the thermal cycle, disappears completely. An equiaxial ferrite-pearlite with a bainitic component is formed with a finely dispersed structure, with an increase in $W_{6/5}$ to 10 ºC/s. The grain size, in this case, slightly increases to 15 mkm and the hardness is almost unchanged, although the strength indicators increase by ≈100 MPa. With a further increase in the cooling rate to $W_{6/5}$= 25°C/s in the imitated CGHAZ metal, a structure is formed consisting of a mixture of upper and lower bainite and a small amount of martensite and ferrite. Due to this fact, the hardness of the metal rises to HV = 2800 MPa, which in turn leads to an increase in the indices of its static strength and the drop in plastic properties. The analysis of the test results shows that the welds made by the FOX EV 50 electrodes, according to the EN 10025-4:2007 norms, correspond to the S460M steel requirements, and the solid wire G3Si1 wire and powder wire Megafil 821R too (Table 4, *). Somewhat lower by 5-13% of the normative indices, the value of the yield stress of welded joints of S460M steel made by UONI-13/55 and Sv-08G2S wires, which are 440 and 400 MPa, respectively. At the same time, the tensile strengths and the elongation (δ5 = 31%) exceed their minimum standard values for steel (Table 4, **).

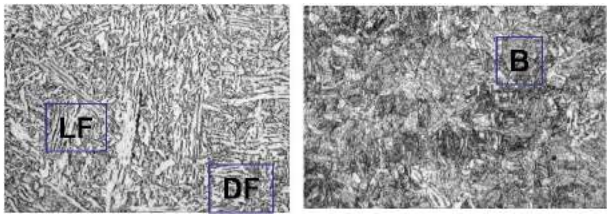

Figure 6. Microstructure of CGHAZ of the S460M steel: left $W_{6/5}$ = 3ºC/c, left; $W_{6/5}$ = 25 ºC/c, right (×500).

Table 4. Mechanical properties of as welded metal.

	YS, MPa	UTS, MPa	Δ_5, %
*	460	540-720	17
**	440	556	31
as	480	600	27
Notes: as = as received * and ** correspond to the consumables listed in Table 3 and similarly marked			

The high values of the yield strength and tensile strength in relation to the welds made with UONI-13/55 electrodes and Sv-08G2S wire correspond to a metal deposited with FOX EV-50 electrodes, as well as in a gas mixture of G3Si1 solid wire and Megafil 821R powder wire respectively. On the other hand, the indices of relative elongation in GMAW, although lower than those for the metal deposited by coated electrodes, exceed the standard values for the base metal.

A particular attention is drawn to the fact that the strength and ductility parameters of the welds made by the UONI-13/55 electrodes and solid wire Sv-08G2S are quite close. This is evidenced by the results of metallographic studies, which showed that the structure of such samples is finely dispersed and consists predominantly of polygonal ferrite with insignificant perlite inclusions along the boundaries of ferrite grains with hardness 200 HV. When welding with Megafil 821R powder wire, however, the metal structure results mainly of structurally free ferrite with an insignificant content of coarse-grained ferrite. The hardness, in this case, is 210 HV, which leads to an increase in strength and a reduction of plastic properties. The metal structure in the CGHAZ of welded joints made of S460M steel is identified as coarse-grained ferrite-pearlite with an approximately equal ratio of ferritic and pearlite constituents and a hardness in the range of 200÷221 HV. According to the tests results of specimens with a sharp notch, it is established that all these combinations of steel-welding material are able to provide the impact toughness of both weld metal and the HAZ metal of welded joints of the S460M steel at the level of the requirements of the EuroNorm, namely $KCV_{-40} \geq 27$ J/cm^2.

4. Conclusions

It is proven that in the cooling rates range of $7 \leq W_{6/5} \leq 15$ ºC/s related to the HAZ metal of the S460M steel samples model, the values of static strength, ductility and impact toughness at the level of the base metal are retained.

It is shown that the application of welding consumables such as Megafil 821R powder wire, solid wire G3Si1 and FOX EV 50 electrodes during the welding of S460M steel provides good quality of the welded metal, satisfying the EuroNorm requirements.

Acknowledgements

Financial supports through NAS of Ukraine project (#113) for young scientists "Effect of thermal cycle of welding and high temperature isothermal heating on structure and properties of steel grade S355J2 and S460M" are acknowledged.

REFERENCES

[1] Ufuah E., (2013), *Elevated Temperature Mechanical Properties of Butt-Welded Connections Made with High Strength Steel Grades S355 and S460M*, Design, Fabrication and Economy of Metal Structures International Conference Proceedings, p. 407-412 Hungary

[2] Nazarov N., Yakushev E.,, Shabalov I., Morozov Yu., Kireeva T., (2014), *Comparison of weldability of high-strength pipe steels microalloyed with niobium, niobium and vanadium*, Metallurgist 7(9-10), p. 911-917 Russia

[3] Ragu Nathan S., Balasubramanian V., Malarvizhi S., (2015), *Effect of welding processes on mechanical and microstructural characteristics of high strength low alloy naval grade steel joints*, Defence Technology 11, p. 308-317 Great Britain

[4] Poznyakov V., Jdanov S., Maksimenko A., (2012), *Structure and properties of welds made from S355J2 steel*, Automatic welding 8, p. 7-11 Ukraine

[5] Bilik A., Kurashev R., Gorbatenko V., Konovalov G., (2013), *Application of TMCP rolled in weldwd metallic constructions*, Industrial construction and engineering structures 4, p. 1-4 Ukraine

[6] Odesskiy P., Molodtsov A., Morozov Yu., (2011), *New effective low-alloyed steels for building metallic constructions*, Mounting and especial works in building 5, p. 20-25 Ukraine

[7] Lobanov L., (1993), *Welded building structures*, Naukova Dumka, Ukraine

[8] Tilkin M., Bolshakov V., Odesskiy P., (1983), *Structure and properties of building steel*, Metallurgy, Russia

[9] Sarjevskiy V., Sazonov V., (1981), *Equipment for thermal cycle of welding imitating based on MSR-75 machine*, Automatic welding 5, p. 69-70 Ukraina

Zagrijte se za uštedu.

Odabir EVN zemnog plina
nećete ni osjetiti…
Osim toplinom.

Zemni plin jedan je od najpovoljnijih izvora energije na tržištu.
Potrošnja se može precizno regulirati i kontrolirati kako biste plaćali ono što zaista trebate.
Odaberite EVN i cijele godine budite ugodno i sigurno opskrbljeni zemnim plinom.

Priključite se na EVN zemni plin.
0800 820 820

www.evn.hr

Za ugodniji život. EVN